



UNIVERSITY OF
PORTSMOUTH

Modelling non-linear structure formation with modified gravity and massive neutrinos

William Simcoe Wright

Institute of Cosmology and Gravitation

This thesis is submitted in partial fulfilment of
the requirements for the award of the degree of
Doctor of Philosophy of the University of Portsmouth.

SUPERVISORS:

Kazuya Koyama

Gong-bo Zhao

David Wands



Science & Technology
Facilities Council

December 2019

Abstract

The observation that distant Type Ia supernovae, the explosive death of massive stars, were fainter than possible in a non-accelerating expanding universe lead to one of the most significant paradigm shifts in cosmology since Einstein's introduction of General Relativity. Yet could the former have been the first signal that the latter's reign as the dominant theory of gravity is approaching its own demise? Within the bounds of General Relativity, the simplest way to explain the late-time accelerating expansion of the Universe required by the supernovae observations is to add a small, positive valued cosmological constant Λ , whose negative pressure causes the acceleration. Along with cold dark matter, the cosmological constant forms the basic of the current concordance cosmological model. Other additional components of the Universe, under the general label of dark energy, can replace Λ . However, what if a modification to the theory of gravity could explain the observed acceleration instead? We will see that the quest to answer this question is an uphill path which entails many steps that have been overcome already and many that have yet to be surmounted.

Modified gravity theories exist that can produce accelerating expansion without a cosmological constant, typically through the introduction of a scalar field that couples to matter via the gravitational metric, thus modifying the strength of gravity. In some modified gravity theories, the expansion history of the Universe in the Λ -cold-dark-matter model can be reproduced almost perfectly. For such theories, the best signal to search for becomes the modification to the strength of gravity. However, some theories have a so-called screening mechanism built in, whereby in high density environments the modifications to the strength of gravity become negligible, making tests of these theories in the confines of the solar system ineffective. Therefore, one of the best regimes to investigate modified gravity is on cosmological scales, where the large-scale clustering of structure in the Universe would be enhanced relative to General Relativity. Indeed, many upcoming galaxy surveys plan to constrain just such an enhancement.

However, this too is not as simple as it might seem. Neutrinos, one of the fundamental particles of the Universe, have been shown to have mass since the observation of accelerating expansion. As a result, massive neutrinos don't cluster on scales smaller

than their free-streaming length. This free-streaming effect causes a suppression of structure formation that is dependent on the neutrino masses. Again, placing a constraint on neutrino masses is a key aim of many upcoming galaxy surveys. However, this sets up a potential degeneracy between the enhancement of structure formation due to modified gravity and the suppression due to massive neutrinos. For example, the large-scale structure of a universe with General Relativity and light neutrinos could be statistically similar to that of a universe with a strong modification to gravity and heavier neutrinos. Finding ways to break this degeneracy is vital if upcoming galaxy surveys are to simultaneously constrain modified gravity and neutrino masses.

In this thesis, we present a code, **MG-PICOLA**, which is capable of simulating structure formation with the scale-dependent effects of both modified gravity and massive neutrinos. We have included a method to estimate the screening effect for three different mechanisms, which allowed us to build a variety of modified gravity models in to **MG-PICOLA**. We show that while **MG-PICOLA** uses a fast, approximate simulation method, its output matches that of full N -body simulations up to quasi-non-linear scales. We next investigate whether redshift-space distortions in the clustering of large-scale structure offer a way to break the modified gravity-massive neutrino degeneracy. We do so by including both effects in the Taruya-Nishimichi-Saito model of redshift-space distortions that is implemented in the **MG-Copter** perturbation theory code, and compare the output of the model to that of **MG-PICOLA** simulations at the level of the dark matter distribution. We find that our model is capable of capturing the degeneracy breaking potential that we present in the redshift-space dark matter power spectrum multipoles. We also investigate how the degeneracy evolves with redshift and demonstrate again how our model captures the redshift evolution at the level of the dark matter distribution. However, we cannot observe the distribution of dark matter directly, only through galaxies, which act as a biased tracer. Therefore, we extend our **MG-Copter**-based redshift-space distortion model to include bias and fit it to friends-of-friends halo catalogues produced from **MG-PICOLA** simulations using a Markov Chain Monte Carlo approach. We demonstrate that the model fits recover a linear bias that is consistent with that estimated from the simulations. Throughout we find that the best-fit parameters are sensitive to the fitting setup only when the modified gravity and neutrino mass parameters in the model don't match those in the simulation, which can help constrain the two effects. We also find that the redshift-space halo power spectrum multipoles have larger degeneracy breaking potential than their dark matter counterparts, and that our extended model is effective at capturing the behaviour seen in the multipoles of the simulated halo catalogues.

Table of Contents

Abstract	i
List of Tables	vi
List of Figures	vii
Declaration	xi
Dissemination	xii
Acknowledgements and Dedication	xiii
Conventions, Constants, and Abbreviations	xiv
1 Introduction	1
1.1 Cosmological overview	1
1.2 Modified Gravity	5
1.3 Massive Neutrinos	9
1.4 Degeneracy	12
1.5 Structure formation	14
1.5.1 Standard perturbation theory	16
1.5.1.1 SPT for Λ CDM	16
1.5.1.2 SPT with modified gravity	20
1.5.2 Lagrangian perturbation theory	21
1.5.2.1 LPT in Λ CDM	24
1.5.3 Redshift-space distortions	27
1.5.3.1 TNS Model	29
1.6 Simulations	31
2 COLA with scale-dependent modified gravity and massive neutrinos	35
2.1 2LPT for general scale-dependent growth	36

2.2	2LPT for modified gravity	44
2.3	2LPT for massive neutrinos	45
2.4	2LPT for modified gravity and massive neutrinos	51
2.5	Modifying the particle mesh computation	57
2.5.1	Screened modified gravity theories in PM	57
2.5.1.1	$f(R)$ gravity	57
2.5.1.2	nDGP	58
2.5.2	Massive neutrinos in PM	59
2.6	MG-PICOLA results	60
2.6.1	Modified Gravity without massive neutrinos	60
2.6.1.1	$f(R)$ gravity	60
2.6.1.2	nDGP	61
2.6.1.3	Dependence on the number of steps	62
2.6.2	Adding massive neutrinos	64
3	Dark matter redshift-space distortions with MG and m_ν	78
3.1	Implementation of massive neutrinos	79
3.2	Validation	81
3.3	Degeneracy	87
3.3.1	Real- and redshift-space	88
3.3.2	Redshift evolution	90
4	Halo redshift-space distortions with MG and m_ν	95
4.1	Halo RSD Model	95
4.2	Simulations	101
4.3	Results	102
5	Discussion and Conclusions	111
5.1	Summary of results	111
5.2	Future work	114
A	MG-PICOLA implementation details	116
B	Summary of the general equations solved by MG-PICOLA	117
C	MG-PICOLA implementation of general $\{m(a), \beta(a)\}$ models	119
D	Modified gravity models	121
D.1	$f(R)$ gravity	121

D.2	nDGP gravity	122
D.3	Symmetron	122
D.4	Dilaton	123
E	Comparison of MG-PICOLA neutrino approach to SPT and alternative schemes for modelling the non-linear neutrino density	124
	UPR16 Form	127
	Ethics Certificate	128
	Bibliography	130

List of Tables

1	Physical Constants	xv
2	Abbreviations	xv
2.1	The cosmological parameters for the simulations performed for Chapter 2.	71
3.1	Survey parameters for a DESI-like survey computed from the information for emission line galaxies (ELGs) in Table V of [1] used in in Section 3.3.	87
4.1	The cosmological parameters for the simulations performed for Chapter 4.	101
4.2	Best fit model parameters, χ^2 and convergence values for the halo RSD model fits using the initial fitting setup.	102
4.3	Best fit model parameters, χ^2 and convergence values for the halo RSD model fits using the refined fitting setup.	104

List of Figures

1.1	The suppression of the matter power spectrum by different masses of neutrinos at $z = \{0, 1, 9\}$	12
1.2	The combined enhancement and suppression of the matter power spectrum by different strengths of $f(R)$ gravity and masses of neutrinos at redshift $z = 1$	13
2.1	The ratio of $D_2(k, k_1, k_2, \cos \theta, a = 1)$ to the approximation $D_2(k, a = 1)(1 - \cos^2 \theta)$ for three different triangle configurations.	46
2.2	Comparison between CAMB and the fitting formula method Eq. (2.42) for the ratio of the first order CDM+baryon growth factor at $z = 0$ to $z = 1$ for a GR + massive neutrino cosmology with $m_\nu = \{0.2, 0.4, 0.6\}$ eV.	49
2.3	The value of μ_{m_ν} as a function of k calculated using Eq. (2.38) at $z = 0$ for both GR and F4 cosmologies with neutrinos of mass $m_\nu = \{0.2, 0.4, 0.6\}$ eV.	50
2.4	Comparison between MGCAMB and the fitting formula method Eq. (2.42) for the ratio of the first order CDM+baryon growth factor at $z = 0$ to $z = 1$ for a $f(R)$ + massive neutrino cosmology with $ f_{R0} = 10^{-4}$ and $m_\nu = \{0.2, 0.4, 0.6\}$ eV.	52
2.5	Comparison between MGCAMB and the fitting formula method Eq. (2.42) for the ratio of the first order CDM+baryon growth factor at $z = 0$ to $z = 1$ for a symmetron + massive neutrino cosmology with $\beta_\star = 1$, $a_\star = 0.5$, $\xi_\star = 1/2998$, and $m_\nu = \{0.2, 0.4, 0.6\}$ eV.	53
2.6	Comparison between MGCAMB and the fitting formula method Eq. (2.42) for the ratio of the first order CDM+baryon growth factor at $z = 0$ to $z = 1$ for a dilaton + massive neutrino cosmology with $\beta_0 = 0.41$, $\xi_0 = 1/2998$, $S = 0.24$, $R = 1$, and $m_\nu = \{0.2, 0.4, 0.6\}$ eV.	53
2.7	The linear total matter power spectrum at $z = 1.3$ for a GR + massive neutrino cosmology with $m_\nu = \{0.2, 0.4, 0.6\}$ eV, calculated using both CAMB and the fitting formula method Eq. (2.42).	54

2.8	The linear total matter power spectrum at $z = 1.3$ for a $f(R)$ + massive neutrino cosmology with $ f_{R0} = 10^{-4}$ and $m_\nu = \{0.0, 0.2, 0.4, 0.6\}$ eV, calculated using both MGCAMB and the fitting formula method Eq. (2.42).	55
2.9	The linear total matter power spectrum at $z = 1.3$ for a symmetron + massive neutrino cosmology with $\beta_\star = 1$, $a_\star = 0.5$, $\xi_\star = 1/2998$, and $m_\nu = \{0.0, 0.2, 0.4, 0.6\}$ eV, calculated using both MGCAMB and the fitting formula method Eq. (2.42).	55
2.10	The linear total matter power spectrum at $z = 1.3$ for a dilaton + massive neutrino cosmology with $\beta_0 = 0.41$, $\xi_0 = 1/2998$, $S = 0.24$, $R = 1$, and $m_\nu = \{0.0, 0.2, 0.4, 0.6\}$ eV, calculated using both MGCAMB and the fitting formula method Eq. (2.42).	56
2.11	The matter power spectrum at $z = 0$ obtained from L-PICOLA using a fixed mesh with $N = 1024^3$ gridcells in a box of size $B = 1024$ Mpc/ h and using $n = 30$ time steps compared to a high-resolution N -body simulation (RAMSES) using the same initial conditions.	63
2.12	The ratio of the matter power spectrum in $f(R)$ to that in Λ CDM at $z = 0$ when using the true growth-factor(s) or using the Λ CDM ones plus the effect of including the screening method. Here we have used $n = 10$ time steps.	64
2.13	The ratio of the matter power spectrum in $f(R)$ to that in Λ CDM at $z = 0$.	65
2.14	The ratio of the velocity divergence power spectrum in $f(R)$ to that in Λ CDM at $z = 0$.	66
2.15	The ratio of the halo mass function at $z = 0$ in $f(R)$ to that in Λ CDM.	67
2.16	The ratio of the matter power spectrum at $z = 0$ in nDGP to that in Λ CDM.	68
2.17	The ratio of the velocity divergence power spectrum in nDGP to that in Λ CDM at $z = 0$.	69
2.18	The ratio of the halo mass function in nDGP to that in Λ CDM at $z = 0$.	70
2.19	The ratio of the matter power spectrum (left) and halo mass function (right) in $f(R)$ to that in Λ CDM at $z = 0$ for the two $f(R)$ models F5 and F6 for different number of time steps.	71
2.20	The ratio of the matter power spectrum (left) and halo mass function (right) in nDGP to that in Λ CDM at $z = 0$ for the two nDGP models nDGP2 and nDGP3 for different number of time steps.	72

2.21	The CDM matter power spectrum $P(k, z = 0)$ for Λ CDM in our COLA simulations compared with the result of [2].	73
2.22	The matter power spectrum $P(k, z = 0)$ for several values of the sum of neutrino masses relative to the power spectrum with $m_\nu = 0.0$ for Λ CDM.	74
2.23	The matter power spectrum $P(k, z = 0)$ for several values of the sum of neutrino masses relative to the power spectrum with $m_\nu = 0.0$ for $f(R)$ gravity with $ f_{R0} = 10^{-4}$	75
2.24	The halo mass-function $n(M, z = 0)$ for Λ CDM for several values of the sum of neutrino masses relative to the mass-function with $m_\nu = 0.0$	76
2.25	The halo mass-function $n(M, z = 0)$ for $f(R)$ for several values of the sum of neutrino masses relative to the mass-function in Λ CDM with $m_\nu = 0.0$	77
3.1	Real-space non-linear power spectra for various gravity models and neutrino masses at $z = 1$	83
3.2	Non-linear to linear ratio of real-space power spectra for various gravity models and neutrino masses at $z = 1$	84
3.3	Ratio of real-space non-linear power spectra for various gravity models with and without neutrino mass at $z = 1$	85
3.4	Redshift-space non-linear power spectra for various gravity models and neutrino masses at $z = 1$	86
3.5	Non-linear to linear (Kaiser) ratio of redshift-space power spectra for various gravity models and neutrino masses at $z = 1$	87
3.6	Ratio of redshift-space non-linear power spectra for various gravity models with and without neutrino mass at $z = 1$	88
3.7	Difference between the redshift-space multipoles with and without neutrino mass $\chi^2_{m_\nu}$ as a function of the maximum scale k_{max} at $z = 1$ for GR, F5, and F4.	89
3.8	Ratio of real-space power spectra in F4 with $m_\nu = 0.06\text{eV}$ or $m_\nu = 0.2\text{eV}$ to the fiducial model of GR with $m_\nu = 0.06\text{eV}$ at $z = 1$	90
3.9	Degeneracy between F4 with $m_\nu = 0.2\text{eV}$ and the fiducial model of GR with $m_\nu = 0.06\text{eV}$ in the redshift-space power spectrum multipoles at $z = 1$, represented as the ratio of power spectra in the two models.	92
3.10	Evolution with redshift of the ratio of real-space power spectra in F4 with $m_\nu = 0.06\text{eV}$ or $m_\nu = 0.2\text{eV}$ to the fiducial model of GR with $m_\nu = 0.06\text{eV}$	93

3.11	Evolution with redshift of the degeneracy between F4 with $m_\nu = 0.2\text{eV}$ and the fiducial model of GR with $m_\nu = 0.06\text{eV}$ in the redshift-space power spectrum multipoles at $z = 1$, represented as the ratio of power spectra in the two models.	93
3.12	The redshift evolution of $\chi^2_{\text{MG}+m_\nu}(k_{\text{max}})$ which quantifies the difference between the redshift-space multipoles of the two degenerate models as a function of maximum comparison scale.	94
4.1	Redshift-space halo power spectrum multipoles at $z = 1$	103
4.2	Contours for the MCMC halo RSD model fitted to GR+0.06eV simulation data.	106
4.3	Contours for the MCMC halo RSD model fitted to F4+0.2eV simulation data.	107
4.4	Contours for the MCMC halo RSD model fitted to F4+0.2eV simulation data with N fixed at 0.	108
4.5	The ratio of the redshift-space halo power spectrum multipoles in F4+0.2eV and GR+0.06eV at $z = 1$	110
E.1	The total matter power spectrum for a GR+ m_ν cosmology relative to the GR case where $m_\nu = 0.0$ at $z = 0.0$ and $z = 1.0$	125

Declaration

Whilst registered as a candidate for the above degree, I have not been registered for any other research award. The results and conclusions embodied in this thesis are the work of the named candidate and have not been submitted for any other academic award.

Approximate word count: 27,121

Dissemination

This thesis is based on the following published works:

1. Winther et al; *COLA with scale-dependent growth: applications to screened modified gravity models*; JCAP 1708 (2017) 006
2. Wright, Winther, and Koyama; *COLA with massive neutrinos*; JCAP 1710 (2017) 054
3. Wright et al; *Investigating the degeneracy between modified gravity and massive neutrinos with redshift-space distortions*; JCAP 1906 (2019) 040

Acknowledgements and Dedication

Firstly, I would like to sincerely thank all three of my supervisors for their guidance and support over the past three or so years. I am especially grateful to Kazuya for his invaluable feedback throughout my PhD studies, as well as his willingness to provide it at any hour. I also owe Hans Winther a great debt for consistently identifying my coding mistakes and always being available to answer questions.

There are two people without whom I might not have started my PhD at all. Firstly, Baojiu Li, who first introduced me to cosmology research while supervising my Masters project; and secondly, Paula Chadwick, my former academic advisor, who first told me of all the fascinating cosmology research being carried out at Portsmouth. I am grateful to them both.

I am very lucky to have a fantastic extended family and to have been part of a wonderful group of PhD students at the ICG. The long path towards finishing a PhD can be plagued by mental health issues for any student, and I cannot imagine how difficult the past three and a bit years would have been without having friends and family like them to talk to.

Lastly, I would like to thank my amazing partner Anabel and my wonderful mother Julia. Annie, thank you for always being there for me and for never failing to make me smile. Mum, thank you for your limitless interest in my research and for nurturing my curiosity in the first place. I couldn't have done this without either of you, and I love you both dearly.

This thesis is dedicated to Dad.

Conventions, Constants, and Abbreviations

The following notation and conventions are used throughout this work:

- Greek indices for vectors and tensors will take values from the set $(0, 1, 2, 3)$ which will refer to general four-dimensional spacetime coordinates, 0 being the time coordinate and $(1, 2, 3)$ being the spatial coordinates.
- Roman indices for vectors will take values from the set $(1, 2, 3)$. These will be used both to indicate spatial coordinates as well as order for the kernels and perturbations. This distinction will be clear in the context.
- The Einstein Summation convention will be used, in which if an index appears as both an upper and lower index, it indicates a summation over all coordinates. For example $g_{\mu\nu}u^\mu = \sum_{i=0}^3 g_{i\nu}u^i$.
- The signature $(-, +, +, +)$ is used for all spacetime metrics.
- The partial derivative with respect to the variable x^μ will be written ∂_μ : $\frac{\partial}{\partial x^\mu} = \partial_\mu$.
- A subscript of 0 on any time dependent parameter (not spacetime coordinate) value will generally denote a present day value.
- Unless otherwise stated, an overdot $\dot{}$ will denote a derivative with respect to the FLRW metric time coordinate t .
- Unless otherwise stated, an overbar $\bar{}$ will denote a background average quantity.
- We will use the summation convention $\vec{k}_{1\dots n} = \vec{k}_1 + \dots + \vec{k}_n$.
- Unless otherwise stated, we work in the system of units in which $c = 1$. The value of c and other physical constants in S.I. units are given in Table 1.

In addition to the above, a number of abbreviations are made use of throughout this work, which are listed in Table 2.

Table 1: Physical Constants

Physical Constant	Symbol	Value (S.I)
Gravitational constant	G	$6.67428 \times 10^{-11} \text{ m}^3\text{kg}^{-1}\text{s}^{-2}$
Speed of light (vacuum)	c	$299,792,458 \text{ m s}^{-1}$
Solar Mass	M_{\odot}	$1.988 \times 10^{30} \text{ kg}$

Table 2: Abbreviations

Abbreviation	Expression
2PCF	2-point correlation function
BAO	Baryon Acoustic Oscillations
CDM	Cold Dark Matter
CMB	Cosmic Microwave Background
COLA	COmoving Lagrangian Acceleration
DGP	Dvali-Gabadadze-Porratti
DoF	Degree(s) of freedom
EdS	Einstein-de Sitter
FLRW	Friedman-Lemaître-Robertson-Walker
FoG	Fingers of God
FT	Fourier Transform
GR	General Relativity
JBD	Jordan-Brans-Dicke
Λ CDM	Λ -CDM model of Cosmology
LoS	Line of Sight
LPT	Lagrangian Perturbation Theory
LSS	Large Scale Structure
MCMC	Markov Chain Monte Carlo
MG	Modified Gravity
PT	Perturbation Theory
RSD	Redshift-Space Distortions
SPT	Standard Perturbation Theory
TNS	Taruya-Nishimichi-Saito

Chapter 1

Introduction

1.1 Cosmological overview

The current best model for the Universe is one that expands outwards after an initial Big Bang [3]. Quantum fluctuations in the very early Universe are thought to have created microscopic inhomogeneities. The Universe underwent an early period of accelerated expansion called inflation [4, 5, 6, 7] (see also [8, 9] for reviews), during which the primordial fluctuations were amplified to create density perturbations that seed the subsequent growth of structure in the Universe [10, 11, 12, 13, 14, 15]. These density perturbations have an approximately Gaussian distribution and are characterised by an approximately scale-invariant primordial power spectrum. The density perturbations can be seen as minute temperature fluctuations in the cosmic microwave background (CMB) [16] with a magnitude of $\delta T/\bar{T} \approx 10^{-5}$ [17, 18, 19]. Inflation also explains why the Universe today is isotropic and homogeneous on large scales, almost completely flat in terms of its curvature, and devoid of magnetic monopole relics.

After inflation ends, the energy in the scalar field of inflation - the inflaton - is transferred to the fundamental particles we see in our Universe today - photons, quarks, leptons, cold dark matter (CDM), and force-mediating bosons - in a process known as reheating [20] (see [21, 22] for reviews). We must also assume dark energy, the evidence for which we will discuss at the end of this section, is present at this time. For an as yet unknown reason, there was an extremely small preference for the formation of matter over antimatter, and thus after matter-antimatter annihilation only a small excess of matter is left. The energy density of the photons and relativistic particles (collectively called radiation) dominates over matter and dark energy. Even though the inflaton is no longer present to accelerate the expansion, the Universe continues to expand as

described by the Friedmann equations for a homogeneous, isotropic universe

$$H^2 = \left(\frac{\dot{a}}{a}\right)^2 = \frac{8\pi G\rho}{3} - \frac{Kc^2}{3}, \quad (1.1)$$

$$\frac{\ddot{a}}{a} = -\frac{4\pi G}{3} \left(\rho + \frac{3P}{c^2}\right), \quad (1.2)$$

where a is the scale factor, $H = \dot{a}/a$ is the Hubble parameter, G is Newton's gravitational constant, c is the speed of light in a vacuum, K is the spatial curvature, and $\rho = \rho_r + \rho_m + \rho_{\text{DE}}$ and $P = P_r + P_m + P_{\text{DE}}$ are the total energy density and total pressure respectively, both of which are the sum of the contributions from radiation, matter, and dark energy. A quantity known as the critical density can be expressed as $\rho_{\text{crit}} = 3H^2/8\pi G$, and each component's contribution to the content of the Universe is then $\Omega_i = \rho_i/\rho_{\text{crit}}$. If we assume dark energy is a cosmological constant then $\rho_{\text{DE}} = \rho_\Lambda = \Lambda c^2/(8\pi G)$ where Λ is the value of the cosmological constant. We shall discuss the evidence for the cosmological constant at the end of this chapter, but for now will take it to be positive with an energy density that is initially smaller than both ρ_r and ρ_m . For simplicity, in this section only we will (incorrectly) assume that neutrinos are massless and so act as radiation at all times. We will cover the evidence for and consequences of massive neutrinos in Section 1.3. Finally, there is strong evidence from cosmological observations using a combination of probes that the Universe is spatially flat which we will discuss further at the end of this section, so we will assume $K = 0$.

As stated above, radiation is dominant in this initial post-inflationary epoch, and therefore we can neglect the effects of matter and dark energy in the Friedmann equations. For radiation, $\rho_r \propto a^{-4}$ and $P_r = \rho_r c^2/3$ which leads to $a(t) \propto t^{1/2}$, which indicates that the Universe will continue expanding, albeit at a gradually decreasing rate due to gravity.

As the Universe expands it cools, first allowing quarks to combine to form baryons such as protons and neutrons. Free protons can become neutrons by reacting with leptons and vice versa; initially these paired reactions happened in equilibrium and therefore the ratio of neutrons to protons was essentially 1:1. However, as the temperature dropped further, the lower mass of protons meant that their production was energetically favoured, causing the neutron to proton ratio to drop to around 1:6 by the time these reactions freeze-out. Additionally, free neutrons decay into protons with a half-life of around 10 minutes; thus the ratio continues to drop after freeze-out until all the neutrons are contained in nuclei, reaching approximately 1:7. The period in which neutrons join with protons via nuclear fusion to form different nuclei in the early Universe is called Big Bang nucleosynthesis (BBN). The first process that happens in BBN is the combination of individual protons and neutrons to form deuterium ${}^2_1\text{H}$.

Since further fusion reactions require deuterium, nothing further can occur until the Universe has cooled sufficiently for the deuterium not to be immediately destroyed by high energy photons; this is known as the deuterium bottleneck. Once the critical temperature is reached, approximately 25% of the free protons fuse with nearly all of the free neutrons to form deuterium. The deuterium then rapidly reacts with more free protons and neutrons, as well as other deuterium nuclei to form helium-4 and small amounts of intermediate nuclei such as unstable tritium ${}^3_1\text{H}$ and stable helium-3. Additionally, tiny amounts of lithium and beryllium isotopes, such as stable lithium-7 and unstable beryllium-7, are produced. A bottleneck due to the absence of stable nuclei with 5 or 8 nucleons restricts the formation of heavier nuclei. At the end of BBN, the only stable nuclei remaining are hydrogen ($\sim 75\%$ of total baryonic mass), helium-4 ($\sim 25\%$), deuterium ($\sim 0.01\%$), helium-3 ($\sim 0.01\%$), and lithium-7 ($\sim 10^{-9}\%$). See Chapter 23 of [23] for a complete review of BBN.

In this initial post-inflationary epoch, the Universe has been radiation-dominated. During this period, matter perturbations smaller than the size of the horizon $d_{\text{H}} \approx cH^{-1} = c^2\sqrt{3/(8\pi G\rho)}$ only grow logarithmically due to the rapid expansion of the Universe. However, the energy density of radiation decreases as $\rho_{\text{r}} \propto a^{-4}$ while the energy densities of matter and the cosmological constant evolve as $\rho_{\text{m}} \propto a^{-3}$ and $\rho_{\Lambda} = \text{const}$ respectively. Therefore, as the Universe expands, matter, and then subsequently the cosmological constant, will become dominant. Once the Universe becomes matter-dominated, we can neglect the contributions of radiation and dark energy in the Friedmann equations. For matter $\rho_{\text{m}} \propto a^{-3}$ and $P_{\text{m}} = 0$, and thus solving Eqs. (1.1) and (1.2) with these yields $a \propto t^{2/3}$. In this regime, sub-horizon matter density perturbations grow as $\delta_{\text{m}} \propto a$. However, in practice this only applies to the CDM component for a time. This is because, since the end of inflation, baryons and photons have been coupled together as a single baryon-photon fluid. Electromagnetic (EM) interactions within this baryon-fluid produce an outwards pressure that counteracts gravitational collapse, leading to baryon acoustic oscillations (BAO) analagous to sound waves. Thus perturbations within this fluid are prevented from collapsing under gravity. However, there will be an overdensity in the baryon-photon fluid at the sound horizon due to the interaction. Since CDM particles only interact gravitationally, the density perturbations in the CDM grow via gravitationally instability [24] as $\delta_{\text{CDM}} \propto a$. The CDM overdensities grow to form halos, as well as filaments and sheets, while the CDM underdensities grow to form voids [25, 26].

When the Universe cools enough for electrons to recombine with nuclei to form neutral atoms, the baryonic matter can decouple from the photons. The photons stream

away and are seen today as the CMB. Once decoupled, the baryonic matter is able to fall into the gravitational potential wells formed by the CDM overdensities to create the first stars and stellar clusters, then later galaxies or clusters and superclusters of galaxies [27]. Because of the overdensity in the baryon-photon fluid at the scale of the fluid’s sound horizon before decoupling, there is also an enhancement to the clustering of matter on this BAO scale. The BAO scale evolves as the Universe expands, and can thus act as a standard ruler to measure the expansion of the Universe.

Unlike CDM, galaxies are luminous and so act as biased tracers of the underlying, invisible CDM. Much research is being done on computing just how biased galaxies are as tracers of CDM (see [28] for a review). Alternatively, weak lensing offers a method of measuring the distribution of CDM more directly (see [29, 30] for reviews). We will discuss more about structure formation in Section 1.5.

Since, unlike radiation or matter, the energy density of the cosmological constant does not fall as the Universe expands, the cosmological constant eventually becomes the dominant component of the Universe. In this epoch we can neglect the contributions of radiation and matter in the Friedmann equations. For the cosmological constant, $P_{\text{Lambda}} = -\rho_{\Lambda}c^2$, and thus the Friedmann equations yield $a \propto \exp(Ht)$ where $H = \sqrt{\Lambda/3}$. At this point, the rate of expansion is too great to allow large-scale perturbations to grow further. The expansion of the Universe will continue to accelerate, leading to the eventual heat death of the Universe when a state of maximum entropy is reached.

Throughout the above description of the chronology of the Universe, we have assumed that the concordance cosmological model known as Λ CDM holds. The Λ CDM model stipulates: a flat universe with an initial post-inflationary decelerating expansion, followed by a late-time acceleration caused by a small positive-valued cosmological constant; Einstein’s General Relativity (GR) is the correct theory of gravity; and a universe currently consisting of around 70% cosmological constant, 25% cold dark matter, and 5% baryons in terms of energy density. The first evidence for the late-time acceleration came from observations of Type Ia supernovae (SNe Ia), which can act as standardisable candles, allowing observations to yield measurements of the expansion history of the Universe. The distant SNe Ia are fainter (thus further away) than expected in any universe except one with a late-time accelerating expansion [31, 32]. Other probes of expansion history (CMB [33] and BAO [34]), as well as large-scale structure formation (galaxy clustering [35, 36] and weak lensing [37, 38]) and the relative abundances of primordial nuclei (BBN; Chapter 23 of [23]), are generally consistent with this model.

However, there are some signs of discord. Firstly, the measurements of H_0 from local probes such as SNe Ia and strong lensing which are generally accepted to be model independent are higher in an inconsistent fashion than those found while assuming Λ CDM for early Universe probes such as the CMB [39]. Secondly, measurements of structure growth via σ_8 (the amplitude of the linear matter power spectrum at a scale of 8 Mpc/ h) at low redshift from weak lensing are lower than the value implied by high redshift observations from the CMB assuming Λ CDM [40, 41]. These twin discrepancies could be explained by unaccounted for systematic errors in either the low or high redshift observations, but may also point towards flaws in the Λ CDM model. There is also some recent analysis that suggests CMB observations alone prefer a closed rather than flat universe [42, 43].

1.2 Modified Gravity

Einstein's General Relativity (GR) has long been established as the accepted theory of gravity. It is characterised by the Einstein-Hilbert action

$$S = \int d^4x \sqrt{-g} R + \int d^4x \sqrt{-g} \mathcal{L}_m, \quad (1.3)$$

where R is the Ricci curvature, $g_{\mu\nu}$ is the metric, and \mathcal{L}_m is the Lagrangian for the standard model particles. It has been tested extensively within the solar system and more recently in strong-field environments as well [44]. So far, GR has withstood every test on these scales. It is known that an extension to GR that unifies the theory of gravity with quantum field theory will be required in order to describe the pre-inflation Universe, and there is a wide variety of ongoing attempts to do so (see [45, 46] for reviews). However, the surprising measurement that the expansion of the Universe is accelerating instead of decelerating as expected [32, 31] has led some cosmologists to consider whether an alternative to GR is required in the post-inflation Universe. The current leading candidate for the origin of the accelerating late-time expansion is a small, positive cosmological constant Λ [47, 48]. This is a resurrection of a correction term that Einstein put into GR by hand in order to ensure a static Universe. It is thought that the theoretical cosmological constant is the physical quantum vacuum energy. However, the value predicted for the energy density of the quantum vacuum fluctuations scales as M^4 where M is the cut-off mass of the theory. Depending on where this cut-off is set, this prediction yields values between 10^{54} and 10^{120} orders of magnitude larger than the value of the cosmological constant that is required by cosmological observations [49]. If the quantum vacuum energy is to act as the cosmological constant, it is thought that there must be a finely-tuned cancellation of the vacuum

energy that leaves behind only a small, positive contribution. This requirement of fine-tuning is known as the cosmological constant problem [49]. A further issue with the late-time accelerated expansion being caused by a small, positive cosmological constant is that the current values of the cosmological constant and matter energy densities are of the same order of magnitude, despite evolving very differently over the age of the Universe. This is known as the coincidence problem [50].

Thus, as a result of these issues with the cosmological constant, investigations considering alternative theories of gravity have resumed (see [51, 52] for reviews). Lovelock’s theorem tells us that Einstein’s equations are the only second-order, local equations of motion from an action in 4D spacetime involving solely the metric tensor and its derivatives. [53, 54]. This therefore requires that modifications to GR must include at least one of the following [51, 52]: extra degrees of freedom (such as Brans-Dicke gravity [55, 56]), higher order derivatives (such as $f(R)$ gravity [57, 4]), higher dimensional spacetime (such as DGP braneworld gravity [58]), or non-locality. These modifications can usually be expressed as an extra scalar field ϕ , which couples to matter to produce a fifth force.

The difficulty with considering alternatives to GR is that the extensive tests of gravity within the solar system place tight constraints on deviations from GR within such environments. In order to allow alternative theories to deviate from GR on cosmological scales where they might be able to produce the late-time accelerating expansion but still obey the constraints that come from solar system scales, many modified gravity theories include a screening mechanism that essentially reduces the alternative theory to GR on solar system scales but leaves the modifications of the alternative theory untouched otherwise [59]. An alternative approach is to break the weak equivalence principle, such that the extra scalar field couples only to dark matter and not baryons. This alternative approach is followed in theories of interacting dark energy (see [60, 61] for reviews).

There are a variety of possible screening mechanisms. Consider a general Lagrangian for a scalar field ϕ

$$\mathcal{L} = -\frac{1}{2}Z^{\mu\nu}(\phi, \partial\phi, \partial^2\phi)\partial_\mu\phi\partial_\nu\phi - V(\phi) + \beta(\phi)T_\mu^\mu. \quad (1.4)$$

The dynamics of fluctuations around the background field $\bar{\phi}$ are determined by three parameters: the mass of fluctuations $m(\bar{\phi})$, the coupling to matter $\beta(\bar{\phi})$ and the kinetic function $Z^{\mu\nu}(\bar{\phi})$. In addition to this, in the presence of non-relativistic matter $T_\mu^\mu = -\rho$, the scalar field’s dynamics, and therefore $\bar{\phi}$, depends on the local density of the system. The three parameters can each be utilised to screen the fifth force mediated by the additional scalar field in high density environments such as the solar system. Firstly,

if $m^2(\bar{\phi})$ is large in high density environments then the scalar field will not propagate above the Compton wavelength $m^{-1}(\bar{\phi})$ and therefore the additional force is suppressed, while in low density environments outside the solar system $m^2(\bar{\phi})$ can be light and the fifth force can be significant. An example of this type of mechanism is chameleon screening [62, 63]. Secondly, if $\beta(\bar{\phi})$ is small in high density environments the strength of the fifth force is weak, while in low density environments $\beta(\bar{\phi})$ can be large and the fifth force can be of the same order strength as gravity. Example of this type of screening are the dilaton [64] and symmetron [65] mechanisms. Finally, if $Z^{\mu\nu}(\bar{\phi})$ is large in high density environments, either by the first (as in k-mouflage screening [66]) or second (as in Vainshtein screening [67]) derivative of the field becoming large, then $\beta(\bar{\phi})$, and therefore the strength of the fifth force, is effectively suppressed.

A further constraint on theories of gravity comes from the recent near-simultaneous observation of electromagnetic radiation and gravitational waves from the binary neutron star merger GW170817 [68]. The difference between the speed of gravitational waves c_{GW} and the speed of light in a vacuum c was determined to be constrained as

$$-3 \times 10^{-15} \leq \frac{c_{\text{GW}}}{c} - 1 \leq 7 \times 10^{-15} . \quad (1.5)$$

This effectively rules out any theory of gravity where the speed of gravitational waves is not equal to that of electromagnetic radiation [69, 70, 71, 72, 73, 74, 75]. However, there have been some attempts to get around this constraint, for example [76].

A model that is frequently considered when looking for signatures of modified gravity in structure formation is $f(R)$ gravity [57, 4]. Here, we generalise the Einstein-Hilbert action such that it becomes a function of the Ricci curvature R

$$S = \int d^4x \sqrt{-g} f(R) + \int d^4x \sqrt{-g} \mathcal{L}_{\text{m}} . \quad (1.6)$$

The resulting equation of motion is fourth order and as such $f(R)$ can be classified as a higher derivative theory. However, it is also possible to introduce a scalar field ϕ and make the equation of motion second order, thus reclassifying the model as an extra degree of freedom theory. The action above is equivalent to

$$S = \int d^4x \sqrt{-g} (f(\phi) + (R - \phi)f'(\phi)) , \quad (1.7)$$

where $f' = \partial f / \partial \phi$, and by taking a further variation with respect to ϕ , we obtain $(R - \phi)f''(\phi) = 0$. Therefore, provided $f''(\phi) \neq 0$ and $R = \phi$, we recover the original action. Furthermore, if we define $\psi = f'(\phi)$ and a potential $V = f(\phi) - \phi f'(\phi)$, the action can be rewritten

$$S = \int d^4x \sqrt{-g} (\psi R - V(\psi)) . \quad (1.8)$$

Ignoring the potential, this model would be excluded by solar system constraints. However, by choosing the form of the potential, i.e. the form of $f(R)$, appropriately, it is possible to incorporate the chameleon screening mechanism to evade these constraints. One particular form of $f(R)$ that achieves this, as well as producing an expansion history close to that of Λ CDM, was identified by Hu and Sawicki [77]

$$f(R) = R - \frac{\mu R_c}{1 + (R - R_c)^{-2n}} , \quad (1.9)$$

where μ , n , and R_c are all positive constants. The theory can be rewritten such that the free parameters are n , which typically takes the value of unity, and $|f_{R0}|$, which is typically a negative power of 10. Common notation is to refer to $|f_{R0}| = 10^{-4}$ as ‘F4’ and so on. F4 is a stronger modification to GR than F5, which in turn is a stronger modification than F6. There is no deviation of the speed of gravitational waves from the speed of electromagnetic waves in this theory and thus it satisfies the GW170817 constraints mentioned above.

Another frequently considered modified gravity theory is the Dvali-Gabadadze-Porrati (DGP) model [58] which is the simplest variant of a braneworld model, in which it is posited we live on a 4D membrane (brane) in a higher dimensional spacetime (bulk). In braneworld theories, gravity propagates throughout the whole spacetime, while standard model particles are confined to the brane. DGP is a 5D model described by the action

$$S = \frac{M_5^3}{2} \int d^5x \sqrt{-^{(5)}g} {}^{(5)}R + \frac{M_4^2}{2} \int d^4x \sqrt{-g} ({}^{(4)}R + \mathcal{L}_m) , \quad (1.10)$$

where ${}^{(5)}g$ is the metric in the bulk, and ${}^{(4)}R$ and ${}^{(5)}R$ are 4D and 5D Ricci curvature respectively. The key parameter of this model is the cross-over scale; the ratio between the 4D and 5D Newton’s constants $r_c = M_4^2/2M_5^3$. The Friedmann equation in DGP is

$$H^2 = \pm \frac{H}{r_c} + \frac{8\pi G}{3} \rho . \quad (1.11)$$

At early times, $Hr_c \gg 1$ and the usual 4D Friedmann equation is recovered. However, at late times, there are two branches to the solution. In the upper branch, the Hubble parameter tends towards a constant $H \rightarrow 1/r_c$, which causes the the expansion of the Universe to accelerate without the need for a cosmological constant. Thus this branch is known as the self-accelerating branch; however this solution is not viable as it suffers from a ghost instability [78, 79, 80, 81, 82, 83]. The lower branch solution requires a cosmological constant to yield accelerated expansion, and is thus called the normal branch of the DGP theory, often shortened to nDGP. The Vainshtein mechanism is

present in this theory, allowing it to evade solar system constraints. The speed of gravitational waves is equal to the speed of electromagnetic waves in this theory and thus it does not fall foul of the GW170817 constraints mentioned above.

Introducing modified gravity theories such as these may also have consequences for large scale structure formation. Most modified gravity theories enhance the growth of structure formation at intermediate scales because of the addition of a fifth force. Such an enhancement of growth can leave observable signatures in clustering statistics computed from galaxy surveys [84, 85]. It is vital to be able to model the effects of modified gravity on structure formation in simulations so that the output can be compared to galaxy surveys in order to determine whether the observations show any evidence for deviations from GR in the clustering statistics. For the connection between a variety of modified gravity models and perturbation theory, see Appendix D.

There is also the possibility that modifying gravity can affect the intrinsic luminosities of Type Ia supernovae (SNe Ia) standardisable candles [86]. This could affect the evidence from SNe Ia for late-time accelerating expansion [87], or help constrain modified gravity if SNe Ia observations are combined with measurements from other probes of expansion that support late-time acceleration [88].

1.3 Massive Neutrinos

Neutrinos have been shown to have mass by flavour oscillation experiments [89, 90]. However, these experiments only measure the differences between the squared masses of the neutrino mass eigenstates $\Delta m_{ij}^2 = m_i^2 - m_j^2$ rather than the absolute masses m_i . There is strong evidence from the analysis of the invisible Z-boson width at LEP for three neutrino mass eigenstates [91], and the three flavours ν_e , ν_μ , and ν_τ are linear combinations of these mass eigenstates. The oscillation experiments show that Δm_{21}^2 is small and positive, but only constrain the magnitude $|\Delta m_{31}^2|$, which is relatively larger than $|\Delta m_{21}^2|$. This leads to two possible hierarchies of the three mass eigenstates; the normal hierarchy (NH) where Δm_{31}^2 is positive and thus $m_3 \gg m_2 > m_1$, or the inverted hierarchy (IH) where Δm_{31}^2 is negative and thus $m_2 > m_1 \gg m_3$. The lower bound on the sum of the neutrino masses $M_\nu = \sum_i m_i$ that comes from these constraints depends on the hierarchy; it is approximately $M_\nu > 0.06\text{eV}$ or $M_\nu > 0.1\text{eV}$ for NH and IH respectively [92, 93]. An upper bound on the sum of neutrino masses $M_\nu < 2\text{eV}$ comes from tritium decay experiments [23].

Massive neutrinos affect cosmology. We can express how their contribution to the

content of the Universe at $z = 0$ depends on their mass with

$$\Omega_\nu = \frac{\rho_\nu}{\rho_{\text{crit}}} = \frac{M_\nu}{93.14 h^2 \text{eV}} , \quad (1.12)$$

where $h = H_0/[100 \text{km s}^{-1} \text{Mpc}^{-1}]$ is the reduced Hubble constant. This expression is derived by assuming standard neutrino decoupling and taking moments of the neutrino momentum distribution, which has a Fermi-Dirac form. In the very early post-inflationary Universe, the temperature was high enough that massive neutrinos were relativistic, and acted as radiation. However, once the temperature of the neutrinos fell such that $3T_\nu < m_i$, that mass eigenstate became non-relativistic. The redshift of non-relativistic transition is approximately

$$1 + z_{\text{nr}} \approx 1987 \left(\frac{m_i}{1 \text{eV}} \right) . \quad (1.13)$$

If any of the neutrino states has $m_i \gtrsim 0.57 \text{eV}$, they will have become non-relativistic before photon decoupling and therefore have had direct effects on the CMB temperature and polarisation anisotropies, as described in [94]. Since such effects are well constrained by current CMB data [33], it is generally safe to assume that all of the neutrino states became non-relativistic after photon decoupling and therefore have $m_i \lesssim 0.57 \text{eV}$. However, this constraint does not prevent massive neutrinos from producing indirect signatures in CMB observables due to their effects on the Universe as the CMB photons propagate to reach us at late-time. There are four key effects of massive neutrinos that indirectly impact the CMB observations. Firstly, massive neutrinos contribute to the total non-relativistic density at late times. The evolution of the total non-relativistic density at late times can affect the CMB via the relationship between scales on the last-scattering surface and angles on the sky, and through the late ISW effect [95], which depend on the angular diameter distance to recombination $d_A(z_{\text{rec}})$ and the redshift of matter- Λ equality $z_{\Lambda, \text{eq}}$ respectively. Although both $d_A(z_{\text{rec}})$ and $z_{\Lambda, \text{eq}}$ respond to changes in M_ν , by also varying H_0 and Ω_Λ it is possible to keep either one fixed, but not both at the same time. Thus the exact impact on the CMB observation depends on which one is chosen to stay fixed. Since CMB observations measure the angular scale of acoustic oscillations very well, it makes more sense to vary H_0 and Ω_Λ with M_ν in such a way as to keep $d_A(z_{\text{rec}})$ fixed. Therefore, increasing M_ν leads to a decrease in the late ISW effect and thus a depletion of the CMB temperature anisotropy power spectrum C_l^{TT} for $l \leq 20$. Secondly, when massive neutrinos become non-relativistic it affects the total pressure-to-density ratio of the Universe and causes a small variation of the metric fluctuations. If this transition takes place soon after photon decoupling, then this variation causes a dip in C_l^{TT} for $20 \leq l \leq 200$ via the

early ISW effect [95]. Thirdly, due to the suppression of the matter power spectrum by massive neutrinos (see below), the effect of weak lensing on the CMB [96] will be reduced which can lead to oscillatory features in C_l^{TT} for $l \geq 200$. Finally, since the massive neutrinos will have a distribution of momenta, those with the smallest momenta will become non-relativistic before those with average momenta, which can lead to a small enhancement of C_l^{TT} for $l \geq 500$ when the photon perturbations respond to this transition through their gravitational coupling to the neutrinos.

The relatively small masses of neutrinos means that they essentially act as a warm dark matter (WDM) component of the Universe, with a large thermal velocity at late times [97, 98, 99, 100, 101, 102]. This large thermal velocity prevents massive neutrinos from clustering at scales smaller than the corresponding free-streaming length l_{FS} , while on large scales they behave like CDM. The comoving wave number corresponding to l_{FS} is approximately

$$k_{\text{FS}} \approx 0.81 \frac{\sqrt{\Omega_\Lambda + \Omega_m(1+z)^3}}{(1+z)^2} \frac{m_i}{1\text{eV}} h \text{ Mpc}^{-1} . \quad (1.14)$$

After its non-relativistic transition, the free-streaming scale of each eigenstate evolves as $k_{\text{FS}} \propto (1+z)^{-1/2}$, and thus k_{FS} has a minimum at z_{nr} given by

$$k_{\text{nr}} \approx 0.018 \left(\frac{m_i}{1\text{eV}} \right)^{1/2} (\Omega_m h^2)^{1/2} \text{ Mpc}^{-1} . \quad (1.15)$$

Thus density modes with $k < k_{\text{nr}}$ are never affected by neutrino free-streaming. Massive neutrinos not contributing to the clustering of total matter for $k > k_{\text{fs}}$ leads to a suppression of the matter power spectrum by a factor of approximately $(1-2f_\nu)$ at these small scales. Additionally, neutrinos not clustering below the free-streaming length also means that the CDM component feels a reduced gravitational potential. Thus CDM clustering and the growth of CDM structure is suppressed below the neutrino free-streaming scale by a factor of approximately $(1-6f_\nu)$. Thus the total suppression factor of the small-scale linear matter power spectrum is approximately $(1-8f_\nu)^1$, although more precise computations show this may not be entirely valid, especially for larger f_ν [103, 104]. The suppression of the non-linear matter power spectrum is even more extreme. Figure 1.1 shows the ratio of the matter power spectrum with and without massive neutrinos for several different neutrino masses at 3 different redshifts to highlight the suppression effect and its evolution. The computations for both the linear and non-linear power spectra in this figure were carried out using the Boltzmann code **CAMB** [105], with the non-linear results produced by the built-in **HALOFIT** protocol

¹For further information about these suppression factors, see Section 25.2.4 of [23], or Section 4.5.6 (specifically Eqs. (135)-(142)) of [103] for a derivation.

[106]. We included massive neutrinos by increasing Ω_ν at the expense of Ω_{CDM} ; Ω_{m} and all other cosmological parameters were held fixed. Figure 1.1 shows that even for the lower bound $M_\nu > 0.06\text{eV}$ the suppression of the matter power spectrum is on the order of a few percent at redshifts relevant for galaxy surveys [103, 107].

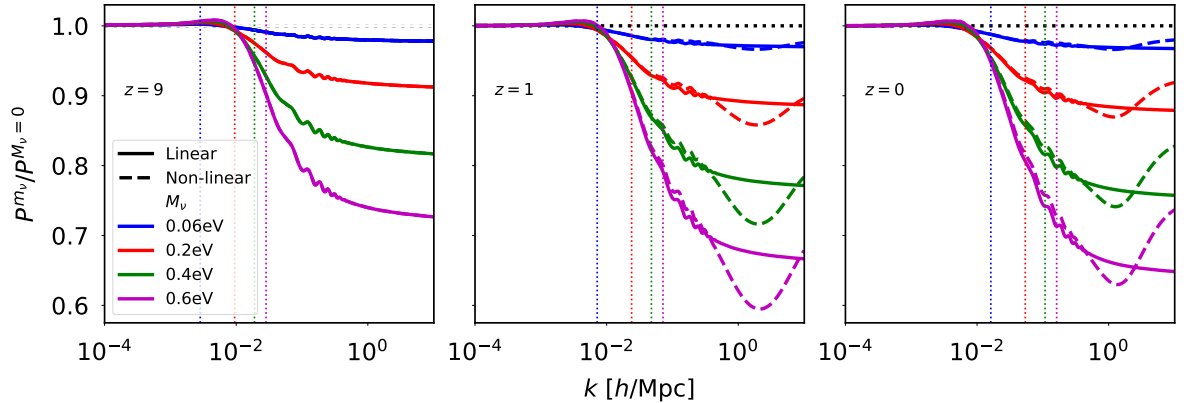


Figure 1.1: The suppression of the matter power spectrum by different masses of neutrinos at $z = 9$ (left), $z = 1$ (centre), and $z = 0$ (right). Both the linear (solid lines) and non-linear (dashed lines) results were produced with the Boltzmann code **CAMB** [105], with the non-linear results using the built-in **HALOFIT** protocol [106]. Massive neutrinos were included by increasing Ω_ν at the expense of Ω_{CDM} ; Ω_{m} and all other cosmological parameters were held fixed. The vertical dotted lines show k_{FS} for each case assuming a degenerate hierarchy of neutrino masses.

Given that this is similar to the accuracy to which the matter power spectrum will be measured by future galaxy surveys, it is vital to be able to model the effects of massive neutrinos in simulations such that comparison to data from surveys is accurate. While some of the effects described above are dependent on the individual masses m_i , most of them only depend on the total mass M_ν . Thus when modelling structure formation a degenerate hierarchy is usually assumed where $m_1 = m_2 = m_3 = \frac{1}{3}M_\nu$. However, there is also potential for cosmology to determine the correct hierarchy or even measure the individual masses [108, 109, 110].

1.4 Degeneracy

With the potential for scale-dependent enhancement of structure formation arising from modified gravity and the scale-dependent suppression due to massive neutrinos, there is a risk of degeneracy whereby large-scale structure in a universe with a strong modification to gravity and heavy neutrinos can be difficult to distinguish from that of a universe with GR and light neutrinos [111, 112, 2, 113, 114, 115, 116, 117]. This

degrades the ability of surveys to achieve their twin goals of testing gravity and constraining the neutrino masses in any theories of gravity beyond GR. Indeed, it has been shown that the non-linear matter power spectrum [2] and halo mass function [118] in $f(R)$ models are difficult to distinguish from their equivalents in GR when the neutrino masses are allowed to vary. A demonstration of this degeneracy is shown in Figure 1.2, where we computed the linear and non-linear matter power spectra for various combinations of $|f_{R0}|$ and M_ν using the modified Boltzmann code **MGCAMB** [119, 120, 121] and the built-in **HALOFIT** protocol [106] respectively. The results show that for these particular combinations of $|f_{R0}|$ and M_ν the scale-dependent enhancement due to $f(R)$ gravity and scale-dependent suppression due to the free-streaming of heavy massive neutrinos leads to a matter power spectrum that is difficult to distinguish from that of a Universe with GR and minimal neutrino masses. Two points should be noted here. Firstly, which particular values of $|f_{R0}|$ and M_ν yield a degenerate matter power spectrum depends on H_0 , Ω_m and other cosmological parameters. Secondly, values of $|f_{R0}|$ and M_ν that lead to a degenerate matter power spectrum at one redshift may not do so at another redshift due to the different evolution of the modified gravity and massive neutrino free-streaming effects.

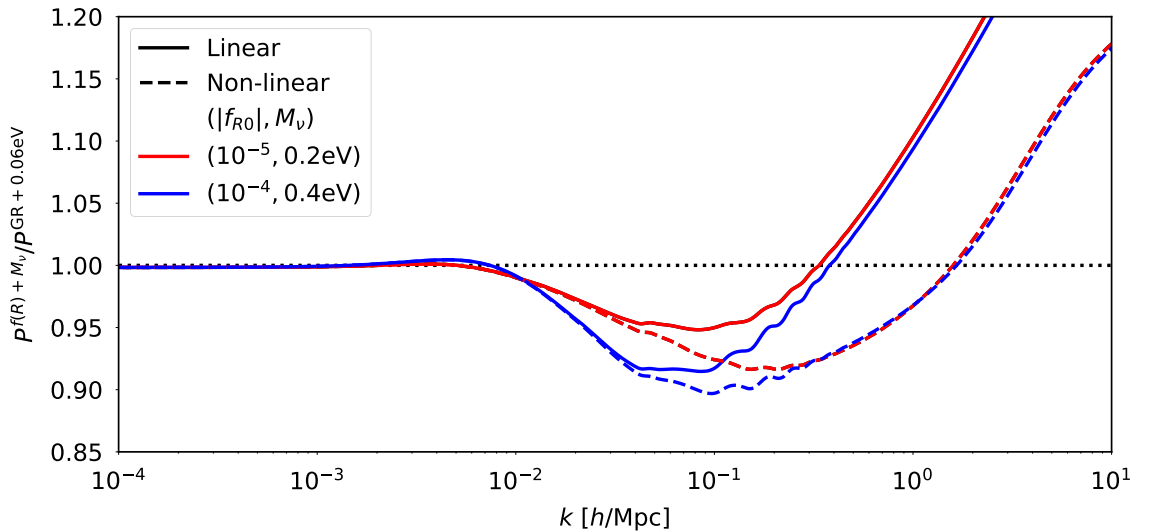


Figure 1.2: The combined enhancement and suppression of the matter power spectrum by different strengths of $f(R)$ gravity and masses of neutrinos at redshift $z = 1$. Both the linear (solid lines) and non-linear (dashed lines) results were produced with the modified Boltzmann code **MGCAMB** [119, 120, 121], with the non-linear results using the built-in **HALOFIT** protocol [106]. Massive neutrinos were included by increasing Ω_ν at the expense of Ω_{CDM} ; Ω_m and all other cosmological parameters were held fixed.

This potential degeneracy is seldom considered in the analysis of data from large

surveys. The DES Collaboration considers neutrino mass and extensions to GR in the same analysis [122], although they only state the resulting constraints on the MG parameters and not the neutrino masses. There are some promising signs that certain observables may be better at reducing or even breaking this degeneracy, such as higher-order weak lensing statistics [123] and weak lensing tomographic information at multiple redshifts [124]; as well as techniques that are superior at distinguishing models such as machine learning [125, 126].

A different observable that has degeneracy breaking potential is that of redshift-space distortions (RSD), which we will discuss in detail in Section 1.5. For combinations of MG parameters and neutrino masses whose enhancement and suppression of *structure growth* produce matter power spectra that are difficult to differentiate between, the *structure growth rate* can still be different in each case and allow for models to be distinguished between. It has recently been shown that growth rate information imprinted in velocity statistics in real-space can be used to break the degeneracy [127]. However, real-space velocity statistics are not directly observable at high redshifts, only in the local Universe where we can assume the Hubble flow is negligible and thereby measure the peculiar velocities of objects from their redshifts. Fortunately, because of the velocity information encoded in them, RSD observations can be used to extract the linear growth rate of structure f . However, in order to extract f and break the degeneracy, it is necessary to accurately model the non-linearities of RSD with MG and massive neutrinos.

1.5 Structure formation

In Section 1.1, we introduced the concept that galaxies act as biased tracers of the invisible, underlying CDM which makes up the majority of matter in the Universe. By mapping the positions of galaxies in the observable Universe through galaxy surveys (such as eBOSS [128], DES [129], HSC [130], DESI [131], LSST [132], Euclid [133], 4MOST [134] and WFIRST [135]), we can compute statistical measures of clustering such as N -point correlation functions and their Fourier space equivalents [136]. By comparing the clustering statistics of observational data to theoretical models and computational simulations, we can discriminate between cosmological models and place constraints on model parameters in order to learn about the underlying physical laws governing our Universe [137, 138].

The simplest clustering statistic is ξ , the 2-point correlation function (2PCF), de-

defined as the joint ensemble average of the density δ at two different points

$$\xi(\vec{x}, \vec{y}) = \langle \delta(\vec{x}) \delta(\vec{y}) \rangle. \quad (1.16)$$

Statistical homogeneity states that the statistical properties of the translated density field $\delta(\vec{x} - \vec{a})$ are the same as those of the original field $\delta(\vec{x})$. This implies that the 2PCF is only dependent on the vector separating the two points. So if $\vec{y} = \vec{x} + \vec{r}$, then

$$\xi(\vec{x}, \vec{y}) = \langle \delta(\vec{x}) \delta(\vec{y}) \rangle = \langle \delta(\vec{x}) \delta(\vec{x} + \vec{r}) \rangle = \xi(\vec{r}). \quad (1.17)$$

Statistical isotropy states that the statistical properties of the rotated density field $\delta(R^{-1}\vec{x})$ are the same as those of the original field $\delta(\vec{x})$. Combined with statistical homogeneity, this implies that the 2PCF is only dependent on the magnitude of the vector, i.e. the distance, separating the two points:

$$\xi(\vec{x}, \vec{y}) = \langle \delta(\vec{x}) \delta(\vec{y}) \rangle = \langle \delta(\vec{x}) \delta(\vec{x} + \vec{r}) \rangle = \xi(r). \quad (1.18)$$

Thus $\xi(r)$ is a measure of the probability above random that two galaxies are separated by a distance r . Often it is useful to consider the density in Fourier space

$$\delta(\vec{k}) = \int \frac{d^3\vec{x}}{(2\pi)^3} \delta(\vec{x}) \exp[-i\vec{k} \cdot \vec{x}]. \quad (1.19)$$

While the wavemode $\delta(\vec{k})$ is a complex random variable, since $\delta(\vec{x})$ is real it follows that $\delta(\vec{k}) = \delta^*(-\vec{k})$, such that the density field is determined entirely by the statistical properties of the random variable $\delta(\vec{k})$. The 2-point correlator in Fourier space is then

$$\begin{aligned} \langle \delta(\vec{k}) \delta(\vec{k}') \rangle &= \int \frac{d^3\vec{x} d^3\vec{r}}{(2\pi)^6} \langle \delta(\vec{x}) \delta(\vec{r}) \rangle \exp[-i\vec{k} \cdot \vec{x}] \exp[-i\vec{k}' \cdot (\vec{x} + \vec{r})] \\ &= \int \frac{d^3\vec{x} d^3\vec{r}}{(2\pi)^6} \xi(r) \exp[-i(\vec{k} + \vec{k}') \cdot \vec{x}] \exp[-i\vec{k}' \cdot \vec{r}] \\ &= \delta_D(\vec{k} + \vec{k}') \int \frac{d^3\vec{r}}{(2\pi)^3} \xi(r) \exp[-i\vec{k}' \cdot \vec{r}] \\ &= \delta_D(\vec{k} + \vec{k}') P(k), \end{aligned} \quad (1.20)$$

where the power spectrum $P(k)$ is the Fourier space equivalent of $\xi(r)$:

$$P(k) = \int \frac{d^3\vec{r}}{(2\pi)^3} \xi(r) \exp[-i\vec{k}' \cdot \vec{r}] \quad (1.21)$$

$P(k)$ depends only on the magnitude of the wavevector due to statistical homogeneity and isotropy, in the same way that ξ depends only on the distance r .

Statistical measures of clustering such as these can be computed directly from particle distributions that are the output of simulations of structure formation (see Section 1.6). Another method is to use perturbation theory to understand how the initial density fields evolve and use this to write expressions for the clustering statistics.

1.5.1 Standard perturbation theory

1.5.1.1 SPT for Λ CDM

To study the dynamics of particles in an expanding homogeneous and isotropic universe, it is convenient to use the comoving position \vec{x} , which is related to the proper position \vec{r} through

$$\vec{r} = a(\eta)\vec{x} , \quad (1.22)$$

where the scale factor $a(\eta)$ is a universal function of time due to homogeneity and isotropy, and we have chosen to define it in terms of the conformal time η , which is related to proper time through $dt = a(\eta)d\eta$. The expansion rate of such a universe can be expressed through the conformal Hubble factor $\mathcal{H} = d \ln a / d\eta = aH$. Considering particle velocities, we find the proper particle velocity $\vec{v} = d\vec{r}/dt$ in terms of comoving position and conformal time is written as

$$\vec{v}(\vec{x}, \eta) = \mathcal{H}\vec{x} + \vec{u} , \quad (1.23)$$

where $\vec{u} = d\vec{x}/d\eta$. The first term in the above expression represents the background expansion, while the second term \vec{u} represents the peculiar velocity; the motion of the particle relative to an observer comoving with the background. The Lagrangian for a particle with mass m moving in a smooth, Newtonian gravitational potential $\varphi(\vec{x}, \eta)$ is

$$\mathcal{L} = \frac{1}{2}mv^2 - m\varphi = \frac{1}{2}m(\mathcal{H}\vec{x} + \vec{u})^2 - m\varphi . \quad (1.24)$$

Applying the canonical transformation $\mathcal{L} \rightarrow \mathcal{L} - d\psi/d\eta$, where $\psi = m\mathcal{H}x^2/2$, which will preserve the form of the equations of motion, reduces the Lagrangian to

$$\mathcal{L} = \frac{1}{2}mu^2 - m\Phi(\vec{x}, \eta) , \quad (1.25)$$

where $\Phi(\vec{x}, \eta)$ is the cosmological gravitational potential defined as

$$\Phi(\vec{x}, \eta) = \frac{1}{2} \frac{\partial \mathcal{H}}{\partial \eta} x^2 + \varphi(\vec{x}, \eta) . \quad (1.26)$$

For Λ CDM, Φ is sourced only by fluctuations around the average mass density of the universe $\bar{\rho}$, and thus describes the deviation from the Newtonian background potential φ . Lagrangian mechanics show that the canonical momentum is defined as $\vec{p} = \partial \mathcal{L} / \partial \dot{\vec{x}}$ where $\dot{\vec{x}} = d\vec{x}/dt = \vec{u}/a$, and can therefore be written as

$$\vec{p}(\vec{x}, \eta) = ma\vec{u}(\vec{x}, \eta) . \quad (1.27)$$

Finally, the Newtonian equation of motion derived from the Euler-Lagrange equations $dp_i/dt = d\mathcal{L}/dx_i$ is

$$\frac{d\vec{p}}{d\eta} = -ma\vec{\nabla}_{\vec{x}}\Phi(\vec{x}, \eta) . \quad (1.28)$$

The Vlasov equation describes the conservation of the particle number density in phase-space $f(\vec{x}, \vec{p}, \eta)$:

$$\frac{df}{d\eta} = \frac{\partial f}{\partial \eta} + \frac{\vec{p}}{am} \cdot \vec{\nabla} f - am\vec{\nabla}\Phi \cdot \frac{\partial f}{\partial \vec{p}} = 0 . \quad (1.29)$$

Taking the zeroth momentum moment of the Vlasov equation yields the continuity equation, and subtracting $\vec{u}(\vec{x}, \eta)$ times the continuity equation from the first moment leads to the Euler equation. Then taking the Fourier transform of both the continuity equation and the divergence of the Euler equation, we obtain

$$\frac{\partial \delta(\vec{k})}{\partial \eta} + \theta(\vec{k}) = - \int \frac{d^3\vec{k}_1 d^3\vec{k}_2}{(2\pi)^3} \delta_D(\vec{k} - \vec{k}_{12}) \alpha(\vec{k}_1, \vec{k}_2) \theta(\vec{k}_1) \delta(\vec{k}_2) , \quad (1.30)$$

$$\frac{\partial \theta(\vec{k})}{\partial \eta} + \mathcal{H}\theta(\vec{k}) - k^2\Phi(\vec{k}) = - \int \frac{d^3\vec{k}_1 d^3\vec{k}_2}{(2\pi)^3} \delta_D(\vec{k} - \vec{k}_{12}) \beta(\vec{k}_1, \vec{k}_2) \theta(\vec{k}_1) \theta(\vec{k}_2) , \quad (1.31)$$

where $\vec{k}_{12} = \vec{k}_1 + \vec{k}_2$, the density contrast $\delta(\vec{k})$ is defined through $\rho(\vec{x}, \eta) = \bar{\rho}(\eta)[1 + \delta(\vec{x}, \eta)]$, $\rho(\vec{x}, \eta)$ and $\bar{\rho}(\eta)$ are the local and average mass densities respectively, and the time dependence has been suppressed. We have also assumed fluid quantities to be irrotational such that the peculiar velocity field \vec{u} can be expressed in terms of the velocity divergence $\theta = (\vec{\nabla} \cdot \vec{u})/\mathcal{H}$ with $\mathcal{H} = aH$ being the conformal Hubble factor. Changing time variables from η to a yields

$$a \frac{\partial \delta(\vec{k})}{\partial a} + \theta(\vec{k}) = - \int \frac{d^3\vec{k}_1 d^3\vec{k}_2}{(2\pi)^3} \delta_D(\vec{k} - \vec{k}_{12}) \alpha(\vec{k}_1, \vec{k}_2) \theta(\vec{k}_1) \delta(\vec{k}_2) , \quad (1.32)$$

$$a \frac{\partial \theta(\vec{k})}{\partial a} + \left(2 + \frac{aH'}{H}\right) \theta(\vec{k}) - \left(\frac{k}{aH}\right)^2 \Phi(\vec{k}) = -\frac{1}{2} \int \frac{d^3\vec{k}_1 d^3\vec{k}_2}{(2\pi)^3} \delta_D(\vec{k} - \vec{k}_{12}) \times \beta(\vec{k}_1, \vec{k}_2) \theta(\vec{k}_1) \theta(\vec{k}_2) , \quad (1.33)$$

where $H' = \partial H/\partial a$, $y' = \partial y/\partial a$ and the kernels α and β are given by

$$\alpha(\vec{k}_1, \vec{k}_2) = 1 + \frac{\vec{k}_1 \cdot \vec{k}_2}{|\vec{k}_1|^2} , \quad (1.34)$$

$$\beta(\vec{k}_1, \vec{k}_2) = \frac{(\vec{k}_1 \cdot \vec{k}_2)|\vec{k}_1 + \vec{k}_2|^2}{|\vec{k}_1|^2 |\vec{k}_2|^2} . \quad (1.35)$$

The Poisson equation completes the above modified continuity and Euler equations. For Λ CDM, this is given by

$$-\left(\frac{k}{aH}\right)^2 \Phi(\vec{k}) = \frac{3\Omega_m(a)}{2} \delta(\vec{k}) , \quad (1.36)$$

where $\Omega_m(a) = 8\pi G\rho_m/3H^2$. We want the n^{th} order solutions of Eqs. (1.32) and (1.33) to be of the form

$$\delta_n(\vec{k}, a) = \int d^3\vec{k}_1 \dots d^3\vec{k}_n \delta_D(\vec{k} - \vec{k}_{1\dots n}) F_n(\vec{k}_1, \dots, \vec{k}_n, a) \Delta(\vec{k}_1) \dots \Delta(\vec{k}_n) , \quad (1.37)$$

$$\theta_n(\vec{k}, a) = \int d^3\vec{k}_1 \dots d^3\vec{k}_n \delta_D(\vec{k} - \vec{k}_{1\dots n}) G_n(\vec{k}_1, \dots, \vec{k}_n, a) \Delta(\vec{k}_1) \dots \Delta(\vec{k}_n) , \quad (1.38)$$

where $\vec{k}_{1\dots n} = \vec{k}_1 + \dots + \vec{k}_n$ and $\Delta(\vec{k}) = \delta(\vec{k}, a_{\text{ini}})$ is the initial density field. Inserting these forms of the solutions and the Λ CDM Poisson equation into Eqs. (1.32) and (1.33) yields a generalised system of equations for the n^{th} order kernels [139]

$$\hat{\mathcal{L}} \begin{bmatrix} F_n(\vec{k}_1, \dots, \vec{k}_n) \\ G_n(\vec{k}_1, \dots, \vec{k}_n) \end{bmatrix} = \sum_{j=1}^{n-1} \begin{bmatrix} -\alpha(\vec{k}_{1\dots j}, \vec{k}_{j+1\dots n}) G_j(\vec{k}_1, \dots, \vec{k}_j) F_{n-j}(\vec{k}_{j+1}, \dots, \vec{k}_n) \\ -\frac{1}{2}\beta(\vec{k}_{1\dots j}, \vec{k}_{j+1\dots n}) G_j(\vec{k}_1, \dots, \vec{k}_j) G_{n-j}(\vec{k}_{j+1}, \dots, \vec{k}_n) \end{bmatrix} , \quad (1.39)$$

where

$$\hat{\mathcal{L}} = \begin{bmatrix} a \frac{d}{da} & 1 \\ \frac{3\Omega_m}{2} & a \frac{d}{da} + \left(2 + \frac{aH'}{H}\right) \end{bmatrix} . \quad (1.40)$$

This system of equations must be solved to compute the kernels F_i and G_i . It is necessary to symmetrise these kernels by summing over all permutations in their spatial arguments and dividing by the number of permutations. An example of a code that does this is **MG-Copter** [140] which is built on the original code **Copter** [141] but based on the approach developed by [139]. Briefly, we will note that the kernel for the first order densities F_1 is equivalent to the first order growth factor D_1 , which for Λ CDM is scale-independent i.e. $F_1(k, z) = D_1(k, z) = D_1(z)$.

In SPT formalism, the power spectra up to 1-loop order are given as

$$P_{ij}^{1\text{-loop}}(k) = P_{ij}^{\text{L}}(k) + P_{ij}^{13}(k) + P_{ij}^{22}(k) , \quad (1.41)$$

where the 1-loop corrections are defined by

$$\begin{aligned} \langle x_2(\vec{k}) y_2(\vec{k}') \rangle &= (2\pi)^3 \delta_D(\vec{k} + \vec{k}') P_{xy}^{22}(k) , \\ \langle x_1(\vec{k}) y_3(\vec{k}') + x_3(\vec{k}) y_1(\vec{k}') \rangle &= (2\pi)^3 \delta_D(\vec{k} + \vec{k}') P_{xy}^{13}(k) , \end{aligned} \quad (1.42)$$

where x and y can be δ or θ . Working these through, the expressions for the 1-loop corrections in terms of the primordial power spectra $P_{\text{ini}}(k) = P^{\text{L}}(k, z_{\text{ini}})$ are, for the 22 correction,

$$P_{\delta\delta}^{22}(k, z) = 2 \frac{k^3}{(2\pi)^2} \int_0^\infty r^2 dr \int_{-1}^1 \frac{P_{\text{ini}}(kr) P_{\text{ini}}(k\sqrt{1+r^2-2rx})}{[D_1(z_{\text{ini}})]^4} F_2^2(k, r, x, z) dx, \quad (1.43)$$

$$P_{\theta\theta}^{22}(k, z) = 2 \frac{k^3}{(2\pi)^2} \int_0^\infty r^2 dr \int_{-1}^1 \frac{P_{\text{ini}}(kr) P_{\text{ini}}(k\sqrt{1+r^2-2rx})}{[D_1(z_{\text{ini}})]^4} F_2(k, r, x, z) \times G_2(k, r, x, z) dx, \quad (1.44)$$

$$P_{\theta\theta}^{22}(k, z) = 2 \frac{k^3}{(2\pi)^2} \int_0^\infty r^2 dr \int_{-1}^1 \frac{P_{\text{ini}}(kr) P_{\text{ini}}(k\sqrt{1+r^2-2rx})}{[D_1(z_{\text{ini}})]^4} G_2^2(k, r, x, z) dx, \quad (1.45)$$

while for the 13 correction we have

$$P_{\delta\delta}^{13}(k, z) = 2 \frac{k^3}{(2\pi)^2} F_1(k, z) \frac{P_{\text{ini}}(k)}{[D_1(z_{\text{ini}})]^2} \int_0^\infty r^2 \frac{P_{\text{ini}}(kr)}{[D_1(z_{\text{ini}})]^2} F_3(k, r, x, z) dr, \quad (1.46)$$

$$P_{\theta\theta}^{13}(k, z) = \frac{k^3}{(2\pi)^2} F_1(k, z) \frac{P_{\text{ini}}(k)}{[D_1(z_{\text{ini}})]^2} \int_0^\infty r^2 \frac{P_{\text{ini}}(kr)}{[D_1(z_{\text{ini}})]^2} G_3(k, r, x, z) dr + \frac{k^3}{(2\pi)^2} G_1(k, z) \frac{P_{\text{ini}}(k)}{[D_1(z_{\text{ini}})]^2} \int_0^\infty r^2 \frac{P_{\text{ini}}(kr)}{[D_1(z_{\text{ini}})]^2} F_3(k, r, x, z) dr, \quad (1.47)$$

$$P_{\theta\theta}^{13}(k, z) = 2 \frac{k^3}{(2\pi)^2} G_1(k, z) \frac{P_{\text{ini}}(k)}{[D_1(z_{\text{ini}})]^2} \int_0^\infty r^2 \frac{P_{\text{ini}}(kr)}{[D_1(z_{\text{ini}})]^2} G_3(k, r, x, z) dr. \quad (1.48)$$

For implementation in **MG-Copter**, the $z = 0$ linear power spectra $P_0(k) = P^{\text{L}}(k, z = 0) = P_{\text{ini}}(k)[D_1(z = 0)/D_1(z_{\text{ini}})]^2$ are used as input instead of the primordial power spectra. Rewriting the expressions, for the 22 correction we find

$$P_{\delta\delta}^{22}(k, z) = 2 \frac{k^3}{(2\pi)^2} \int_0^\infty r^2 dr \int_{-1}^1 \frac{P_0(kr) P_0(k\sqrt{1+r^2-2rx})}{[D_1(z = 0)]^4} F_2^2(k, r, x, z) dx, \quad (1.49)$$

$$P_{\theta\theta}^{22}(k, z) = 2 \frac{k^3}{(2\pi)^2} \int_0^\infty r^2 dr \int_{-1}^1 \frac{P_0(kr) P_0(k\sqrt{1+r^2-2rx})}{[D_1(z = 0)]^4} F_2(k, r, x, z) \times G_2(k, r, x, z) dx, \quad (1.50)$$

$$P_{\theta\theta}^{22}(k, z) = 2 \frac{k^3}{(2\pi)^2} \int_0^\infty r^2 dr \int_{-1}^1 \frac{P_0(kr) P_0(k\sqrt{1+r^2-2rx})}{[D_1(z = 0)]^4} G_2^2(k, r, x, z) dx, \quad (1.51)$$

while for the 13 correction we have

$$P_{\delta\delta}^{13}(k, z) = 2 \frac{k^3}{(2\pi)^2} F_1(k, z) \frac{P_0(k)}{[D_1(z=0)]^2} \int_0^\infty r^2 \frac{P_0(kr)}{[D_1(z=0)]^2} F_3(k, r, x, z) dr, \quad (1.52)$$

$$\begin{aligned} P_{\delta\theta}^{13}(k, z) &= \frac{k^3}{(2\pi)^2} F_1(k, z) \frac{P_0(k)}{[D_1(z=0)]^2} \int_0^\infty r^2 \frac{P_0(kr)}{[D_1(z=0)]^2} G_3(k, r, x, z) dr \\ &+ \frac{k^3}{(2\pi)^2} G_1(k, z) \frac{P_0(k)}{[D_1(z=0)]^2} \int_0^\infty r^2 \frac{P_0(kr)}{[D_1(z=0)]^2} F_3(k, r, x, z) dr, \end{aligned} \quad (1.53)$$

$$P_{\theta\theta}^{13}(k, z) = 2 \frac{k^3}{(2\pi)^2} G_1(k, z) \frac{P_0(k)}{[D_1(z=0)]^2} \int_0^\infty r^2 \frac{P_0(kr)}{[D_1(z=0)]^2} G_3(k, r, x, z) dr. \quad (1.54)$$

1.5.1.2 SPT with modified gravity

Modified gravity models have been previously added to the original **Copter** [141] to create **MG-Copter** [140]. The computation of the kernels F_n and G_n are affected by the inclusion of modified gravity in SPT, as are the expressions for the 1-loop corrections of the real-space power spectra given in Eqs. (1.49)-(1.54). We shall reproduce here the essentials of the implementation of modified gravity in the SPT part of **MG-Copter**.

The modifications to gravity can be included in the Poisson equation, which up to 3rd order becomes

$$-\left(\frac{k}{aH}\right)^2 \Phi(\vec{k}) = \frac{3\Omega_m(a)}{2} \delta(\vec{k}) \mu(k, a) + S(\vec{k}), \quad (1.55)$$

where $\mu(k, a) = G_{\text{eff}}(k, a)/G$ is an effective Newton's constant² and the non-linear source term $S(\vec{k})$ up to 3rd order is

$$\begin{aligned} S(\vec{k}) &= \int \frac{d^3\vec{k}_1 d^3\vec{k}_2}{(2\pi)^3} \delta_D(\vec{k} - \vec{k}_{12}) \gamma_2(\vec{k}, \vec{k}_1, \vec{k}_2, a) \Delta(\vec{k}_1) \Delta(\vec{k}_2) \\ &+ \int \frac{d^3\vec{k}_1 d^3\vec{k}_2 d^3\vec{k}_3}{(2\pi)^3} \delta_D(\vec{k} - \vec{k}_{123}) \gamma_3(\vec{k}, \vec{k}_1, \vec{k}_2, \vec{k}_3, a) \Delta(\vec{k}_1) \Delta(\vec{k}_2) \Delta(\vec{k}_3). \end{aligned} \quad (1.56)$$

While the effective Newton's constant $\mu(k, a)$ is generally responsible for the (scale-dependent) growth of linear perturbations, at the fully non-linear level modified gravity models typically include a screening mechanism that will affect the growth of non-linearities, and the γ_2 and γ_3 terms provide the leading order description of this screening in perturbation theory.

²Not to be confused with the line-of-sight angle parameter μ , which will always be presented without arguments.

Using the same form for the n^{th} order solutions as in Eqs. (1.37) and (1.38), the new system of equations for the n^{th} order kernels is

$$\begin{aligned} \hat{\mathcal{L}} \begin{bmatrix} F_n(\vec{k}_1, \dots, \vec{k}_n) \\ G_n(\vec{k}_1, \dots, \vec{k}_n) \end{bmatrix} \\ = \sum_{j=1}^{n-1} \begin{bmatrix} -\alpha(\vec{k}_{1\dots j}, \vec{k}_{j+1\dots n}) G_j(\vec{k}_1, \dots, \vec{k}_j) F_{n-j}(\vec{k}_{j+1}, \dots, \vec{k}_n) \\ -\frac{1}{2}\beta(\vec{k}_{1\dots j}, \vec{k}_{j+1\dots n}) G_j(\vec{k}_1, \dots, \vec{k}_j) G_{n-j}(\vec{k}_{j+1}, \dots, \vec{k}_n) - N_n(\vec{k}, \vec{k}_1, \dots, \vec{k}_n) \end{bmatrix}, \end{aligned} \quad (1.57)$$

where

$$\hat{\mathcal{L}} = \begin{bmatrix} a \frac{d}{da} & 1 \\ \frac{3\Omega_m}{2} \mu(k, a) & a \frac{d}{da} + \left(2 + \frac{aH'}{H}\right) \end{bmatrix}, \quad (1.58)$$

and

$$N_2 = \gamma_2(\vec{k}, \vec{k}_1, \vec{k}_2) F_1(\vec{k}_1) F_1(\vec{k}_2), \quad (1.59)$$

$$\begin{aligned} N_3 = & \gamma_2(\vec{k}, \vec{k}_1, \vec{k}_{23}) F_1(\vec{k}_1) F_2(\vec{k}_2, \vec{k}_3) + \gamma_2(\vec{k}, \vec{k}_{12}, \vec{k}_3) F_2(\vec{k}_1, \vec{k}_2) F_1(\vec{k}_3) \\ & + \gamma_3(\vec{k}, \vec{k}_1, \vec{k}_2, \vec{k}_3) F_1(\vec{k}_1) F_1(\vec{k}_2) F_1(\vec{k}_3). \end{aligned} \quad (1.60)$$

In modified gravity, generally the first order growth factor will be scale-dependent. However, if we consider only models where modified gravity becomes active at late times, $P_{\text{ini}}(k)$ and $D_1(z_{\text{ini}})$ will be unchanged from Λ CDM. Therefore Eqs. (1.49)-(1.54) are still applicable as long as we leave $P_0(k)$ and $D_1(z=0)$ as in Λ CDM and only modify the kernels F_i and G_i to include the effects of modified gravity. This is the approach taken in the standard version of **MG-Copter**.

1.5.2 Lagrangian perturbation theory

In Lagrangian dynamics, the position of a particle x_i is written as the sum of its initial position q_i and the displacement field Ψ_i :

$$x_i(\tau) = q_i + \Psi_i(\vec{q}, \tau). \quad (1.61)$$

Unless stated otherwise all time-derivatives in this subsection are with respect to the super-comoving time coordinate τ defined by $d\tau = \frac{dt}{a^2}$. The equation of motion in conformal time η , where $d\eta = dt/a$, given in Eq. (1.28) can be rewritten as

$$\frac{d^2 \vec{x}}{d\eta^2} + \mathcal{H}(\eta) \frac{d\vec{x}}{d\eta} = -\vec{\nabla}_{\vec{x}} \Phi(\vec{x}, \eta). \quad (1.62)$$

Converting to super-comoving time τ , and writing vectors as $\vec{y} = y_i$, this becomes

$$\frac{d^2 x_i}{d\tau^2} = -\nabla_{x_i} \Phi(\vec{x}, \tau) . \quad (1.63)$$

Substituting in Eq.(1.61) and taking the divergence of Eq.(1.63) yields the Lagrangian equation of motion:

$$\nabla_x^i \left[\frac{d^2 \Psi_i(\vec{q}, \tau)}{d\tau^2} \right] = -\nabla_x^2 \Phi(\vec{x}, \tau) . \quad (1.64)$$

This is tricky, since we're applying a differentiation w.r.t. x to a variable that is a function of q . However, the density of particles in Lagrangian coordinates is simply the average particle density of the universe, so we can use mass conservation to write

$$\bar{\rho}(\vec{x}) (1 + \delta(\vec{x})) d^3 \vec{x} = \bar{\rho}(\vec{q}) d^3 \vec{q} . \quad (1.65)$$

But the conservation is defined through the Jacobian:

$$\bar{\rho}(\vec{x}) d^3 \vec{x} = \bar{\rho}(\vec{q}) J(\vec{q}, \tau) d^3 \vec{q} , \quad (1.66)$$

therefore we have

$$\frac{1}{J(\vec{q}, \tau)} = \left| \frac{d^3 q}{d^3 x} \right| = 1 + \delta(\vec{x}) , \quad (1.67)$$

where Eq. (1.61) yields

$$J(\vec{q}, \tau) = \det(\delta_{ij} + \Psi_{i,j}(\vec{q}, \tau)) , \quad (1.68)$$

and we define

$$\Psi_{i,j} = \frac{\partial \Psi_i}{\partial q_j} . \quad (1.69)$$

The chain rule gives us

$$\nabla_x^i = \left[\frac{d^3 q}{d^3 x} \right]_{ij} \nabla_q^j = \frac{1}{\delta_{ij} + \Psi_{i,j}} \frac{\partial}{\partial q_j} , \quad (1.70)$$

such that we can rewrite Eq. (1.64) as

$$\frac{1}{\delta_{ij} + \Psi_{i,j}} \nabla_q^j \left[\frac{d^2 \Psi_i(\vec{q}, \tau)}{d\tau^2} \right] = -\nabla_x^2 \Phi(\vec{x}, \tau) . \quad (1.71)$$

We can approximate $[\delta_{ij} + \Psi_{i,j}]^{-1} \approx \delta_{ij} - \Psi_{i,j}$, and using the perturbative expansion of $\Psi_i(\vec{q}, \tau)$:

$$\Psi_i(\vec{q}, \tau) = \epsilon \Psi_i^{(1)} + \epsilon^2 \Psi_i^{(2)} + \dots , \quad (1.72)$$

we find Eq.(1.71) can be rewritten up to 2nd order as

$$\left(\frac{\partial}{\partial q_i} - \epsilon \frac{\partial \Psi_j^{(1)}}{\partial q_i} \frac{\partial}{\partial q_j} - \epsilon^2 \frac{\partial \Psi_j^{(2)}}{\partial q_i} \frac{\partial}{\partial q_j} \right) \left[\epsilon \frac{d^2 \Psi_i^{(1)}}{d\tau^2} + \epsilon^2 \frac{d^2 \Psi_i^{(2)}}{d\tau^2} \right] = -\nabla_x^2 \Phi(\vec{x}, \tau) . \quad (1.73)$$

To 1st order, Eq.(1.73) becomes

$$\frac{\partial}{\partial q_i} \left[\frac{d^2 \Psi_i^{(1)}}{d\tau^2} \right] = \frac{d^2 \Psi_{i,i}^{(1)}}{d\tau^2} = -\nabla_x^2 \Phi(\vec{x}, \tau) , \quad (1.74)$$

and to 2nd order Eq.(1.73) becomes

$$\frac{\partial}{\partial q_i} \left[\frac{d^2 \Psi_i^{(2)}}{d\tau^2} \right] - \frac{\partial \Psi_j^{(1)}}{\partial q_i} \frac{\partial}{\partial q_j} \left[\frac{d^2 \Psi_i^{(1)}}{d\tau^2} \right] = \frac{d^2 \Psi_{i,i}^{(2)}}{d\tau^2} - \Psi_{j,i}^{(1)} \frac{d^2 \Psi_{i,j}^{(1)}}{d\tau^2} = -\nabla_x^2 \Phi(\vec{x}, \tau) . \quad (1.75)$$

We can use the Jacobian of the transform of between x and q to write the density contrast in terms of Ψ order by order. Starting from $1 + \delta(\vec{x}) = 1/J(\vec{q}, \tau)$, where $J(\vec{q}, \tau) = \det(\delta_{ij} + \Psi_{i,j})$. Using the matrix identities

$$\det(I + A) = 1 + \text{tr}(A) + \frac{1}{2} [\text{tr}^2(A) - \text{tr}(A^2)] + (O)(A^3) , \quad (1.76)$$

and

$$\frac{1}{\det(I + A)} = 1 - \text{tr}(A) + \frac{1}{2} [\text{tr}^2(A) + \text{tr}(A^2)] + (O)(A^3) , \quad (1.77)$$

we can approximate the Jacobian and its inverse up to 2nd order as

$$J \approx 1 + \Psi_{i,i}^{(1)} + \Psi_{i,i}^{(2)} + \frac{1}{2} \left[\left(\Psi_{i,i}^{(1)} \right)^2 - \Psi_{i,j}^{(1)} \Psi_{j,i}^{(1)} \right] , \quad (1.78)$$

$$J^{-1} \approx 1 - \Psi_{i,i}^{(1)} - \Psi_{i,i}^{(2)} + \frac{1}{2} \left[\left(\Psi_{i,i}^{(1)} \right)^2 + \Psi_{i,j}^{(1)} \Psi_{j,i}^{(1)} \right] , \quad (1.79)$$

which finally yields

$$\delta^{(1)}(\vec{x}, \tau) = -\Psi_{i,i}^{(1)}(\vec{q}, \tau) , \quad (1.80)$$

$$\delta^{(2)}(\vec{x}, \tau) = -\Psi_{i,i}^{(2)}(\vec{q}, \tau) + \frac{1}{2} \left[\Psi_{i,i}^{(1)} \Psi_{j,j}^{(1)} + \Psi_{i,j}^{(1)} \Psi_{j,i}^{(1)} \right] . \quad (1.81)$$

For simplicity, we choose to work in Fourier space. Taking the Fourier transforms of Eqs. (1.74) and (1.75) with respect to q leads to

$$\mathcal{F}_q \left[\frac{d^2 \Psi_{i,i}^{(1)}}{d\tau^2} \right] (\vec{k}) = -\mathcal{F}_q [\nabla_x^2 \Phi(\vec{x}, \tau)] , \quad (1.82)$$

$$\mathcal{F}_q \left[\frac{d^2 \Psi_{i,i}^{(2)}}{d\tau^2} \right] (\vec{k}) - \mathcal{F}_q \left[\Psi_{j,i}^{(1)} \frac{d^2 \Psi_{i,j}^{(1)}}{d\tau^2} \right] (\vec{k}) = -\mathcal{F}_q [\nabla_x^2 \Phi(\vec{x}, \tau)] . \quad (1.83)$$

Therefore, we also need the Fourier transforms of our perturbatively expanded densities w.r.t. q . Applying this Fourier transform to Eqs. (1.80) and (1.81) yields are:

$$\tilde{\delta}^{(1)}(\vec{k}, \tau) = \mathcal{F}_q [\delta^{(1)}(\vec{x}, \tau)](\vec{k}) = -\mathcal{F}_q [\Psi_{i,i}^{(1)}(\vec{q}, \tau)](\vec{k}) , \quad (1.84)$$

$$\begin{aligned} \tilde{\delta}^{(2)}(\vec{k}, \tau) = \mathcal{F}_q [\delta^{(2)}(\vec{x}, \tau)](\vec{k}) = & -\mathcal{F}_q [\Psi_{i,i}^{(2)}(\vec{q}, \tau)](\vec{k}) \\ & + \frac{1}{2} \mathcal{F}_q [\Psi_{i,i}^{(1)}\Psi_{j,j}^{(1)} + \Psi_{i,j}^{(1)}\Psi_{j,i}^{(1)}](\vec{k}) . \end{aligned} \quad (1.85)$$

Since Ψ_i is curl-free up to second order, we can write it as the gradient of a scalar field: $\Psi_i(\vec{q}, \tau) = \nabla_i \phi(\vec{q}, \tau)$, and thus $\Psi_{i,i}(\vec{q}, \tau) = \nabla_i \nabla^i \phi(\vec{q}, \tau)$. After a Fourier transform, we have

$$\mathcal{F}_q [\Psi_i(\vec{q}, \tau)](\vec{k}) = ik_i \phi(\vec{k}, \tau) , \quad (1.86)$$

$$\mathcal{F}_q [\Psi_{i,i}(\vec{q}, \tau)](\vec{k}) = ik_i ik^i \phi(\vec{k}, \tau) = -k^2 \phi(\vec{k}, \tau) . \quad (1.87)$$

To solve the above set of equations, it is necessary to specify a form for the Poisson equation.

1.5.2.1 LPT in Λ CDM

In Λ CDM, assuming matter-domination, the only matter content contributing to the Poisson equation is CDM and baryons:

$$\mathcal{F}_q [\nabla_x^2 \Phi_N](\vec{k}) = \kappa \tilde{\delta}(\vec{k}, \tau) = \kappa \left(\tilde{\delta}^{(1)} + \tilde{\delta}^{(2)} + \dots \right) , \quad (1.88)$$

where $\kappa \equiv 4\pi G \bar{\rho} a^4 = \frac{3}{2} \Omega_m H_0^2 a$ and $\tilde{\delta}$ is the CDM+baryon density.

To solve for the 1st order displacement $\Psi_i^{(1)}$, we begin by inserting this into Eq. (1.82), and utilising Eq. (1.84) yields

$$\mathcal{F}_q \left[\frac{d^2 \Psi_{i,i}^{(1)}}{d\tau^2} \right](\vec{k}) = -\kappa \tilde{\delta}_{\text{cb}}^{(1)} = \kappa \mathcal{F}_q [\Psi_{i,i}^{(1)}](\vec{k}) , \quad (1.89)$$

and after using Eq. (1.87), this becomes

$$-k^2 \frac{d^2 \phi(\vec{k}, \tau)}{d\tau^2} = -k^2 \kappa \phi(\vec{k}, \tau) . \quad (1.90)$$

Because the growth of density perturbations is scale-independent in Λ CDM, we can write $\phi(\vec{k}, \tau) = D_1(\tau) \phi(\vec{k}, \tau_{\text{ini}})$ where $D_1(\tau)$ is the 1st order growth factor, dependent only on τ , and $\phi(\vec{k}, \tau_{\text{ini}})$ is the initial state of the scalar field. With these definitions, Eq. (1.89) reduces to

$$\left[\frac{d^2}{d\tau^2} - \kappa \right] D_1(\tau) = 0 , \quad (1.91)$$

where $\phi(\vec{k}, \tau_{\text{ini}}) = \tilde{\delta}(\vec{k}, \tau_{\text{ini}})/k^2$ is specified by Eqs. (1.84) and (1.87). This differential equation can be solved analytically, as long as initial conditions for D_1 and $dD_1/d\tau$ are provided. The initial conditions are set such that $D_{1,\text{cb}}(\tau_{\text{ini}}) = 1$ and $\frac{dD_{1,\text{cb}}(\tau_{\text{ini}})}{d\tau} = \left(\frac{1}{a} \frac{da}{d\tau}\right)\bigg|_{\tau=\tau_{\text{ini}}}$ corresponding to the growing mode in a Λ CDM, matter-dominated universe (Einstein-de Sitter). Once $D_1(\tau)$ is known, we can finally express

$$\Psi^{(1)}(\vec{k}, \tau) = ik_i \phi^{(1)}(\vec{k}, \tau) = ik_i \frac{D_1(\vec{k}, \tau) \tilde{\delta}^{(1)}(\vec{k}, \tau_{\text{ini}})}{k^2}, \quad (1.92)$$

and then use an inverse Fourier transform to get the real-space 1st order displacement:

$$\Psi^{(1)}(\vec{q}, \tau) = D_1(\tau) \int \frac{d^3 k}{(2\pi)^3} e^{i\vec{k} \cdot \vec{q}} \frac{ik_i}{k^2} \tilde{\delta}^{(1)}(\vec{k}, \tau_{\text{ini}}). \quad (1.93)$$

For the 2nd order displacement $\Psi_i^{(2)}$, we insert Eq. (1.88) into Eq. (1.85), and then substitute Eq. (1.85), which yields

$$\begin{aligned} \mathcal{F}_q \left[\frac{d^2 \Psi_{i,i}^{(2)}}{d\tau^2} \right] (\vec{k}) - \mathcal{F}_q \left[\Psi_{j,i}^{(1)} \frac{d^2 \Psi_{i,j}^{(1)}}{d\tau^2} \right] (\vec{k}) &= -\kappa \tilde{\delta}_{\text{cb}}^{(2)} \\ &= \kappa \mathcal{F}_q \left[\Psi_{i,i}^{(2)}(\vec{q}, \tau) \right] (\vec{k}) \\ &\quad - \frac{\kappa}{2} \mathcal{F}_q \left[\Psi_{i,i}^{(1)} \Psi_{j,j}^{(1)} + \Psi_{i,j}^{(1)} \Psi_{j,i}^{(1)} \right] (\vec{k}). \end{aligned} \quad (1.94)$$

Using the 1st order solution for $d^2 \Psi^{(1)}/d\tau^2$ yields

$$\begin{aligned} \mathcal{F}_q \left[\frac{d^2 \Psi_{i,i}^{(2)}}{d\tau^2} \right] (\vec{k}) - \kappa \mathcal{F}_q \left[\Psi_{j,i}^{(1)} \Psi_{i,j}^{(1)} \right] (\vec{k}) &= \kappa \mathcal{F}_q \left[\Psi_{i,i}^{(2)}(\vec{q}, \tau) \right] (\vec{k}) \\ &\quad - \frac{\kappa}{2} \mathcal{F}_q \left[\Psi_{i,i}^{(1)} \Psi_{j,j}^{(1)} + \Psi_{i,j}^{(1)} \Psi_{j,i}^{(1)} \right] (\vec{k}). \end{aligned} \quad (1.95)$$

Simplifying, this reduces to

$$\left[\frac{d^2}{d\tau^2} - \kappa \right] \mathcal{F}_q \left[\Psi_{i,i}^{(2)}(\vec{q}, \tau) \right] (\vec{k}) = -\frac{\kappa}{2} \mathcal{F}_q \left[\Psi_{i,i}^{(1)} \Psi_{j,j}^{(1)} - \Psi_{i,j}^{(1)} \Psi_{j,i}^{(1)} \right] (\vec{k}). \quad (1.96)$$

In a similar way to Eq.(1.93), the quantity $\Psi_{l,m}^{(1)}(\vec{q}, \tau)$ needed to simplify Eq. (1.96) can be written as an inverse Fourier transform:

$$\Psi_{l,m}^{(1)}(\vec{q}, \tau) = D_1(\tau) \int \frac{d^3 \vec{k}_1}{(2\pi)^3} ik_1^m e^{i\vec{k}_1 \cdot \vec{q}} \frac{ik_{1l}}{k_1^2} \tilde{\delta}(\vec{k}_1, \tau_{\text{ini}}). \quad (1.97)$$

Therefore, the convolutions are

$$\begin{aligned} &\Psi_{l,m}^{(1)}(\vec{q}, \tau) \Psi_{m,l}^{(1)}(\vec{q}, \tau) \\ &= D_1^2(\tau) \int \frac{d^3 \vec{k}_1}{(2\pi)^3} \frac{d^3 \vec{k}_2}{(2\pi)^3} ik_1^m e^{i\vec{k}_1 \cdot \vec{q}} \frac{ik_{1l}}{k_1^2} ik_2^l e^{i\vec{k}_2 \cdot \vec{q}} \frac{ik_{2m}}{k_2^2} \tilde{\delta}(\vec{k}_1, \tau_{\text{ini}}) \tilde{\delta}(\vec{k}_2, \tau_{\text{ini}}) \\ &= D_1^2(\tau) \int \frac{d^3 \vec{k}_1}{(2\pi)^3} \frac{d^3 \vec{k}_2}{(2\pi)^3} i^4 e^{i(\vec{k}_1 + \vec{k}_2) \cdot \vec{q}} \frac{k_1^m k_{1l} k_2^l k_{2m}}{k_1^2 k_2^2} \tilde{\delta}(\vec{k}_1, \tau_{\text{ini}}) \tilde{\delta}(\vec{k}_2, \tau_{\text{ini}}) \\ &= D_1^2(\tau) \int \frac{d^3 \vec{k}_1}{(2\pi)^3} \frac{d^3 \vec{k}_2}{(2\pi)^3} e^{i(\vec{k}_1 + \vec{k}_2) \cdot \vec{q}} \frac{(\vec{k}_1 \cdot \vec{k}_2)^2}{k_1^2 k_2^2} \tilde{\delta}(\vec{k}_1, \tau_{\text{ini}}) \tilde{\delta}(\vec{k}_2, \tau_{\text{ini}}), \end{aligned} \quad (1.98)$$

$$\begin{aligned}
& \Psi_{l,l}^{(1)}(\vec{q}, \tau) \Psi_{m,m}^{(1)}(\vec{q}, \tau) \\
&= D_1^2(\tau) \int \frac{d^3 \vec{k}_1}{(2\pi)^3} \frac{d^3 \vec{k}_2}{(2\pi)^3} i k_1^l e^{i \vec{k}_1 \cdot \vec{q}} \frac{i k_{1l}}{k_1^2} i k_2^m e^{i \vec{k}_2 \cdot \vec{q}} \frac{i k_{2m}}{k_2^2} \tilde{\delta}(\vec{k}_1, \tau_{\text{ini}}) \tilde{\delta}(\vec{k}_2, \tau_{\text{ini}}) \\
&= D_1^2(\tau) \int \frac{d^3 \vec{k}_1}{(2\pi)^3} \frac{d^3 \vec{k}_2}{(2\pi)^3} e^{i(\vec{k}_1 + \vec{k}_2) \cdot \vec{q}} \tilde{\delta}(\vec{k}_1, \tau_{\text{ini}}) \tilde{\delta}(\vec{k}_2, \tau_{\text{ini}}) , \quad (1.99)
\end{aligned}$$

such that

$$\begin{aligned}
& \Psi_{l,l}^{(1)}(\vec{q}, \tau) \Psi_{m,m}^{(1)}(\vec{q}, \tau) - \Psi_{l,m}^{(1)}(\vec{q}, \tau) \Psi_{m,l}^{(1)}(\vec{q}, \tau) \\
&= D_1^2(\tau) \int \frac{d^3 \vec{k}_1}{(2\pi)^3} \frac{d^3 \vec{k}_2}{(2\pi)^3} e^{i(\vec{k}_1 + \vec{k}_2) \cdot \vec{q}} \left(1 - \frac{(\vec{k}_1 \cdot \vec{k}_2)^2}{k_1^2 k_2^2} \right) \tilde{\delta}(\vec{k}_1, \tau_{\text{ini}}) \tilde{\delta}(\vec{k}_2, \tau_{\text{ini}}) . \quad (1.100)
\end{aligned}$$

Then taking the Fourier transform yields

$$\begin{aligned}
& \mathcal{F} \left[\Psi_{l,l}^{(1)}(\vec{q}, \tau) \Psi_{m,m}^{(1)}(\vec{q}, \tau) - \Psi_{l,m}^{(1)}(\vec{q}, \tau) \Psi_{m,l}^{(1)}(\vec{q}, \tau) \right] \\
&= D_1^2(\tau) \int d^3 \vec{q} e^{-i \vec{k} \cdot \vec{q}} \int \frac{d^3 \vec{k}_1}{(2\pi)^3} \frac{d^3 \vec{k}_2}{(2\pi)^3} e^{i(\vec{k}_1 + \vec{k}_2) \cdot \vec{q}} \left(1 - \frac{(\vec{k}_1 \cdot \vec{k}_2)^2}{k_1^2 k_2^2} \right) \tilde{\delta}(\vec{k}_1, \tau_{\text{ini}}) \tilde{\delta}(\vec{k}_2, \tau_{\text{ini}}) \\
&= D_1^2(\tau) \int \frac{d^3 \vec{k}_1}{(2\pi)^3} \frac{d^3 \vec{k}_2}{(2\pi)^3} \int d^3 \vec{q} e^{-i(\vec{k} - (\vec{k}_1 + \vec{k}_2)) \cdot \vec{q}} \left(1 - \frac{(\vec{k}_1 \cdot \vec{k}_2)^2}{k_1^2 k_2^2} \right) \tilde{\delta}(\vec{k}_1, \tau_{\text{ini}}) \tilde{\delta}(\vec{k}_2, \tau_{\text{ini}}) \\
&= D_1^2(\tau) \int \frac{d^3 \vec{k}_1 d^3 \vec{k}_2}{(2\pi)^3} \delta_D(\vec{k} - \vec{k}_{12}) \left(1 - \frac{(\vec{k}_1 \cdot \vec{k}_2)^2}{k_1^2 k_2^2} \right) \tilde{\delta}(\vec{k}_1, \tau_{\text{ini}}) \tilde{\delta}(\vec{k}_2, \tau_{\text{ini}}) . \quad (1.101)
\end{aligned}$$

Substituting Eqs. (1.87) and (1.101) into Eq. (1.96) leads to

$$\begin{aligned}
& -k^2 \left[\frac{d^2}{d\tau^2} - \kappa \right] \phi^{(2)}(\vec{k}, \tau) = -\frac{\kappa}{2} D_1^2(\tau) \int \frac{d^3 \vec{k}_1 d^3 \vec{k}_2}{(2\pi)^3} \delta_D(\vec{k} - \vec{k}_{12}) \\
& \quad \times \left(1 - \frac{(\vec{k}_1 \cdot \vec{k}_2)^2}{k_1^2 k_2^2} \right) \tilde{\delta}(\vec{k}_1, \tau_{\text{ini}}) \tilde{\delta}(\vec{k}_2, \tau_{\text{ini}}) . \quad (1.102)
\end{aligned}$$

If we define the following form for $\phi^{(2)}$:

$$\phi^{(2)}(\vec{k}, \tau) = \frac{D_2(\tau)}{2k^2} \int \frac{d^3 k_1 d^3 k_2}{(2\pi)^3} \delta_D^{(3)}(\vec{k} - \vec{k}_{12}) \tilde{\delta}(\vec{k}_1, \tau_{\text{ini}}) \tilde{\delta}(\vec{k}_2, \tau_{\text{ini}}) , \quad (1.103)$$

then Eq. (1.102) reduces to

$$\left[\frac{d^2}{d\tau^2} - \kappa \right] D_2(\tau) = \kappa \left(1 - \frac{(\vec{k}_1 \cdot \vec{k}_2)^2}{k_1^2 k_2^2} \right) D_1^2(\tau) . \quad (1.104)$$

We can solve this differential equation for D_2 , provided we know D_1 and supply initial conditions for D_2 and $dD_2/d\tau$. For Λ CDM during matter domination, the physically relevant Einstein-de Sitter solution has $D_2 = -\frac{3}{7}D_1^2$ so the initial conditions can be

taken as $D_2(\tau_{\text{ini}}) = -\frac{3}{7}$ and $\frac{dD_2(\tau_{\text{ini}})}{d\tau} = -\frac{6}{7} \left(\frac{1}{a} \frac{da}{d\tau} \right) \Big|_{\tau=\tau_{\text{ini}}}$. The real-space second order displacement $\Psi_i^{(2)}(\vec{q}, \tau)$ can then be written as an inverse Fourier transform:

$$\begin{aligned} \Psi_i^{(2)}(\vec{q}, \tau) = & \frac{D_2(\tau)}{2} \int \frac{d^3 \vec{k}}{(2\pi)^3} e^{i\vec{k} \cdot \vec{q}} \frac{ik_i}{k^2} \\ & \times \int \frac{d^3 k_1 d^3 k_2}{(2\pi)^3} \delta_D^{(3)}(\vec{k} - \vec{k}_{12}) \tilde{\delta}(\vec{k}_1, \tau_{\text{ini}}) \tilde{\delta}(\vec{k}_2, \tau_{\text{ini}}) , \end{aligned} \quad (1.105)$$

which allows the full 2nd order solution $\Psi_i^{(2)}(\vec{q}, \tau)$ to be recovered using the $D_2(\tau)$ values from solving Eq. (1.104) as long as the initial density field $\tilde{\delta}(\vec{k}, \tau_{\text{ini}})$ is known.

1.5.3 Redshift-space distortions

When computing clustering statistics from observational data, it is necessary to know the three-dimensional positions of whatever astrophysical object is being considered as a biased tracer of the underlying matter distribution. Such positions are usually mapped as two angles which determine location in the sky, and the radial distance to the object. However, since we generally cannot measure the radial distance to an astrophysical object directly, we must infer it from the object's redshift, which can introduce redshift-space distortions (RSD) to the clustering [142]. RSD occur when the radial distances to tracers are computed using their observed redshifts without accounting for the effect of the tracers' peculiar velocities on the redshifts which adds to the contribution from the Hubble flow. The cosmological distance, the one given purely by the Hubble flow, that we want to use for mapping is given by

$$r(z_{\text{cos}}) = \int_0^{z_{\text{cos}}} \frac{c}{H(z)} dz , \quad (1.106)$$

where z_{cos} is the contribution to the observational redshift z_{obs} that comes purely from Hubble flow³. However, as mentioned above, the object's peculiar velocity can also contribute to z_{obs} :

$$1 + z_{\text{obs}} = \frac{1 + z_{\text{cos}}}{1 - \frac{v_{\parallel}(\vec{r})}{c}} , \quad (1.107)$$

where v_{\parallel} is the component of the object's peculiar velocity directed along the line-of-sight (LoS). Consider an object with a small peculiar velocity such that there is only

³Note that this conversion between cosmological distance and cosmological redshift requires knowledge of $H(z)$. If the wrong cosmological model, and thus form of $H(z)$, is assumed there will again be distortions created in the clustering; this is known as the Alcock-Paczynski effect [143] and can be detected by comparing angular and radial clustering.

a small perturbation of Δz to the observed redshift $z_{\text{obs}} = z_{\text{cos}} + \Delta z$. The comoving distance for this perturbed redshift is

$$\begin{aligned}
r(z_{\text{obs}}) &= r(z_{\text{cos}} + \Delta z) = \int_0^{z_{\text{cos}} + \Delta z} \frac{c}{H(z)} dz \\
&= \int_0^{z_{\text{cos}}} \frac{c}{H(z)} dz + \int_{z_{\text{cos}}}^{z_{\text{cos}} + \Delta z} \frac{c}{H(z)} dz \\
&= r(z_{\text{cos}}) + \frac{c\Delta z}{H(z_{\text{cos}})}, \tag{1.108}
\end{aligned}$$

where we have evaluated the second integral assuming Δz is very small. Using the approximation $(1+x)^{-1} \approx 1-x$, Eq. (1.107) leads to $c\Delta z \approx (1+z_{\text{cos}})v_{\parallel}(\vec{r})$. Thus, we find that the consequence of ignoring the peculiar velocity contribution to an object's redshift and mistakenly assuming $z_{\text{obs}} = z_{\text{cos}}$ is that the object's measured position in redshift-space is displaced along the LoS:

$$\vec{s} = \vec{r} + \frac{(1+z_{\text{cos}})v_{\parallel}(\vec{r})}{H(z_{\text{cos}})} \hat{r}. \tag{1.109}$$

For distant objects, the second term in the above expression is usually much smaller than the first. While it can thus usually be considered negligible for individual objects, the same cannot be said when assessing the impact on clustering statistics. This is primarily because the peculiar velocity term breaks down rotational invariance and thus makes the clustering anisotropic in redshift-space such that for the redshift-space power spectrum $P^{(s)}(\vec{k}) = P^{(s)}(k, \mu) \neq P^{(s)}(k)$, where $\mu = \cos(\theta)$ and θ is the angle between \vec{k} and the LoS \hat{r} .

On linear scales, objects tend to coherently fall in to (flow out from) an overdensity (underdensity), which results in a slight squashing (stretching) along the LoS. This enhances (suppresses) the clustering amplitude along the LoS, which is the so-called Kaiser effect [144]. On non-linear scales, objects tend to be virialised with large random motions, causing a strong stretching along the LoS commonly known as the Fingers-of-God (FoG) effect [145], which damps the clustering amplitude on these smaller scales along the LoS.

RSD depend on the growth rate of cosmological structure formation through the peculiar velocities of objects. In order to extract this information, it is necessary to model RSD. A simple way to model the redshift-space power spectrum at linear order is with the Kaiser model:

$$P_g^{(s),L}(k, \mu) = b^2(1 + \beta\mu^2)^2 P_m^L(k), \tag{1.110}$$

where $\beta = f/b$, b is the linear bias of the tracer and $f(k, a) = \frac{d \log D_1(k, a)}{d \log a}$ is the growth

rate. We can decompose $P^{(s)}(k, \mu)$ using the Legendre polynomials $\mathcal{P}_l(\mu)$:

$$P_l^{(s)}(k) = \frac{2l+1}{2} \int_{-1}^1 d\mu P^{(s)}(k, \mu) \mathcal{P}_l(\mu) . \quad (1.111)$$

In the Kaiser model, $P^{(s)}$ only contains terms up to μ^4 , so only the monopole P_0 , quadrupole P_2 , and hexadecapole P_4 are non-vanishing:

$$P_{g,l=0}^{(s)}(k) = \left(1 + \frac{2}{3}\beta + \frac{1}{5}\beta^2\right) b^2 P_m^L(k) , \quad (1.112)$$

$$P_{g,l=2}^{(s)}(k) = \left(\frac{4}{3}\beta + \frac{4}{7}\beta^2\right) b^2 P_m^L(k) , \quad (1.113)$$

$$P_{g,l=4}^{(s)}(k) = \frac{8}{35}\beta^2 b^2 P_m^L(k) . \quad (1.114)$$

However, the Kaiser approach fails to accurately model non-linear RSD effects. One way to improve upon the Kaiser approach is the TNS model.

1.5.3.1 TNS Model

The TNS model for the redshift-space power spectrum $P^{(s)}$ as a function of scale k and line-of-sight (LoS) angle parameter $\mu = \cos(\theta)$ is given by Eq. (18) of [146], which we reproduce here with subtle changes due to the different definition of θ :

$$P_{\text{TNS}}^{(s)}(k, \mu) = D_{\text{FoG}} [k\mu\sigma_v] \left\{ P_{\delta\delta}(k) - 2\mu^2 P_{\delta\theta}(k) + \mu^4 P_{\theta\theta}(k) + A(k, \mu) + B(k, \mu) \right\} , \quad (1.115)$$

where D_{FoG} is the Fingers-of-God damping function which we will discuss later. It is generally a function of k , μ , and the velocity dispersion σ_v . The power spectra $P_{\delta\delta}(k)$, $P_{\delta\theta}(k)$, and $P_{\theta\theta}(k)$ correspond to the density auto-correlation, density-velocity divergence cross correlation, and the velocity divergence auto-correlation respectively. $A(k, \mu)$ and $B(k, \mu)$ are correction terms given by

$$A(k, \mu) = -k\mu \int \frac{d^3\vec{p}}{(2\pi)^3} \frac{p_z}{p^2} \left\{ B_\sigma(\vec{p}, \vec{k} - \vec{p}, -\vec{k}) - B_\sigma(\vec{p}, \vec{k}, -\vec{k} - \vec{p}) \right\} , \quad (1.116)$$

$$B(k, \mu) = (k\mu)^2 \int \frac{d^3\vec{p}}{(2\pi)^3} F(\vec{p}) F(\vec{k} - \vec{p}) , \quad (1.117)$$

where B_σ is the cross bispectrum defined by

$$\begin{aligned} & \left\langle \theta(\vec{k}_1) \left\{ \delta(\vec{k}_2) - \frac{k_{2z}^2}{k_2^2} \theta(\vec{k}_2) \right\} \left\{ \delta(\vec{k}_3) - \frac{k_{3z}^2}{k_3^2} \theta(\vec{k}_3) \right\} \right\rangle \\ & = (2\pi)^3 \delta_D(\vec{k}_1 + \vec{k}_2 + \vec{k}_3) B_\sigma(\vec{k}_1, \vec{k}_2, \vec{k}_3) , \end{aligned} \quad (1.118)$$

and $F(\vec{p})$ is defined as

$$F(\vec{p}) = \frac{p_z}{p^2} \left\{ P_{\delta\theta}(p) - \frac{p_z^2}{p^2} P_{\theta\theta}(p) \right\} . \quad (1.119)$$

B_σ can be written up to second order in P_0 by expanding the perturbations up to second order, leading to

$$\begin{aligned} B_\sigma(\vec{k}_1, \vec{k}_2, \vec{k}_3) = & \\ & 2 \left[\left(F_1(k_2) - \frac{k_{2z}^2}{k_2^2} G_1(k_2) \right) \left(F_1(k_3) - \frac{k_{3z}^2}{k_3^2} G_1(k_3) \right) G_2(\vec{k}_2, \vec{k}_3) \frac{P_0(k_2)P_0(k_3)}{[D_1(z=0)]^4} \right. \\ & + G_1(k_1) \left(F_1(k_3) - \frac{k_{3z}^2}{k_3^2} G_1(k_3) \right) \left(F_2(\vec{k}_1, \vec{k}_3) - \frac{k_{2z}^2}{k_2^2} G_2(\vec{k}_1, \vec{k}_3) \right) \frac{P_0(k_1)P_0(k_3)}{[D_1(z=0)]^4} \\ & \left. + G_1(k_1) \left(F_1(k_2) - \frac{k_{2z}^2}{k_2^2} G_1(k_2) \right) \left(F_2(\vec{k}_1, \vec{k}_2) - \frac{k_{3z}^2}{k_3^2} G_2(\vec{k}_1, \vec{k}_2) \right) \frac{P_0(k_1)P_0(k_2)}{[D_1(z=0)]^4} \right] , \end{aligned} \quad (1.120)$$

while $F(\vec{p})$ is already 2nd order in P_0 , and can be written in terms of perturbation kernels as

$$F(\vec{p}) = \frac{p_z}{p^2} \left[G_1(p) F_1(p) \frac{P_0(k)}{[D_1(z=0)]^2} - \frac{p_z^2}{p^2} G_1(p) G_1(p) \frac{P_0(p)}{[D_1(z=0)]^2} \right] . \quad (1.121)$$

The Fingers-of-God damping factor is phenomenological; two of the most commonly used forms are the Gaussian

$$D_{\text{FoG}}^{\text{Gauss}} [k\mu\sigma_v] = \exp(-k^2\mu^2\sigma_v^2) , \quad (1.122)$$

and Lorentzian

$$D_{\text{FoG}}^{\text{Lor}} [k\mu\sigma_v] = \frac{1}{1 + (k^2\mu^2\sigma_v^2/2)} . \quad (1.123)$$

The velocity dispersion σ_v in the Fingers-of-God damping factor is a free parameter and needs to be fitted using some other $P^{(s)}$ data. For example, to fit using simulations we can minimise the likelihood function

$$\begin{aligned} -2 \ln \mathcal{L} = & \sum_n \sum_{l, l'} \left(P_{l, \text{TNS}}^{(s)}(k_n) - P_{l, \text{sim}}^{(s)}(k_n) \right) \text{Cov}_{l, l'}^{-1}(k_n) \\ & \times \left(P_{l', \text{TNS}}^{(s)}(k_n) - P_{l', \text{sim}}^{(s)}(k_n) \right) , \end{aligned} \quad (1.124)$$

where P_l are the multipoles of the redshift-space power spectrum described in Eq. (1.111).

With the SPT real-space power spectra $P_{\delta\delta}$, $P_{\delta\theta}$, $P_{\theta\theta}$ computed up to 1-loop order, **MG-Copter** can then input these to the TNS model to calculate the redshift-space power spectrum $P^{(s)}(k)$. We note that the TNS model of Eq. (1.115) is still applicable when modelling RSD with modified gravity and/or massive neutrinos without changes, although the components will be affected as described in Section 1.5.1.2 for modified gravity and Section 3.1 for massive neutrinos.

1.6 Simulations

As the growth of structure progresses, the process becomes non-linear. As such, perturbation theory can no longer accurately describe structure formation. One of the most common ways to model structure formation in this non-linear regime is to use a cosmological N -body simulation [147, 148, 149, 150]. The system is set up as a collection of particles inside a box. At each timestep, the force acting on each particle due to the other particles is computed by solving the Newtonian equation of gravity

$$\vec{F}_i = - \sum_{i \neq j} \frac{G m_i m_j (\vec{r}_i - \vec{r}_j)}{|\vec{r}_i - \vec{r}_j|^3}. \quad (1.125)$$

Between timesteps, the particles move under the influence of the set of forces computed at the previous timestep, before the forces are then recalculated for the new arrangement of particles. In order to maintain accuracy, the timesteps must be small which makes the N -body method highly computationally expensive. Several different codes have been created [151, 152, 153, 154, 155, 156, 157, 158, 159] to produce high-resolution simulations for a wide variety of cosmological models. A recent code-comparison project of such codes [160] demonstrated agreement at the 1% level deep into the non-linear regime (e.g. $k \sim 5h/\text{Mpc}$ for the power spectrum).

Since traditional N -body simulations solve the Newtonian equations of motion, they are incapable of modelling relativistic effects. However, there is ongoing research working towards creating simulation codes that solve the equations of GR. One such effort is **gevolution** [161], a code that is based on a weak-field expansion of GR.

Some Newtonian N -body codes have also implemented modified gravity. Originally, modified gravity simulations were much slower than simulations of ΛCDM (typically by a factor of 5 – 20 depending on model) due to having to solve complicated, highly non-linear partial differential equations. However, recently some very interesting approaches have been proposed to speed up such simulations making them only a factor of ~ 1.5 – 2 times slower than a corresponding ΛCDM simulation without sacrificing much accuracy [162, 163, 164]. We discuss some of the practicalities of implementing modified gravity in Section 2.5.

When including massive neutrinos in N -body simulations, ideally we would solve the collisionless Boltzmann equation

$$\frac{d}{dt} f(\vec{x}, \vec{p}, t) = 0. \quad (1.126)$$

However, unlike for CDM, the thermal velocities of massive neutrinos are comparable to, or even larger than, the gravitationally-induced streaming velocities. This means

that this equation should be solved in its full 6+1 dimensions, rather than the reduced 3+1 case that is applicable for CDM. Unfortunately, solving the above equation in 6+1 dimensions is not numerically feasible with current computational resources. This leaves several options. Firstly, the full neutrinos' distribution function $f(\vec{x}, \vec{p}, t)$ can be represented as particles [165, 166, 167, 168, 169, 170, 171]. This leads to noise-related problems when neutrino masses are small because a huge number of particles are needed to sample the thermal velocity component of $f(\vec{x}, \vec{p}, t)$ properly. It is also difficult to understand how to treat the particles when the masses are small enough to yield relativistic velocities, unless the simulation is relativistic as in [161]. Alternatively, a second method is to assume that neutrino perturbations remain linear. The simplest way to implement this assumption is to realise the linear neutrino transfer function, computed with a Boltzmann code, onto a grid to create a linear neutrino density field [172]. This can be improved upon by solving the linear theory equations for neutrinos with the Boltzmann code, but then computing the evolution of the neutrino perturbations using the gravitational potential sourced by non-linear CDM perturbations rather than the potential sourced purely by linear CDM [173, 174]. However, any assumption that neutrino perturbations remain linear at all times breaks down when the neutrino masses are large. A third approach is a hybrid combination of the first two methods, where the neutrinos are initially followed using linear theory and then later on treated as particles when the thermal velocities approach the magnitude of the gravitationally-induced streaming velocities [175]. Finally, the full momentum-dependent Boltzmann equation can be converted to a hierarchy of velocity moment equations. Since neutrinos have a large anisotropic stress component, they cannot be treated as a perfect fluid and the hierarchy cannot simply be closed at order 1. Instead, the hierarchy can be closed at the second moment. One way to do this is to estimate the second moment using the motion of test particles [176], which restricts the method to non-relativistic fluids. Conversely, the first two moment equations can be solved in full non-linear theory and the stress and pressure perturbations treated with linear theory (scaled by the non-linear density field) [177], which has the advantage of guaranteeing the solution behaves correctly in the linear regime while still describing the fully non-linear evolution of structure and being able to describe relativistic fluids. Some additional examples of how N -body simulations including the effects of modified gravity can be used to make predictions for cosmological observables are presented in [178, 179, 180].

There are many situations where the high computational expense of N -body simulations limits their applicability, even for Λ CDM. Several fast, approximate methods for simulating structure formation have been proposed over the last decade such

as PINOCCHIO (PINpointing Orbit-Crossing Collapsed Hierarchical Objects) [181], which recently has been extended to including massive neutrinos and modified gravity [182], as well as Peak-Patch [183], PTHalos [184, 185, 186], QPM (Quick Particle Mesh) [187], PATCHY (PerturbAtion Theory Catalog generator of Halo and galaxY distributions) [188], HALOGEN [189] and COLA (COmoving Lagrangian Acceleration) [190, 191, 192, 193, 194, 195, 196].

The COLA approach differs from traditional N -body simulations in that the particle trajectories are written as the sum of the path predicted by Lagrangian perturbation theory and the deviation of the full trajectory from this LPT-predicted path

$$\vec{x} = \vec{x}_{\text{LPT}} + \vec{x}_{\text{dev}}. \quad (1.127)$$

Thus instead of computing the full particle trajectories, the N -body equations are modified to be solved for the deviations about the LPT path

$$\frac{d^2 \vec{x}_{\text{dev}}}{d\tau^2} = -\vec{\nabla}_{\vec{x}} \Phi - \frac{d^2 \vec{x}_{\text{LPT}}}{d\tau^2}, \quad (1.128)$$

where the extra term $d^2 \vec{x}_{\text{LPT}}/d\tau^2$ is a ‘fictitious force’ computed separately to the N -body using LPT. The deviations are typically much smaller than the distances involved in computing the full particle trajectories, which allows large N -body timesteps to be taken. This makes COLA simulations faster than traditional N -body by a factor $O(100 - 1000)$, while at the same time keeping accuracy on the largest scales. As the number of timesteps used increases, the method will converge to the result of a standard N -body simulation (with the same simulation parameters). A comprehensive study of the accuracy of COLA with respect to the simulations parameters can be found in [197, 195, 196].

For any N -body simulation, traditional or otherwise, the initial distribution of N -body particles must be set. A typical method is to run a Boltzmann code and output the CDM power spectrum $P(k)$ at the simulation’s starting redshift and use it to construct a Gaussian density field. The distribution of Fourier modes can be expressed as

$$\delta(\vec{k}) = A e^{i\theta}, \quad (1.129)$$

where A is the amplitude of the mode and θ is its phase, both of which depend on \vec{k} . For a Gaussian field, θ is a random variable distributed uniformly between 0 and 2π , and A follows a Raleigh distribution

$$p(A)dA = \frac{A}{\sigma^2} e^{-A^2/2\sigma^2} dA, \quad (1.130)$$

where $\sigma^2 = VP(k)/(16\pi^3)$ and $V = L^3$ is the volume of the simulation box with length L . The clustering statistics of simulations produced using this approach have a so called sample variance that arises from the finite size of the simulation box limiting the number of modes it can contain. This is especially punitive at scales close to the box length, where there are very few Fourier modes. To overcome this issue, one can run a large ensemble of simulations each with a different random realisation of the initial density distribution and compute the mean clustering statistics.

However, there is also an alternative approach. Firstly, the amplitude of the density modes A can be fixed such that the power spectrum of the density modes exactly matches the amplitude of the input power spectrum i.e. $\langle \delta(\vec{k})\delta(\vec{k}) \rangle = VP(k)/(2\pi)^3$, and has no intrinsic scatter. This is achieved with a distribution of A given by the Dirac delta function

$$p(A)dA = \delta^D \left(A - \sqrt{\frac{VP(k)}{(2\pi)^3}} \right) dA . \quad (1.131)$$

Secondly, a paired field is created with the same amplitude A , but inverted phase $\theta \rightarrow \theta + \pi$. By running a pair of simulations with this pair of initial density fields, a variety of clustering statistics can be obtained with comparable variance to that of a large ensemble of simulations produced with the typical Gaussian initial density fields [198]. This approach has also been shown not to introduce a bias to the recovery of the mean properties of the Gaussian ensemble, despite the fixing procedure introducing non-Gaussianity [199].

Chapter 2

COLA with scale-dependent modified gravity and massive neutrinos

The work in this chapter was carried out by the author and his supervisory team in collaboration with Hans Winther. The author's contribution was the addition of modified gravity and massive neutrinos in the 2LPT formalism, as well as helping to test MG-PICOLA. Hans Winther wrote MG-PICOLA and produced all the simulations used in this chapter. Figures 2.2-2.10 were created by the author; the other plots in this chapter were created by Hans Winther. The supervisory team provided direction and advice throughout.

In this chapter we present a code, MG-PICOLA¹, based on the publicly available L-PICOLA code [200], that allows us to perform numerical simulation of structure formation for general theories that exhibit scale-dependent growth using the COLA approach. The code computes the second order Lagrangian displacement-fields for these theories and also includes general methods to take into account the all important screening effect in modified gravity theories. We have implemented three types of common screening mechanisms: potential (chameleon [201, 202], symmetron [203, 204, 205] etc.), gradient (k-Mouflage [206]) and density (the Vainhstein mechanism [207]; DGP, Galileon models). We have implemented often studied models like $f(R)$ and DGP together with a general $\{m(a), \beta(a)\}$ parameterization [208, 209] of modified gravity models with chameleon-like screening. Our approach is therefore able to cover most of

¹The code can be found at <https://github.com/HAWinther/MG-PICOLA-PUBLIC>. The original L-PICOLA code can be found at <https://github.com/CullanHowlett/l-picola>

the popular models that have been proposed in the literature. Furthermore, we have implemented massive neutrinos using the grid-based approach.

The structure of this chapter is as follows: starting from the general Lagrangian perturbation theory equations from Sec. 1.5.2 we describe how to extend the formalism for a general model with scale-dependent growth of density perturbations up to second order in Sec. 2.1. Following this, we focus on how this extended formalism allows the implementation of modified gravity (Sec. 2.2), massive neutrinos (Sec. 2.3), and the combination of the two (Sec. 2.4). In Sec. 2.5 we describe how to implement the fifth force, including an approximation for the vital screening mechanism, and massive neutrinos in the particle-mesh (PM) part of the simulation. Finally, in Sec. 2.6 we show the results of testing our code against a variety of other methods.

Unless stated otherwise all time-derivatives are with respect to the super-comoving time-coordinate τ defined by $d\tau = \frac{dt}{a^2}$ and $\kappa \equiv 4\pi G\bar{\rho}a^4 = \frac{3}{2}\Omega_m H_0^2 a$.

The research on adding modified gravity to the COLA method was lead by Hans A. Winther. My contribution was to co-derive the 2LPT equations including the effects of modified gravity. I lead the research on adding massive neutrinos to the COLA method.

2.1 2LPT for general scale-dependent growth

For the general case where the scale-dependence at n^{th} order is encapsulated by an effective Newton's constant $\mu^{(n)}(\vec{k}, \tau)$ and a mode coupling γ_n^{E} above 1st order, the Fourier transform of $\nabla_x^2 \Phi(\vec{x}, \tau)$ with respect to x up to second order is

$$\begin{aligned} \mathcal{F}_x [\nabla_x^2 \Phi(\vec{x}, \tau)] &= \kappa \mu^{(1)}(\vec{k}_{\text{E}}, \tau) \delta^{(1)}(\vec{k}_{\text{E}}, \tau) + \kappa \mu^{(2)}(\vec{k}_{\text{E}}, \tau) \delta^{(2)}(\vec{k}_{\text{E}}, \tau) \\ &+ a^4 H^2 \int \frac{d^3 k_1 d^3 k_2}{(2\pi)^3} \delta_D^{(3)}(\vec{k} - \vec{k}_{12}) \\ &\times \gamma_2^{\text{E}}(\vec{k}, \vec{k}_1, \vec{k}_2, \tau) \delta^{(1)}(\vec{k}_1, \tau) \delta^{(1)}(\vec{k}_2, \tau) , \end{aligned} \quad (2.1)$$

where $\kappa \equiv 4\pi G\bar{\rho}a^4 = \frac{3}{2}\Omega_m H_0^2 a$, $\delta(\vec{k}_{\text{E}}, \tau) = \mathcal{F}_x [\delta(\vec{x}, \tau)](\vec{k}_{\text{E}})$ and $\vec{k}_{12} = \vec{k}_1 + \vec{k}_2$. There will be a frame lagging effect due to the fact we need the Fourier transform w.r.t. q instead of x [210]. We can show that the corresponding Fourier transform of the

Poisson equation w.r.t. q is then

$$\begin{aligned}
\mathcal{F}_q [\nabla_x^2 \Phi(\vec{x}, \tau)] &= \kappa \mu^{(1)}(\vec{k}, \tau) \tilde{\delta}^{(1)}(\vec{k}, \tau) + \kappa \mu^{(2)}(\vec{k}, \tau) \tilde{\delta}^{(2)}(\vec{k}, \tau) \\
&+ \kappa \int \frac{d^3 k_1 d^3 k_2}{(2\pi)^3} \delta_D^{(3)}(\vec{k} - \vec{k}_{12}) \\
&\times \left[\mu^{(1)}(\vec{k}, \tau) - \mu^{(1)}(\vec{k}_1, \tau) \right] \frac{\vec{k}_1 \cdot \vec{k}_2}{k_2^2} \delta^{(1)}(\vec{k}_1, \tau) \delta^{(1)}(\vec{k}_2, \tau) \\
&+ a^4 H^2 \int \frac{d^3 k_1 d^3 k_2}{(2\pi)^3} \delta_D^{(3)}(\vec{k} - \vec{k}_{12}) \\
&\times \gamma_2^E(\vec{k}, \vec{k}_1, \vec{k}_2, \tau) \delta^{(1)}(\vec{k}_1, \tau) \delta^{(1)}(\vec{k}_2, \tau) , \tag{2.2}
\end{aligned}$$

where

$$\begin{aligned}
\tilde{\delta}^{(n)}(\vec{k}, \tau) &= \mathcal{F}_q [\delta^{(n)}(\vec{x}, \tau)] (\vec{k}) \\
&= \mathcal{F}_q [\delta^{(n)}(\vec{q}, \tau)] (\vec{k}) + i \int d^3 q \int \frac{d^3 k_E}{(2\pi)^3} e^{-i(\vec{k} - \vec{k}_E) \cdot \vec{q}} (\vec{k}_E \cdot \vec{\Psi}^{(1)}) \delta^{(n)}(\vec{k}_E, \tau) . \tag{2.3}
\end{aligned}$$

The 1st order densities are unaffected:

$$\delta^{(1)}(\vec{k}, \tau) = \mathcal{F}_x [\delta^{(1)}(\vec{x}, \tau)] (\vec{k}) = \mathcal{F}_q [\delta^{(1)}(\vec{x}, \tau)] (\vec{k}) = \tilde{\delta}^{(1)}(\vec{k}, \tau) , \tag{2.4}$$

so we can safely rewrite Eq. (2.2) as

$$\begin{aligned}
\mathcal{F}_q [\nabla_x^2 \Phi(\vec{x}, \tau)] &= \kappa \mu^{(1)}(\vec{k}, \tau) \tilde{\delta}^{(1)}(\vec{k}, \tau) + \kappa \mu^{(2)}(\vec{k}, \tau) \tilde{\delta}^{(2)}(\vec{k}, \tau) \\
&+ \kappa \int \frac{d^3 k_1 d^3 k_2}{(2\pi)^3} \delta_D^{(3)}(\vec{k} - \vec{k}_{12}) \left[\mu^{(1)}(\vec{k}, \tau) - \mu^{(1)}(\vec{k}_1, \tau) \right] \\
&\times \frac{\vec{k}_1 \cdot \vec{k}_2}{k_2^2} \tilde{\delta}^{(1)}(\vec{k}_1, \tau) \tilde{\delta}^{(1)}(\vec{k}_2, \tau) \\
&+ a^4 H^2 \int \frac{d^3 k_1 d^3 k_2}{(2\pi)^3} \delta_D^{(3)}(\vec{k} - \vec{k}_{12}) \\
&\times \gamma_2^E(\vec{k}, \vec{k}_1, \vec{k}_2, \tau) \tilde{\delta}^{(1)}(\vec{k}_1, \tau) \tilde{\delta}^{(1)}(\vec{k}_2, \tau) . \tag{2.5}
\end{aligned}$$

Note that there is also a frame lagging effect on γ_2^E , but this would be a third order term so it is not included here.

To find the 1st order solution, we can use these various expressions to rewrite Eq. (1.82) as

$$-k^2 \frac{d^2 \phi^{(1)}(\vec{k}, \tau)}{d\tau^2} = -\kappa \mu^{(1)} \tilde{\delta}^{(1)}(\vec{k}, \tau) = -\kappa \mu^{(1)}(\vec{k}, \tau) k^2 \phi^{(1)}(\vec{k}, \tau) . \tag{2.6}$$

We can separate a time dependence for each k mode by writing

$$\phi^{(1)}(\vec{k}, \tau) = D_1(\vec{k}, \tau) \phi_{\text{ini}}^{(1)}(\vec{k}, \tau) , \tag{2.7}$$

where $\phi_{\text{ini}}^{(1)}(\vec{k}, \tau) = \tilde{\delta}_{\text{ini}}^{(1)}(\vec{k}, \tau)/k^2$ and Eq. (2.6) simplifies to

$$\left[\frac{d^2}{d\tau^2} - \kappa \mu^{(1)}(\vec{k}, \tau) \right] D_1(\vec{k}, \tau) = 0 . \quad (2.8)$$

This second order ODE can be solved for $D_1(\vec{k}, \tau)$ numerically at each (\vec{k}, τ) as long as we set initial conditions (ICs) for $D_1(\vec{k}, \tau_{\text{ini}})$ and $dD_1/d\tau|_{\vec{k}, \tau_{\text{ini}}}$. We can finally express $\Psi^{(1)}(\vec{k}, \tau) = ik_i \phi^{(1)}(\vec{k}, \tau) = ik_i D_1(\vec{k}, \tau) \tilde{\delta}^{(1)}(\vec{k}, \tau_{\text{ini}})/k^2$, and then use an inverse Fourier transform to get the displacement

$$\Psi^{(1)}(\vec{q}, \tau) = \int \frac{d^3 k}{(2\pi)^3} e^{i\vec{k} \cdot \vec{q}} \frac{ik_i}{k^2} D_1(\vec{k}, \tau) \tilde{\delta}^{(1)}(\vec{k}, \tau_{\text{ini}}) . \quad (2.9)$$

For the second order solution, we rewrite Eq. (1.83) as

$$\begin{aligned} \mathcal{F}_q \left[\frac{d^2 \Psi_{i,i}^{(2)}}{d\tau^2} \right] (\vec{k}) \\ - \mathcal{F}_q \left[\Psi_{j,i}^{(1)} \frac{d^2 \Psi_{i,j}^{(1)}}{d\tau^2} \right] (\vec{k}) \\ = - \kappa \mu^{(2)}(\vec{k}, \tau) \tilde{\delta}^{(2)}(\vec{k}, \tau) \\ - \kappa \int \frac{d^3 k_1 d^3 k_2}{(2\pi)^3} \delta_D^{(3)}(\vec{k} - \vec{k}_{12}) \\ \times \left[\mu^{(1)}(\vec{k}, \tau) - \mu^{(1)}(\vec{k}_1, \tau) \right] \\ \times \frac{\vec{k}_1 \cdot \vec{k}_2}{k_2^2} \tilde{\delta}^{(1)}(\vec{k}_1, \tau) \tilde{\delta}^{(1)}(\vec{k}_2, \tau) \\ - a^4 H^2 \int \frac{d^3 k_1 d^3 k_2}{(2\pi)^3} \delta_D^{(3)}(\vec{k} - \vec{k}_{12}) \\ \times \gamma_2^{\text{E}}(\vec{k}, \vec{k}_1, \vec{k}_2, \tau) \tilde{\delta}^{(1)}(\vec{k}_1, \tau) \times \tilde{\delta}^{(1)}(\vec{k}_2, \tau) , \quad (2.10) \end{aligned}$$

and then substitute in our expression for $\tilde{\delta}_{\text{cb}}^{(2)}$ to get

$$\begin{aligned}
& \mathcal{F}_q \left[\frac{d^2 \Psi_{i,i}^{(2)}}{d\tau^2} \right] (\vec{k}) \\
& - \mathcal{F}_q \left[\Psi_{j,i}^{(1)} \frac{d^2 \Psi_{i,j}^{(1)}}{d\tau^2} \right] (\vec{k}) \\
& = \kappa \mu^{(2)}(\vec{k}, \tau) \mathcal{F}_q \left[\Psi_{i,i}^{(2)}(\vec{q}, \tau) \right] (\vec{k}) \\
& - \kappa \mu^{(2)}(\vec{k}, \tau) \frac{1}{2} \mathcal{F}_q \left[\Psi_{i,i}^{(1)} \Psi_{j,j}^{(1)} + \Psi_{i,j}^{(1)} \Psi_{j,i}^{(1)} \right] (\vec{k}) \\
& - \kappa \int \frac{d^3 k_1 d^3 k_2}{(2\pi)^3} \delta_D^{(3)}(\vec{k} - \vec{k}_{12}) \\
& \quad \times \left[\mu^{(1)}(\vec{k}, \tau) - \mu^{(1)}(\vec{k}_1, \tau) \right] \\
& \quad \times \frac{\vec{k}_1 \cdot \vec{k}_2}{k_2^2} \tilde{\delta}^{(1)}(\vec{k}_1, \tau) \tilde{\delta}^{(1)}(\vec{k}_2, \tau) \\
& - a^4 H^2 \int \frac{d^3 k_1 d^3 k_2}{(2\pi)^3} \delta_D^{(3)}(\vec{k} - \vec{k}_{12}) \\
& \quad \times \gamma_2^{\text{E}}(\vec{k}, \vec{k}_1, \vec{k}_2, \tau) \tilde{\delta}^{(1)}(\vec{k}_1, \tau) \tilde{\delta}^{(1)}(\vec{k}_2, \tau) . \quad (2.11)
\end{aligned}$$

We can use the 1st order solution to write

$$\mathcal{F}_q \left[\Psi_{j,i}^{(1)} \frac{d^2 \Psi_{i,j}^{(1)}}{d\tau^2} \right] (\vec{k}) = \kappa \mu^{(1)}(\vec{k}_1, \tau) \mathcal{F}_q \left[\Psi_{j,i}^{(1)} \Psi_{i,j}^{(1)} \right] (\vec{k}) , \quad (2.13)$$

and thus Eq. (2.11) becomes

$$\begin{aligned}
& \left[\frac{d^2}{d\tau^2} - \kappa \mu^{(2)}(\vec{k}, \tau) \right] \mathcal{F}_q \left[\Psi_{i,i}^{(2)}(\vec{q}, \tau) \right] (\vec{k}) \\
& = \kappa \left[\mu^{(1)}(\vec{k}_1, \tau) - \frac{1}{2} \mu^{(2)}(\vec{k}, \tau) \right] \mathcal{F}_q \left[\Psi_{j,i}^{(1)} \Psi_{i,j}^{(1)} \right] (\vec{k}) \\
& - \frac{1}{2} \kappa \mu^{(2)}(\vec{k}, \tau) \mathcal{F}_q \left[\Psi_{i,i}^{(1)} \Psi_{j,j}^{(1)} \right] (\vec{k}) \\
& - \kappa \int \frac{d^3 k_1 d^3 k_2}{(2\pi)^3} \delta_D^{(3)}(\vec{k} - \vec{k}_{12}) \\
& \quad \times \left[\mu^{(1)}(\vec{k}, \tau) - \mu^{(1)}(\vec{k}_1, \tau) \right] \frac{\vec{k}_1 \cdot \vec{k}_2}{k_2^2} \tilde{\delta}^{(1)}(\vec{k}_1, \tau) \tilde{\delta}^{(1)}(\vec{k}_2, \tau) \\
& - a^4 H^2 \int \frac{d^3 k_1 d^3 k_2}{(2\pi)^3} \delta_D^{(3)}(\vec{k} - \vec{k}_{12}) \\
& \quad \times \gamma_2^{\text{E}}(\vec{k}, \vec{k}_1, \vec{k}_2, \tau) \tilde{\delta}^{(1)}(\vec{k}_1, \tau) \tilde{\delta}^{(1)}(\vec{k}_2, \tau) . \quad (2.14)
\end{aligned}$$

In a similar way to Eq.(2.9), the quantity $\Psi_{l,m}^{(1)}(\vec{q}, \tau)$ needed to simplify Eq. (2.14)

further can be written as an inverse Fourier transform:

$$\Psi_{l,m}^{(1)}(\vec{q}, \tau) = \int \frac{d^3 \vec{k}_1}{(2\pi)^3} i k_1^m e^{i \vec{k}_1 \cdot \vec{q}} \frac{i k_{1l}}{k_1^2} D_1(\vec{k}_1, \tau) \tilde{\delta}(\vec{k}_1, \tau_{\text{ini}}) . \quad (2.15)$$

Therefore, the convolutions are

$$\begin{aligned} & \Psi_{l,l}^{(1)}(\vec{q}, \tau) \Psi_{m,m}^{(1)}(\vec{q}, \tau) \\ &= \int \frac{d^3 \vec{k}_1}{(2\pi)^3} \frac{d^3 \vec{k}_2}{(2\pi)^3} i k_1^l e^{i \vec{k}_1 \cdot \vec{q}} \frac{i k_{1l}}{k_1^2} i k_2^m e^{i \vec{k}_2 \cdot \vec{q}} \frac{i k_{2m}}{k_2^2} D_1(\vec{k}_1, \tau) D_1(\vec{k}_2, \tau) \tilde{\delta}(\vec{k}_1, \tau_{\text{ini}}) \tilde{\delta}(\vec{k}_2, \tau_{\text{ini}}) \\ &= \int \frac{d^3 \vec{k}_1}{(2\pi)^3} \frac{d^3 \vec{k}_2}{(2\pi)^3} e^{i(\vec{k}_1 + \vec{k}_2) \cdot \vec{q}} D_1(\vec{k}_1, \tau) D_1(\vec{k}_2, \tau) \tilde{\delta}(\vec{k}_1, \tau_{\text{ini}}) \tilde{\delta}(\vec{k}_2, \tau_{\text{ini}}) , \quad (2.16) \end{aligned}$$

$$\begin{aligned} & \Psi_{l,m}^{(1)}(\vec{q}, \tau) \Psi_{m,l}^{(1)}(\vec{q}, \tau) \\ &= \int \frac{d^3 \vec{k}_1}{(2\pi)^3} \frac{d^3 \vec{k}_2}{(2\pi)^3} i k_1^m e^{i \vec{k}_1 \cdot \vec{q}} \frac{i k_{1l}}{k_1^2} i k_2^l e^{i \vec{k}_2 \cdot \vec{q}} \frac{i k_{2m}}{k_2^2} D_1(\vec{k}_1, \tau) D_1(\vec{k}_2, \tau) \tilde{\delta}(\vec{k}_1, \tau_{\text{ini}}) \tilde{\delta}(\vec{k}_2, \tau_{\text{ini}}) \\ &= \int \frac{d^3 \vec{k}_1}{(2\pi)^3} \frac{d^3 \vec{k}_2}{(2\pi)^3} i^4 e^{i(\vec{k}_1 + \vec{k}_2) \cdot \vec{q}} \frac{k_1^m k_{1l} k_2^l k_{2m}}{k_1^2 k_2^2} D_1(\vec{k}_1, \tau) D_1(\vec{k}_2, \tau) \tilde{\delta}(\vec{k}_1, \tau_{\text{ini}}) \tilde{\delta}(\vec{k}_2, \tau_{\text{ini}}) \\ &= \int \frac{d^3 \vec{k}_1}{(2\pi)^3} \frac{d^3 \vec{k}_2}{(2\pi)^3} e^{i(\vec{k}_1 + \vec{k}_2) \cdot \vec{q}} \frac{(\vec{k}_1 \cdot \vec{k}_2)^2}{k_1^2 k_2^2} D_1(\vec{k}_1, \tau) D_1(\vec{k}_2, \tau) \tilde{\delta}(\vec{k}_1, \tau_{\text{ini}}) \tilde{\delta}(\vec{k}_2, \tau_{\text{ini}}) . \quad (2.17) \end{aligned}$$

Then taking the Fourier transform yields

$$\begin{aligned} & \mathcal{F}_q \left[\Psi_{l,l}^{(1)}(\vec{q}, \tau) \Psi_{m,m}^{(1)}(\vec{q}, \tau) \right] (\vec{k}) \\ &= \int d^3 \vec{q} e^{-i \vec{k} \cdot \vec{q}} \int \frac{d^3 \vec{k}_1}{(2\pi)^3} \frac{d^3 \vec{k}_2}{(2\pi)^3} e^{i(\vec{k}_1 + \vec{k}_2) \cdot \vec{q}} D_1(\vec{k}_1, \tau) D_1(\vec{k}_2, \tau) \tilde{\delta}(\vec{k}_1, \tau_{\text{ini}}) \tilde{\delta}(\vec{k}_2, \tau_{\text{ini}}) \\ &= \int \frac{d^3 \vec{k}_1}{(2\pi)^3} \frac{d^3 \vec{k}_2}{(2\pi)^3} \int d^3 \vec{q} e^{-i(\vec{k} - (\vec{k}_1 + \vec{k}_2)) \cdot \vec{q}} D_1(\vec{k}_1, \tau) D_1(\vec{k}_2, \tau) \tilde{\delta}(\vec{k}_1, \tau_{\text{ini}}) \tilde{\delta}(\vec{k}_2, \tau_{\text{ini}}) \\ &= \int \frac{d^3 \vec{k}_1 d^3 \vec{k}_2}{(2\pi)^3} \delta_D(\vec{k} - \vec{k}_{12}) D_1(\vec{k}_1, \tau) D_1(\vec{k}_2, \tau) \tilde{\delta}(\vec{k}_1, \tau_{\text{ini}}) \tilde{\delta}(\vec{k}_2, \tau_{\text{ini}}) , \quad (2.18) \end{aligned}$$

and

$$\begin{aligned} & \mathcal{F}_q \left[\Psi_{l,m}^{(1)}(\vec{q}, \tau) \Psi_{m,l}^{(1)}(\vec{q}, \tau) \right] (\vec{k}) \\ &= \int \frac{d^3 \vec{k}_1 d^3 \vec{k}_2}{(2\pi)^3} \delta_D(\vec{k} - \vec{k}_{12}) \frac{(\vec{k}_1 \cdot \vec{k}_2)^2}{k_1^2 k_2^2} D_1(\vec{k}_1, \tau) D_1(\vec{k}_2, \tau) \tilde{\delta}(\vec{k}_1, \tau_{\text{ini}}) \tilde{\delta}(\vec{k}_2, \tau_{\text{ini}}) . \quad (2.19) \end{aligned}$$

We can substitute these expressions into Eq. (2.14) and use $\tilde{\delta}^{(1)}(\vec{k}, \tau) = D_1(\vec{k}, \tau) \times \tilde{\delta}^{(1)}(\vec{k}, \tau_{\text{ini}})$, as well as $\mathcal{F}_q \left[\Psi_{i,i}^{(2)}(\vec{q}, \tau) \right] (\vec{k}) = \mathcal{F}_q \left[\nabla^2 \phi^{(2)}(\vec{q}, \tau) \right] (\vec{k}) = -k^2 \phi^{(2)}(\vec{k}, \tau)$, to

write

$$\begin{aligned}
& -k^2 \left[\frac{d^2}{d\tau^2} - \kappa \mu^{(2)}(\vec{k}, \tau) \right] \phi^{(2)}(\vec{k}, \tau) \\
& = \int \frac{d^3 k_1 d^3 k_2}{(2\pi)^3} \delta_D^{(3)}(\vec{k} - \vec{k}_{12}) \left[\kappa \left(\mu^{(1)}(\vec{k}_1, \tau) - \frac{1}{2} \mu^{(2)}(\vec{k}, \tau) \right) \frac{(\vec{k}_1 \cdot \vec{k}_2)^2}{k_1^2 k_2^2} \right. \\
& \quad - \frac{1}{2} \kappa \mu^{(2)}(\vec{k}, \tau) - \kappa \left(\mu^{(1)}(\vec{k}, \tau) - \mu^{(1)}(\vec{k}_1, \tau) \right) \frac{\vec{k}_1 \cdot \vec{k}_2}{k_2^2} \\
& \quad \left. - a^4 H^2 \gamma_2^E(\vec{k}, \vec{k}_1, \vec{k}_2, \tau) \right] D_1(\vec{k}_1, \tau) D_1(\vec{k}_2, \tau) \\
& \quad \times \tilde{\delta}^{(1)}(\vec{k}_1, \tau_{\text{ini}}) \tilde{\delta}^{(1)}(\vec{k}_2, \tau_{\text{ini}}) . \quad (2.20)
\end{aligned}$$

We now need an expression for the 2nd order displacement field term $\Psi_i^{(2)}(\vec{q}, \tau) = \nabla_i \phi^{(2)}(\vec{q}, \tau)$, which in Fourier space is $\Psi_i^{(2)}(\vec{k}, \tau) = i k_i \phi^{(2)}(\vec{k}, \tau)$. If we make the definition

$$\phi^{(2)}(\vec{k}, \tau) = \frac{1}{2k^2} \int \frac{d^3 k_1 d^3 k_2}{(2\pi)^3} \delta_D^{(3)}(\vec{k} - \vec{k}_{12}) D_2(\vec{k}, \vec{k}_1, \vec{k}_2, \tau) \tilde{\delta}(\vec{k}_1, \tau_{\text{ini}}) \tilde{\delta}(\vec{k}_2, \tau_{\text{ini}}) , \quad (2.21)$$

then Eq. (2.20) can be rewritten as

$$\begin{aligned}
& \frac{1}{2} \left[\frac{d^2}{d\tau^2} - \kappa \mu^{(2)}(\vec{k}, \tau) \right] \\
& \times \int \frac{d^3 k_1 d^3 k_2}{(2\pi)^3} \delta_D^{(3)}(\vec{k} - \vec{k}_{12}) D_2(\vec{k}, \vec{k}_1, \vec{k}_2, \tau) \tilde{\delta}(\vec{k}_1, \tau_{\text{ini}}) \tilde{\delta}(\vec{k}_2, \tau_{\text{ini}}) \\
& = \int \frac{d^3 k_1 d^3 k_2}{(2\pi)^3} \delta_D^{(3)}(\vec{k} - \vec{k}_{12}) \left[\kappa \left(\frac{1}{2} \mu^{(2)}(\vec{k}, \tau) - \mu^{(1)}(\vec{k}_1, \tau) \right) \frac{(\vec{k}_1 \cdot \vec{k}_2)^2}{k_1^2 k_2^2} \right. \\
& \quad + \frac{1}{2} \kappa \mu^{(2)}(\vec{k}, \tau) \kappa \left[\mu^{(1)}(\vec{k}, \tau) - \mu^{(1)}(\vec{k}_1, \tau) \right] \frac{\vec{k}_1 \cdot \vec{k}_2}{k_2^2} \\
& \quad \left. + a^4 H^2 \gamma_2^E(\vec{k}, \vec{k}_1, \vec{k}_2, \tau) \right] D_1(\vec{k}_1, \tau) D_1(\vec{k}_2, \tau) \\
& \quad \times \tilde{\delta}^{(1)}(\vec{k}_1, \tau_{\text{ini}}) \tilde{\delta}^{(1)}(\vec{k}_2, \tau_{\text{ini}}) , \quad (2.22)
\end{aligned}$$

which simplifies to

$$\begin{aligned}
& \left[\frac{d^2}{d\tau^2} - \kappa \mu^{(2)}(\vec{k}, \tau) \right] D_2(\vec{k}, \vec{k}_1, \vec{k}_2, \tau) \\
& = \left[\kappa \left(\mu^{(2)}(\vec{k}, \tau) - 2\mu^{(1)}(\vec{k}_1, \tau) \right) \frac{(\vec{k}_1 \cdot \vec{k}_2)^2}{k_1^2 k_2^2} + \kappa \mu^{(2)}(\vec{k}, \tau) \right. \\
& \quad + 2\kappa \left(\mu^{(1)}(\vec{k}, \tau) - \mu^{(1)}(\vec{k}_1, \tau) \right) \frac{\vec{k}_1 \cdot \vec{k}_2}{k_2^2} \\
& \quad \left. + 2a^4 H^2 \gamma_2^E(\vec{k}, \vec{k}_1, \vec{k}_2, \tau) \right] D_1(\vec{k}_1, \tau) D_1(\vec{k}_2, \tau) . \quad (2.23)
\end{aligned}$$

This can be solved numerically for D_2 for each $(\vec{k}, \vec{k}_1, \vec{k}_2, \tau)$ assuming the solutions for $D_1(\vec{k}, \tau)$ are already known and ICs for D_2 and $dD_2/d\tau$ are supplied. $\Psi_i^{(2)}(\vec{q}, \tau)$ can then be written as an inverse Fourier transform:

$$\Psi_i^{(2)}(\vec{q}, \tau) = \frac{1}{2} \int \frac{d^3 \vec{k}}{(2\pi)^3} e^{i\vec{k} \cdot \vec{q}} \frac{k_i}{k^2} \int \frac{d^3 k_1 d^3 k_2}{(2\pi)^3} \delta_D^{(3)}(\vec{k} - \vec{k}_{12}) \times D_2(\vec{k}, \vec{k}_1, \vec{k}_2, \tau) \tilde{\delta}(\vec{k}_1, \tau_{\text{ini}}) \tilde{\delta}(\vec{k}_2, \tau_{\text{ini}}) , \quad (2.24)$$

which allows the full 2nd order solution $\Psi_i^{(2)}(\vec{q}, \tau)$ to be recovered using the $D_2(\vec{k}, \vec{k}_1, \vec{k}_2, \tau)$ values from solving Eq. (2.23) as long as the initial density field $\tilde{\delta}(\vec{k}, \tau_{\text{ini}})$ is known.

A subset of this general scale-dependent case is when $\mu^{(1)} = \mu^{(2)} = \mu$, where Eq. (2.23) reduces to

$$\begin{aligned} & \left[\frac{d^2}{d\tau^2} - \kappa \mu(\vec{k}, \tau) \right] D_2(\vec{k}, \vec{k}_1, \vec{k}_2, \tau) \\ &= \left[\kappa \mu(\vec{k}, \tau) \left(1 + 2 \left(\frac{\mu(\vec{k}, \tau) - \mu(\vec{k}_1, \tau)}{\mu(\vec{k}, \tau)} \right) \frac{\vec{k}_1 \cdot \vec{k}_2}{k_2^2} \right. \right. \\ & \quad \left. \left. - \left(\frac{2\mu(\vec{k}_1, \tau) - \mu(\vec{k}, \tau)}{\mu(\vec{k}, \tau)} \right) \frac{(\vec{k}_1 \cdot \vec{k}_2)^2}{k_1^2 k_2^2} \right) \right. \\ & \quad \left. + 2a^4 H^2 \gamma_2^{\text{E}}(\vec{k}, \vec{k}_1, \vec{k}_2, \tau) \right] D_1(\vec{k}_1, \tau) D_1(\vec{k}_2, \tau) . \quad (2.25) \end{aligned}$$

However, Eq. (2.24) will still be very slow to solve numerically as the dependence of D_2 on \vec{k}_1 and \vec{k}_2 means the integral over \vec{k}_1 and \vec{k}_2 must be done for each timestep, and without being able to utilise fast Fourier transforms the speed advantage of the COLA method will be ruined. To speed up the code, we can make the following redefinition at 2nd order, replacing Eq.(2.21) with

$$\begin{aligned} \phi^{(2)}(\vec{k}, \tau) &= \frac{\hat{D}_2(\vec{k}, \tau)}{2k^2} \int \frac{d^3 k_1 d^3 k_2}{(2\pi)^3} \delta_D^{(3)}(\vec{k} - \vec{k}_{12}) \\ & \quad \times \left(1 - \frac{(\vec{k}_1 \cdot \vec{k}_2)^2}{k_1^2 k_2^2} \right) \tilde{\delta}(\vec{k}_1, \tau_{\text{ini}}) \tilde{\delta}(\vec{k}_2, \tau_{\text{ini}}) , \quad (2.26) \end{aligned}$$

such that $\Psi_i^{(2)}(\vec{q}, \tau)$ becomes

$$\begin{aligned} \Psi_i^{(2)}(\vec{q}, \tau) &= \frac{i}{2} \int \frac{d^3 \vec{k}}{(2\pi)^3} e^{i\vec{k} \cdot \vec{q}} \frac{k_i}{k^2} \hat{D}_2(\vec{k}, \tau) \int \frac{d^3 k_1 d^3 k_2}{(2\pi)^3} \delta_D^{(3)}(\vec{k} - \vec{k}_{12}) \\ & \quad \times \left(1 - \frac{(\vec{k}_1 \cdot \vec{k}_2)^2}{k_1^2 k_2^2} \right) \tilde{\delta}(\vec{k}_1, \tau = 0) \tilde{\delta}(\vec{k}_2, \tau = 0) . \quad (2.27) \end{aligned}$$

Removing the \vec{k}_1 and \vec{k}_2 dependence from \hat{D}_2 means that the integral over \vec{k}_1 and \vec{k}_2 can be carried out only once instead of at each timestep. The equation for $\hat{D}_2(\vec{k})$ is then

$$\begin{aligned} & \left[\frac{d^2}{d\tau^2} - \kappa \mu(\vec{k}, \tau) \right] \left(1 - \frac{(\vec{k}_1 \cdot \vec{k}_2)^2}{k_1^2 k_2^2} \right) \hat{D}_2(\vec{k}, \tau) \\ &= \left[\kappa \mu(\vec{k}, \tau) \left(1 + 2 \left(\frac{\mu(\vec{k}, \tau) - \mu(\vec{k}_1, \tau)}{\mu(\vec{k}, \tau)} \right) \frac{\vec{k}_1 \cdot \vec{k}_2}{k_2^2} \right. \right. \\ & \quad \left. \left. - \left(\frac{2\mu(\vec{k}_1, \tau) - \mu(\vec{k}, \tau)}{\mu(\vec{k}, \tau)} \right) \frac{(\vec{k}_1 \cdot \vec{k}_2)^2}{k_1^2 k_2^2} \right) \right. \\ & \quad \left. + 2a^4 H^2 \gamma_2^E(\vec{k}, \vec{k}_1, \vec{k}_2, \tau) \right] D_1(\vec{k}_1, \tau) D_1(\vec{k}_2, \tau) . \quad (2.28) \end{aligned}$$

If we make the approximation that $\mu(\vec{k}, \tau) \approx \mu(\vec{k}_1, \tau)$, then $\frac{\mu(\vec{k}, \tau) - \mu(\vec{k}_1, \tau)}{\mu(\vec{k}, \tau)} \approx 0$ and $\frac{2\mu(\vec{k}_1, \tau) - \mu(\vec{k}, \tau)}{\mu(\vec{k}, \tau)} \approx 1$. Thus Eq. (2.28) can be approximated as

$$\begin{aligned} & \left[\frac{d^2}{d\tau^2} - \kappa \mu(\vec{k}, \tau) \right] \left(1 - \frac{(\vec{k}_1 \cdot \vec{k}_2)^2}{k_1^2 k_2^2} \right) \hat{D}_2(\vec{k}, \tau) \\ &= \left[\kappa \mu(\vec{k}, \tau) \left(1 - \frac{(\vec{k}_1 \cdot \vec{k}_2)^2}{k_1^2 k_2^2} \right) + 2a^4 H^2 \gamma_2^E(\vec{k}, \vec{k}_1, \vec{k}_2, \tau) \right] \\ & \quad \times D_1(\vec{k}_1, \tau) D_1(\vec{k}_2, \tau) . \quad (2.29) \end{aligned}$$

and finally, if we approximate

$$\frac{\gamma_2^E(\vec{k}, \vec{k}_1, \vec{k}_2, \tau)}{\left(1 - \frac{(\vec{k}_1 \cdot \vec{k}_2)^2}{k_1^2 k_2^2} \right)} \approx \gamma_2^E(\vec{k}, \vec{k}/\sqrt{2}, \vec{k}/\sqrt{2}, \tau) , \quad (2.30)$$

then Eq. (2.29) reduces to

$$\begin{aligned} & \left[\frac{d^2}{d\tau^2} - \kappa \mu(\vec{k}, \tau) \right] \hat{D}_2(\vec{k}, \tau) \\ &= \left[\kappa \mu(\vec{k}, \tau) + 2a^4 H^2 \gamma_2^E(\vec{k}, \vec{k}/\sqrt{2}, \vec{k}/\sqrt{2}, \tau) \right] D_1^2(\vec{k}, \tau) , \quad (2.31) \end{aligned}$$

which, along with Eq. (2.27), will be much faster to solve than the paired Eqs. (2.24) and (2.25).

The choice of arguments for γ_2^E in our approximation above is chosen such that it gives the correct equation for the triangle configurations of $\vec{k}, \vec{k}_1, \vec{k}_2$ giving rise to most of the weight in the integral Eq. (2.21).

2.2 2LPT for modified gravity

The case of modified gravity theories with scale-dependent growth of density perturbations is covered by the formalism laid out in Sec. 2.1. For a generic scale-dependent theory of gravity, $\mu^{(1)}(\vec{k}, \tau) = \mu^{(2)}(\vec{k}, \tau) \rightarrow \mu_{\text{MG}}(k, \tau)$ and $\gamma_2^{\text{E}}(\vec{k}, \vec{k}_1, \vec{k}_2, \tau) \rightarrow \gamma_{2,\text{MG}}^{\text{E}}(k, k_1, k_2, \tau)$. Note that because μ_{MG} and $\gamma_{2,\text{MG}}^{\text{E}}$ are dependent only on the magnitude of the wavevector(s), the same will be true of the density perturbations. Thus, the Fourier transform of the Poisson equation w.r.t. \vec{q} can be parameterised as [140, 210, 211]

$$\begin{aligned} \mathcal{F}_q [\nabla_x^2 \Phi(\vec{x}, \tau)] &= \kappa \mu_{\text{MG}}(k, \tau) \tilde{\delta}_{\text{cb}}^{(1)}(k, \tau) + \kappa \mu_{\text{MG}}(k, \tau) \tilde{\delta}_{\text{cb}}^{(2)}(k, \tau) \\ &+ \kappa \int \frac{d^3 k_1 d^3 k_2}{(2\pi)^3} \delta_D^{(3)}(\vec{k} - \vec{k}_{12}) [\mu_{\text{MG}}(k, \tau) - \mu_{\text{MG}}(k_1, \tau)] \\ &\quad \times \frac{\vec{k}_1 \cdot \vec{k}_2}{k_2^2} \tilde{\delta}_{\text{cb}}^{(1)}(k_1, \tau) \tilde{\delta}_{\text{cb}}^{(1)}(k_2, \tau) \\ &+ a^4 H^2 \int \frac{d^3 k_1 d^3 k_2}{(2\pi)^3} \delta_D^{(3)}(\vec{k} - \vec{k}_{12}) \\ &\quad \times \gamma_{2,\text{MG}}^{\text{E}}(k, k_1, k_2, \tau) \tilde{\delta}_{\text{cb}}^{(1)}(k_1, \tau) \tilde{\delta}_{\text{cb}}^{(1)}(k_2, \tau) . \quad (2.32) \end{aligned}$$

Consequently, the equations for the first and second order growth factors D_1 and D_2 become

$$\left[\frac{d^2}{d\tau^2} - \kappa \mu_{\text{MG}}(k, \tau) \right] D_1(k, \tau) = 0 , \quad (2.33)$$

$$\begin{aligned} &\left[\frac{d^2}{d\tau^2} - \kappa \mu_{\text{MG}}(k, \tau) \right] D_2(k, k_1, k_2, \tau) \\ &= \left[\kappa \mu_{\text{MG}}(k, \tau) \left(1 + 2 \left(\frac{\mu_{\text{MG}}(k, \tau) - \mu_{\text{MG}}(k_1, \tau)}{\mu_{\text{MG}}(k, \tau)} \right) \frac{\vec{k}_1 \cdot \vec{k}_2}{k_2^2} \right. \right. \\ &\quad \left. \left. - \left(\frac{2\mu_{\text{MG}}(k_1, \tau) - \mu_{\text{MG}}(k, \tau)}{\mu_{\text{MG}}(k, \tau)} \right) \frac{(\vec{k}_1 \cdot \vec{k}_2)^2}{k_1^2 k_2^2} \right) \right. \\ &\quad \left. + 2a^4 H^2 \gamma_{2,\text{MG}}^{\text{E}}(k, k_1, k_2, \tau) \right] D_1(k_1, \tau) D_1(k_2, \tau) , \quad (2.34) \end{aligned}$$

while the corresponding speed-up equation for the approximate second order growth factor \hat{D}_2 becomes

$$\begin{aligned} &\left[\frac{d^2}{d\tau^2} - \kappa \mu_{\text{MG}}(k, \tau) \right] \hat{D}_2(k, \tau) \\ &= \left[\kappa \mu_{\text{MG}}(k, \tau) + 2a^4 H^2 \gamma_{2,\text{MG}}^{\text{E}}(k, k/\sqrt{2}, k/\sqrt{2}, \tau) \right] D_1^2(k, \tau) , \quad (2.35) \end{aligned}$$

In **MG-PICOLA**, the base assumption is that at early times the modified gravity effects are negligible such that the ICs are still those for an Einstein-de Sitter (EdS) universe: $D_1(k, \tau_{\text{ini}}) = 1$, $\frac{dD_1(k, \tau_{\text{ini}})}{d\tau} = \left(\frac{1}{a} \frac{da}{d\tau}\right)\bigg|_{\tau=\tau_{\text{ini}}}$, $\hat{D}_2^{\text{ini}} = -\frac{3}{7}$ and $\frac{d\hat{D}_2^{\text{ini}}}{d\tau} = -\frac{6}{7} \left(\frac{1}{a} \frac{da}{d\tau}\right)\bigg|_{\tau=\tau_{\text{ini}}}$. This is true for the main models we considered ($f(R)$ and nDGP), but is not true in full generality. We list $\mu_{\text{MG}}(k, \tau)$ and $\gamma_{2,\text{MG}}^{\text{E}}$ formulae for different modified gravity models in Appendix D.

The changes required to the other equations from Sec. 2.1 that are necessary to complete the 2LPT formalism for general scale-dependent modified gravity are essentially negligible, amounting to dropping the dependence on the direction of wavevectors so that there is only a dependence on the magnitude.

If $\gamma_{2,\text{MG}}^{\text{E}} = 0$ (Λ CDM), then Eq. (2.35) is exact. Another case we can do exactly is when $\gamma_{2,\text{MG}}^{\text{E}} = f(\tau)(1 - \cos^2 \theta)$ and² $\mu_{\text{MG}}(k, \tau) = \mu_{\text{MG}}(\tau)$, as is true in nDGP. Here the angular dependence of the $\gamma_{2,\text{MG}}^{\text{E}}$ term is the same as the other term in Eq. (2.34) and we can factor out $(1 - \cos^2 \theta)$ to get $D_2(k_1, k_2, k, \tau) = (1 - \cos^2 \theta) \hat{D}_2(\tau)$ where

$$\frac{d^2 \hat{D}_2}{d\tau^2} - \kappa \mu_{\text{MG}}(\tau) \hat{D}_2 = -\kappa \mu_{\text{MG}}(\tau) D_1^2(k, \tau) \left(1 + \frac{2a^4 H^2}{\kappa \mu_{\text{MG}}(\tau)} f(\tau)\right). \quad (2.36)$$

To get an idea about how good the approximation for \hat{D}_2 is, in Fig. 2.1 we show the ratio of our approximation³ Eq. (2.35) to $D_2(k, k_1, k_2, a = 1)$ in Eq. (2.34) for different Fourier space triangle configurations of $\vec{k} = \vec{k}_1 + \vec{k}_2$. For the orthogonal and equilateral cases these agree to $\sim 1 - 2\%$ up to $k = 5h/\text{Mpc}$ for the models F5 and F6 (defined below) while for the squeezed triangle configuration the difference can be up to 10% for $k \gtrsim 1h/\text{Mpc}$.

2.3 2LPT for massive neutrinos

In the method that follows, we treat the massive neutrinos as entirely linear such that $\delta_\nu = \delta_\nu^{(1)}$. Thus the only non-linearity comes from the CDM+baryon component $\delta_{\text{cb}} = \delta_{\text{cb}}^{(1)} + \delta_{\text{cb}}^{(2)}$. This idea has been implemented and tested in N -body simulations [172] and in Standard Perturbation Theory (SPT) [212, 213, 214]. Reference [215] raised the issue that the treatment of massive neutrinos as purely linear causes problems stemming from the violation of momentum conservation. We discuss the impact of this on our work in Appendix E.

When we include massive neutrinos, the gravitational potential is sourced by both CDM+baryons and the neutrinos, and thus the Fourier space Poisson equation up to

²We must require μ_{MG} to be independent of scale in order to put $D_1(k_1, \tau) D_1(k_2, \tau) \equiv D_1^2(\tau)$.

³We multiply our approximation by $(1 - \cos^2 \theta)$ when comparing this to $D_2(k, k_1, k_2, a = 1)$ as this is the equivalent expression for Λ CDM. This can be seen from comparing Eq. (2.21) to Eq. (2.26).

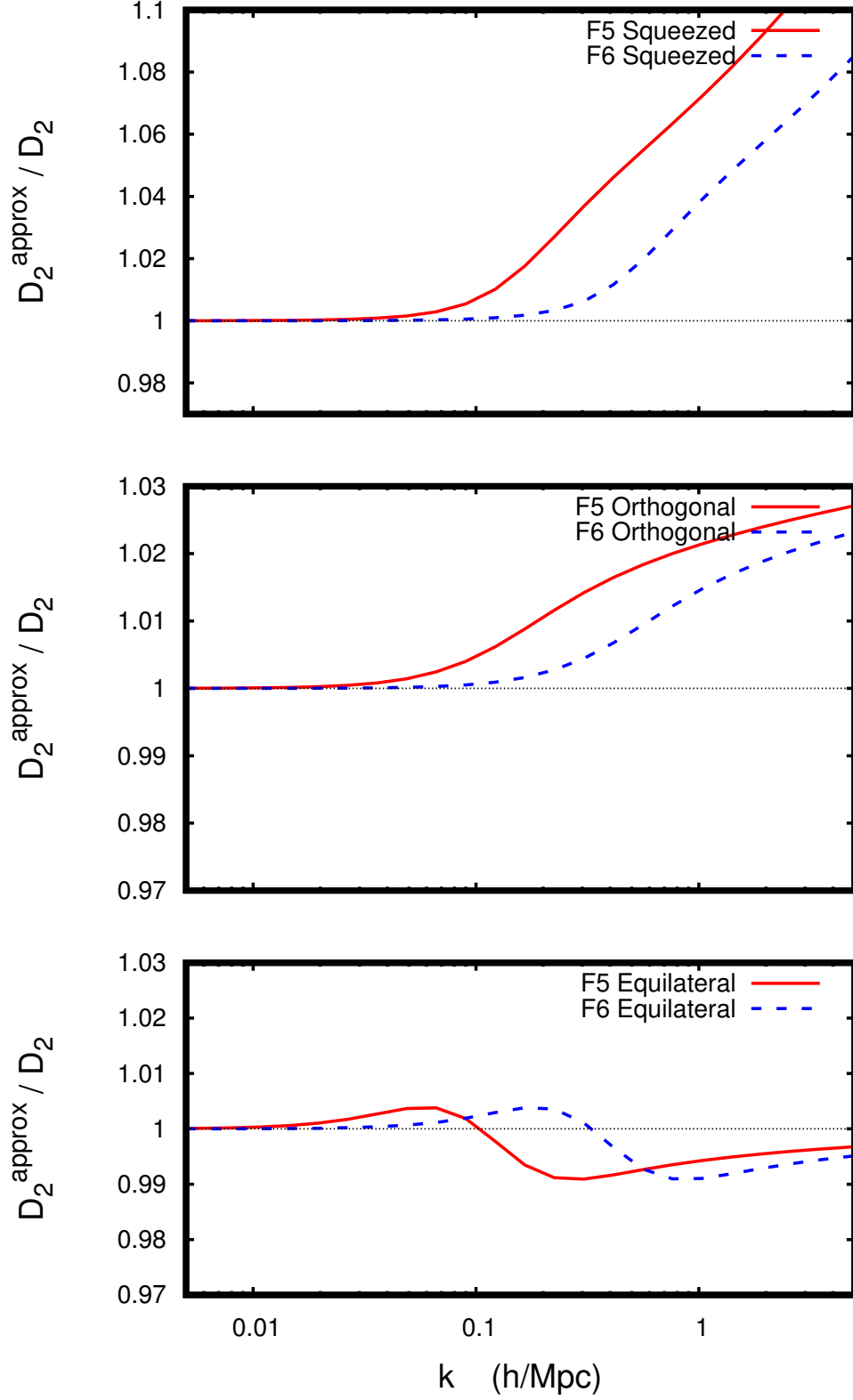


Figure 2.1: The ratio of $D_2(k, k_1, k_2, \cos \theta, a = 1)$ to the approximation $D_2(k, a = 1)(1 - \cos^2 \theta)$ for three different triangle configurations; equilateral $k = k_1 = k_2$, orthogonal $k_1 = k_2 = k/\sqrt{2}$ and squeezed $k = k_1$ with $k_2 \approx 0$. Here F5 (F6) refers to a Hu-Sawicki $f(R)$ model with $n = 1$ and $|f_{R0}| = 10^{-5}$ ($|f_{R0}| = 10^{-6}$).

second order is

$$\mathcal{F}_x [\nabla_x^2 \Phi_N(\vec{x}, \tau)] (\vec{k}) = \kappa (\delta_m^{(1)} + \delta_m^{(2)}) = 4\pi G a^4 \bar{\rho}_m (\delta_m^{(1)} + \delta_m^{(2)}) . \quad (2.37)$$

We can expand the expression $\bar{\rho}_m (\delta_m^{(1)} + \delta_m^{(2)})$ as

$$\begin{aligned} \bar{\rho}_m (\delta_m^{(1)} + \delta_m^{(2)}) &= \bar{\rho}_{cb} \delta_{cb}^{(1)} + \bar{\rho}_\nu \delta_\nu^{(1)} + \bar{\rho}_{cb} \delta_{cb}^{(2)} = \left(\frac{\bar{\rho}_{cb}}{\bar{\rho}_m} + \frac{\bar{\rho}_\nu}{\bar{\rho}_m} \frac{\delta_\nu^{(1)}}{\delta_{cb}^{(1)}} \right) \bar{\rho}_m \delta_{cb}^{(1)} + f_{cb} \bar{\rho}_m \delta_{cb}^{(2)} \\ &= \left(f_{cb} + f_\nu \frac{D_{1,\nu}(k, \tau)}{D_{1,cb}(k, \tau)} \right) \bar{\rho}_m \delta_{cb}^{(1)} + f_{cb} \bar{\rho}_m \delta_{cb}^{(2)} \\ &= \left(f_{cb} + f_\nu \frac{T_\nu(k, \tau)}{T_{cb}(k, \tau)} \right) \bar{\rho}_m \delta_{cb}^{(1)} + f_{cb} \bar{\rho}_m \delta_{cb}^{(2)} \\ &= \bar{\rho}_m \left(\mu_{m_\nu}(k, \tau) \delta_{cb}^{(1)} + f_{cb} \delta_{cb}^{(2)} \right) , \end{aligned} \quad (2.38)$$

where $T_s(k, \tau)$ is the transfer function for species ‘s’ that can be extracted from a Boltzmann code. The quantity μ_{m_ν} acts as an effective Newton’s constant, and in our code we compute it using the transfer functions from **CAMB** [105]. The result of this is that Eq. (2.37) becomes

$$\mathcal{F}_x [\nabla_x^2 \Phi_N(\vec{x}, \tau)] (\vec{k}) = \kappa \left(\mu_{m_\nu}(k, \tau) \delta_{cb}^{(1)} + f_{cb} \delta_{cb}^{(2)} \right) . \quad (2.39)$$

Thus massive neutrinos are covered by the general formalism laid out in Sec. 2.1, with $\mu^{(1)}(\vec{k}, \tau) \rightarrow \mu_{m_\nu}(k, \tau)$, $\mu^{(2)}(\vec{k}, \tau) \rightarrow f_{cb}$, and $\gamma_2^E(\vec{k}, \vec{k}_1, \vec{k}_2, \tau) \rightarrow 0$. Therefore the Fourier transform with respect to q instead of x is

$$\begin{aligned} \mathcal{F}_q [\nabla_x^2 \Phi(\vec{x}, \tau)] (\vec{k}) &= \kappa \mu_{m_\nu}(k, \tau) \tilde{\delta}_{cb}^{(1)}(k, \tau) + \kappa f_{cb} \tilde{\delta}_{cb}^{(2)}(k, \tau) \\ &\quad + \kappa \int \frac{d^3 \vec{k}_1 d^3 \vec{k}_2}{(2\pi)^3} \delta_D(\vec{k} - \vec{k}_{12}) [\mu_{m_\nu}(k, \tau) - \mu_{m_\nu}(k_1, \tau)] \\ &\quad \times \frac{\vec{k}_1 \cdot \vec{k}_2}{k_2^2} \tilde{\delta}_{cb}^{(1)}(k_1, \tau) \tilde{\delta}_{cb}^{(1)}(k_2, \tau) . \end{aligned} \quad (2.40)$$

Consequently, the equation for the first order growth factors D_1 becomes

$$\frac{d^2 D_{1,cb}(k, \tau)}{d\tau^2} - \kappa \mu_{m_\nu}(k, \tau) D_{1,cb}(k, \tau) = 0 , \quad (2.41)$$

Ideally, we would include the impact of massive neutrinos at early times in the ICs, for example by passing the EdS ICs through the fitting functions we will mention below. However, for simplicity we assume that at early times the massive neutrino effects are negligible such that the ICs are still those for an EdS universe. We estimate that the inaccuracy produced by this assumption will be minimal as long as we deal with growth factors normalised to their value at $z = 0$, as is required in **MG-PICOLA**.

Another way to account for the additional effect of massive neutrinos on the first order growth factor $D_{1,\text{cb}}^{m_\nu=0}$ for matter perturbations in ΛCDM without massive neutrinos, is to follow the practice of [216] and use the following fitting formulae to calculate the first order growth factor of CDM+baryon perturbations $D_{1,\text{cb}}$ and total matter perturbations $D_{1,\text{cb}\nu}$ in cosmologies with massive neutrinos:

$$D_{1,\text{cb}}(k, \tau) = \left[1 + \left(\frac{D_{1,\text{cb}}^{m_\nu=0}(\tau)}{1 + y_{fs}(\chi; f_\nu)} \right)^{0.7} \right]^{p_{\text{cb}}/0.7} D_{1,\text{cb}}^{m_\nu=0}(\tau)^{1-p_{\text{cb}}} , \quad (2.42)$$

$$D_{1,\text{cb}\nu}(k, \tau) = \left[f_{\text{cb}}^{0.7/p_{\text{cb}}} + \left(\frac{D_{1,\text{cb}}^{m_\nu=0}(\tau)}{1 + y_{fs}(\chi; f_\nu)} \right)^{0.7} \right]^{p_{\text{cb}}/0.7} D_{1,\text{cb}}^{m_\nu=0}(\tau)^{1-p_{\text{cb}}} , \quad (2.43)$$

where

$$p_{\text{cb}}(f_{\text{cb}}) \equiv \frac{1}{4} \left[5 - \sqrt{1 + 24f_{\text{cb}}} \right] \geq 0 , \quad (2.44)$$

$$y_{fs}(\chi; f_\nu) = 17.2 f_\nu (1 + 0.488 f_\nu^{-7/6}) (N_\nu \chi / f_\nu)^2 , \quad (2.45)$$

$$\chi(k) = \frac{k}{\text{Mpc}^{-1}} \Theta_{2.7}^2 (\Omega_0 h^2)^{-1} = \frac{k}{19.0} (\Omega_0 H_0^2)^{-1/2} (1 + z_{\text{eq}})^{-1/2} , \quad (2.46)$$

and $f_i = \Omega_i / \Omega_{\text{m}}$ is the density ratio for species i , N_ν is the number of massive neutrino species, and $\Theta_{2.7}$ is a measure of the CMB temperature at $z = 0$ using $T_{\text{CMB}} = 2.7\Theta_{2.7}\text{K}$.

This method allows us to insert ΛCDM $D_{1,\text{cb}}^{m_\nu=0}$ values that we calculate by solving Eq. (1.91) into Eqs. (2.42, 2.43) to calculate $D_{1,\text{cb}}^{m_\nu}$ and $D_{1,\text{cb}\nu}^{m_\nu}$ which then include the effect of massive neutrinos at linear order. This alternative method for computing the first order growth factor including the effects of massive neutrinos could be included in our implementation alongside the current Boltzmann code method, where we use the transfer functions T_ν and T_{cb} to compute μ_{m_ν} and solve the ODE numerically. Either method could then be used as per the user's preference. The alternative method may be useful if we need to run a large number of simulations with various different masses as we could avoid storing the Boltzmann code outputs.

Figure 2.2 displays a comparison between the outputs of Eq. (2.42) and **CAMB**. Specifically, the figure plots the ratio of the first order CDM+baryon growth factor at $z = 0$ and $z = 1$, $D_{1,\text{cb}}(k, z = 0) / D_{1,\text{cb}}(k, z = 1)$. The comparison is done for three GR+massive neutrino cosmologies with $m_\nu = \{0.2, 0.4, 0.6\}$ eV. The ratio has also been normalised to the ΛCDM case without massive neutrinos. Figure 2.2 shows that the output of Eq. (2.42) matches **CAMB** to an accuracy of $< 1\%$ for neutrino masses $m_\nu \lesssim 0.6$ eV up to $k = 1.0 h/\text{Mpc}$.

With the first order growth factor dealt with, we turn our attention to the second

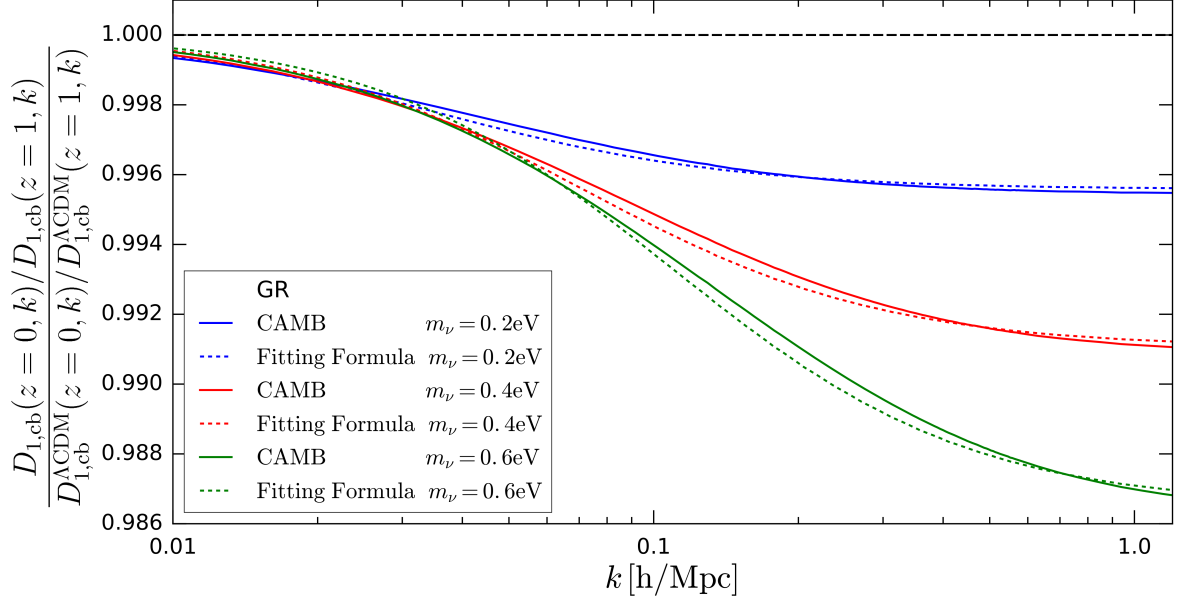


Figure 2.2: Comparison between **CAMB** and the fitting formula method Eq. (2.42) for the ratio of the first order CDM+baryon growth factor at $z = 0$ to $z = 1$ for a GR + massive neutrino cosmology with $m_\nu = \{0.2, 0.4, 0.6\}$ eV. The ratio has been normalised to the Λ CDM case without neutrinos, which is given by the horizontal dashed line.

order growth factor D_2 . The equation for $D_2(k, k_1, k_2, \tau)$ becomes

$$\left[\frac{d^2}{d\tau^2} - \kappa f_{\text{cb}} \right] D_2(\vec{k}, \vec{k}_1, \vec{k}_2, \tau) = \left[\kappa \left(f_{\text{cb}} - 2\mu_{m_\nu}(\vec{k}_1, \tau) \right) \frac{(\vec{k}_1 \cdot \vec{k}_2)^2}{k_1^2 k_2^2} + \kappa f_{\text{cb}} + 2\kappa \left[\mu_{m_\nu}(\vec{k}, \tau) - \mu_{m_\nu}(\vec{k}_1, \tau) \right] \frac{\vec{k}_1 \cdot \vec{k}_2}{k_2^2} \right] \times D_1(\vec{k}_1, \tau) D_1(\vec{k}_2, \tau), \quad (2.47)$$

and if $\mu_{m_\nu}(k, \tau) = \mu_{m_\nu}(k_1, \tau) \approx f_{\text{cb}}$, then the equation for the approximate second order growth factor $\hat{D}_2(k)$ becomes

$$\left[\frac{d^2}{d\tau^2} - \kappa f_{\text{cb}} \right] \hat{D}_2(k, \tau) = \kappa f_{\text{cb}} D_1^2(k, \tau). \quad (2.48)$$

For a matter dominated Universe and for scales smaller than the neutrino free-streaming scale we have $D_{2,\text{cb}} \simeq -\frac{3f_{\text{cb}}}{3f_{\text{cb}}+4(1-p_{\text{cb}})^2} D_{1,\text{cb}}^2$, which could be used to derive the ICs when solving Eq. (2.48) numerically. However, as at first order, we have again chosen to use the EdS ICs under the same assumptions. The $\mu_{m_\nu} \rightarrow f_{\text{cb}}$ approximation was previously made in [212, 213] for a Λ CDM+massive neutrino cosmology in Standard Perturbation Theory. They argued that the small value of f_ν suppresses the non-linear corrections to the above approximation of treating the massive neutrinos as an exclusively linear density perturbation. We have tested the effect of using μ_{m_ν} instead of

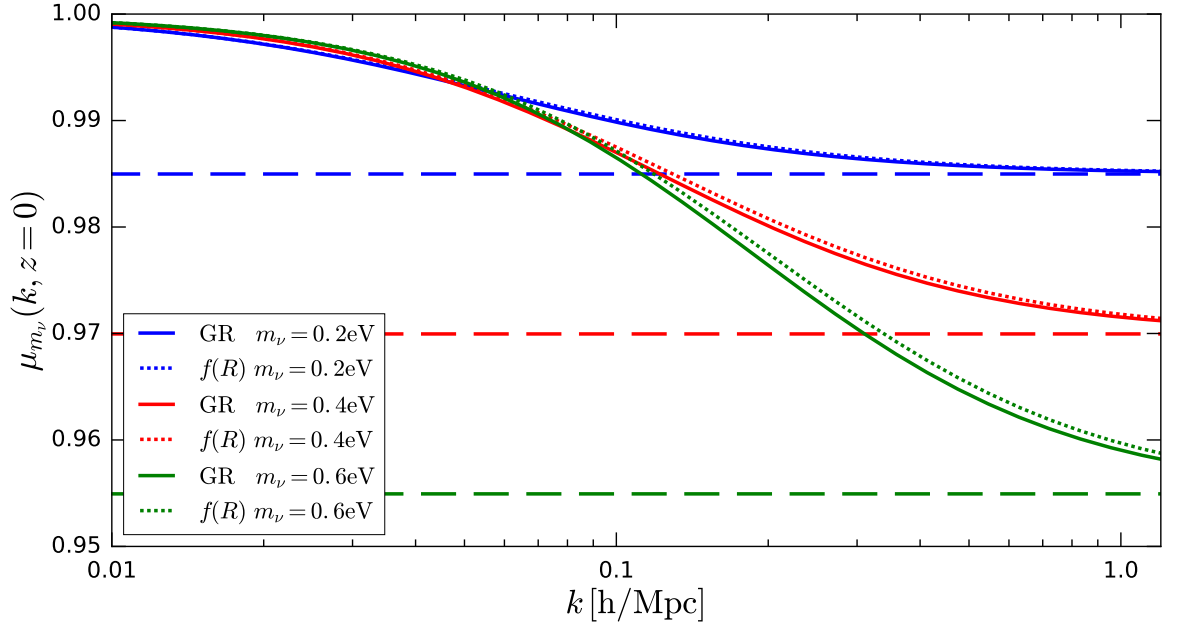


Figure 2.3: The value of μ_{m_ν} as a function of k calculated using Eq. (2.38) at $z = 0$ for both GR and F4 cosmologies with neutrinos of mass $m_\nu = \{0.2, 0.4, 0.6\}$ eV. The horizontal dashed lines plotted are the values of f_{cb} at each neutrino mass, which highlight the consequences of setting $\mu_{m_\nu} \rightarrow f_{cb}$ in the approximate second order growth factor equations Eqs. (2.48) and (2.59).

f_{cb} in Eq. (2.48) for the second order growth-factor in our COLA implementation (to be presented in the upcoming section). This change was found to have a negligible effect ($\lesssim 0.1 - 0.5\%$) on the total matter power spectrum for wavenumbers $k \lesssim 1$ h/Mpc. Making the $\mu_{m_\nu} \rightarrow f_{cb}$ approximation also means that Eq. (2.48), unlike Eq. (2.47), can be solved without the Boltzmann code output, since we know f_{cb} and D_1 can be computed with the fitting formulae.

In Figure 2.3 we show the difference between μ_{m_ν} , calculated using Eq. (2.38), and f_{cb} in the range $0.01 \leq k \leq 1.0$ h/Mpc to highlight the consequences of making this approximation. Figure 2.3 shows that the approximation is less important as $k \rightarrow 1.0$ h/Mpc, but also shows that the approximation becomes less accurate as m_ν increases. Specifically, at $k = 0.01$ h/Mpc, the percentage difference between μ_{m_ν} and f_{cb} is 1.5/3.0/4.5% for $m_\nu = 0.2/0.4/0.6$ eV respectively.

2.4 2LPT for modified gravity and massive neutrinos

The effects of modified gravity and massive neutrinos on 2LPT can be combined in a simple manner that is covered by the formalism laid out in Sec. 2.1:

$$\mu^{(1)}(\vec{k}, \tau) \rightarrow \mu_{\text{MG}}(k, \tau) \times \mu_{m_\nu}(k, \tau) , \quad (2.49)$$

$$\mu^{(2)}(\vec{k}, \tau) \rightarrow \mu_{\text{MG}}(k, \tau) \times f_{\text{cb}} , \quad (2.50)$$

$$\gamma_2^{\text{E}}(\vec{k}, \vec{k}_1, \vec{k}_2, \tau) \rightarrow \gamma_{2,\text{MG}}^{\text{E}}(k, k_1, k_2, \tau) . \quad (2.51)$$

This leads to the Fourier transform of the Poisson equation w.r.t. \vec{q} becoming

$$\begin{aligned} \mathcal{F}_q [\nabla_x^2 \Phi(\vec{x}, \tau)] &= \kappa \left[\mu_{\text{MG}}(k, \tau) \mu_{m_\nu}(k, \tau) \tilde{\delta}^{(1)}(\vec{k}, \tau) + \mu_{\text{MG}}(k, \tau) f_{\text{cb}} \tilde{\delta}^{(2)}(\vec{k}, \tau) \right. \\ &\quad + \int \frac{d^3 k_1 d^3 k_2}{(2\pi)^3} \delta_D^{(3)}(\vec{k} - \vec{k}_{12}) \\ &\quad \times [\mu_{\text{MG}}(k, \tau) \mu_{m_\nu}(k, \tau) - \mu_{\text{MG}}(k_1, \tau) \mu_{m_\nu}(k_1, \tau)] \\ &\quad \times \frac{\vec{k}_1 \cdot \vec{k}_2}{k_2^2} \delta^{(1)}(\vec{k}_1, \tau) \delta^{(1)}(\vec{k}_2, \tau) \Big] \\ &\quad + a^4 H^2 \int \frac{d^3 k_1 d^3 k_2}{(2\pi)^3} \delta_D^{(3)}(\vec{k} - \vec{k}_{12}) \\ &\quad \times \gamma_{2,\text{MG}}^{\text{E}}(\vec{k}, \vec{k}_1, \vec{k}_2, \tau) \delta^{(1)}(\vec{k}_1, \tau) \delta^{(1)}(\vec{k}_2, \tau) , \end{aligned} \quad (2.52)$$

This leads to the following equation for the first order growth factor D_1 :

$$\left[\frac{d^2}{d\tau^2} - \kappa \mu_{\text{MG}}(k, \tau) \mu_{m_\nu}(k, \tau) \right] D_1(k, \tau) = 0 . \quad (2.53)$$

We again assume that at early times the modified gravity effects are negligible. However, ideally we would account for the effect of massive neutrinos in the early Universe through the ICs, for example using the Eisenstein-Hu fitting formulae, which we will show below are applicable to modified gravity cosmologies as well as Λ CDM ones. For simplicity, we use the ICs for an EdS universe under the same assumptions as described for D_1 in Sec. 2.3.

Eisenstein and Hu originally only considered Λ CDM $D_{1,\text{cb}}^{m_\nu=0}$ values as input to Eqs. (2.42, 2.43). We extend their idea by using $D_{1,\text{cb}}^{m_\nu=0}$ values for modified gravity cosmologies without massive neutrinos as input instead, these having been calculated numerically by solving Eq. (2.33). This adds the effect of massive neutrinos to the

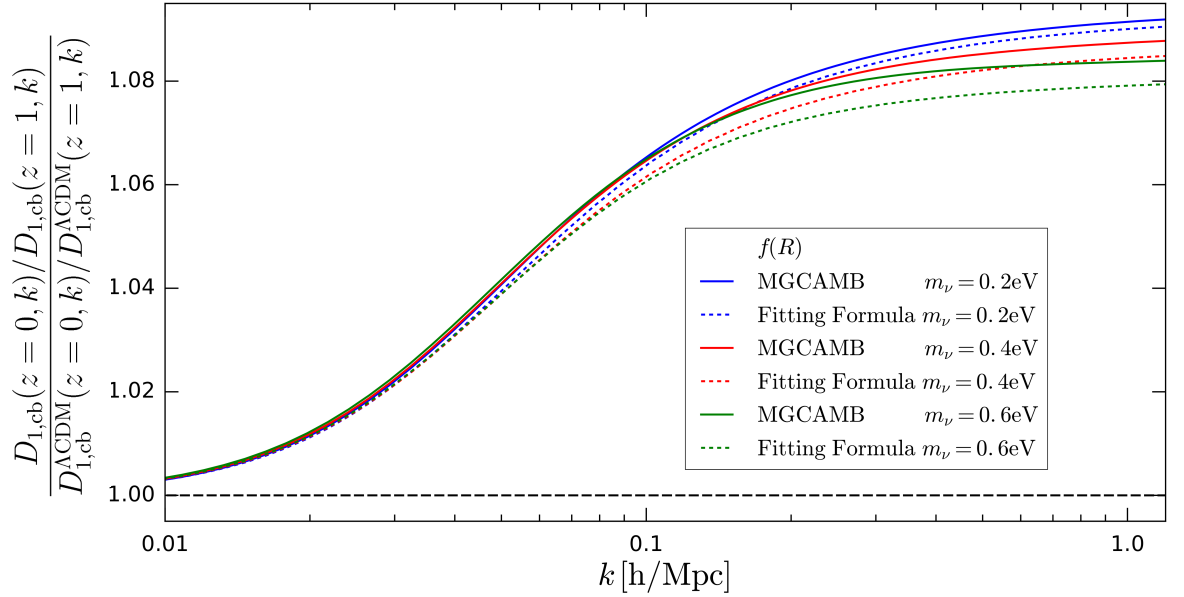


Figure 2.4: Comparison between **MGCAMB** and the fitting formula method Eq. (2.42) for the ratio of the first order CDM+baryon growth factor at $z = 0$ to $z = 1$ for a $f(R)$ + massive neutrino cosmology with $|f_{R0}| = 10^{-4}$ and $m_\nu = \{0.2, 0.4, 0.6\}$ eV. The ratio has been normalised to the Λ CDM case without massive neutrinos, which is given by the horizontal dashed line.

modified gravity models, enabling us to compute growth factor values for modified gravity + massive neutrino (MG+ m_ν) cosmologies at linear order.

To test the fitting formula method for growth factors in MG+ m_ν cosmologies, we first verified that our extension to the fitting formula method gives accurate values of $D_{1,cb}$ and $D_{1,cb\nu}$ by comparison with the output from **MGCAMB**, which is an extension of **CAMB** for modified gravity models [119, 120]. These comparisons can be seen in Figures 2.4-2.6 for $D_{1,cb}$ in the Hu-Sawicki $f(R)$, symmetron, and dilaton modified gravity models. As in Figure 2.2, the plots show the ratio of the first order CDM+baryon growth factor at $z = 0$ and $z = 1$, $D_{1,cb}(k, z = 0)/D_{1,cb}(k, z = 1)$, the ratios have been normalised to the Λ CDM case without massive neutrinos, and the comparison is made for three different neutrino masses $m_\nu = \{0.2, 0.4, 0.6\}$ eV. Figure 2.4 shows that the ability of the fitting formula to recover **MGCAMB** first order growth values for $f(R)$ + m_ν cosmologies decreases as m_ν increases. However, for the F4 model of $f(R)$ gravity (where $|f_{R0}| = 10^{-4}$) that we consider in Figure 2.4 the output of Eq. (2.42) matches that of **MGCAMB** to an accuracy of $< 1\%$ up to $k = 1.0$ h/Mpc even for $m_\nu = 0.6$ eV. Similarly, for the values of parameters we have considered here, Eq. (2.42) matches **MGCAMB** to an accuracy of $< 1\%$ up to $k = 1.0$ h/Mpc for both the symmetron and dilaton cosmologies with neutrino masses $m_\nu \lesssim 0.6$ eV.

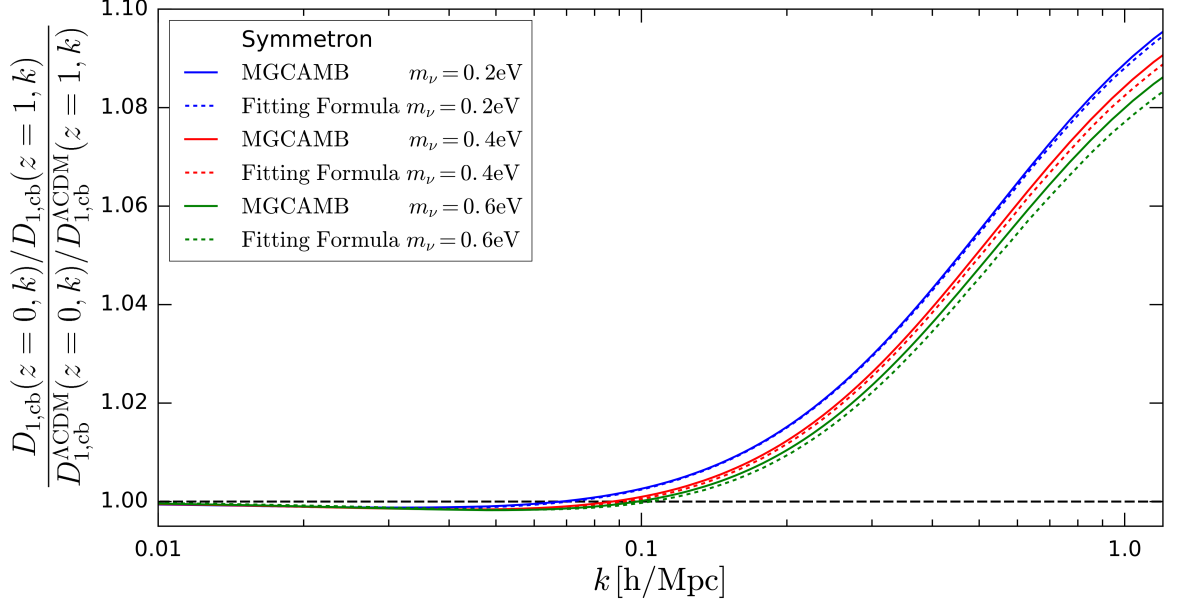


Figure 2.5: Comparison between **MGCAMB** and the fitting formula method Eq. (2.42) for the ratio of the first order CDM+baryon growth factor at $z = 0$ to $z = 1$ for a symmetron + massive neutrino cosmology with $\beta_\star = 1$, $a_\star = 0.5$, $\xi_\star = 1/2998$, and $m_\nu = \{0.2, 0.4, 0.6\}$ eV. The ratio has been normalised to the Λ CDM case without massive neutrinos, which is given by the horizontal dashed line.

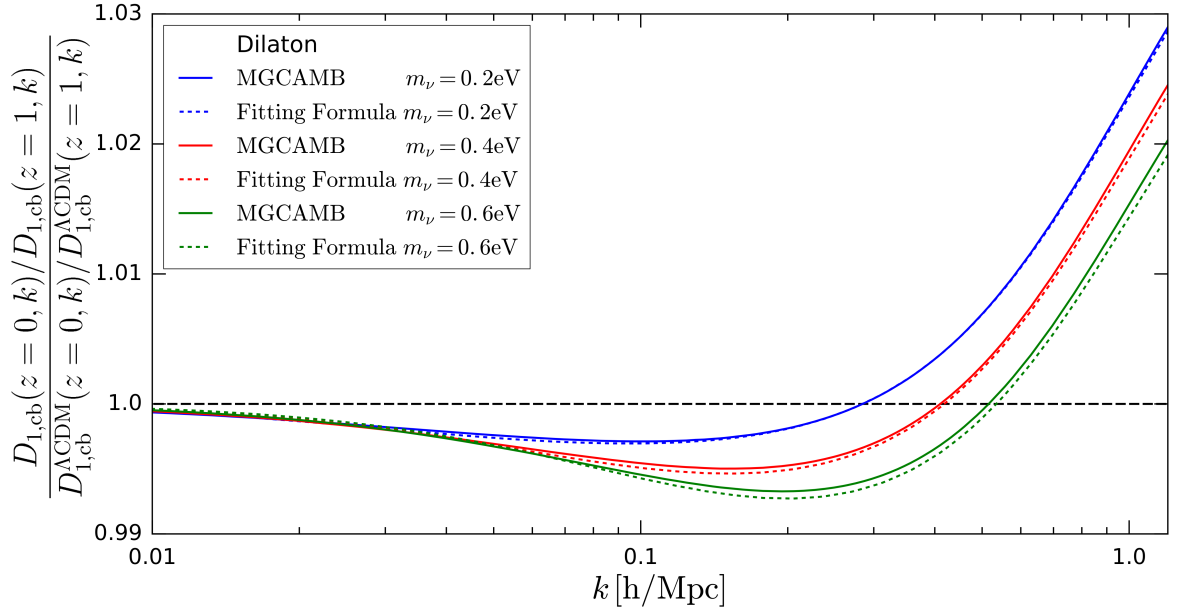


Figure 2.6: Comparison between **MGCAMB** and the fitting formula method Eq. (2.42) for the ratio of the first order CDM+baryon growth factor at $z = 0$ to $z = 1$ for a dilaton + massive neutrino cosmology with $\beta_0 = 0.41$, $\xi_0 = 1/2998$, $S = 0.24$, $R = 1$, and $m_\nu = \{0.2, 0.4, 0.6\}$ eV. The ratio has been normalised to the Λ CDM case without massive neutrinos, which is given by the horizontal dashed line.

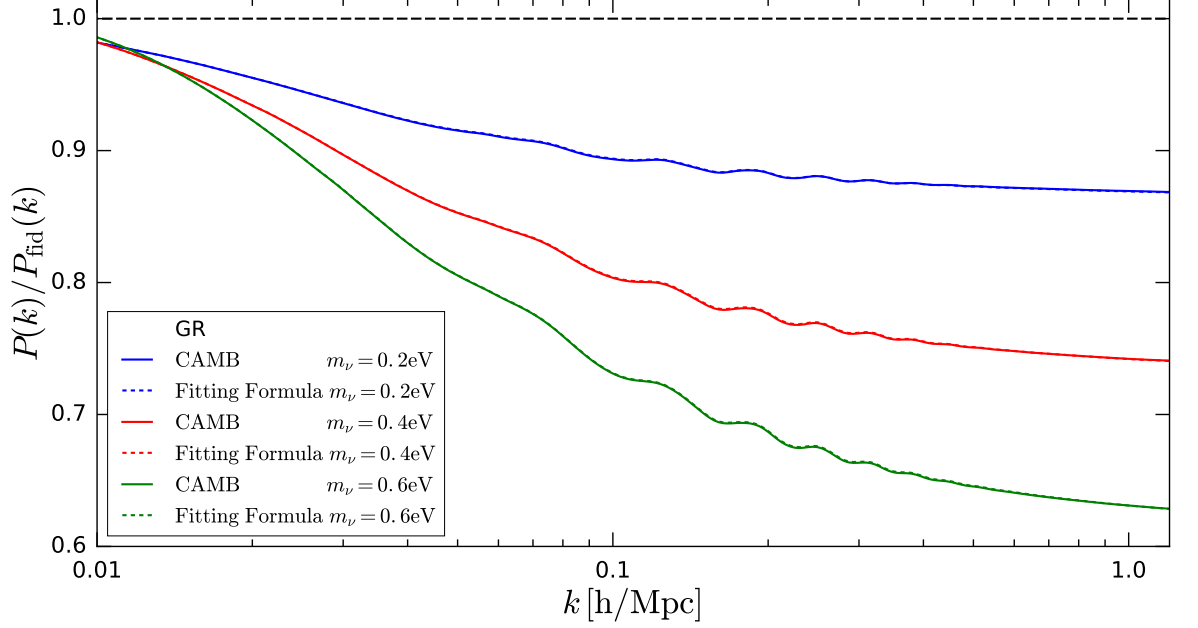


Figure 2.7: The linear total matter power spectrum at $z = 1.3$ for a GR + massive neutrino cosmology with $m_\nu = \{0.2, 0.4, 0.6\}$ eV, calculated using both **CAMB** and the fitting formula method Eq. (2.42). This power spectrum is normalised to the fiducial Λ CDM case without massive neutrinos, which is shown by the horizontal dashed line.

We also wanted to test whether the growth factors calculated using this method could be used to accurately ‘backscale’ the linear total matter (CDM + baryon + massive neutrino) power spectra at $z = 0$ so that they closely matched the linear total matter power spectra output at earlier z by **MGCAMB** directly. This was done using the relationship

$$P_{\text{cb}\nu}(k, z) = \left[\frac{D_{1,\text{cb}\nu}(k, z)}{D_{1,\text{cb}\nu}(k, z = 0)} \right]^2 P_{\text{cb}\nu}(k, z = 0) . \quad (2.54)$$

In Figures 2.7-2.10, we display the resulting backscaled total matter linear power spectra for the GR, $f(R)$, symmetron, and dilaton gravity models with $m_\nu = [0, 0.2, 0.4, 0.6]$ eV at $z = 1.3$. As for the first order growth factors, we find that, for the values of the model parameters considered, using the fitting formula method to backscale the $z = 0$ linear total matter power spectrum to $z = 1.3$ recovers the same result as is output by **MGCAMB** directly at $z = 1.3$ to an accuracy of $< 1\%$ up to $k = 1.0$ h/Mpc for each of the cosmologies with neutrino masses $m_\nu \lesssim 0.6$ eV.

Switching our consideration from first order to second order, the equation for the

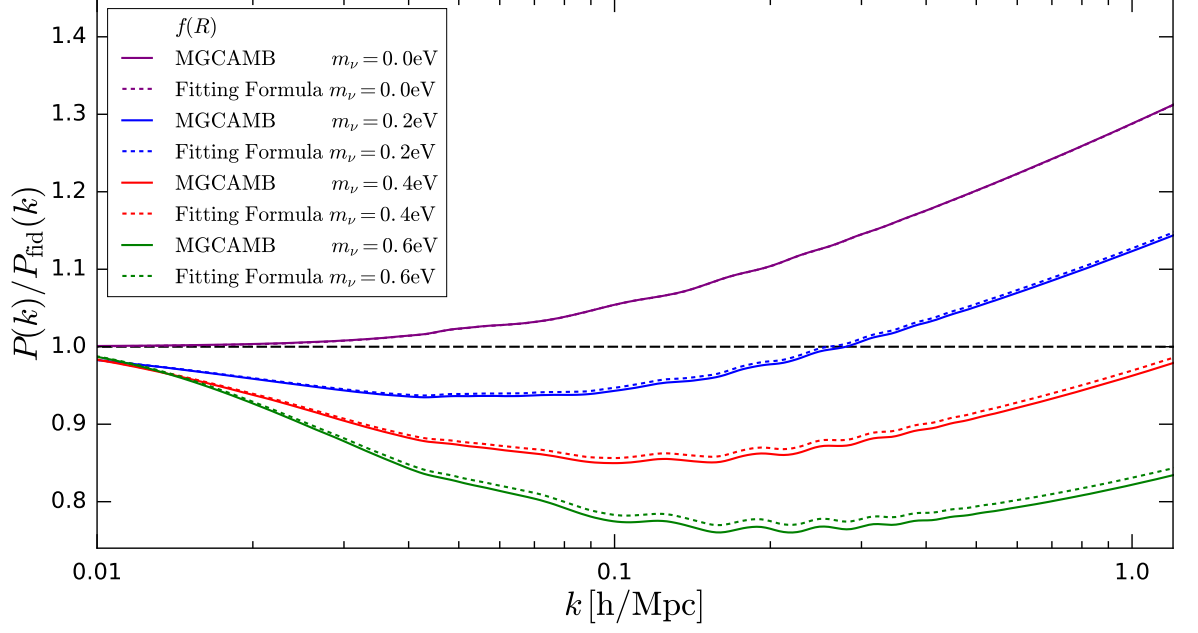


Figure 2.8: The linear total matter power spectrum at $z = 1.3$ for a $f(R)$ + massive neutrino cosmology with $|f_{R0}| = 10^{-4}$ and $m_\nu = \{0.0, 0.2, 0.4, 0.6\}$ eV, calculated using both MGCAMB and the fitting formula method Eq. (2.42). This power spectrum is normalised to the fiducial Λ CDM case without massive neutrinos, which is shown by the horizontal dashed line.

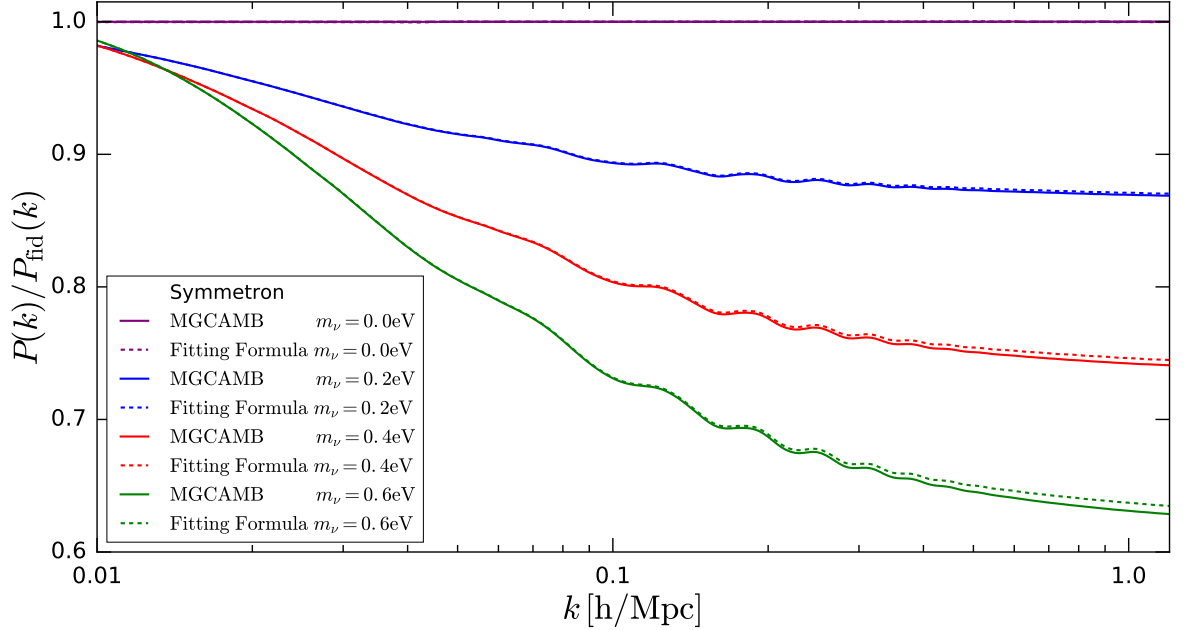


Figure 2.9: The linear total matter power spectrum at $z = 1.3$ for a symmetron + massive neutrino cosmology with $\beta_\star = 1$, $a_\star = 0.5$, $\xi_\star = 1/2998$, and $m_\nu = \{0.0, 0.2, 0.4, 0.6\}$ eV, calculated using both MGCAMB and the fitting formula method Eq. (2.42). This power spectrum is normalised to the fiducial Λ CDM case without massive neutrinos, which is shown by the horizontal dashed line.

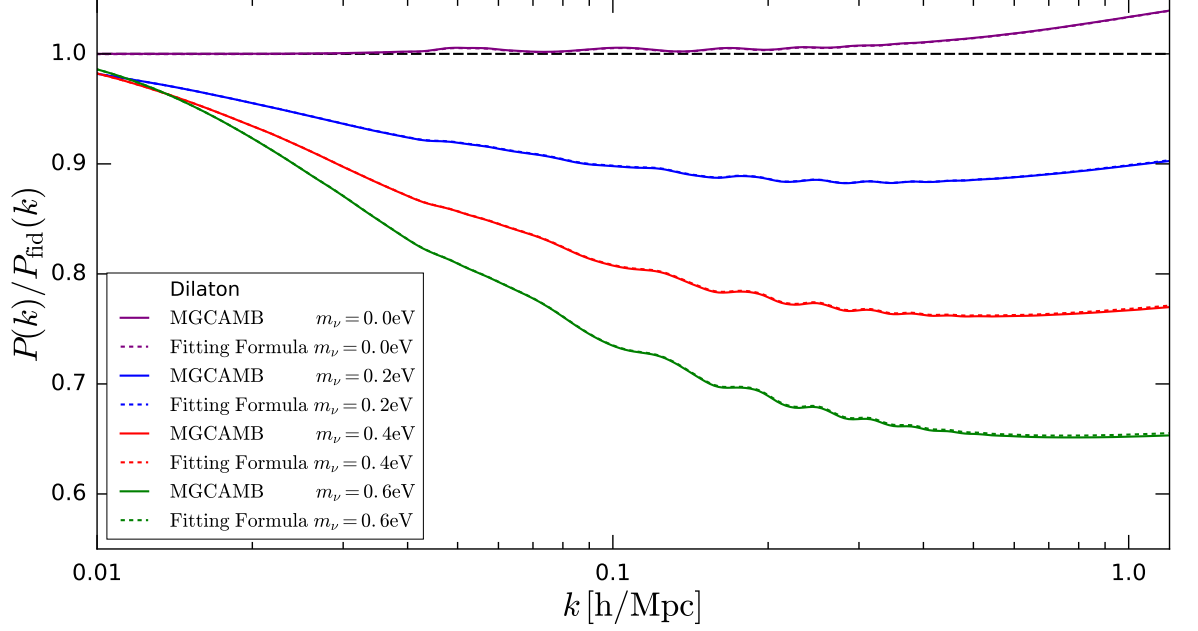


Figure 2.10: The linear total matter power spectrum at $z = 1.3$ for a dilaton + massive neutrino cosmology with $\beta_0 = 0.41$, $\xi_0 = 1/2998$, $S = 0.24$, $R = 1$, and $m_\nu = \{0.0, 0.2, 0.4, 0.6\}$ eV, calculated using both MGCAMB and the fitting formula method Eq. (2.42). This power spectrum is normalised to the fiducial Λ CDM case without massive neutrinos, which is shown by the horizontal dashed line.

second order growth factor $D_2(k, k_1, k_2, \tau)$ becomes

$$\begin{aligned}
& \left[\frac{d^2}{d\tau^2} - \kappa \mu_{\text{MG}}(k, \tau) f_{\text{cb}} \right] D_2(k, k_1, k_2, \tau) \\
&= \left[\kappa \mu_{\text{MG}}(k, \tau) f_{\text{cb}} + \kappa (\mu_{\text{MG}}(k, \tau) f_{\text{cb}} - 2\mu_{\text{MG}}(k_1, \tau) \mu_{m_\nu}(k_1, \tau)) \frac{(\vec{k}_1 \cdot \vec{k}_2)^2}{k_1^2 k_2^2} \right. \\
&\quad \left. + 2\kappa [\mu_{\text{MG}}(k, \tau) \mu_{m_\nu}(k, \tau) - \mu_{\text{MG}}(k_1, \tau) \mu_{m_\nu}(k_1, \tau)] \frac{\vec{k}_1 \cdot \vec{k}_2}{k_2^2} \right. \\
&\quad \left. + 2a^4 H^2 \gamma_{2, \text{MG}}^{\text{E}}(k, k_1, k_2, \tau) \right] D_1(k_1, \tau) D_1(k_2, \tau) . \quad (2.55)
\end{aligned}$$

By making the approximations

$$\mu_{\text{MG}}(k, \tau) \approx \mu_{\text{MG}}(k_1, \tau) , \quad (2.56)$$

$$\mu_{m_\nu}(k, \tau) = \mu_{m_\nu}(k_1, \tau) \approx f_{\text{cb}} , \quad (2.57)$$

$$\frac{\gamma_{2, \text{MG}}^{\text{E}}(k, k_1, k_2, \tau)}{\left(1 - \frac{\vec{k}_1 \cdot \vec{k}_2}{k_1^2 k_2^2}\right)} \approx \gamma_{2, \text{MG}}^{\text{E}}(k, k/\sqrt{2}, k/\sqrt{2}, \tau) , \quad (2.58)$$

we find the following equation for the approximate second order growth factor \hat{D}_2 :

$$\begin{aligned} \left[\frac{d^2}{d\tau^2} - \kappa \mu_{\text{MG}}(k, \tau) f_{\text{cb}} \right] \hat{D}_2(k, \tau) \\ = \left[\kappa \mu_{\text{MG}}(k, \tau) f_{\text{cb}} + 2a^4 H^2 \gamma_{2,\text{MG}}^{\text{E}}(k, k/\sqrt{2}, k/\sqrt{2}, \tau) \right] D_1^2(k, \tau) . \end{aligned} \quad (2.59)$$

As before, we use the EdS ICs following the same arguments presented previously. Figure 2.3 shows that there is a negligible difference between the F4 model of $f(R)$ gravity and GR in the comparison between the values of μ_{m_ν} and f_{cb} in the range $0.01 \leq k \leq 1.0 \text{ h/Mpc}$. Since we do approximate $\mu_{m_\nu} \rightarrow f_{\text{cb}}$, Eq. (2.59), unlike Eq. (2.55), can be solved without the output of a Boltzmann code, provided we use the fitting formulae to compute D_1 .

2.5 Modifying the particle mesh computation

2.5.1 Screened modified gravity theories in PM

N -body simulations of modified gravity models with screening (see e.g. [217, 218, 153, 156]) have shown that it is crucial to include the screening effect to get accurate results, for example linear perturbation theory might predict a 50% enhancement of the matter power spectrum relative to Λ CDM at some scale while simulations on the other hand might only show deviations at the few % level.

In [164] a simplified approximate method to include screening was proposed which relies on combining spherically symmetric analytical or semi-analytical solutions for the screening effect with a linear field equation. In effect it estimates from the amplitude of the density-field, the gravitational potential or its gradient (depending on the model in question) how much of the mass contributes to the fifth-force and then uses this to correct the linearised field-equation. The linearised field equation can be rapidly solved using Fourier transforms instead of using a time consuming relaxation method to solve a highly non-linear field equation with bad convergence properties, as is done in most modified gravity N -body codes today.

2.5.1.1 $f(R)$ gravity

For $f(R)$ gravity [219], which has the chameleon screening mechanism [201], we have that the fifth-force on an object (ignoring for now the finite range of the force) is given approximately by

$$\vec{F}_\phi = \frac{1}{3} \cdot \vec{F}_{\text{Newton}} \cdot \epsilon_{\text{screen}}(\Phi_N) , \quad (2.60)$$

where

$$\epsilon_{\text{screen}}(\Phi_N) = \text{Min} \left[1, \left| \frac{3f_R(a)}{2\Phi_N} \right| \right], \quad (2.61)$$

and Φ_N is the standard Newtonian gravitational potential. The linearised field-equation on the other hand is given by

$$\nabla_{\mathbf{x}}^2 \phi = a^2 m^2(a) \phi + \frac{1}{3} \cdot \kappa \delta, \quad (2.62)$$

where $m(a) = \frac{1}{3f_{RR}}$ is a model dependent function describing the inverse range of the fifth-force on cosmological scales and ϕ is related to f_R via $\phi \equiv -\frac{1}{2} \log(f_R + 1) \simeq -\frac{f_R}{2}$. The field is normalised here such that $\vec{\nabla}_{\mathbf{x}} \phi$ corresponds to the fifth-force (i.e. the total force is $\vec{\nabla}_{\mathbf{x}} \Phi_N + \vec{\nabla}_{\mathbf{x}} \phi$). To include the effects of screening we solve the linear field equation

$$\nabla_{\mathbf{x}}^2 \phi = a^2 m^2(a) \phi + \frac{1}{3} \cdot \kappa \delta \cdot \epsilon_{\text{screen}}(\Phi_N), \quad (2.63)$$

in our simulation. Φ_N is easily computed from the density field which allows us to quickly solve for the effects of the fifth-force using Fourier transforms. This method allows us to perform modified gravity simulations at a computational cost that is not much larger (20 – 50% is a reasonable estimate) than for Λ CDM.

2.5.1.2 nDGP

For the normal-branch DGP model [220, 221] with a Λ CDM background expansion, the modifications to the Poisson equation are given by $\Phi = \Phi_N + \phi$ where the scalar field ϕ is determined by

$$\nabla_{\mathbf{x}}^2 \phi + \frac{2r_c^2}{a^4} ((\nabla_{\mathbf{x}}^2 \phi)^2 - (\nabla_{\mathbf{x}_i} \nabla_{\mathbf{x}_j} \phi)^2) = \frac{\kappa \delta}{3\beta_{\text{DGP}}(a)}. \quad (2.64)$$

This equation is solved in modified gravity N -body simulations of this model.

For spherically symmetrical mass distributions the solution for the force $\vec{F}_\phi = \vec{\nabla}_{\mathbf{x}} \phi$ is given by

$$\vec{F}_\phi = \frac{1}{3\beta_{\text{DGP}}(a)} \cdot \vec{F}_{\text{Newton}} \cdot \epsilon_{\text{screen}}(\rho), \quad (2.65)$$

where

$$\epsilon_{\text{screen}}(\rho) = \frac{2\sqrt{1+x}}{x}, \quad (2.66)$$

$$x = \frac{8(r_c H_0)^2 \Omega_m \rho}{9\beta_{\text{DGP}}^2(a) \bar{\rho}}, \quad (2.67)$$

where ρ is the average density within a given radius. From this we can make the approximate linear field equation

$$\nabla_{\mathbf{x}}^2 \phi = \frac{1}{3\beta_{\text{DGP}}(a)} \cdot \kappa \delta \cdot \epsilon_{\text{screen}}(\rho), \quad (2.68)$$

which can be solved in the code to give the fifth-force. One problem with this equation is that the screening factor depends on density which means that the result will depend on the resolution of the simulation. To get around this issue we first smooth the density field with a Gaussian filter of a given radius R ($R \sim 1\text{Mpc}/h$ works well in practice) and use the smoothed density field to compute the screening factor above. This choice is motivated by the fact that the screening (Vainshtein) radius for the nDGP models we consider here is $\mathcal{O}(1)\text{Mpc}/h$ for typical halos we expect to have in our simulations. We have verified that the exact value of the smoothing radius does not significantly change our results by comparing the results we find for $R = 0.5, 1$ and $2 \text{ Mpc}/h$.

2.5.2 Massive neutrinos in PM

The implementation of massive neutrinos in the particle mesh part of the COLA algorithm is the grid-based method suggested in [172]. This method has been demonstrated to produce a matter power spectrum that is accurate to $< 1\%$ for neutrino masses $\sum m_\nu \lesssim 0.6 \text{ eV}$. When we create the initial conditions for the CDM (CDM+baryon) particles we use the same initial seed to create a realisation of massive neutrinos using

$$\delta_\nu(\vec{k}, \tau_{\text{ini}}) = \delta_{\text{cb}}(\vec{k}, \tau_{\text{ini}}) \frac{T_\nu(k, \tau_{\text{ini}})}{T_{\text{cb}}(k, \tau_{\text{ini}})} = \delta_{\text{cb}}(\vec{k}, \tau_{\text{ini}}) \frac{D_{1,\nu}(k, \tau_{\text{ini}})}{D_{1,\text{cb}}(k, \tau_{\text{ini}})}, \quad (2.69)$$

where T_ν and T_{cb} are the transfer functions of massive neutrinos and CDM+baryons respectively, which we compute using **CAMB**.

The massive neutrinos are kept in Fourier space for the duration of the simulation and are added to the source of the Poisson equation

$$-k^2 \Phi(\vec{k}, \tau) = \frac{3}{2} \Omega_{\text{m}} a \left[f_{\text{cb}} \delta_{\text{cb}}(\vec{k}, \tau) + f_\nu \delta_\nu(\vec{k}, \tau) \right], \quad (2.70)$$

where the neutrino density at a given time τ is computed as

$$\delta_\nu(\vec{k}, \tau) = \delta_\nu(\vec{k}, \tau_{\text{ini}}) \frac{T_\nu(k, \tau)}{T_\nu(k, \tau_{\text{ini}})} = \delta_\nu(\vec{k}, \tau_{\text{ini}}) \frac{D_{1,\nu}(k, \tau)}{D_{1,\nu}(k, \tau_{\text{ini}})}. \quad (2.71)$$

In Appendix E we show a comparison of this scheme to an alternative scheme of modelling the non-linear neutrino density.

We have compared the consequences of computing the growth factors using the EH fitting functions to directly solving the growth-ODEs with $\mu_\nu(k, \tau) = f_{\text{cb}} + f_\nu \frac{T_\nu(k, \tau)}{T_{\text{cb}}(k, \tau)}$

computed using transfer functions from **CAMB** or its alternatives. The difference between these two approaches was found to be negligible.

As long as the cosmological model we simulate already has scale-dependent growth then the additional computational cost of adding in massive neutrinos this way is almost negligible, but it does require some extra memory as we need to store the initial neutrino density field.

2.6 MG-PICOLA results

2.6.1 Modified Gravity without massive neutrinos

In this section we show test runs of our code for some example models.

To start with we made sure the code is working correctly by performing some simple tests. First we use the scale-dependent solver to solve for Λ CDM and compare to the standard L-PICOLA code. The agreement is found to be excellent (\ll % accuracy on all scales for $P(k)$).

Below we show comparisons of our code with results from true N -body simulations. To do this we created a module that reads in initial conditions from a given simulation and uses this to generate the displacement-fields which allow us to do a comparison without cosmic variance. In Fig. 2.11 we show a comparison of $P(k)$ for Λ CDM using L-PICOLA (with $n = 30$ time steps) compared to the results of the N -body code **RAMSES** [222]. The agreement is excellent on large scales, while for wavenumbers larger than $\sim k_{\text{Nyquist}}/4 \sim 0.7h/\text{Mpc}$ the results starts to deviate as we cannot resolve smaller scales. In the rest of this sub-section we show the results relative to Λ CDM for runs with modified gravity models.

The (friend-of-friend) halo finder used in the analysis below is **MatchMaker**⁴ and it was run with the linking-length $b = 0.2$. The errors bars in the mass function plots are Poisson errors. Since the simulations were started from the same initial conditions these errors should be considered an upper limit to the shot noise and that it is likely significantly smaller than that.

2.6.1.1 $f(R)$ gravity

The N -body simulation suite we used to test the $f(R)$ result of our code is taken from the modified gravity code comparison project [160] (run with the **ISIS** code [159]) and consists of a $N = 512^3$ particle simulation in a $B = 250\text{Mpc}/h$ box with a cosmology

⁴<https://github.com/damonge/MatchMaker>

defined by $\Omega_m = 0.269$, $h = 0.704$, $n_s = 0.966$ and $\sigma_8 = 0.8$. The two $f(R)$ models have $|f_{R0}| = 10^{-5}$ (F5) and $|f_{R0}| = 10^{-6}$ (F6). The $f(R)$ simulations were run with the same initial condition as the Λ CDM simulation.

In Fig. 2.12 we show a comparison of the result we get when using the true $f(R)$ growth-factor versus using the Λ CDM growth-factor in the simulations. For this plot we have used $n = 10$ time steps in the COLA simulations and we see a small difference in the power spectrum at $z = 0$. For $n > 20$ the results are pretty much indistinguishable which happens because the more time steps we take the less effect the COLA approximation has on the final results. For a small number of time steps the COLA approximation is more important and the difference in the results comes from the true growth-factor taking some screening into account leading to a small reduction in power on non-linear scales. We also see that we significantly overestimate the true power spectrum if we don't take screening of the fifth-force into account.

In Fig. 2.13 we show the fractional difference in the matter power spectrum for $f(R)$ with respect to Λ CDM for our simulations including screening compared to the results of full N -body simulations. The agreement is $\lesssim 2\%$ for F5 and $< 1\%$ for F6 up to $k \sim 3h/\text{Mpc}$.

In Fig. 2.14 we show the fractional difference in the velocity divergence power spectrum. The agreement is slightly worse than for the matter power spectrum with up to 5% deviation for F5 and up to 8% for F6. This is still a decent agreement compared to the enhancement with respect to Λ CDM which is up to $\sim 50\%$ for F5 and up to $\sim 30\%$ for F6.

In Fig. 2.15 we show the fractional difference in the halo mass function with respect to Λ CDM. The agreement is $\lesssim 2\%$ for all of the mass-range for F5, but for F6 we underestimate the enhancement of the mass function by approximately 5% for $M \lesssim 5 \cdot 10^{13} M_\odot/h$. This is the same as was found when using the screening method in full N -body simulations [164] and this can therefore be attributed to this approximation.

2.6.1.2 nDGP

The N -body simulation suite we used to test the nDGP version of our code was taken from [223] and was run with the ECOSMOG code [157]. The simulations have $N = 1024^3$ particles in a $B = 1024 \text{ Mpc}/h$ box with a WMAP9 cosmology defined by $\Omega_m = 0.281$, $h = 0.697$, and $n_s = 0.971$. The two nDGP simulations have $r_c H_0 = 0.75$ (nDGP2) and $r_c H_0 = 4.5$ (nDGP3). These values correspond to having the same value of $\sigma_8(z = 0)$ as the $f(R)$ models F5 and F6. The nDGP simulations were run with the same initial conditions as the Λ CDM simulation.

In Fig. 2.16 we show the fractional difference in the matter power spectrum for nDGP with respect to Λ CDM for our simulations with and without including screening compared to the results of full N -body simulations. The actual $P(k)$ starts to deviate from the N -body result already around $k \sim 0.5h\text{Mpc}^{-1}$ while the enhancement has good $< 2\%$ accuracy all the way up to $k \sim 3h/\text{Mpc}$.

In Fig. 2.17 we show the fractional difference in the velocity divergence power spectrum with respect to Λ CDM compared to the results of full N -body simulations. The agreement is $\lesssim 2\%$ up to $k \sim 2h/\text{Mpc}$ which is fairly small compared to the large signal relative to Λ CDM which is $\sim 7\%$ and $\sim 20\%$ for the two models respectively.

In Fig. 2.18 we show the fractional difference in the halo mass function with respect to Λ CDM. The agreement is $\lesssim 2\%$ for the entire mass-range $10^{12} - 10^{15}M_{\odot}/h$ probed by this simulation.

The COLA approach for these types of models works nearly as well as for Λ CDM and the computational cost is only $\sim 30\%$ larger and comes from computing the smoothed density-field at every time-step which requires one additional Fourier transform.

2.6.1.3 Dependence on the number of steps

The run-time of the code is roughly proportional to the number of time steps so the fewer steps we can use the better.

In Fig. 2.19 we show how the results for the matter power spectrum and halo mass function in our $f(R)$ simulations depend on the number of time steps. The enhancement of the power spectrum relative to Λ CDM is seen to have converged for $k < 1h/\text{Mpc}$ already when using $n = 10$ time steps for both models. To get a similar convergence on the smaller scales probed by our simulations we need to go up $\sim 20 - 30$ time steps. For the halo mass function we are within 5% of the $n = 30$ result across the whole mass range already at $n = 10$ and for $n = 20$ the results have practically converged.

In Fig. 2.20 we show the corresponding result for our nDGP simulations. The same type of behavior as we saw for $f(R)$ is also found here: $n = 10$ time steps is enough to get the power spectrum boost-factor (ratio with respect to Λ CDM) correct to $\sim 2\%$ up to $k = 1h/\text{Mpc}$ while to get full convergence we need ~ 20 time steps. The boost-factor for the halo mass function is within 4% of the $n = 30$ result in the $n = 10$ run across the whole mass range.

These results show that we can get away with using a fairly low number of time steps $n \sim 10 - 20$ and still maintain percent level accuracy in the boost-factors.

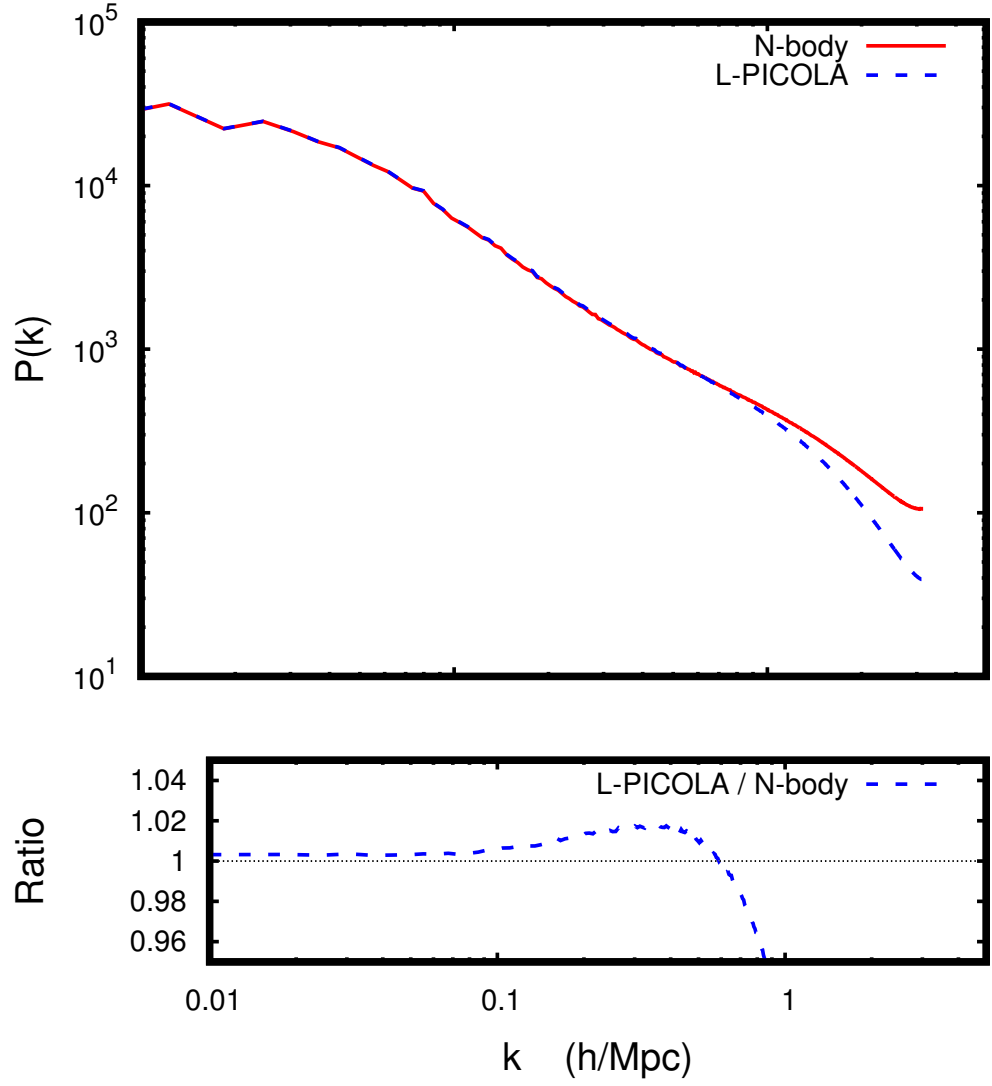


Figure 2.11: The matter power spectrum at $z = 0$ obtained from L-PICOLA using a fixed mesh with $N = 1024^3$ gridcells in a box of size $B = 1024 \text{ Mpc}/h$ and using $n = 30$ time steps compared to a high-resolution N -body simulation (RAMSES) using the same initial conditions.

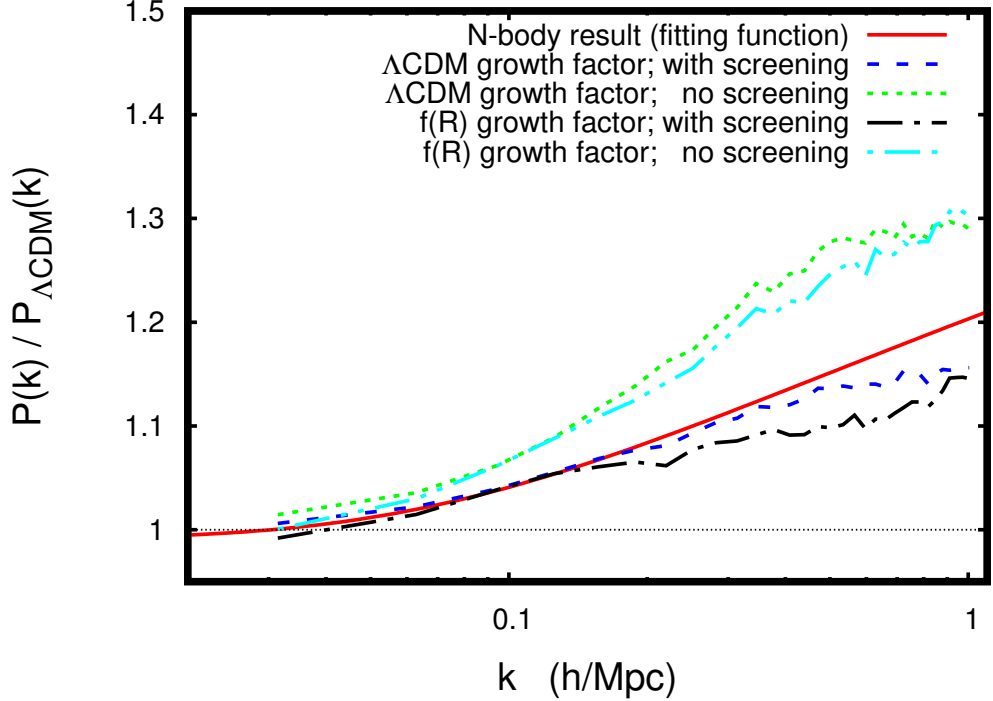


Figure 2.12: The ratio of the matter power spectrum in $f(R)$ to that in Λ CDM at $z = 0$ when using the true growth-factor(s) or using the Λ CDM ones plus the effect of including the screening method. Here we have used $n = 10$ time steps.

2.6.2 Adding massive neutrinos

We ran 5 COLA N -body simulations in a box of $B = 512$ Mpc/ h with $N = 512^3$ particles using the MG-PICOLA code. A smaller box of $B = 256$ Mpc/ h with the same number of particles was used to check the convergence of the results, and Figure 2.21 shows, through comparison to the full N -body simulations of [2], that the CDM matter power spectrum in our simulations can be trusted to percent level up to $k \sim 0.5 - 0.7$ h/Mpc. As found for modified gravity only, the relative enhancement of the power spectrum (i.e. when considering ratios of power spectra as shown in the figures below) is accurate to larger k values. The cosmological parameters for the simulations can be found in Table 2.1 and these are the same parameters as used by [2] where they performed combined massive neutrino and modified gravity simulations using a modified version of the simulation code `Gadget` [224, 158]. We will use these simulations to compare our results below. Ideally we would like to have run our simulations using exactly the same initial seed as the N -body simulations, however this was not available at the time we carried out this research and we leave such a detailed comparison to future work.

In Figure 2.22 we show the suppression of the power spectrum in Λ CDM as a function of neutrino mass in our simulations compared to the N -body results of [2]. We

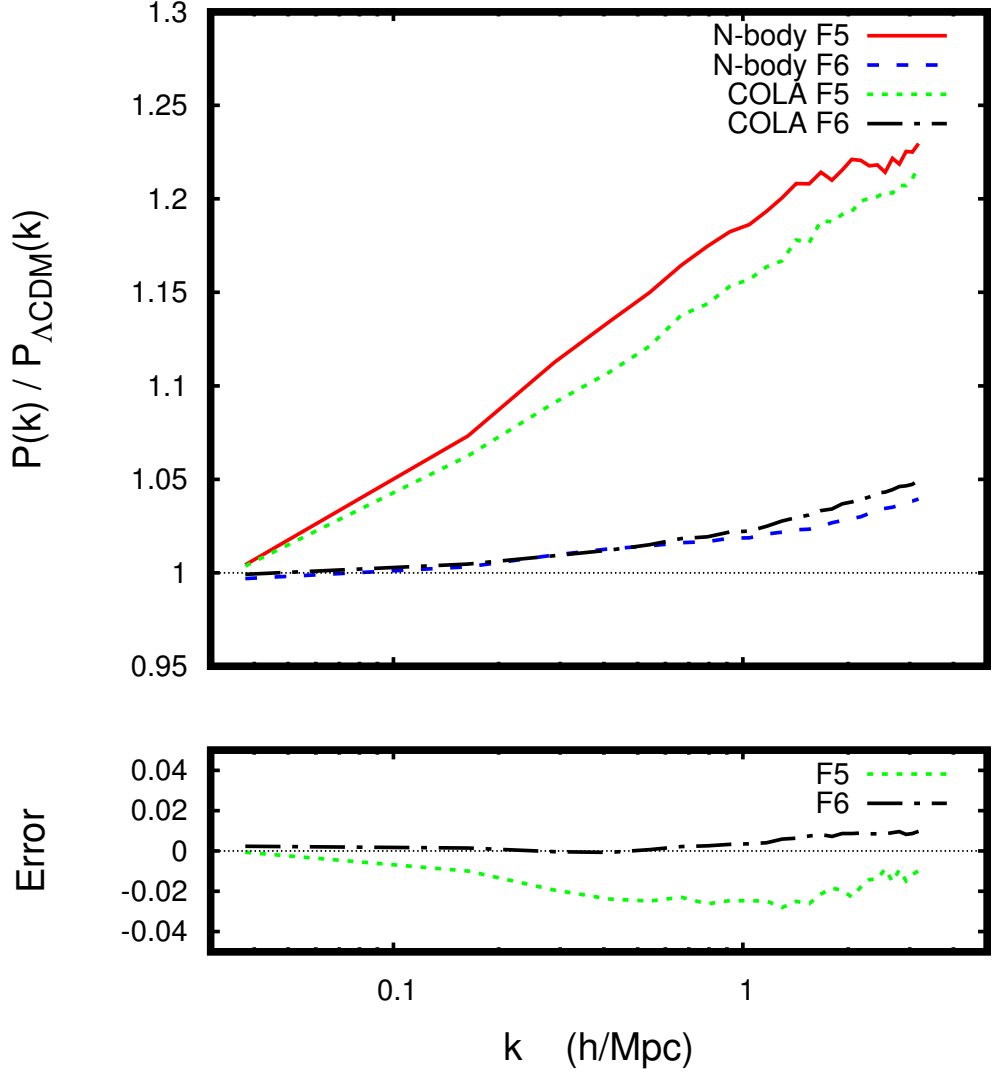


Figure 2.13: The ratio of the matter power spectrum in $f(R)$ to that in ΛCDM at $z = 0$. All simulations have been performed using the same initial conditions and we have used $n = 30$ time-steps in the COLA simulations. The N -body results correspond to modified gravity simulations solving the exact equations to get the fifth-force. For the COLA simulations we used the ΛCDM growth-factor. The lower panel shows $(P_{f(R)}/P_{\Lambda\text{CDM}})^{\text{COLA}} / (P_{f(R)}/P_{\Lambda\text{CDM}})^{N\text{-body}} - 1$.

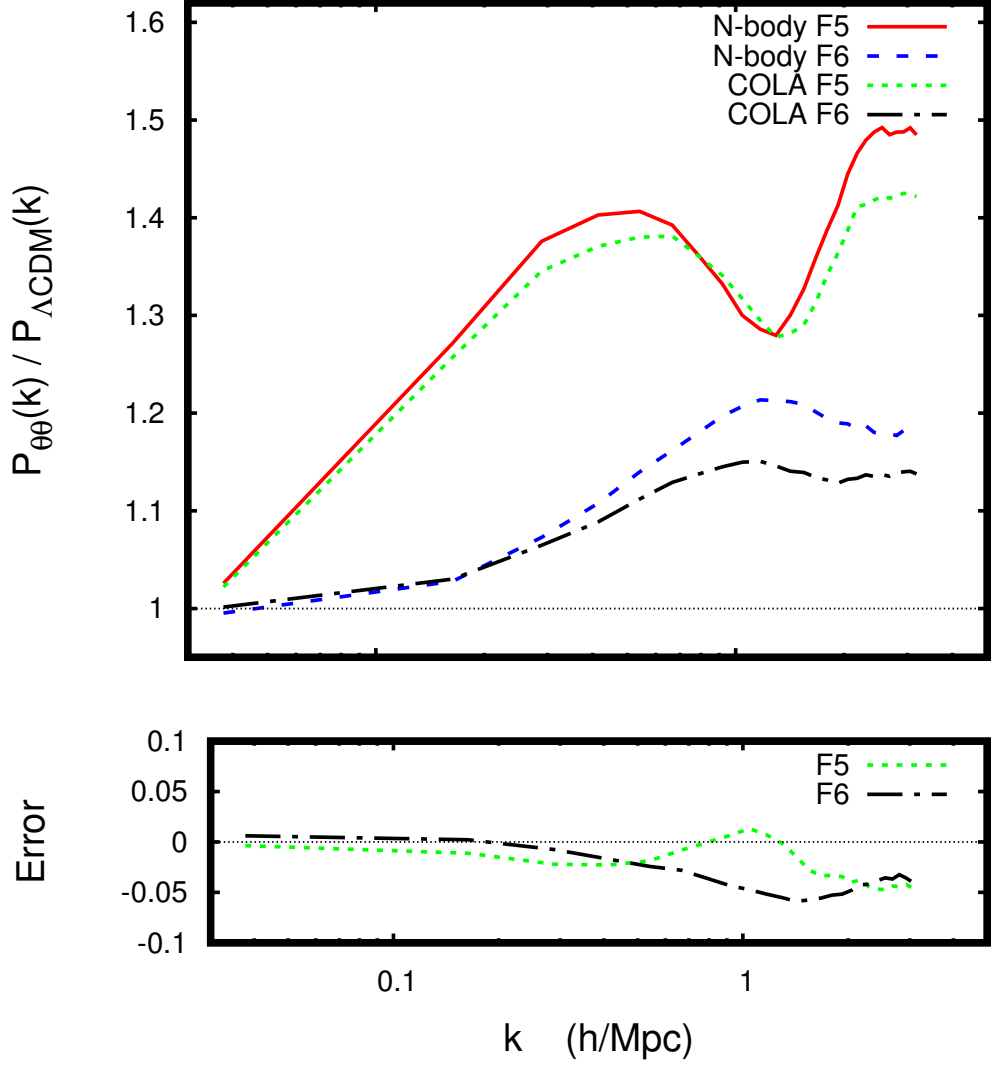


Figure 2.14: The ratio of the velocity divergence power spectrum in $f(R)$ to that in ΛCDM at $z = 0$. All simulations have been performed using the same initial conditions. The N -body results correspond to modified gravity simulations solving the exact equations to get the fifth-force. For the COLA simulations we used the ΛCDM growth-factor and $n = 30$ time-steps. The lower panel shows $(P_{f(R)}/P_{\Lambda\text{CDM}})^{\text{COLA}} / (P_{f(R)}/P_{\Lambda\text{CDM}})^{N\text{-body}} - 1$.

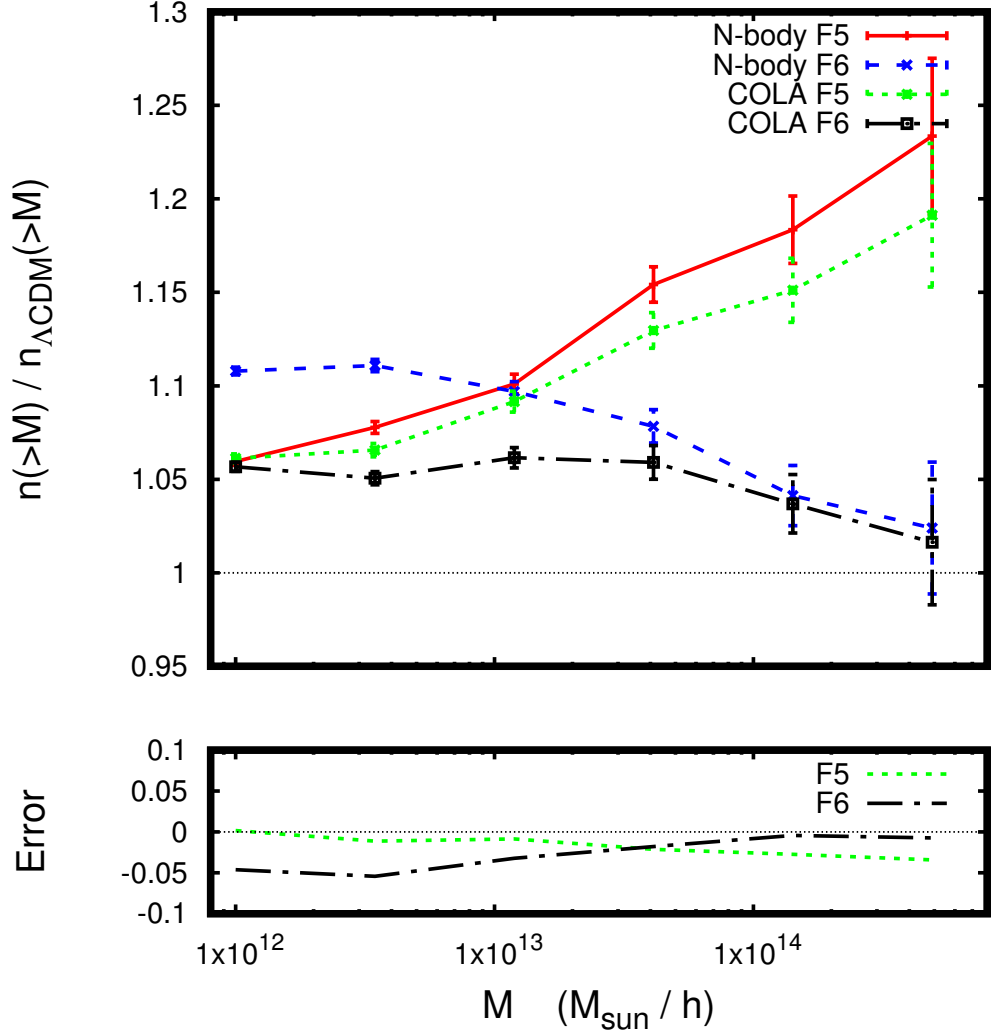


Figure 2.15: The ratio of the halo mass function at $z = 0$ in $f(R)$ to that in ΛCDM . All simulations have been performed using the same initial conditions. The N -body results correspond to modified gravity simulations solving the exact equations to get the fifth-force. For the COLA simulations we used the ΛCDM growth-factor and $n = 30$ time-steps. The error bars for the halo mass function are Poisson errors. The lower panel shows $(n_{f(R)}/n_{\Lambda\text{CDM}})^{\text{COLA}} / (n_{f(R)}/n_{\Lambda\text{CDM}})^{N\text{-body}} - 1$.

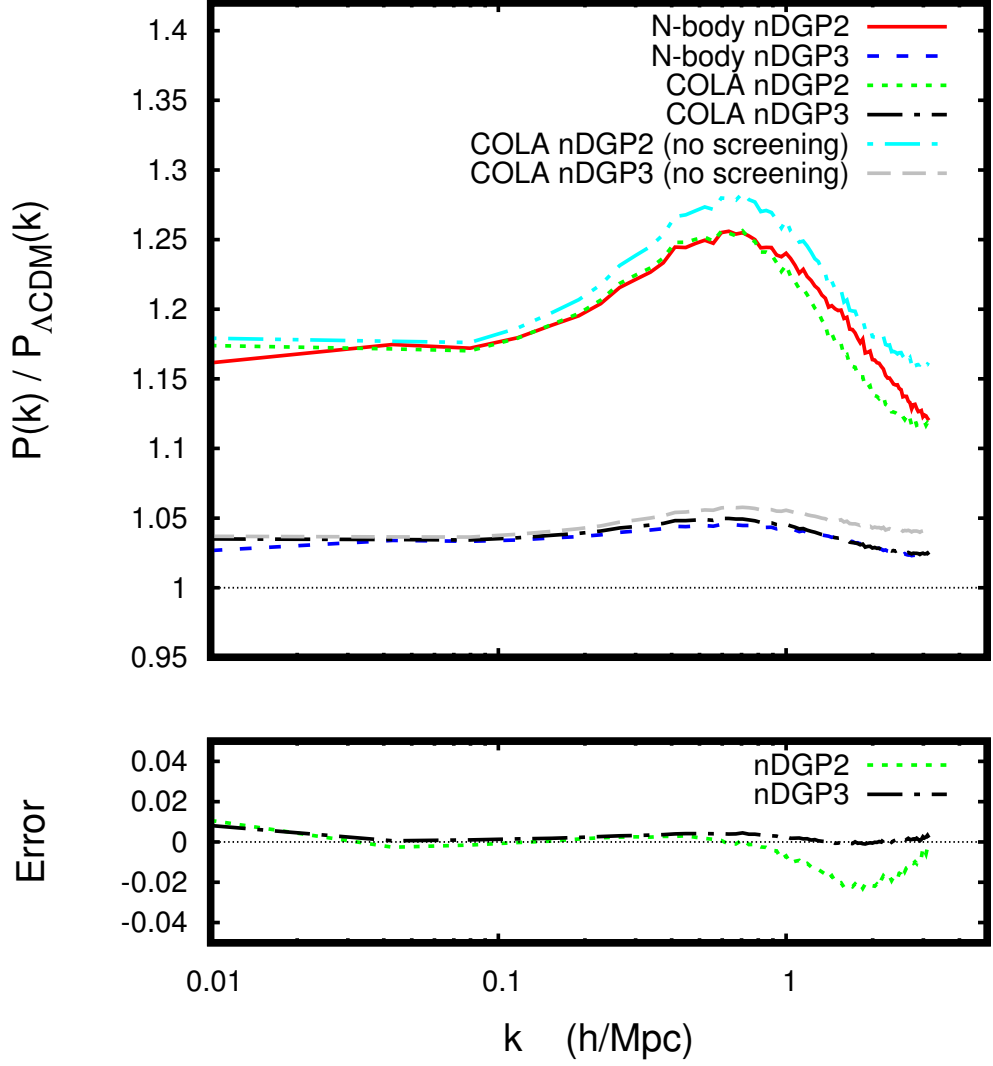


Figure 2.16: The ratio of the matter power spectrum at $z = 0$ in nDGP to that in ΛCDM . All simulations have been performed using the same initial conditions. The N -body results correspond to modified gravity simulations solving the exact equations to get the fifth-force. For the COLA simulations we used $n = 30$ time-steps and a smoothing radius of $R = 1 \text{ Mpc}/h$ to compute the screening factor for nDGP. The lower panel shows $(P_{\text{nDGP}}/P_{\Lambda\text{CDM}})^{\text{COLA}} / (P_{\text{nDGP}}/P_{\Lambda\text{CDM}})^{N\text{-body}} - 1$.

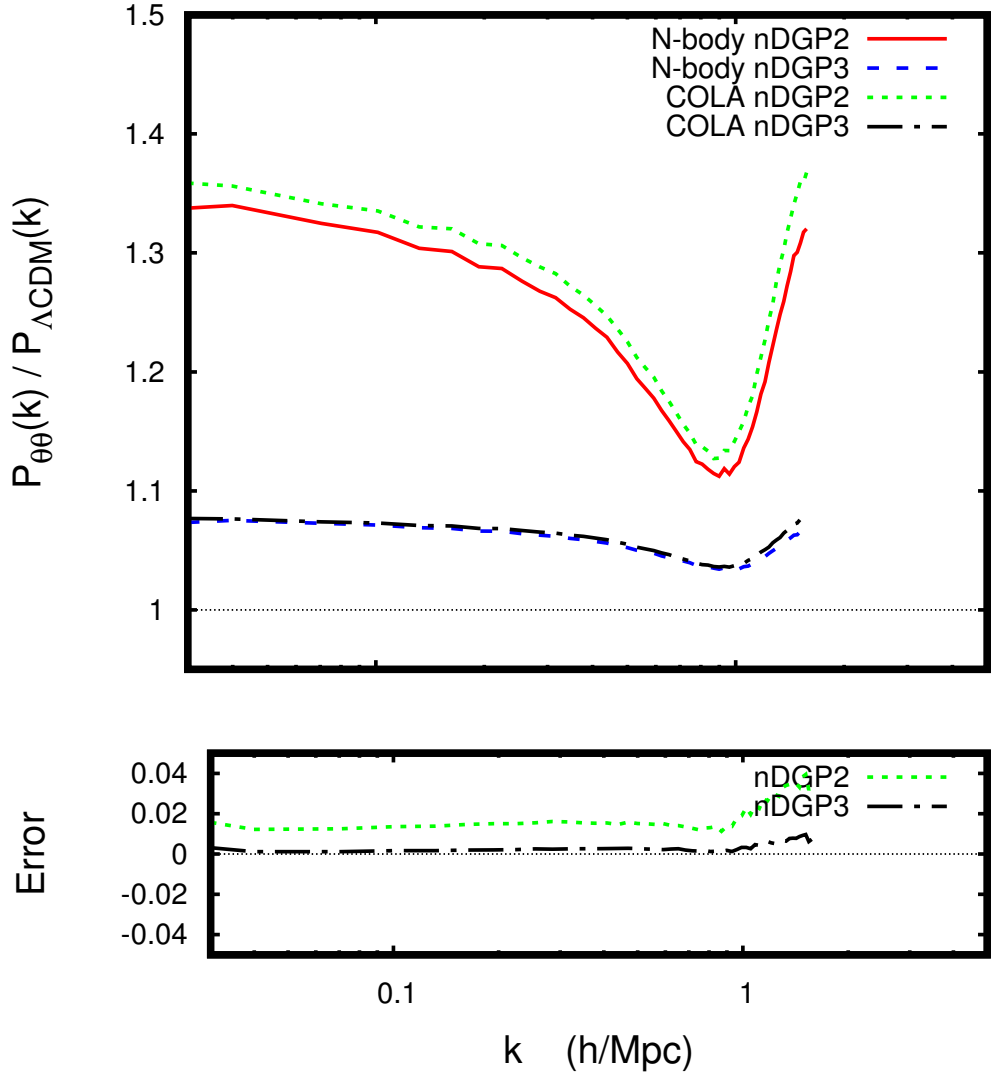


Figure 2.17: The ratio of the velocity divergence power spectrum in nDGP to that in ΛCDM at $z = 0$. All simulations have been performed using the same initial conditions and we have used $n = 30$ time-steps in the COLA simulations. The N -body results correspond to modified gravity simulations solving the exact equations to get the fifth-force. The lower panel shows $(P_{\text{nDGP}}/P_{\Lambda\text{CDM}})^{\text{COLA}} / (P_{\text{nDGP}}/P_{\Lambda\text{CDM}})^{N\text{-body}} - 1$.

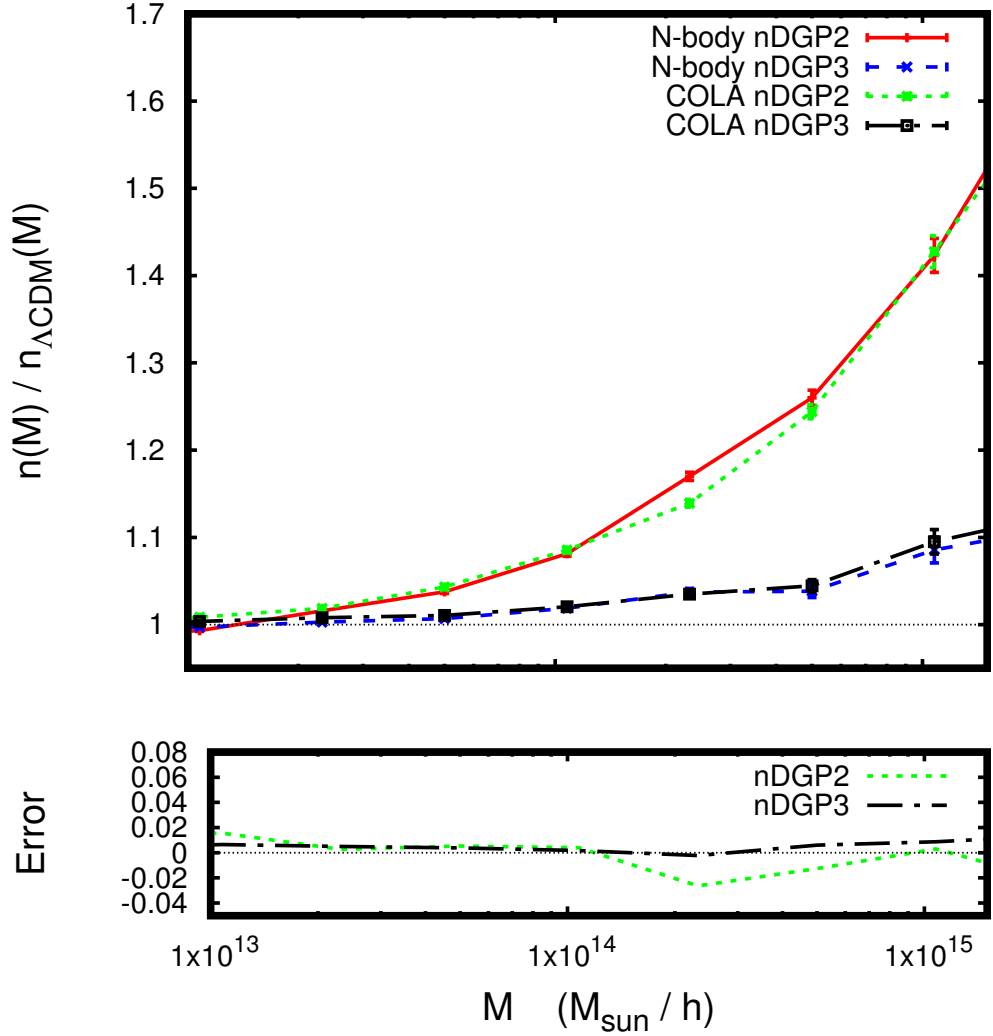


Figure 2.18: The ratio of the halo mass function in nDGP to that in ΛCDM at $z = 0$. All simulations have been performed using the same initial conditions and we have used $n = 30$ time-steps in the COLA simulations. The N -body results correspond to modified gravity simulations solving the exact equations to get the fifth-force. For the COLA simulations we used the smoothing radius of $R = 1 \text{ Mpc}/h$ to compute the screening factor for nDGP. The error bars for the halo mass function are Poisson errors. The lower panel shows $(n_{\text{nDGP}}/n_{\Lambda\text{CDM}})^{\text{COLA}} / (n_{\text{nDGP}}/n_{\Lambda\text{CDM}})^{\text{N-body}} - 1$.

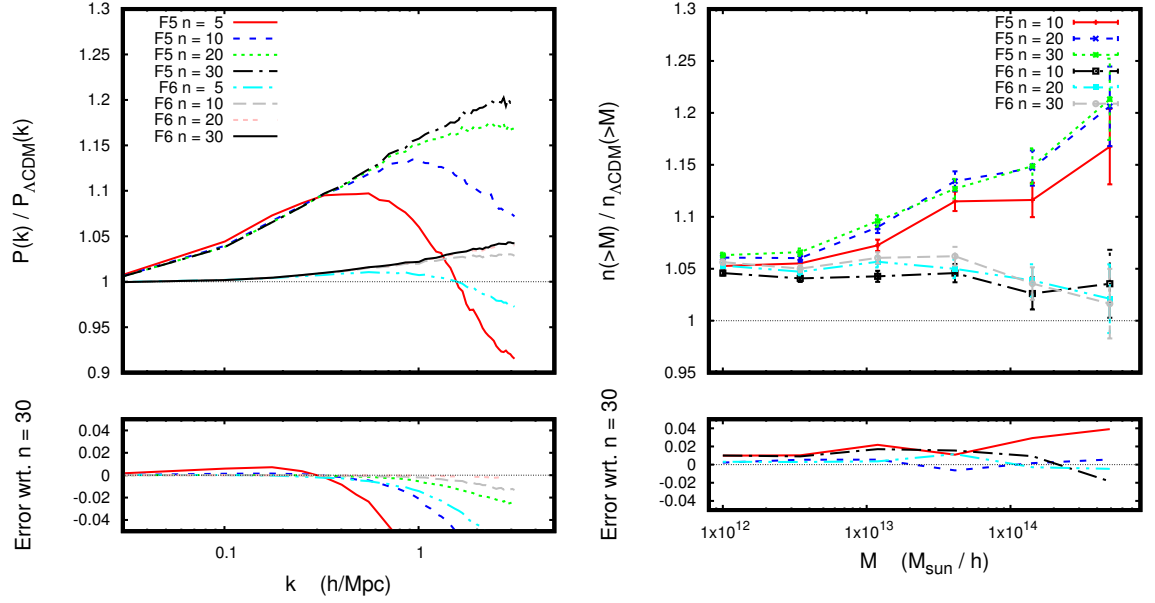


Figure 2.19: The ratio of the matter power spectrum (left) and halo mass function (right) in $f(R)$ to that in ΛCDM at $z = 0$ for the two $f(R)$ models F5 and F6 for different number of time steps. The ratio in each case is with respect to a ΛCDM simulation using the same number of steps. In the lower panel we show the fractional difference in the ratio with respect to the $n = 30$ run. The error bars for the halo mass function are Poisson errors.

m_ν (eV)	Ω_{CDM}	Ω_ν	σ_8 (ΛCDM)
0.0	0.2685	0.0	0.850
0.2	0.2637	0.0048	0.798
0.4	0.259	0.0095	0.752
0.6	0.2542	0.0143	0.712

Table 2.1: The cosmological parameters for the simulations performed for this chapter. Common to all simulations are $\Omega_{\text{m}} = 0.3175$, $\Omega_b = 0.049$, $n_s = 0.966$, $A_s = 2.215 \cdot 10^{-9}$ and $h = 0.671$.

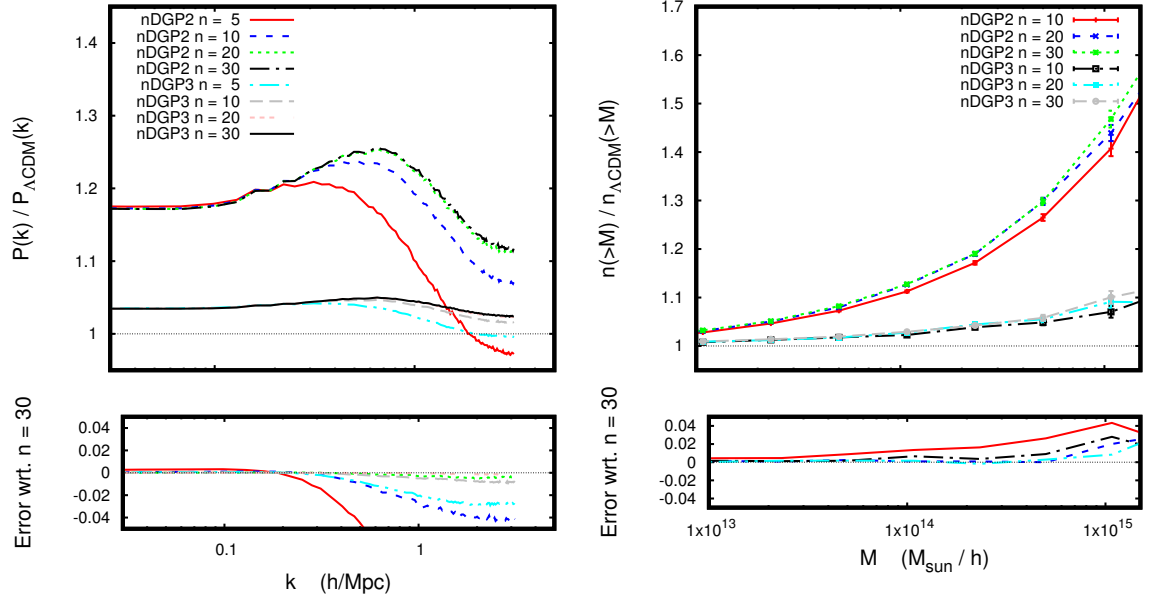


Figure 2.20: The ratio of the matter power spectrum (left) and halo mass function (right) in nDGP to that in ΛCDM at $z = 0$ for the two nDGP models nDGP2 and nDGP3 for different number of time steps. The ratio in each case is with respect to a ΛCDM simulation using the same number of steps. In the lower panel we show the fractional difference in the ratio with respect to the $n = 30$ run. The error bars for the halo mass function are Poisson errors.

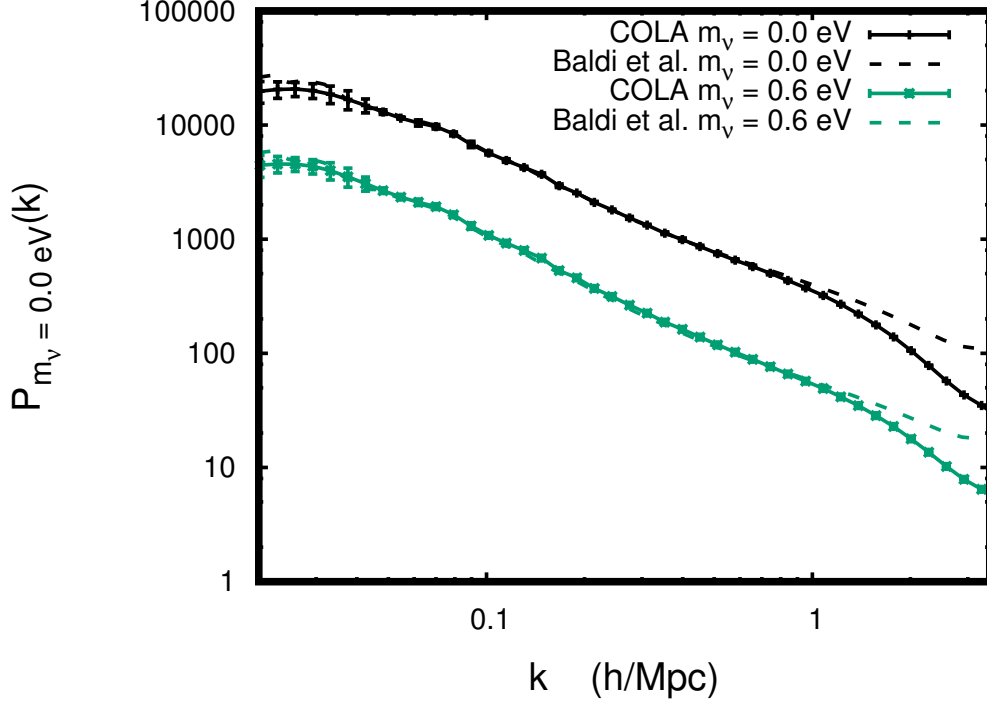


Figure 2.21: The CDM matter power spectrum $P(k, z = 0)$ for Λ CDM in our COLA simulations compared with the result of [2]. The $m_\nu = 0.6$ eV results are offset by a factor of 0.25.

show power spectrum results for both CDM+baryons $P_{\text{cb}}(k, z) = \langle |\delta_{\text{cb}}(\vec{k}, z)|^2 \rangle$ and the total matter content (CDM+baryons+massive neutrinos) $P_{\text{m}}(k, z) = \langle |f_{\text{cb}}\delta_{\text{cb}}(\vec{k}, z) + f_\nu\delta_\nu(\vec{k}, z)|^2 \rangle$.

In Figure 2.23 we show the results from simulations where we have both massive neutrinos and modified gravity. For the particular $f(R)$ model we study here having a total neutrino mass of $m_\nu \sim 0.4$ eV is seen to lead to a power spectrum very similar to that of a standard Λ CDM model with massless neutrinos. This illustrates the degeneracy of massive neutrinos (suppressing growth) and modified gravity (enhancing growth).

Our COLA implementation gives power spectrum (both for CDM and for the total matter) results that agree to $\lesssim 1\%$ accuracy for $k \lesssim 1$ h/Mpc to full N -body simulations of [2] for both Λ CDM and $f(R)$.

In Figures 2.24 and 2.25 we show the results for the halo mass function computed using **Rockstar** [225]. We note that the results of [2] were computed using a different halo-finder (**SUBFIND**) so the results are not directly comparable; however, the enhancement of the halo mass-function generally shows a good agreement.

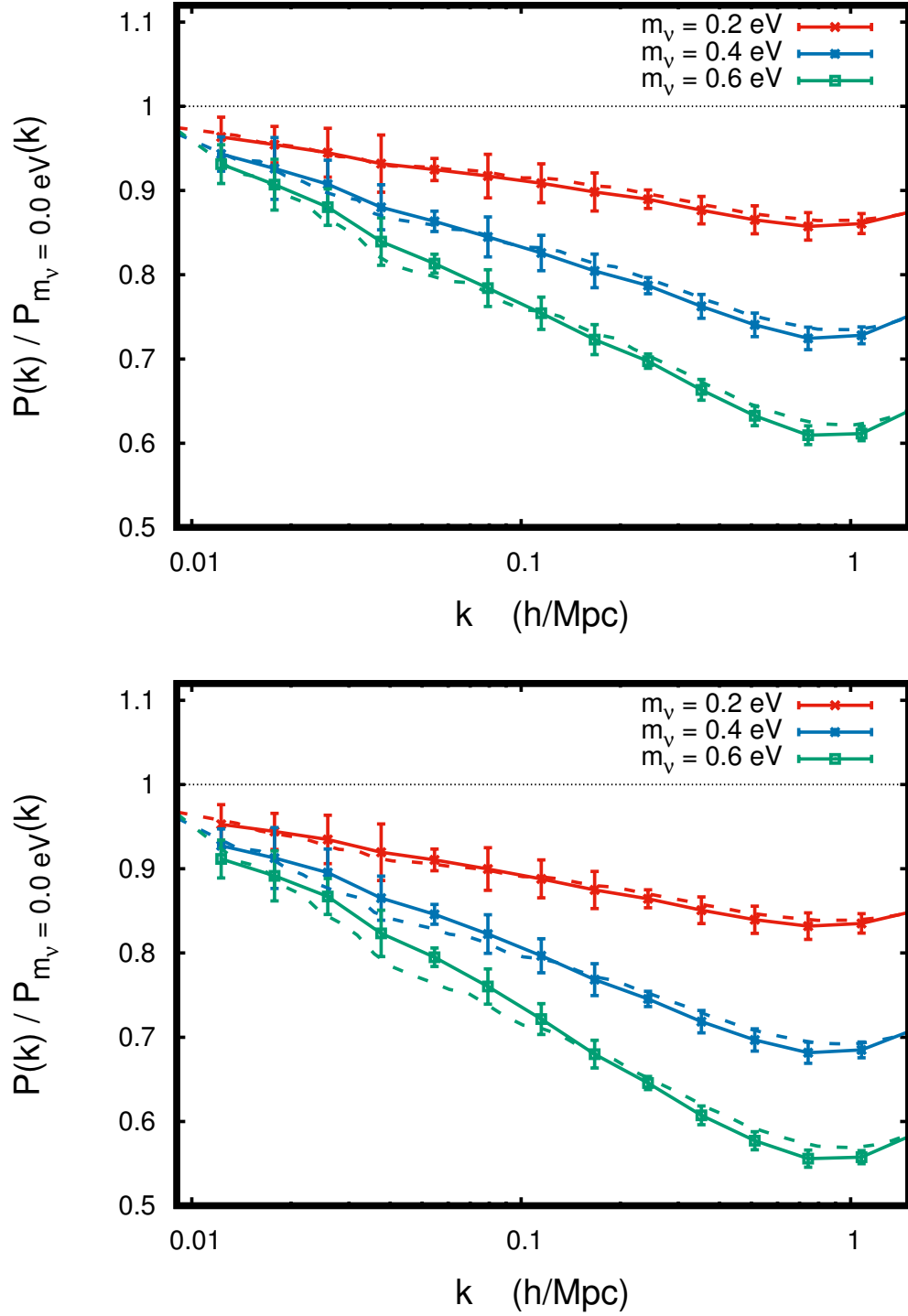


Figure 2.22: The matter power spectrum $P(k, z = 0)$ for several values of the sum of neutrino masses relative to the power spectrum with $m_\nu = 0.0$ for ΛCDM . The solid lines shows the result of [2]. The top panel shows the CDM+baryon power spectrum and the bottom panel shows the total power spectrum.

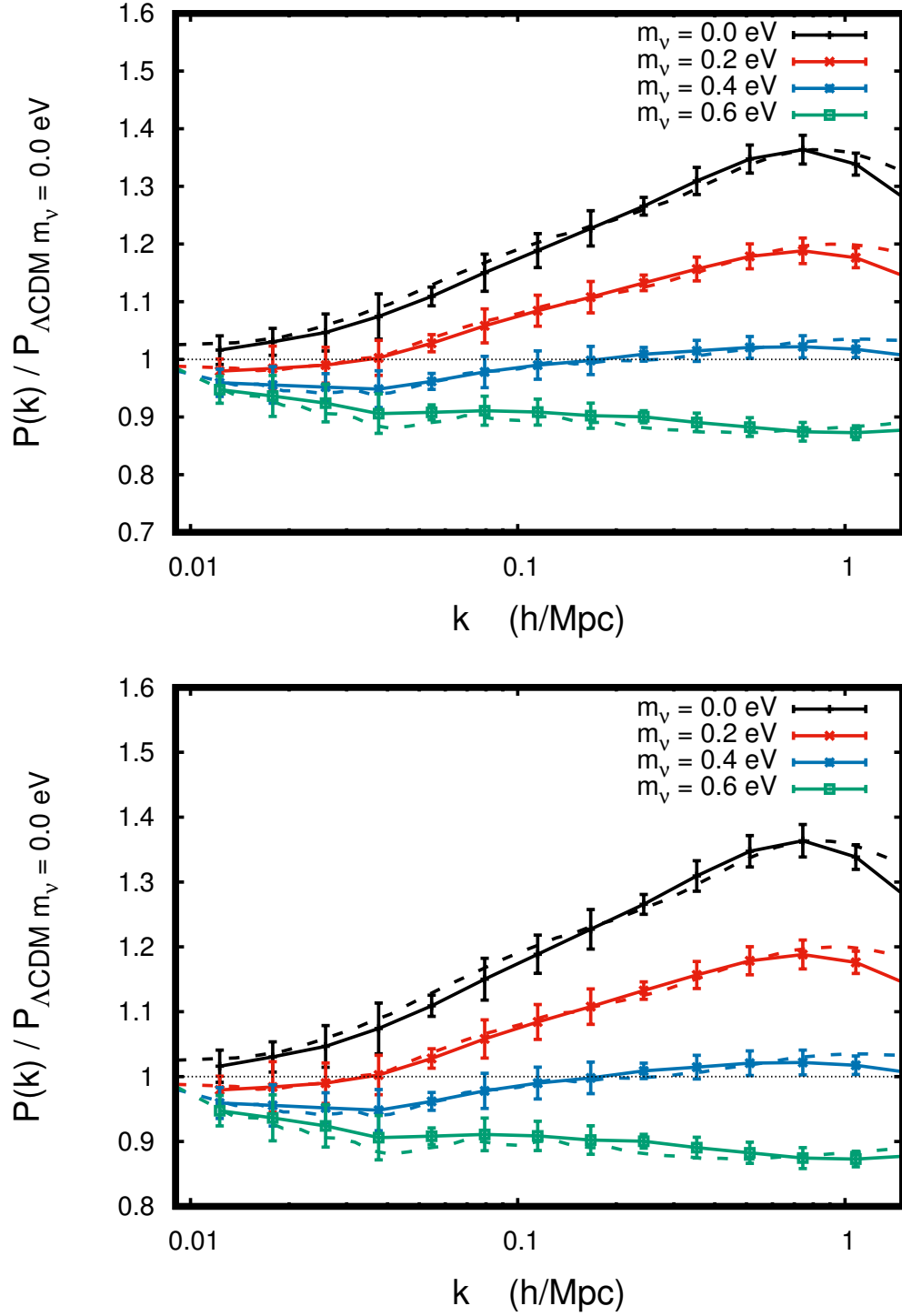


Figure 2.23: The matter power spectrum $P(k, z = 0)$ for several values of the sum of neutrino masses relative to the power spectrum with $m_\nu = 0.0$ for $f(R)$ gravity with $|f_{R0}| = 10^{-4}$. The solid lines shows the result of [2]. The top panel shows the CDM+baryon power spectrum and the bottom panel shows the total power spectrum.

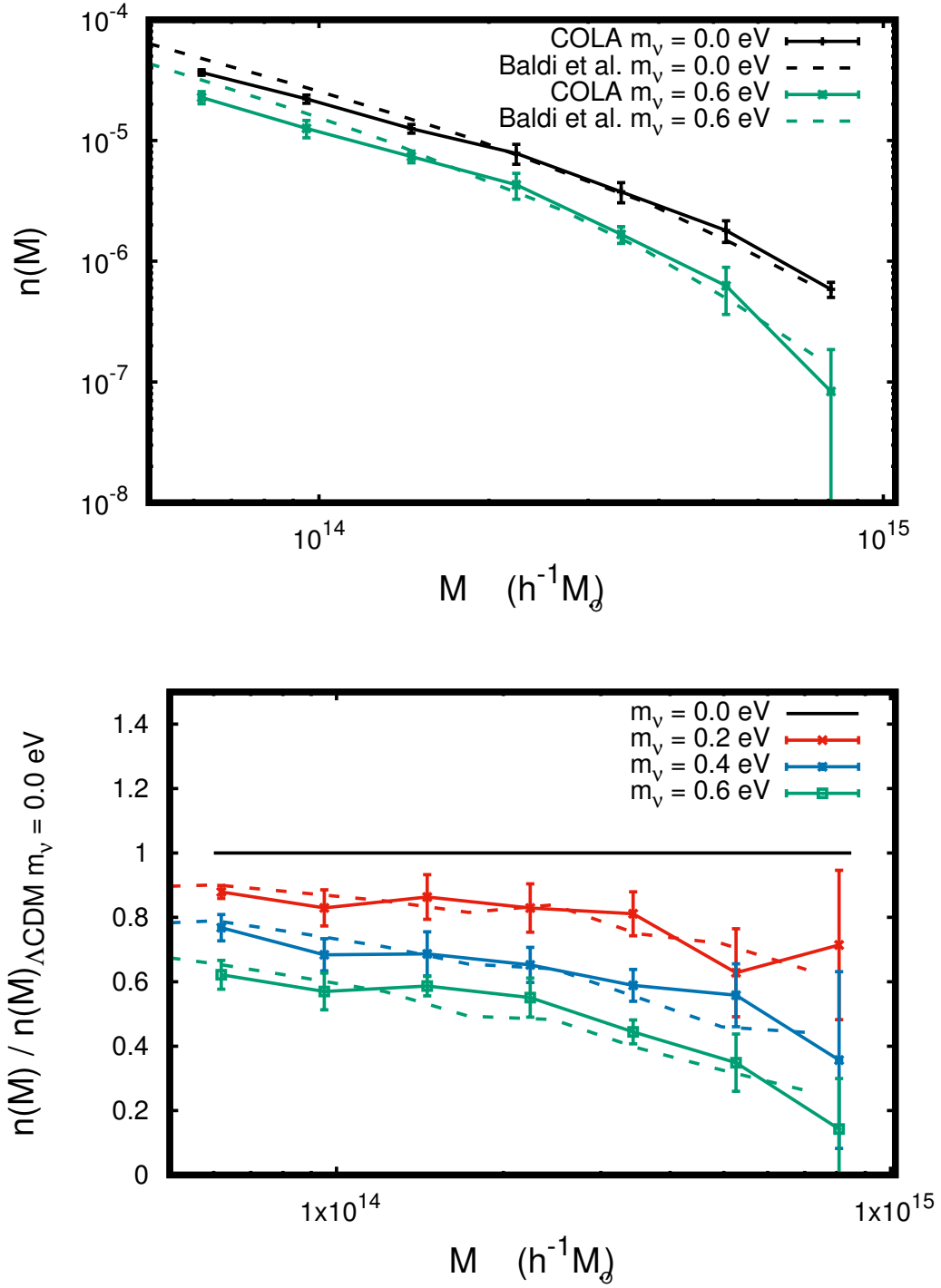


Figure 2.24: The halo mass-function $n(M, z = 0)$ for ΛCDM for several values of the sum of neutrino masses relative to the mass-function with $m_\nu = 0.0$. The dashed lines shows the results from [2].

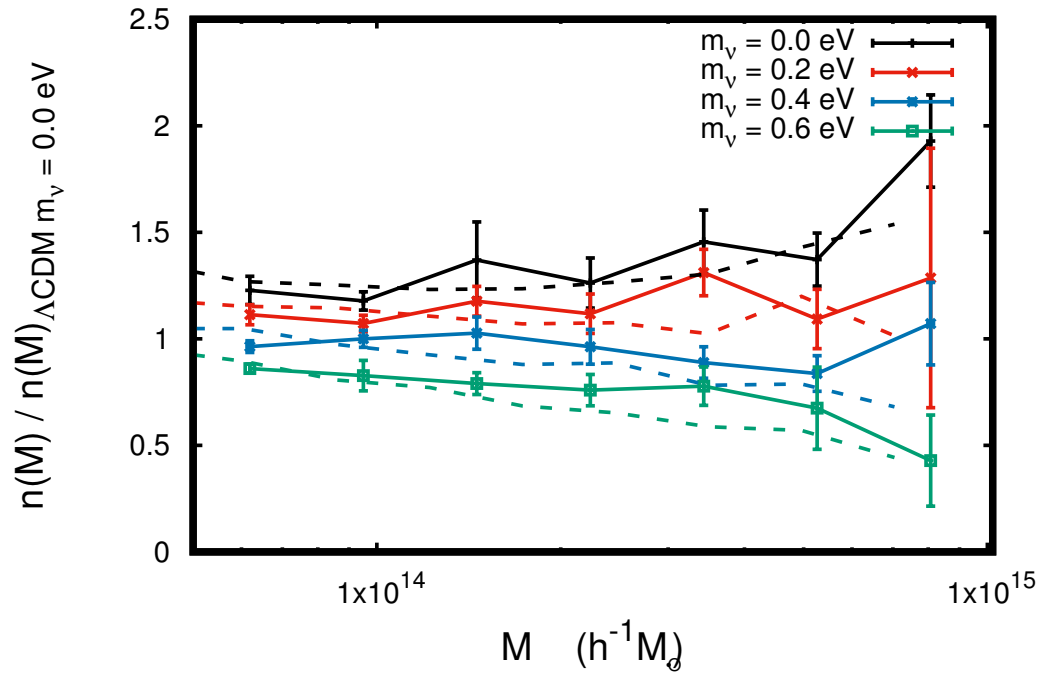


Figure 2.25: The halo mass-function $n(M, z = 0)$ for $f(R)$ for several values of the sum of neutrino masses relative to the mass-function in ΛCDM with $m_\nu = 0.0$. The dashed lines shows the results from [2].

Chapter 3

Dark matter redshift-space distortions with MG and m_ν

*The work in this chapter was carried out by the author and his supervisory team in collaboration with Hans Winther and Ben Bose. Ben Bose had previously written **MG-Copter**, which includes the effects of modified gravity. The author was responsible for implementing massive neutrinos in **MG-Copter**, producing the **MG-PICOLA** simulations used in this chapter, and fitting the RSD model to those simulations. Ben Bose assisted with the initial setup of **MG-Copter** and advised on its running. Hans Winther advised on the running of **MG-PICOLA**. All figures in this chapter were created by the author. The supervisory team provided direction and advice throughout.*

In this chapter, we extend the cosmological perturbation theory code **Copter** [141] to include the effects of massive neutrinos in addition to those of modified gravity allowing us to accurately model non-linear RSD in scenarios with Hu-Sawicki $f(R)$ gravity and non-zero neutrino masses. We build on **MG-Copter**, the modified version of **Copter** developed in [140], which is itself based on the approach presented in [139].

We validate this implementation against simulations using the COmoving Lagrangian Acceleration (COLA) method [226] and then investigate whether the degeneracy between the two effects is broken by RSD at the level of the dark matter field.

The chapter is organised as follows. In Section 3.1 we explain our implementation of massive neutrinos alongside modified gravity in the Standard Perturbation Theory (SPT) formalism and **MG-Copter** code. In Section 3.2, we show the results of tests validating our implementation against simulation results. Finally, in Section 3.3 we use our new implementation to investigate the degeneracy between massive neutrinos and modified gravity.

3.1 Implementation of massive neutrinos

In order to model the combined effect of modified gravity and massive neutrinos on real- and redshift-space power spectra with low computational expense, it is necessary to include both effects in a semi-analytical code such as **Copter** which computes large-scale structure observables using perturbation theory. For the redshift-space quantities, **Copter** depends on the TNS model of redshift-space distortions which is named after the authors of [146] (Taruya, Nishimichi, and Saito).

We have added support for massive neutrinos to the code **MG-Copter** developed in [140]. To do so, we could not use the same trick as for the implementation of modified gravity, where we merely added modified gravity effects to the computation of the SPT kernels and left the power spectra and first order growth factors as their Λ CDM selves. This is because massive neutrinos affect the growth of density perturbations at early times, unlike the modified gravity models we had considered previously. In our implementation, we follow the method of [212, 213] and include massive neutrinos at the level of the linear real-space power spectra P^L , $P_{\delta\theta,L} = f(k)P^L$, and $P_{\theta\theta,L} = f^2(k)P^L$ without modifying the SPT kernels. This allows us to take $P^L(k)$ and $f(k)$, with the effects of massive neutrinos included, from **CAMB** [105] (or **MGCAMB** [119, 120] for MG+ m_ν) as input to **MG-Copter**; note that a small modification to **CAMB**/**MGCAMB** is necessary to get scale-dependent growth rate $f(k)$ as output. This method for including massive neutrinos is general enough to handle the various hierarchies of neutrino mass eigenstates [227], but for simplicity in the results that follow we have modelled the massive neutrinos as a single massive eigenstate with mass m_ν and two massless eigenstates, such that the sum of masses $M_\nu = \sum_i m_i = m_\nu$.

The expressions for the 1-loop power spectra corrections in terms of the $z = 0$ linear power spectrum $P_0(k) = P^L(k, z = 0)$, applicable to cosmologies with massless neutrinos, were given in Section 1.5.1.1 by Eqs. (1.49)-(1.54). For our implementation, we want to take $P^L(k, z)$ and $f(k, z)$, with the effects of massive neutrinos included, at the intended **MG-Copter** output redshift from **CAMB**/**MGCAMB** and use these as input to **MG-Copter**. Therefore we need to rewrite the expressions for the 1-loop power spectra in terms of $P^L(k, z)$ instead of $P_0(k)$. Now that we are no longer using Λ CDM linear power spectra, we need to account for the scale-dependent growth when changing the epoch at which the linear power spectra are defined; $P_0(k) = P^L(k, z)[D_1(k, z = 0)/D_1(k, z)]^2$. As for massless neutrino cosmologies, the kernel for first order densities F_1 is simply the first order growth factor D_1 . Using $D_1(k, z) = F_1(k, z) = G_1(k, z)/f(k, z)$ we can show $P_0(k) = P^L(k, z)[D_1(k, z = 0)/F_1(k, z)]^2 = f^2(k, z)P^L(k, z)[D_1(k, z = 0)/G_1(k, z)]^2$. Let's look at the most complicated term first, $P_{\delta\theta}^{13}$. The full expression based on $P_0(k)$,

now accounting for the scale dependence of D_1 is

$$P_{\delta\theta}^{13}(k, z) = \frac{k^3}{(2\pi)^2} F_1(k, z) \frac{P_0(k)}{[D_1(k, z=0)]^2} \int_0^\infty r^2 \frac{P_0(kr)}{[D_1(kr, z=0)]^2} G_3(k, r, x, z) dr \\ + \frac{k^3}{(2\pi)^2} G_1(k, z) \frac{P_0(k)}{[D_1(k, z=0)]^2} \int_0^\infty r^2 \frac{P_0(kr)}{[D_1(kr, z=0)]^2} F_3(k, r, x, z) dr . \quad (3.1)$$

Using the above expressions, we can rewrite this in terms of $P^L(k, z)$ as

$$P_{\delta\theta}^{13}(k) = \frac{k^3}{(2\pi)^2} P^L(k, z) \int_0^\infty r^2 P^L(kr, z) f(k, z) f^2(kr, z) \frac{G_3(k, r, x)}{G_1(k) G_1^2(kr)} dr \\ + \frac{k^3}{(2\pi)^2} f(k, z) P^L(k, z) \int_0^\infty r^2 P^L(kr, z) \frac{F_3(k, r, x)}{F_1(k) F_1^2(kr)} dr . \quad (3.2)$$

In full generality, all the power spectra, growth rates, and SPT kernels should include the effects of massive neutrinos. However, if we assume that the quantities that are ratios of SPT kernels, e.g. $G_3(k, r, x)/[G_1(k)G_1^2(kr)]$, can be approximated by their massless neutrino form, then we only need to include the effects of massive neutrinos on $P^L(k)$ and $f(k)$, which can be done by **CAMB/MGCAMB**. Using this approach, we do not need to modify the computation of SPT kernels from the standard version of **MG-Copter**. The full list of expressions replacing Eqs. (1.49)-(1.54), starting with the 22 correction terms, are

$$P_{\delta\delta}^{22}(k) = 2 \frac{k^3}{(2\pi)^2} \int_0^\infty r^2 dr \int_{-1}^1 P^L(kr, z) P^L(k\sqrt{1+r^2-2rx}, z) \\ \times \frac{F_2^2(k, r, x)}{F_1^2(kr) F_1^2(k\sqrt{1+r^2-2rx})} dx , \quad (3.3)$$

$$P_{\delta\theta}^{22}(k) = 2 \frac{k^3}{(2\pi)^2} \int_0^\infty r^2 dr \int_{-1}^1 P^L(kr, z) P^L(k\sqrt{1+r^2-2rx}, z) \\ \times f(kr, z) f(k\sqrt{1+r^2-2rx}, z) \frac{G_2(k, r, x)}{G_1(kr) G_1(k\sqrt{1+r^2-2rx})} \\ \times \frac{F_2(k, r, x)}{F_1(kr) F_1(k\sqrt{1+r^2-2rx})} dx , \quad (3.4)$$

$$P_{\theta\theta}^{22}(k) = 2 \frac{k^3}{(2\pi)^2} \int_0^\infty r^2 dr \int_{-1}^1 P^L(kr, z) P^L(k\sqrt{1+r^2-2rx}, z) \\ \times f^2(kr, z) f^2(k\sqrt{1+r^2-2rx}, z) \frac{G_2^2(k, r, x)}{G_1^2(kr) G_1^2(k\sqrt{1+r^2-2rx})} dx , \quad (3.5)$$

while the 13 correction terms are

$$P_{\delta\delta}^{13}(k) = 2 \frac{k^3}{(2\pi)^2} P^L(k, z) \int_0^\infty r^2 P^L(kr, z) \frac{F_3(k, r, x)}{F_1(k) F_1^2(kr)} dr, \quad (3.6)$$

$$P_{\delta\theta}^{13}(k) = \frac{k^3}{(2\pi)^2} P^L(k, z) \int_0^\infty r^2 P^L(kr, z) f(k, z) f^2(kr, z) \frac{G_3(k, r, x)}{G_1(k) G_1^2(kr)} dr \\ + \frac{k^3}{(2\pi)^2} f(k, z) P^L(k, z) \int_0^\infty r^2 P^L(kr, z) \frac{F_3(k, r, x)}{F_1(k) F_1^2(kr)} dr, \quad (3.7)$$

$$P_{\theta\theta}^{13} = 2 \frac{k^3}{(2\pi)^2} P^L(k, z) \int_0^\infty r^2 P^L(kr, z) f^2(k, z) f^2(kr, z) \frac{G_3(k, r, x)}{G_1(k) G_1^2(kr)} dr. \quad (3.8)$$

Remember that in these expressions the only terms to contain massive neutrinos are P^L and f ; all of the kernels F_i and G_i are unmodified. The A and B terms written in Eqs. (1.116) and (1.117) are also computed as convolutions of two linear power spectra with kernels, and thus are rewritten using the same method as for P^{13} and P^{22} . We have implemented these equations in **MG-Copter**. Note that massive neutrinos were also added to the original **Copter** code in [228].

3.2 Validation

In order to validate our implementation of massive neutrinos in the **MG-Copter** code, we have tested its output against results from **MG-PICOLA**. In the legends of the figures that follow we shall refer to our modified **MG-Copter** code simply as **Copter**, and the **MG-PICOLA** code as **COLA**.

Throughout, we use paired-fixed **MG-PICOLA** simulations where we produce two simulations with fixed amplitudes, meaning the initial amplitudes of the Fourier modes of the density field are set to that of the ensemble average power spectrum, and paired, where the initial modes in the second simulation are mirrored compared to those of the first [198]. This procedure significantly reduces variance that arises from the sparse sampling of wavemodes without the need for averaging over a large number of density field realisations, and has been shown not to introduce a bias to the recovery of the mean properties of the Gaussian ensemble, despite the fixing introducing non-Gaussianity [199]. However, we also ran five additional **MG-PICOLA** simulations for each model with randomised realisations of the initial density field. The standard deviation in the power spectra of these additional five simulations is used for the error bars in the figures below unless explicitly stated otherwise. The modified gravity model considered here is the Hu-Sawicki $f(R)$ model, which has one free parameter $|f_{R0}|$ and we refer to $|f_{R0}| = 10^{-5}$

and $|f_{R0}| = 10^{-4}$ as F5 and F4 respectively. The velocity divergence field θ has been computed using the **DTFE** code [229]. The cosmological parameters used in this chapter are the same as in [2]; $h = 0.671$, $\Omega_m = 0.3175$, $\Omega_b = 0.049$, $A_s = 2.215 \times 10^{-9}$, and $n_s = 0.966$.

Note that a recent version update of **MGCAMB** improved the handling of massive neutrinos by including the effect of massive neutrinos in the computation of the time differential of the anisotropic stress for the radiation and photon components [121]. Although our results were produced using the previous version of **MGCAMB**, we have verified that for the parameters we use the difference in the linear power spectrum between the two versions is negligible.

We used the Gaussian form of the Fingers of God damping term. To fit σ_v , we minimised the likelihood first presented in Eq. (1.124) using the **python** package **SciPy**¹ [230], considering the first two multipoles from our paired-fixed **MG-PICOLA** simulations. We used the analytic expressions for the covariance matrix between the different multipoles $\text{Cov}_{l,l'}$ as given in Appendix C of [146]. Non-Gaussianity is not considered in this covariance but the expressions do include the effect of shot-noise. These expressions require the survey volume V_s and galaxy number density \bar{n}_g to be specified; we assume an ideal survey with $V_s = 10 \text{ Gpc}^3/h^3$ and $\bar{n}_g = 4 \times 10^{-3} h^3/\text{Mpc}$. Additionally, since we considered dark matter only, we set the linear bias b to unity. Note that we do not attempt to fit $|f_{R0}|$ and m_ν , or the base cosmological parameters, as this would require the loop integrals in Sec. 3.1 to be recomputed many times which would be prohibitively expensive. This problem has been overcome for the base cosmological parameters in the standard ΛCDM model using the **FFTLog** approach [231].

We first study the comparison between **MG-Copter** and **MG-PICOLA** in the real-space power spectra, in Figs. 3.1 to 3.3. Figure 3.1 shows the real-space non-linear power spectra at $z = 1$ computed with both **MG-PICOLA** and **MG-Copter**. We display the density auto-correlation $P_{\delta\delta}$, the velocity divergence auto-correlation $P_{\theta\theta}$, and the density-velocity divergence cross-correlation $P_{\delta\theta}$, in the form $k^{3/2}P_{ij}$ for ease of viewing, for GR, F5, and F4 each with 0.0eV, 0.06eV, and 0.2eV neutrinos. The error bars on the (paired-fixed) **MG-PICOLA** points are the standard deviation of the 5 additional (non-paired-fixed) **MG-PICOLA** simulations. In all cases, **MG-Copter** reproduces the results of the **MG-PICOLA** simulations very well up to the start of the quasi-non-linear scale around $k = 0.1 \text{ h/Mpc}$ where perturbation theory begins to break down. The agreement between **MG-Copter** and **MG-PICOLA** persists to larger k values for $P_{\theta\theta}$ and $P_{\delta\theta}$ than $P_{\delta\delta}$, which is consistent with the behaviour seen when **MG-Copter** was compared to full

¹Specifically, we used the `scipy.optimize.minimize` function.

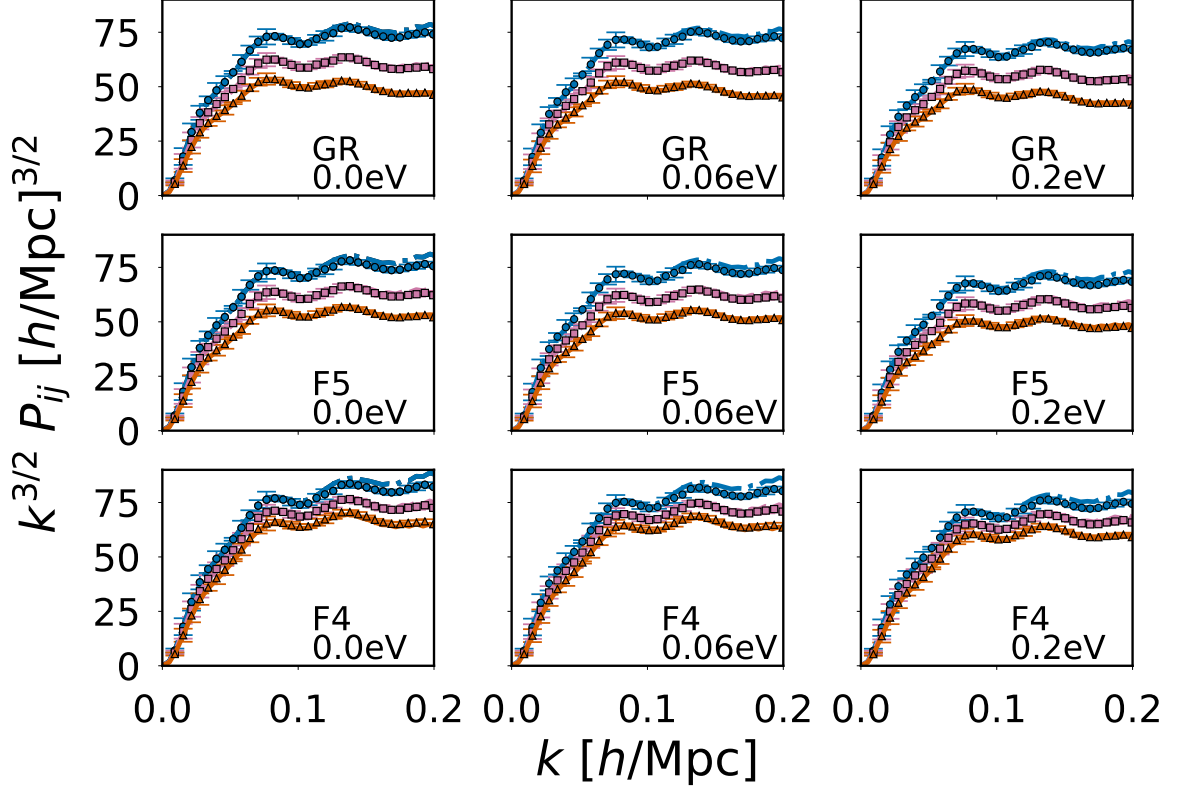


Figure 3.1: Real-space non-linear power spectra for various gravity models and neutrino masses at $z = 1$. Points represent the results of paired-fixed MG-PICOLA N -body simulations, while lines are the result of MG-Copter. The blue circles and dashed-dotted line give the density auto-correlated power spectra $P_{\delta\delta}$, the pink squares and dashed line give the density-velocity divergence cross-correlated power spectra $P_{\delta\theta}$, while the orange triangles and solid line give the velocity divergence auto-correlated power spectra $P_{\theta\theta}$.

N -body simulations in Fig. 10 of [140].

Figure 3.2 displays the same data but presented as the ratio of the full non-linear power spectra to their linear components, which helps to show where the modelling of non-linearities with MG-Copter becomes inaccurate. Figure 3.3 again shows the same data but presented as the ratio of the power spectra with and without massive neutrinos for both the 0.06eV and 0.2eV neutrinos. The scale up to which MG-Copter closely follows the results of the MG-PICOLA simulations is marginally improved due to taking the ratio between power spectra in two models.

Next, we look at the comparison between MG-PICOLA and MG-Copter with σ_v fitted to the MG-PICOLA simulations in the non-linear redshift-space power spectra in Figs. 3.4 to 3.6. Figure 3.4 shows the monopole P_0 and quadrupole P_2 of the redshift-space power spectra for GR, F5, and F4 gravity models each with 0.0eV, 0.06eV, and 0.2eV neutrinos. We display the results computed from paired-fixed MG-PICOLA simulations

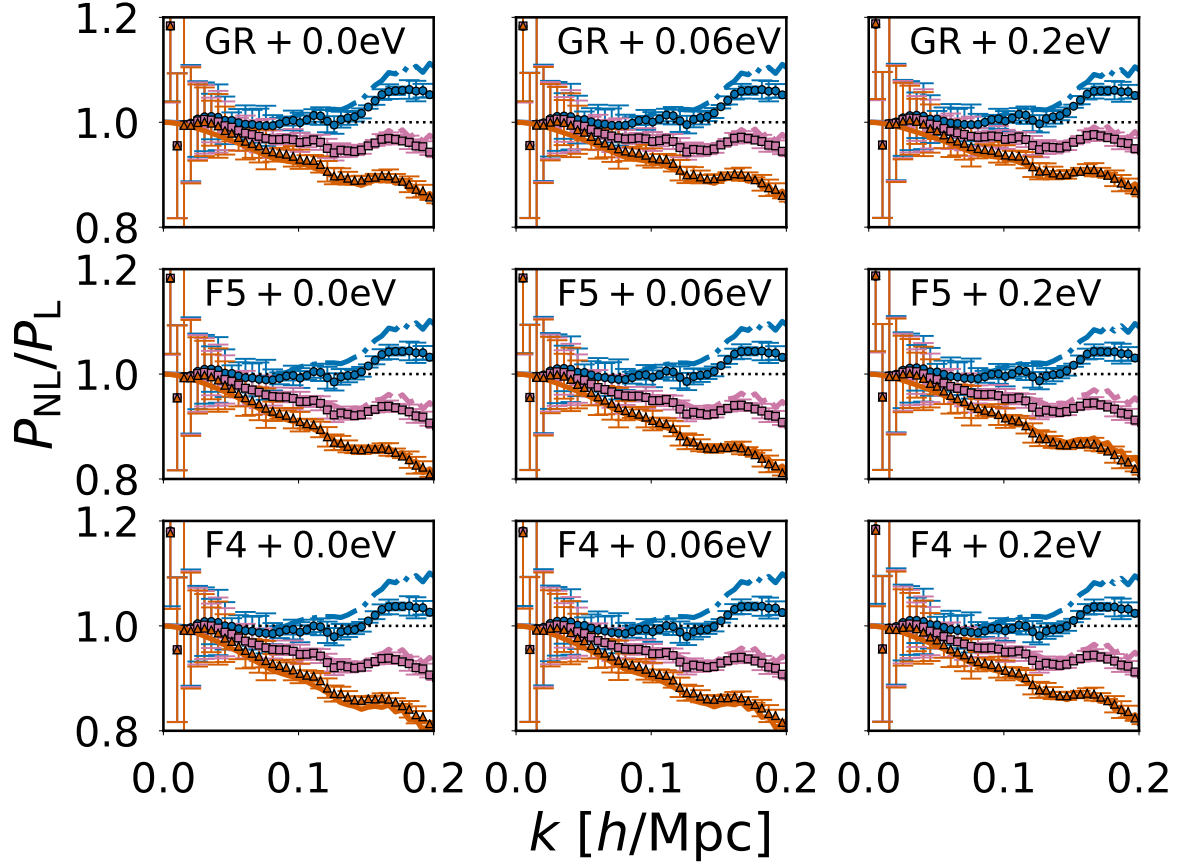


Figure 3.2: As in Fig. 3.1 but for the ratio of the real-space non-linear power spectra to their linear counterparts.

and **MG-Copter** with the TNS velocity dispersion parameter σ_v fitted to the **MG-PICOLA** simulations up to $k = 0.15 \text{ h/Mpc}$ in the form $k^{3/2}P_i(k)$; the figure includes the best-fitting values of σ_v (expressed in RSD displacement units Mpc/h) and the reduced χ^2 for each model $\chi_r^2 = -2 \ln \mathcal{L} / N_{\text{DoF}}$. The degrees of freedom $N_{\text{DoF}} = 2N_k - N_{\text{params}}$, and $N_{\text{params}} = 1$ since we are only fitting for σ_v . The error bars on the **MG-PICOLA** points are taken from the inverse covariance matrices used in the σ_v fitting procedure, whose computation is described at the end of Section 1.5.1.1. The σ_v fitting procedure prioritises recovering the monopole P_0 , and thus the agreement between **MG-Copter** and **MG-PICOLA** is slightly worse for the quadrupole P_2 . As expected, for each gravity model increasing the mass of the neutrinos leads to a decrease in the best-fitting value of σ_v and the quality of the fit increases, while for a fixed neutrino mass increasing the strength of the modification of gravity from GR to F5 and then F4 leads to an increase in the best-fitting value of σ_v and a slightly worse quality of fit. The reason for this behaviour is that enhancement to gravity leads to an increase in the velocities of galaxies around an overdensity, thus increasing the non-linear damping, while massive

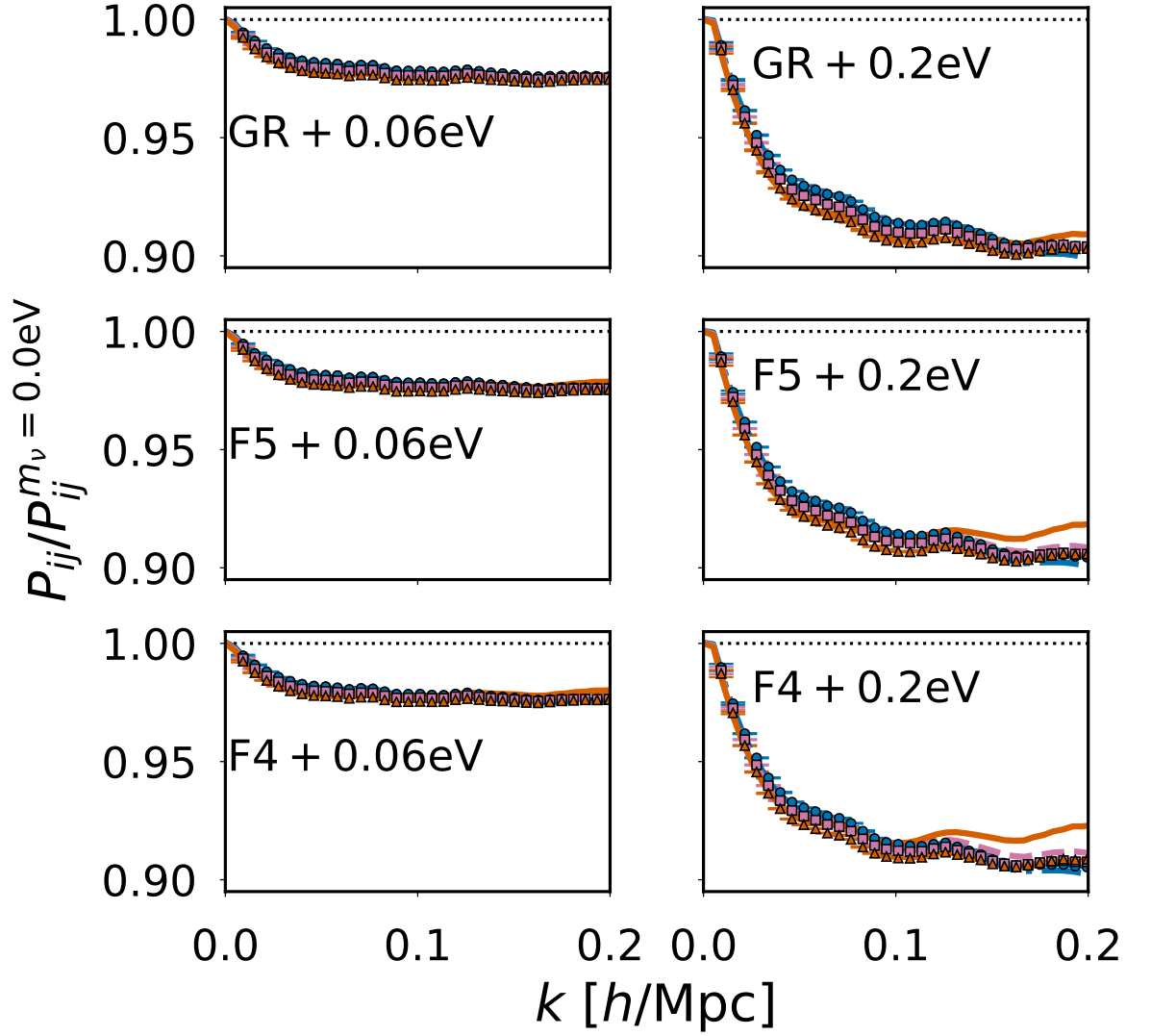


Figure 3.3: As in Fig. 3.1, but for the ratio of real-space non-linear power spectra with and without neutrino mass.

neutrinos have the opposite effect due to their suppression of structure formation. The quality of the fit is better when the non-linearity is smaller and vice versa. However, in all cases the quality of the fit of **MG-Copter** to **MG-PICOLA** is good up to quasi-non-linear scales.

Figure 3.5 displays the same data as Fig. 3.4 but presented as the ratio of the full non-linear multipoles to their linear counterparts computed with the Kaiser RSD model [144], while Fig. 3.6 presents the data of Fig. 3.4 as the ratio of the non-linear power spectra multipoles with and without massive neutrinos for both the 0.06eV and 0.2eV neutrinos. The error bars on the **MG-PICOLA** points in these two figures represent the standard deviation of the 5 additional **MG-PICOLA** simulations. As in real-space, the scale up to which **MG-Copter** closely follows the results of the **MG-PICOLA** simulations

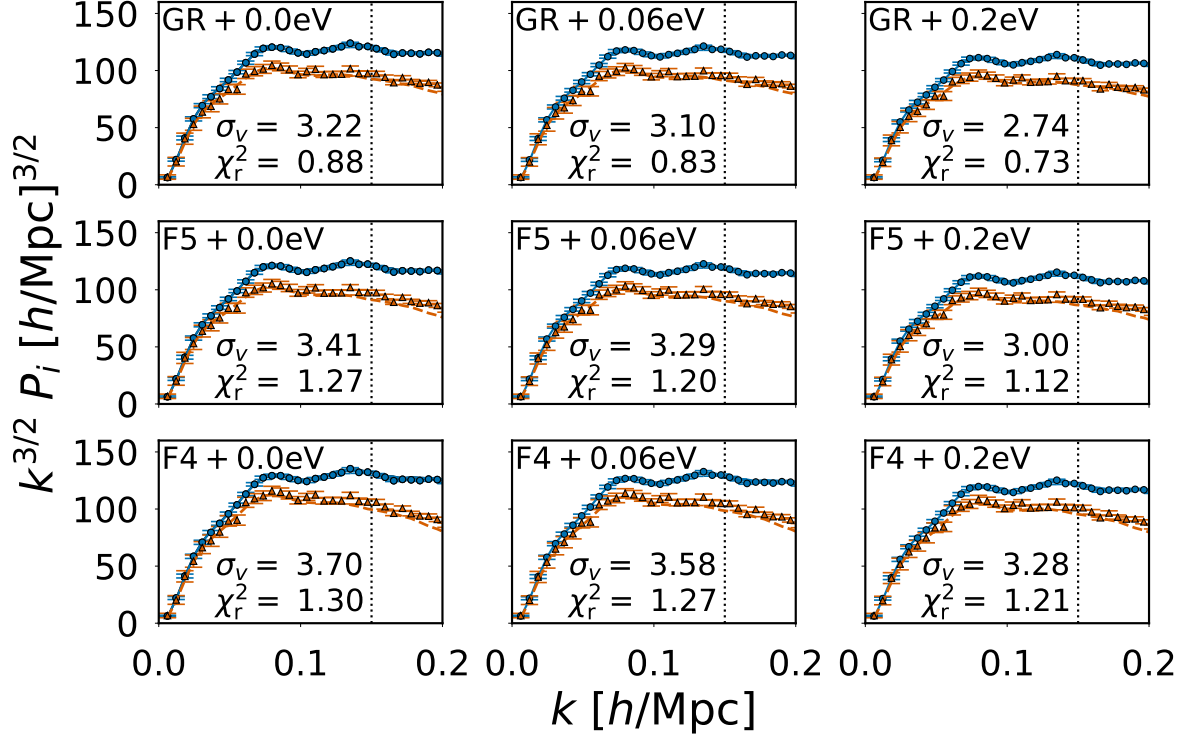


Figure 3.4: Redshift-space non-linear power spectra for various gravity models and neutrino masses at $z = 1$. Points represent the results of paired-fixed MG-PICOLA N -body simulations, while solid lines are the result of MG-Copter with velocity dispersion σ_v fitted to MG-PICOLA up to $k = 0.15 h/\text{Mpc}$, shown by the vertical dashed line. The error bars are those of an ideal survey with survey volume $V_s = 10 \text{ Gpc}^3/h^3$ and galaxy density $\bar{n}_g = 4 \times 10^{-3} h^3/\text{Mpc}^3$. The blue circles and solid line give the monopole P_0 , and the orange squares and dashed line give the quadrupole P_2 .

is slightly improved due to taking the ratio between power spectra in two models.

We also quantify the ability of MG-Copter to recover the redshift-space multipole results of MG-PICOLA through $\chi_{m_\nu}^2$; the difference between the redshift-space multipoles with and without neutrino mass. In Fig. 3.7 we display $\chi_{m_\nu}^2$ as a function of the maximum comparison scale k_{max} for GR, F5, and F4 each with 0.06eV and 0.2eV neutrinos at $z = 1$. Here, MG-Copter is fitted to the MG-PICOLA simulations up to k_{max} with the covariance computed assuming an ideal survey as described at the end of Section 1.5.1.1. The agreement in $\chi_{m_\nu}^2$ between MG-PICOLA and MG-Copter fitted to MG-PICOLA is excellent in all cases. This implies that MG-Copter with σ_v fitted to simulations is capable of capturing the effect of massive neutrinos accurately.

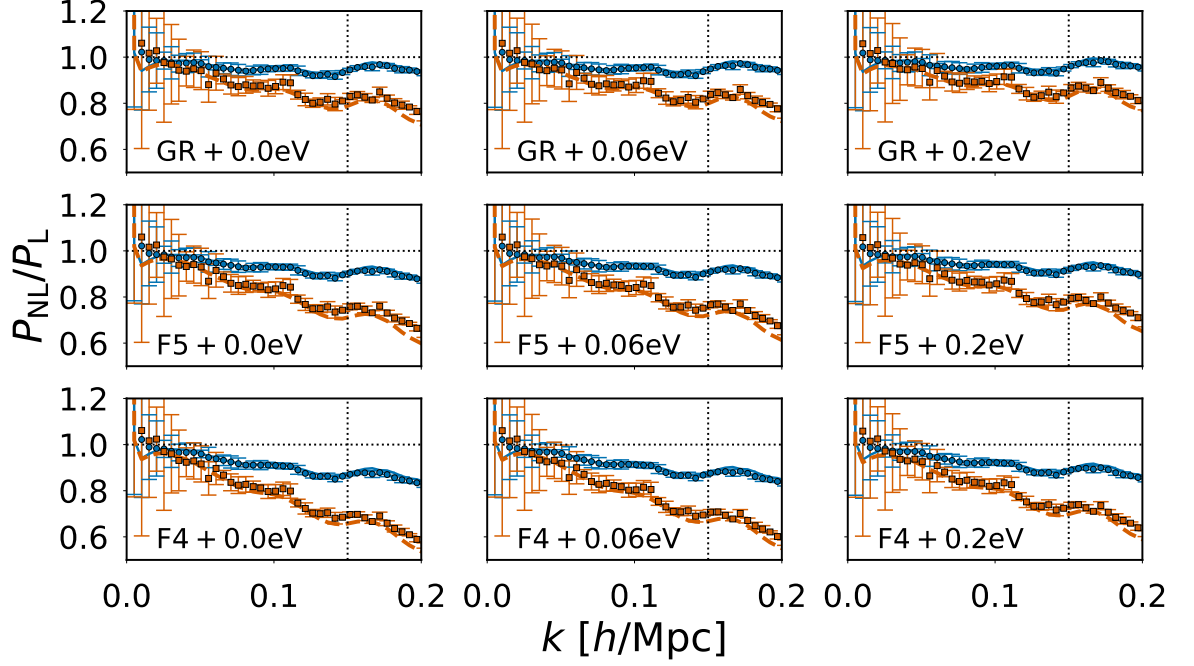


Figure 3.5: As in Fig. 3.4 but for the ratio of the redshift-space power spectrum multipoles to their linear (Kaiser) counterparts. The error bars on the MG-PICOLA points represent the standard deviation of the five additional MG-PICOLA simulations.

3.3 Degeneracy

With the inclusion of modified gravity and massive neutrinos in **MG-Copter** the degeneracy between the two effects can be investigated. For this investigation, we again used the Gaussian form of the Fingers of God damping term. To fit σ_v , we follow the same procedure as in Sec. 3.2, but we want to model a slightly more realistic scenario, so we assume a DESI-like survey with V_s and \bar{n}_g as given in Table 3.1 and redshift bin width $\Delta z = 0.2$. These values are computed using the information for emission line galaxies (ELGs) in Table V of [1].

z	V_s (Gpc^3/h^3)	\bar{n}_g (h^3/Mpc^3)
0.5	3.40	2.95×10^{-4}
1.0	7.68	5.23×10^{-4}
1.5	10.14	1.71×10^{-4}

Table 3.1: Survey parameters for a DESI-like survey computed from the information for emission line galaxies (ELGs) in Table V of [1]. These parameters are used in the computation of the covariance matrices for fitting σ_v in **MG-Copter** in the study of the degeneracy in Section 3.3.

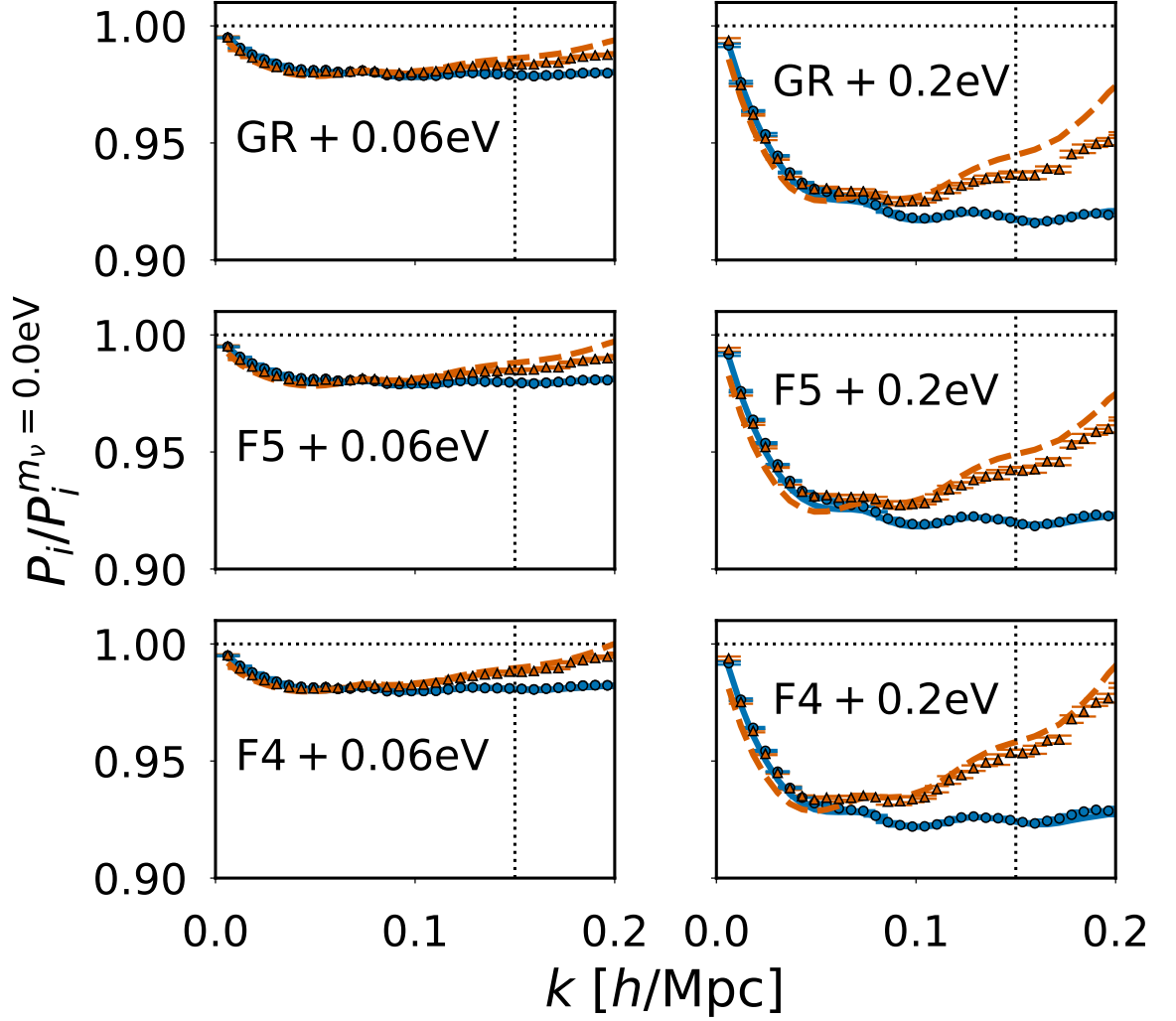


Figure 3.6: As in Fig. 3.4, but for the ratio of redshift-space non-linear power spectra with and without neutrino mass. The error bars on the MG-PICOLA points represent the standard deviation of the five additional MG-PICOLA simulations.

3.3.1 Real- and redshift-space

We start by studying the degeneracy between modified gravity and massive neutrinos in real space.

In Fig. 3.8 we display the ratio of real-space power spectra in F4 gravity with 0.06eV neutrinos in the left panel and 0.2eV neutrinos in the right panel to a fiducial model which we take to be GR with 0.06eV neutrinos at $z = 1$. We show results for the density auto-correlation $P_{\delta\delta}$, the velocity divergence auto-correlation $P_{\theta\theta}$, and the density-velocity divergence cross-correlation $P_{\delta\theta}$. The results of paired-fixed MG-PICOLA simulations and of MG-Copter are plotted. The error bars on the MG-PICOLA results are computed using the standard deviation over the five additional simulations. In all cases, the results of MG-Copter agree well with those of MG-PICOLA up to quasi-non-

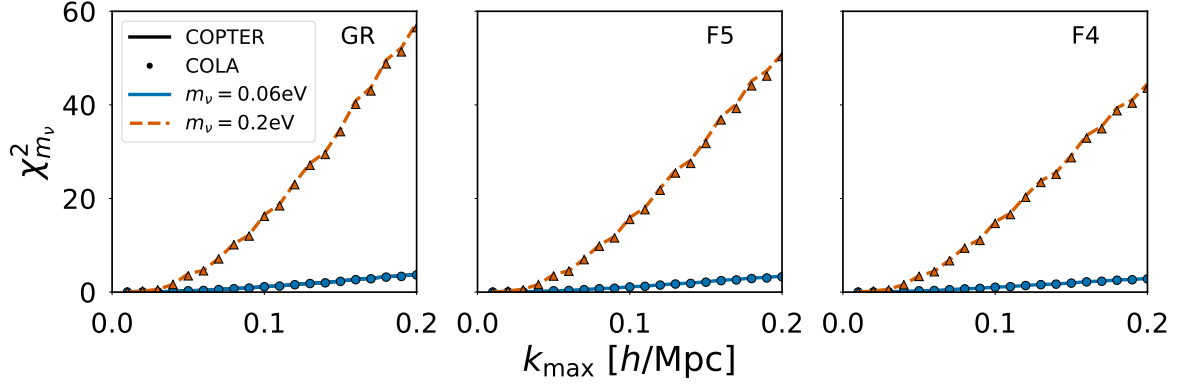


Figure 3.7: Difference between the redshift-space multipoles with and without neutrino mass $\chi_{m_\nu}^2$ as a function of the maximum scale k_{max} at $z = 1$ for GR in the left panel, F5 in the middle panel, and F4 in the right panel. Points represent the results of paired-fixed MG-PICOLA N -body simulations, while solid lines are the result of MG-Copter with velocity dispersion σ_v fitted to MG-PICOLA up to $k = k_{\text{max}}$. Blue data corresponds to $m_\nu = 0.06\text{eV}$, and orange to $m_\nu = 0.2\text{eV}$.

linear scales around $k = 0.1 \text{ h/Mpc}$. The left panel, where the neutrino masses are the same in both GR and F4, shows the scale-dependent enhancement of the real-space power spectra provided by F4 gravity. However, when heavier neutrinos are added to the F4 case, as in the right panel, this enhancement is opposed by the suppression effect of the massive neutrinos. Indeed, the right panel shows that $P_{\delta\delta}$ is a poor probe to distinguish between GR with 0.06eV neutrinos and F4 with 0.2eV neutrinos in this particular case. However, the two models remain distinguishable in $P_{\delta\theta}$ and $P_{\theta\theta}$, showing that velocity information has the potential to break the degeneracy between modified gravity and massive neutrinos. This was recently shown using the results of full N -body simulations [127]. However, neither $P_{\delta\theta}$ nor $P_{\theta\theta}$ can be measured directly by observations at high z (peculiar velocities can only be measured at low z when we can assume an object is in the same Hubble flow patch as us). Instead, it is necessary to extract the velocity information that is encoded within redshift-space distortions, and it is to this we turn our attention. We shall refer to GR with 0.06eV neutrinos and F4 with 0.2eV neutrinos as our two degenerate models.

In Fig. 3.9 we plot the redshift-space monopole and quadrupoles in F4 gravity with 0.2eV neutrinos normalised to GR with 0.06eV neutrinos computed with both MG-Copter and MG-PICOLA. For each model the MG-Copter result has been produced by fitting σ_v to the paired-fixed MG-PICOLA simulation up to $k = 0.15 \text{ h/Mpc}$ with the covariance computed assuming a DESI-like survey as detailed at the end of Section 1.5.1.1. The error bars on the MG-PICOLA results are computed using the standard deviation over five simulations with a boxsize of $1024 \text{ Mpc}/h$ for each model.

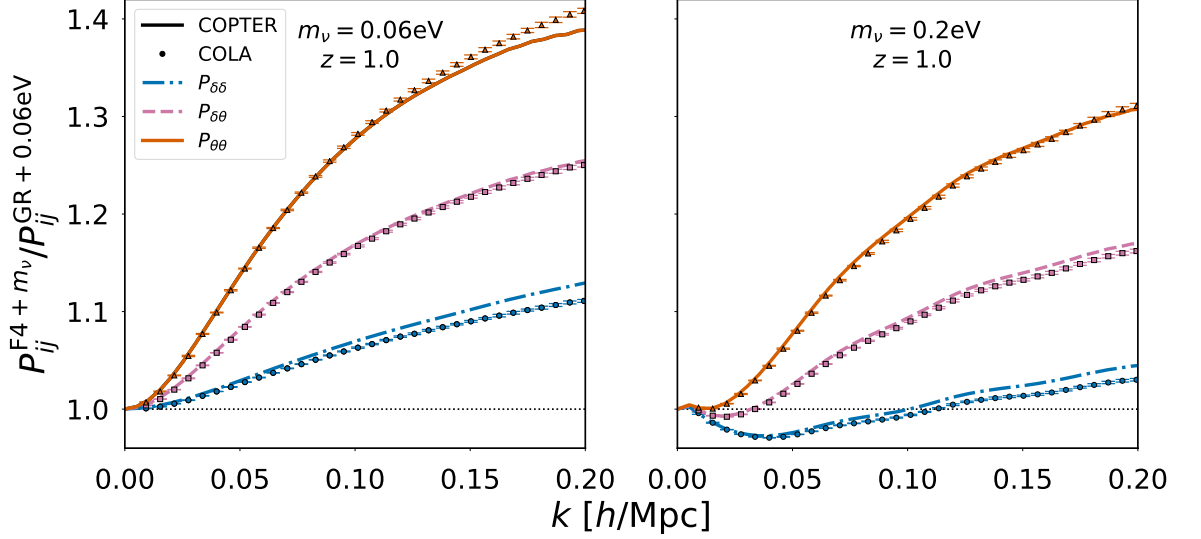


Figure 3.8: Ratio of real-space power spectra in F4 with $m_\nu = 0.06\text{eV}$ (left panel) and $m_\nu = 0.2\text{eV}$ (right panel) to the fiducial model of GR with $m_\nu = 0.06\text{eV}$ at $z = 1$. Points represent the results of paired-fixed MG-PICOLA N -body simulations, while lines are the result of MG-Copter. The blue circles and dashed-dotted line give the density auto-correlated power spectra $P_{\delta\delta}$, the pink squares and dashed line give the density-velocity divergence cross-correlated power spectra $P_{\delta\theta}$, while the orange triangles and solid line give the velocity divergence auto-correlated power spectra $P_{\theta\theta}$.

Firstly, this plot shows that modelling the redshift-space monopole and quadrupole using MG-Copter with σ_v fitted to MG-PICOLA simulations works well. Secondly, for our degenerate models, while the monopole is still a poor probe for distinguishing between the models, the quadrupole, by virtue of the encoding of velocity information, displays differences between the two models and thus has the potential to break the degeneracy.

3.3.2 Redshift evolution

Our method also allows us to investigate how the degeneracy evolves with redshift in both real- and redshift-space.

In Fig. 3.10 we show the real-space power spectra in the ratio between the two degenerate models as in the right panel of Fig. 3.8 but at $z = 0.5$ (left panel) and $z = 1.5$ (right panel). In Fig. 3.11 we show the redshift-space power spectrum multipoles in the ratio between the two degenerate models as in Fig. 3.9 but at $z = 0.5$ (left panel) and $z = 1.5$ (right panel). These figures demonstrate that the degeneracy evolves significantly with redshift, both in real- and redshift-space. Figure 3.10 shows that while our two degenerate models had similar matter power spectra at $z = 1$ it is easier to distinguish between the two models with the matter power spectrum at other

redshifts.

In Fig. 3.12 we plot the difference between the redshift-space multipoles in the two degenerate models quantified through $\chi_{\text{MG}+m_\nu}^2$ as a function of the maximum comparison scale k_{max} . We compute $\chi_{\text{MG}+m_\nu}^2$ as

$$\chi_{\text{MG}+m_\nu}^2(k_{\text{max}}) = \frac{1}{N_{\text{DoF}}} \sum_{l=0,2} \sum_k^{k_{\text{max}}} \text{Cov}_{l,l}^{-1}(k) [P_l^{\text{F4}+0.2\text{eV}}(k) - P_l^{\text{GR}+0.06\text{eV}}(k)]^2, \quad (3.9)$$

where $N_{\text{DoF}} = 2N_k - 1$. This expression is similar to Eq. (3.4) from [223]. The inverse covariance matrix $\text{Cov}_{l,l}^{-1}(k)$ used here is from the same analytic expression used previously; whether this was computed for GR+0.06eV or F4+0.2eV did not affect the result. We show $\chi_{\text{MG}+m_\nu}^2$ as computed by both **MG-PICOLA** and **MG-Copter** with σ_v fitted to **MG-PICOLA** up to k_{max} with the covariance computed assuming a DESI-like survey as detailed at the end of Section 1.5.1.1. The results from both methods agree with each other very well. We plot $\chi_{\text{MG}+m_\nu}^2$ at three redshifts $z = 1.5, 1.0, 0.5$ and it is clear from these results, along with those in Figs. 3.10 and 3.11, that the ability to distinguish between the redshift-space multipoles of these two models evolves with redshift. This emphasises the potential for data at multiple redshifts to break the degeneracy. The tomographic nature of weak lensing observations make them well suited to this task, and the combination of redshift-space distortion measurements with weak lensing observations could prove one of the best probes for breaking the modified gravity-massive neutrino degeneracy. However, it should be noted that systematics associated with weak lensing such as baryonic effects and intrinsic alignments may impact the effectiveness of such a probe.

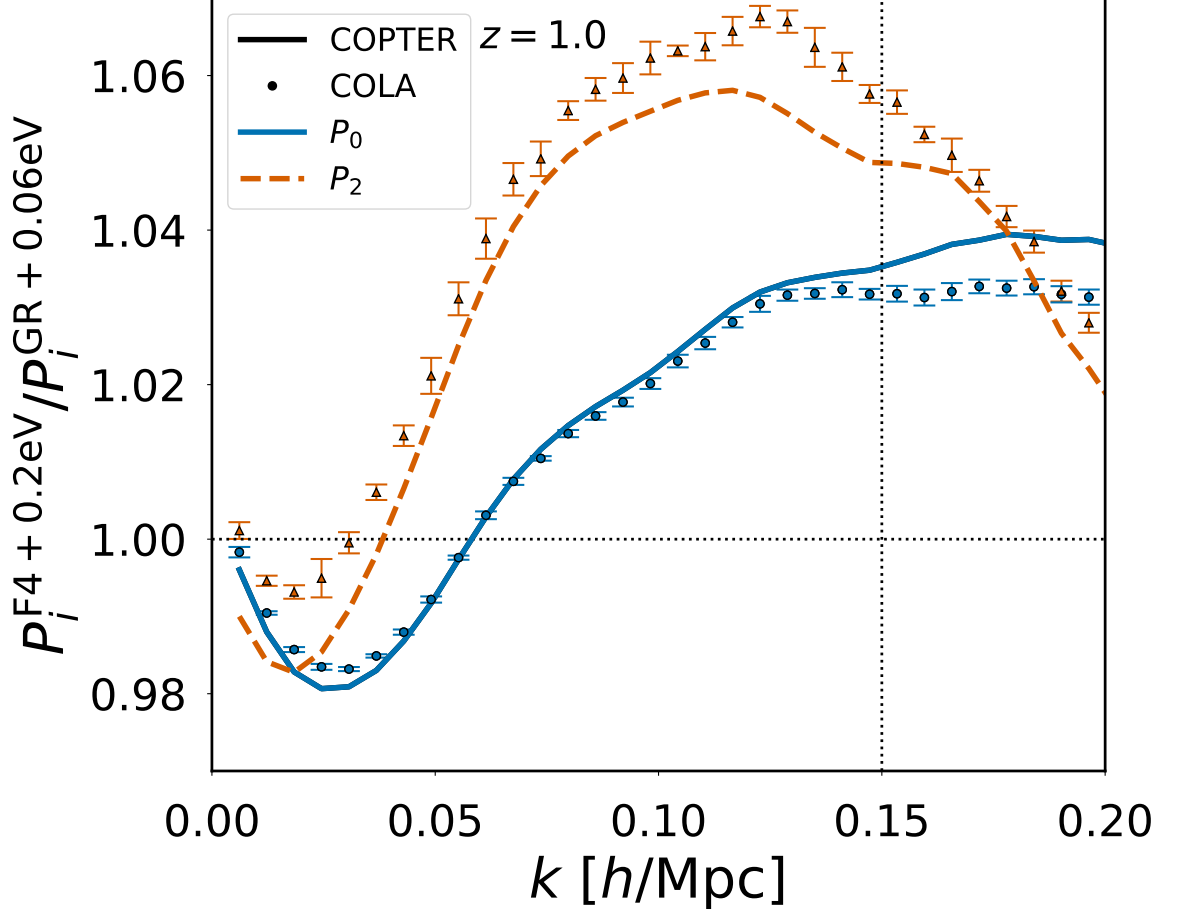


Figure 3.9: Degeneracy between F4 with $m_\nu = 0.2\text{eV}$ and the fiducial model of GR with $m_\nu = 0.06\text{eV}$ in the redshift-space power spectrum multipoles at $z = 1$, represented as the ratio of power spectra in the two models. Points represent the results of paired-fixed MG-PICOLA N -body simulations, while solid lines are the result of MG-Copter with velocity dispersion σ_v fitted to MG-PICOLA up to $k = 0.15 \text{ h/Mpc}$. The blue circles and solid line give the monopole P_0 , while the orange squares and dashed line give the quadrupole P_2 . The best-fitting value of σ_v for each model and the associated reduced χ^2 are $\sigma_v = 3.07 \text{ Mpc/h}$ with $\chi_r^2 = 0.27$ for GR+0.06eV and $\sigma_v = 3.23 \text{ Mpc/h}$ with $\chi_r^2 = 0.39$ for F4+0.2eV.

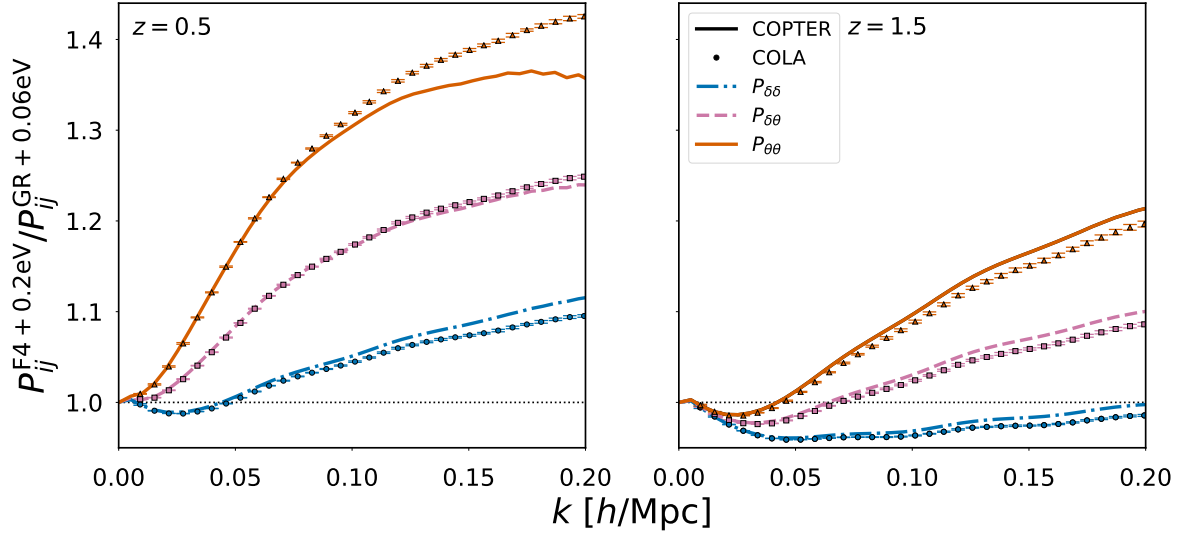


Figure 3.10: As in the right panel of Fig. 3.8, but showing the evolution of the degeneracy with redshift. The left panel corresponds to $z = 0.5$ and the right to $z = 1.5$.

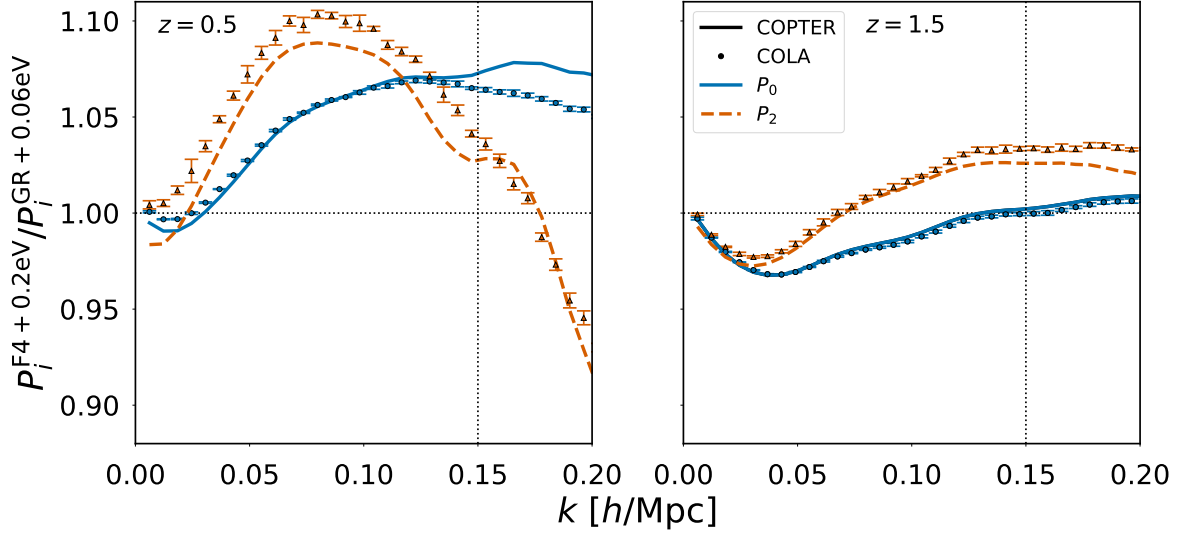


Figure 3.11: As in Fig. 3.9, but showing the evolution of the degeneracy with redshift. The left panel corresponds to $z = 0.5$ and the right to $z = 1.5$. For GR with 0.06eV neutrinos, the best-fitting value of σ_v and the corresponding reduced χ^2 are $\sigma_v = 3.84$ Mpc/h and $\chi_r^2 = 0.29$ for $z = 0.5$, and $\sigma_v = 2.36$ Mpc/h and $\chi_r^2 = 0.065$ for $z = 1.5$. For F4 with 0.2eV neutrinos, the best-fitting value of σ_v and the corresponding reduced χ^2 are $\sigma_v = 4.13$ Mpc/h and $\chi_r^2 = 0.34$ for $z = 0.5$, and $\sigma_v = 2.45$ Mpc/h and $\chi_r^2 = 0.079$ for $z = 1.5$. In all cases σ_v has been fitted to MG-PICOLA up to $k = 0.15$ h/Mpc.

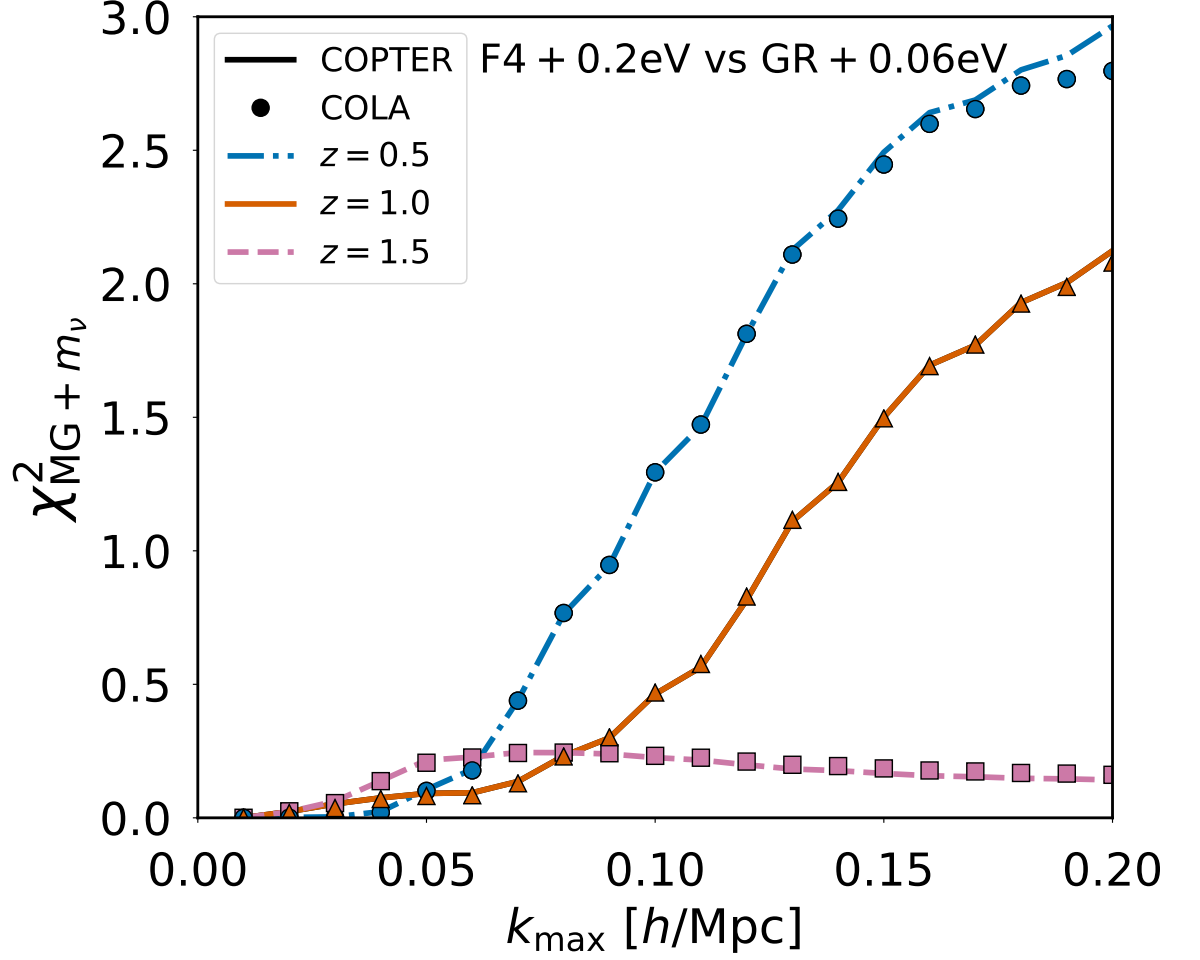


Figure 3.12: The redshift evolution of $\chi^2_{\text{MG}+m_\nu}(k_{\text{max}})$ which quantifies the difference between the redshift-space multipoles of the two degenerate models as a function of maximum comparison scale. The blue circles and dashed-dotted line correspond to $z = 0.5$, the orange triangles and solid line to $z = 1$, and the pink squares and dashed line to $z = 1.5$. Points represent the results of paired-fixed MG-PICOLA N -body simulations, while lines are the result of MG-Copter with velocity dispersion σ_v fitted to MG-PICOLA up to $k = k_{\text{max}}$.

Chapter 4

Halo redshift-space distortions with MG and m_ν

*The work in this chapter was carried out by the author and his supervisory team in collaboration with Hans Winther and Ben Bose. Ben Bose implemented the bias model in **MG-Copter** for Λ CDM cosmologies. The author was responsible for modifying the bias model implemented in **MG-Copter** to work for modified gravity and massive neutrino cosmologies. The author produced the **MG-PICOLA** simulations used in this chapter. Hans Winther advised on use of the **MatchMaker** halo-finding code to produce halo catalogues from the simulation output. Ben Bose also provided the MCMC code used to fit the biased RSD model to the simulated halo catalogues and advised on its use. The author ran the MCMC code and created all of the figures in this chapter. The supervisory team provided direction and advice throughout.*

In the previous chapter we modelled RSD at the level of dark matter. However, as introduced in Chapter 1, we do not observe dark matter directly, and instead infer its presence from the clustering of galaxies, which act as a biased tracer of the underlying dark matter distribution. Therefore in this chapter, we include bias in our **MG-Copter**-based RSD model and investigate the consequences for attempts to break the degeneracy between MG and massive neutrinos by comparing the model against biased halo catalogues created with **MG-PICOLA**.

4.1 Halo RSD Model

In order to model redshift-space distortions in the clustering of biased tracers such as halos, we follow the approach of [232] and combine the TNS model for RSD [146] with

the McDonald and Roy tracer bias model [233]. A similar model was used to analyse BOSS data and infer cosmological constraints [234, 235]. The model in Λ CDM is given by

$$P_{\text{TNS}}^S(k, \mu) = D_{\text{FoG}}(k^2 \mu^2 \sigma_v^2) \left[P_{g,\delta\delta}(k) + 2\mu^2 P_{g,\delta\theta}(k) + \mu^4 P_{\theta\theta}^{1-\text{loop}}(k) + b_1^3 A(k, \mu) + b_1^4 B(k, \mu) \right], \quad (4.1)$$

where $P_{ij}^{1-\text{loop}}$, A , and B are the same as in the TNS model for dark matter, with two options for the phenomenological form of D_{FoG} being the Gaussian and Lorentzian shown in Eqs. (1.122) and (1.123). The two biased power spectra components are given by

$$\begin{aligned} P_{g,\delta\delta}(k, z) = & b_1^2 P_{\delta\delta}^{1-\text{loop}}(k, z) \\ & + \left(\frac{D_1(z)}{D_1(z_{\text{ini}})} \right)^4 \left[2b_2 b_1 P_{b2,\delta,\text{ini}}(k) + 2b_{s2} b_1 P_{bs2,\delta,\text{ini}}(k) \right. \\ & \quad + 2b_{3\text{nl}} b_1 \sigma_{3,\text{ini}}^2(k) P_{\text{ini}}(k) + b_2^2 P_{b22,\text{ini}}(k) \\ & \quad \left. + 2b_2 b_{s2} P_{b2s2,\text{ini}}(k) + b_{s2}^2 P_{bs22,\text{ini}}(k) \right] + N, \end{aligned} \quad (4.2)$$

$$\begin{aligned} P_{g,\delta\theta}(k, z) = & b_1 P_{\delta\theta}^{1-\text{loop}}(k, z) \\ & + \left(\frac{D_1(z)}{D_1(z_{\text{ini}})} \right)^4 \left[2b_2 P_{b2,\theta,\text{ini}}(k) + b_{s2} P_{bs2,\theta,\text{ini}}(k) \right. \\ & \quad \left. + b_{3\text{nl}} \sigma_{3,\text{ini}}^2(k) P_{\text{ini}}(k) \right], \end{aligned} \quad (4.3)$$

where $P_{\text{ini}}(k)$ is the primordial power spectrum and the dependency on the linear bias b_1 , second order local bias b_2 , second order non-local bias b_{s2} , third order non-local bias $b_{3\text{nl}}$, and constant stochasticity N model parameters is expressed explicitly. The bias

terms are given by

$$P_{b2,\delta,\text{ini}}(k) = \int \frac{d^3q}{(2\pi)^3} P_{\text{ini}}(q) P_{\text{ini}}(|\vec{k} - \vec{q}|) \frac{F_2(\vec{q}, \vec{k} - \vec{q}, z)}{D_1^2(z)} , \quad (4.4)$$

$$P_{b2,\theta,\text{ini}}(k) = \int \frac{d^3q}{(2\pi)^3} P_{\text{ini}}(q) P_{\text{ini}}(|\vec{k} - \vec{q}|) \frac{G_2(\vec{q}, \vec{k} - \vec{q}, z)}{D_1^2(z)} , \quad (4.5)$$

$$P_{bs2,\delta,\text{ini}}(k) = \int \frac{d^3q}{(2\pi)^3} P_{\text{ini}}(q) P_{\text{ini}}(|\vec{k} - \vec{q}|) \frac{F_2(\vec{q}, \vec{k} - \vec{q}, z)}{D_1^2(z)} S^{(2)}(\vec{q}, \vec{k} - \vec{q}) , \quad (4.6)$$

$$P_{bs2,\theta,\text{ini}}(k) = \int \frac{d^3q}{(2\pi)^3} P_{\text{ini}}(q) P_{\text{ini}}(|\vec{k} - \vec{q}|) \frac{G_2(\vec{q}, \vec{k} - \vec{q}, z)}{D_1^2(z)} S^{(2)}(\vec{q}, \vec{k} - \vec{q}) , \quad (4.7)$$

$$P_{b22,\text{ini}}(k) = \frac{1}{2} \int \frac{d^3q}{(2\pi)^3} P_{\text{ini}}(q) \left[P_{\text{ini}}(|\vec{k} - \vec{q}|) - P_{\text{ini}}(q) \right] , \quad (4.8)$$

$$P_{b2s2,\text{ini}}(k) = -\frac{1}{2} \int \frac{d^3q}{(2\pi)^3} P_{\text{ini}}(q) \left[\frac{2}{3} P_{\text{ini}}(q) - P_{\text{ini}}(|\vec{k} - \vec{q}|) S^{(2)}(\vec{q}, \vec{k} - \vec{q}) \right] , \quad (4.9)$$

$$P_{bs22,\text{ini}}(k) = -\frac{1}{2} \int \frac{d^3q}{(2\pi)^3} P_{\text{ini}}(q) \left[\frac{4}{9} P_{\text{ini}}(q) - P_{\text{ini}}(|\vec{k} - \vec{q}|) S^{(2)}(\vec{q}, \vec{k} - \vec{q})^2 \right] , \quad (4.10)$$

$$\sigma_{3,\text{ini}}^2(k) = \frac{210}{112} \int \frac{d^3q}{(2\pi)^3} P_{\text{ini}}(q) \left[\left(S^{(2)}(-\vec{q}, \vec{k}) - \frac{2}{3} \right) S^{(2)}(\vec{q}, \vec{k} - \vec{q}) + \frac{4}{9} \right] , \quad (4.11)$$

where the new kernel $S^{(2)}$, which comes from tidal bias, is

$$S^{(2)}(\vec{q}_1, \vec{q}_2) = -\frac{1}{3}(1 - 3\mu_{1,2}^2) , \quad (4.12)$$

and $\mu_{1,2}$ is the cosine of the angle between \vec{q}_1 and \vec{q}_2 . This particular bias model has been derived under the assumption of negligible velocity bias. Following the approach of [234], if we also make the local Lagrangian assumption then we can reduce the number of parameters needed. In the local Lagrangian bias picture, the initial non-local bias is neglected, and the amplitude of the non-local biases is predicted to be [236, 237, 238]

$$b_{s2} = -\frac{4}{7}(b_1 - 1) , \quad (4.13)$$

$$b_{3\text{nl}} = \frac{32}{315}(b_1 - 1) , \quad (4.14)$$

which have been validated by N -body simulations [237]. Thus Eqs. (4.2) and (4.3) become

$$\begin{aligned}
P_{g,\delta\delta}(k, z) = & b_1^2 P_{\delta\delta}^{1-\text{loop}}(k, z) \\
& + \left(\frac{D_1(z)}{D_1(z_{\text{ini}})} \right)^4 \left[2b_2 b_1 P_{b2,\delta,\text{ini}}(k) - \frac{8}{7}(b_1^2 - b_1) P_{bs2,\delta,\text{ini}}(k) \right. \\
& + \frac{64}{315}(b_1^2 - b_1) \sigma_{3,\text{ini}}^2(k) P_{\text{ini}}(k) \\
& + b_2^2 P_{b22,\text{ini}}(k) - \frac{8}{7} b_2 (b_1 - 1) P_{b2s2,\text{ini}}(k) \\
& \left. + \frac{16}{49}(b_1 - 1)^2 P_{bs22,\text{ini}}(k) \right] + N, \tag{4.15}
\end{aligned}$$

$$\begin{aligned}
P_{g,\delta\theta}(k, z) = & b_1 P_{\delta\theta}^{1-\text{loop}}(k, z) \\
& + \left(\frac{D_1(z)}{D_1(z_{\text{ini}})} \right)^4 \left[2b_2 P_{b2,\theta,\text{ini}}(k) - \frac{4}{7}(b_1 - 1) P_{bs2,\theta,\text{ini}}(k) \right. \\
& \left. + \frac{32}{315}(b_1 - 1) \sigma_{3,\text{ini}}^2(k) P_{\text{ini}}(k) \right], \tag{4.16}
\end{aligned}$$

and the set of nuisance parameters is simply $\{b_1, b_2, N, \sigma_v\}$.

This bias model had previously been implemented in **MG-Copter** for the work carried out in [239, 232, 240], but these works only considered GR and massless neutrinos. We also use **MG-Copter** in the work that follows, but since we needed to include the effects of modified gravity and massive neutrinos, it was necessary to modify the implementation in a way similar to what we did in Sec. 3.1. Thus Eqs (4.15) and (4.16) become

$$\begin{aligned}
P_{g,\delta\delta}(k, z) = & b_1^2 P_{\delta\delta}^{1-\text{loop}}(k, z) + \left[2b_2 b_1 P_{b2,\delta}(k, z) - \frac{8}{7}(b_1^2 - b_1) P_{bs2,\delta}(k, z) \right. \\
& + \frac{64}{315}(b_1^2 - b_1) \sigma_3^2(k, z) P^{\text{L}}(k, z) \\
& + b_2^2 P_{b22}(k, z) - \frac{8}{7} b_2 (b_1 - 1) P_{b2s2}(k, z) \\
& \left. + \frac{16}{49}(b_1 - 1)^2 P_{bs22}(k, z) \right] + N, \tag{4.17}
\end{aligned}$$

$$\begin{aligned}
P_{g,\delta\theta}(k, z) = & b_1 P_{\delta\theta}^{1-\text{loop}}(k, z) + \left[2b_2 P_{b2,\theta}(k, z) - \frac{4}{7}(b_1 - 1) P_{bs2,\theta}(k, z) \right. \\
& \left. + \frac{32}{315}(b_1 - 1) \sigma_3^2(k, z) P^{\text{L}}(k, z) \right], \tag{4.18}
\end{aligned}$$

while bias terms become

$$P_{b2,\delta}(k, z) = \int \frac{d^3q}{(2\pi)^3} P^L(q, z) P^L(|\vec{k} - \vec{q}|, z) \frac{F_2(\vec{q}, \vec{k} - \vec{q}, z)}{F_1(q, z) F_1(|\vec{k} - \vec{q}|, z)} , \quad (4.19)$$

$$P_{b2,\theta}(k, z) = \int \frac{d^3q}{(2\pi)^3} P^L(q, z) P^L(|\vec{k} - \vec{q}|, z) f(q, z) f(|\vec{k} - \vec{q}|, z) \times \frac{G_2(\vec{q}, \vec{k} - \vec{q}, z)}{G_1(q, z) G_1(|\vec{k} - \vec{q}|, z)} , \quad (4.20)$$

$$P_{bs2,\delta}(k, z) = \int \frac{d^3q}{(2\pi)^3} P^L(q, z) P^L(|\vec{k} - \vec{q}|, z) \frac{F_2(\vec{q}, \vec{k} - \vec{q}, z)}{F_1(q, z) F_1(|\vec{k} - \vec{q}|, z)} \times S^{(2)}(\vec{q}, \vec{k} - \vec{q}) , \quad (4.21)$$

$$P_{bs2,\theta}(k, z) = \int \frac{d^3q}{(2\pi)^3} P^L(q, z) P^L(|\vec{k} - \vec{q}|, z) f(q, z) f(|\vec{k} - \vec{q}|, z) \times \frac{G_2(\vec{q}, \vec{k} - \vec{q}, z)}{G_1(q, z) G_1(|\vec{k} - \vec{q}|, z)} S^{(2)}(\vec{q}, \vec{k} - \vec{q}) , \quad (4.22)$$

$$P_{b22}(k, z) = \frac{1}{2} \int \frac{d^3q}{(2\pi)^3} P^L(q, z) \left[P^L(|\vec{k} - \vec{q}|, z) - P^L(q, z) \right] , \quad (4.23)$$

$$P_{b2s2}(k, z) = -\frac{1}{2} \int \frac{d^3q}{(2\pi)^3} P^L(q, z) \left[\frac{2}{3} P^L(q, z) - P^L(|\vec{k} - \vec{q}|, z) S^{(2)}(\vec{q}, \vec{k} - \vec{q}) \right] , \quad (4.24)$$

$$P_{bs22}(k, z) = -\frac{1}{2} \int \frac{d^3q}{(2\pi)^3} P^L(q, z) \left[\frac{4}{9} P^L(q, z) - P^L(|\vec{k} - \vec{q}|, z) S^{(2)}(\vec{q}, \vec{k} - \vec{q})^2 \right] , \quad (4.25)$$

$$\sigma_3^2(k, z) = \frac{210}{112} \int \frac{d^3q}{(2\pi)^3} P^L(q, z) \left[\left(S^{(2)}(-\vec{q}, \vec{k}) - \frac{2}{3} \right) S^{(2)}(\vec{q}, \vec{k} - \vec{q}) + \frac{4}{9} \right] . \quad (4.26)$$

As in Sec. 3.1, we implement massive neutrinos only through P_L and f ; the ratio of SPT kernels are left in their pure GR/modified gravity form. Again for simplicity, in the results that follow we have modelled the massive neutrinos as a single massive eigenstate with mass m_ν and two massless eigenstates, such that the sum of masses $M_\nu = \sum_i m_i = m_\nu$.

When working with only dark matter in Chapter 3, we had only one parameter, σ_v , to fit. Now, it is also necessary to fit for b_1 , b_2 , and N . As a result, the simple χ^2 minimisation method we used in Chapter 3 is no longer suitable. Instead, we followed the approach of [239, 232, 240] and utilised an MCMC method to fit our four parameters to simulation data from **MG-PICOLA**. We will discuss the simulation data used later in Sec. 4.2. We chose to use the Lorentzian form for the damping factor seen in Eq. (1.123), as the Gaussian form has been shown to give significantly worse fits to simulation data [241, 232].

The likelihood minimised in this MCMC process is the same as Eq. (1.124), using only the first two multipoles P_0 and P_2 . Initially we limited the fitting to the data to 20

k bins between $k_{\min} = 0.0368 \, h/\text{Mpc}$ and $k_{\max} = 0.153 \, h/\text{Mpc}$ to avoid issues associated with cosmic variance/finite box size at large scales and the breakdown of perturbation theory at small scales. We used the analytic expressions for the covariance matrix between the different multipoles $\text{Cov}_{l,l'}$ as given in Appendix C of [146] and initially assumed an ideal survey of galaxies with average number density $\bar{n}_g = 10^{-3} h^3/\text{Mpc}$ (the same number density used to make the cut to the simulated halo catalogue) over a survey volume $V_s = 10 \, \text{Gpc}^3/h^3$. We also assume the galaxies in this ideal survey have a linear bias equal to that estimated from the simulation being fitted to; $b_1 = \sqrt{P_{\text{halo}}^{\text{sim}}/P_{\text{DM}}^{\text{sim}}}|_{k_{\text{lin}}}$. However, as we will show in Section 4.3, we discovered that this setup leads to overfitting of the data, so we repeated the analysis with 24 k bins such that $k_{\max} = 0.178 \, h/\text{Mpc}$, and also doubled the survey volume to $V_s = 20 \, \text{Gpc}^3/h^3$ which effectively corresponds to tighter errors on the simulation data.

In order to carry out the MCMC sampling at a reasonable pace, it is necessary to split and regroup terms in the bias model according to their explicit dependence on each of the four fitting parameters. The dependence on the fitting parameters for each term was then factored out. Each of these term could then be computed for a range of k values and splined. Subsequently, at each step of the MCMC, $P_{\text{TNS}}^{(s)}(k, \mu)$ could be computed rapidly by assessing the splines and multiplying each term by the appropriate values of the four fitting parameters. Of course, setting up these splines requires some additional computation time at the start of the fitting process, but is ultimately much faster than recomputing the entirety of $P_{\text{TNS}}^{(s)}(k, \mu)$ at each MCMC step.

However, this approach does require the cosmology - both base parameters and $(|f_{R0}|, m_\nu)$ - to be specified at the start, and does not allow us to fit the cosmology to the data, since recomputing the splines at each MCMC step would be prohibitively expensive. We therefore fixed the base cosmological parameters to be the same as those used to generate the simulation data, as specified in Table 4.1. In order to understand the potential constraining power of the model, as well as fitting the model to data with the ‘correct’ matching $(|f_{R0}|, m_\nu)$ values, we also tried fitting the model to data using ‘incorrect’ $(|f_{R0}|, m_\nu)$ values.

For each MCMC fitting we computed 8 chains of 500,000 samples, each starting at a different point in the 4D parameter space, and removed the first 100,000 samples of each chain to reduced the dependence on the starting point. After this, we are left with 3,200,000 samples for each fitting to identify the best-fit from and constrain the model parameters with using GetDist [242].

m_ν (eV)	Ω_{CDM}	Ω_ν
0.06	0.257505	0.001404
0.2	0.254228	0.004681

Table 4.1: The cosmological parameters for the simulations performed for this chapter. Common to all simulations are $\Omega_{\text{m}} = 0.307115$, $\Omega_b = 0.048206$, $\Omega_\Lambda = 0.692885$, $n_s = 0.96$, $A_s = 2.12 \times 10^{-9}$ and $h = 0.6777$.

4.2 Simulations

To test our halo RSD model, we generated simulation data for a universe with GR and $m_\nu = 0.06\text{eV}$ (GR+0.06eV) and a Hu-Sawicki $f(R)$ universe with $|f_{R0}| = 10^{-4}$ and $m_\nu = 0.2\text{eV}$ (F4+0.2eV). For each cosmology, we ran two paired-fixed simulations using **MG-PICOLA** (see Sec. 3.1 for a discussion on paired-fixed simulations), with a box size of $1024^3(h/\text{Mpc})^3$, 1024^3 particles, and 3072^3 mesh grid cells. This large number of grid cells is required as, in order to adequately resolve small mass halos, the mesh must be finer than the mean-inter particle distance. Following the argument made in [226] we chose a particle mesh grid which is three times finer than the mean particle separation. We used 30 time-steps logarithmically spaced in redshift from $z_{\text{ini}} = 19$ to $z = 1$. The base cosmological parameters used were the same as the MultiDark-Planck simulation suite¹. Note that as in previous Chapters we include massive neutrinos at the expense of CDM while keeping the other parameters fixed, as displayed in Table 4.1. This pipeline of producing halo catalogues using **MG-PICOLA** simulations has been tested against the full N -body code **RAMSES** using the same initial conditions, and P_0 and P_2 were found to agree within $\sim 1 - 2\%$ up to $k = 0.3h/\text{Mpc}$ (see Appendix A of [240]).

We then used the **MatchMaker** friends-of-friends algorithm² with linking length $b = 0.2$ to find halos from the **MG-PICOLA** simulation particle data at $z = 1$. We applied a cut to the resulting halo catalogues based on number density $n_{\text{halo}} \leq 10^{-3}(h/\text{Mpc})^3$ (the same value as used for the computation of the analytic covariance). Finally, we computed the multipoles of the redshift-space power spectrum from these cut halo catalogues, and it is these multipoles that we fit our halo RSD model to.

¹<https://www.cosmosim.org/cms/documentation/projects/multidark-bolshoi-project/>

²<https://github.com/damonge/MatchMaker>

4.3 Results

We first investigate the fits in the 20 k bins between $k_{\min} = 0.0368 \text{ h/Mpc}$ and $k_{\max} = 0.153 \text{ h/Mpc}$ and assuming a survey volume of $V_s = 10\text{Gpc}^3/h^3$ when computing the analytic covariance matrices. The best-fitting values of the model parameters for each combination of model and data $(|f_{R0}|, m_\nu)$ in this setup are presented in Table 4.2, along with the reduced-chi-squared $\chi_r^2 = \chi^2/N_{\text{DoF}}$ of the best-fit and the Gelman-Rubin convergence diagnostic $R - 1$. For our fitting procedure, the degrees of freedom $N_{\text{DoF}} = 2N_k - N_{\text{params}}$, where for now $N_k = 20$ and $N_{\text{params}} = 4$ since we are fitting for b_1 , b_2 , N , and σ_v ; therefore $N_{\text{DoF}} = 36$.

Model	Data	b_1	b_2	N	σ_v	χ_r^2	$R - 1$
GR+0.06eV	GR+0.06eV	1.99	-0.115	-26.8	3.13	0.542	0.012
F4+0.2eV	GR+0.06eV	2.05	0.524	-739.	3.91	0.694	0.012
GR+0.06eV	F4+0.2eV	1.84	-1.56	1150	1.23	0.617	0.015
F4+0.2eV	F4+0.2eV	1.88	-1.23	626	2.58	0.606	0.014

Table 4.2: Best fit model parameters, χ^2 and convergence values for each combination of model and data with the fitting restricted to 20 k bins between $k_{\min} = 0.0368 \text{ h/Mpc}$ and $k_{\max} = 0.153 \text{ h/Mpc}$ and assuming a survey volume of $V_s = 10\text{Gpc}^3/h^3$.

We first consider the ‘correct’ fits to data, where the $(|f_{R0}|, m_\nu)$ values specified in the model match those used to create the simulation. The χ_r^2 values are all considerably less than unity, suggesting the model is overfitting the data. The upper panel of Figure 4.1 displays the redshift-space power spectrum multipoles computed using Eq. (4.1) with the best-fit model parameters from Table 4.2 along with the multipoles from the MG-PICOLA simulations that the model was fitted to. The error bars on the simulation data points are the diagonal elements of the inverse covariance matrices. This upper panel of this figure shows that our model achieves a very good fit to the simulation data for the 20 k points between $k_{\min} = 0.0368 \text{ h/Mpc}$ and $k_{\max} = 0.153 \text{ h/Mpc}$ when the $(|f_{R0}|, m_\nu)$ values specified in the model match those used to create the simulation. The model achieves a slightly better fit for the GR+0.06eV case, where there is the smallest deviation from scale-independent growth.

Next, let us consider the ‘incorrect’ fits to data, where the $(|f_{R0}|, m_\nu)$ values specified in the model *do not* match those used to create the simulation. These are useful because, while we cannot vary $(|f_{R0}|, m_\nu)$ as a free parameter in our model with the approach we use, attempting to fit the ‘incorrect’ model can give us an idea of the model’s potential to constrain $(|f_{R0}|, m_\nu)$. Looking at the χ_r^2 values in Table 4.2, it

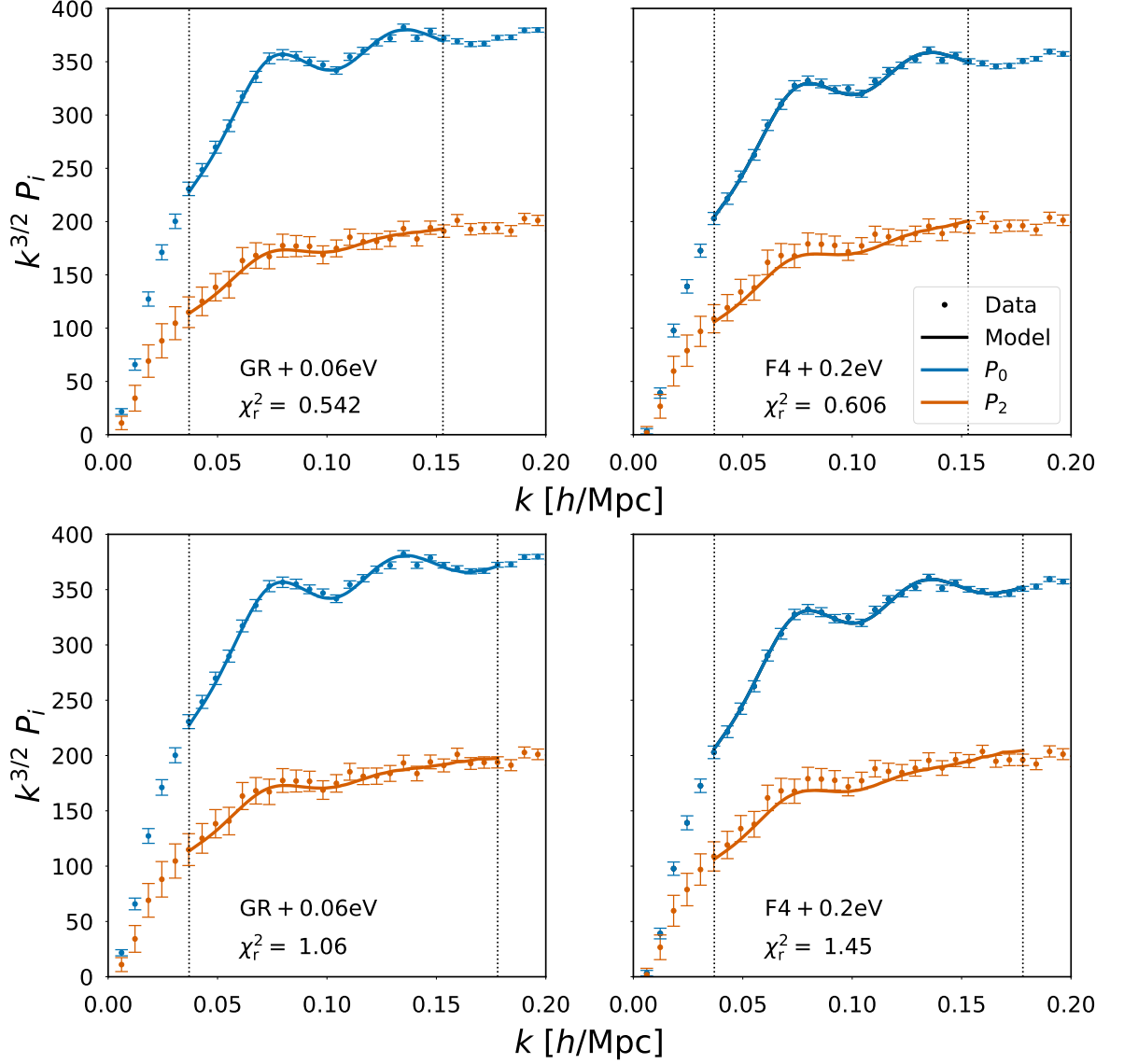


Figure 4.1: Redshift-space halo power spectrum multipoles at $z = 1$. The left panels are for GR+0.06eV and the right panels are for F4+0.2eV. The blue points and line give the monopole P_0 and the orange points and line give the quadrupole P_2 . Points represent the results of paired-fixed MG-PICOLA N -body simulations, while lines are the result of fitting the model in Eq. (4.1) to these simulations. For the upper panels, the fitting used the initial setup with 20 k bins between $k_{\min} = 0.0368 \text{ h/Mpc}$ and $k_{\max} = 0.153 \text{ h/Mpc}$ and $V_s = 10 \text{ Gpc}^3/h^3$. For the lower panels, the fitting used the refined setup with 24 k bins between $k_{\min} = 0.0368 \text{ h/Mpc}$ and $k_{\max} = 0.178 \text{ h/Mpc}$ and $V_s = 20 \text{ Gpc}^3/h^3$. The reduced-chi-squared value for each of these fits is printed in the respective panel. The error bars on the simulation data points are taken from the inverse covariance matrices used in the fitting process.

is clear that the model is overfitting the data even for these ‘incorrect’ $(|f_{R0}|, m_\nu)$ value. For the GR+0.06eV simulation data, the ‘incorrect’ fit using the model with F4+0.2eV are not as good as the ‘correct’ fit using the GR+0.06eV model. However, for the F4+0.2eV simulation data fitting the ‘correct’ F4+0.2eV model yields only a marginally improved fit over the using the ‘incorrect’ GR+0.06eV model.

Because the χ_r^2 values suggested the initial setup lead to the model being overfitted to the data, we decided to increase N_k to 24 such that $k_{\max} = 0.178h/\text{Mpc}$ and assume $V_s = 20\text{Gpc}^3/h^3$ when computing the analytic covariance matrices. We shall refer to this as the refined fitting setup. Note that $N_k = 24$ corresponds to $N_{\text{DoF}} = 44$. The best-fitting values of the model parameters for each combination of model and data $(|f_{R0}|, m_\nu)$ in this setup are presented in Table 4.3, along with the reduced-chi-squared $\chi_r^2 = \chi^2/N_{\text{DoF}}$ of the best-fit and the Gelman-Rubin convergence diagnostic $R-1$. The lower panel of Figure 4.1 displays the redshift-space power spectrum multipoles for the ‘correct’ fits in the refined fitting setup.

Model	Data	b_1	b_2	N	σ_v	χ_r^2	$R-1$
GR+0.06eV	GR+0.06eV	1.99	0.0652	-84.0	3.22	1.06	0.015
F4+0.2eV	GR+0.06eV	1.90	-0.779	300	3.07	1.45	0.0093
GR+0.06eV	F4+0.2eV	1.91	2.06	-576	3.06	1.46	0.10
F4+0.2eV	F4+0.2eV	1.90	-0.813	327	3.05	1.45	0.040

Table 4.3: Best fit model parameters, χ^2 and convergence values for each combination of model and data with the fitting restricted to 24 k bins between $k_{\min} = 0.0368 h/\text{Mpc}$ and $k_{\max} = 0.178 h/\text{Mpc}$ and assuming a survey volume of $V_s = 20\text{Gpc}^3/h^3$.

With this refined fitting setup, $\chi_r^2 > 1$ for every case, so the model is no longer overfitting the data. Compared to the previous fitting setup, the best-fit model parameters for the ‘correct’ fits change only slightly, suggesting they are relatively stable. However, the best-fit model parameters for the ‘incorrect’ fits change significantly. This instability of the ‘incorrect’ fits could help to constrain $(|f_{R0}|, m_\nu)$; for example if the model parameters change significantly as k_{\max} varies for one combination of $(|f_{R0}|, m_\nu)$ and are relatively stable for another, then the latter is likely closer to the true values. As for the previous fitting setup, the GR+0.06eV model fits the GR+0.06eV simulation data moderately better than the F4+0.2eV model does, whereas the difference in the quality of the fits between the models for the F4+0.2eV data is negligible. For the refined fitting setup, the χ_r^2 values make it clearer that the ‘correct’ fit to the GR+0.06eV data is moderately better than the ‘correct’ fit to the F4+0.2eV data. This suggests

the model is struggling to replicate the larger deviation from scale-independent growth in the F4+0.2eV case.

It is also interesting to investigate how well the model recovers the linear bias of the simulated halos. The estimates of the linear bias from the simulations $b_1 = \sqrt{P_{\text{halo}}^{\text{sim}}/P_{\text{DM}}^{\text{sim}}}|_{k_{\text{lin}}}$ were 2.00 and 1.91 for GR+0.06eV and F4+0.2eV respectively. Looking at the MCMC contours for the models fitted to the GR+0.06eV simulation data in Fig. 4.2, while the GR+0.06eV model recovers constraints on b_1 that are fully consistent with the estimate from the simulation for both the initial and refined fitting setup, the F4+0.2eV model is barely consistent at the 1σ level for the initial setup and inconsistent at the 2σ level for the refined setup. In the context of applying our model to real data, if there was a strong prior on b_1 from some other observation then this could be useful for constraining $(|f_{R0}|, m_\nu)$. However, for the F4+0.2eV simulation data in Fig. 4.3 both the F4+0.2eV and GR+0.06eV model fits are fully consistent with the simulation estimate for both the initial and refined setup. Yet the GR+0.06eV model fit to the F4+0.2eV data appears to favour a double peak in the 1D marginalised parameter distributions and suggests the GR+0.06eV model can fit the F4+0.2eV data with significantly different values of b_2 and N . We hypothesize this could be due to the strong degeneracy between b_2 and N that can be seen in the contours. To test this, we repeat the fitting for both models to the F4+0.2eV data with the refined setup, but with N fixed to 0. The best-fit parameters for the GR+0.06eV fit in this case are $b_1 = 1.90$, $b_2 = 0.0456$, and $\sigma_v = 2.61$; the value of b_2 is considerably smaller than in the varying N case. These parameters give a slightly worse fit ($\chi_r^2 = 1.53$) than the best-fit parameters for the varying N case. The best-fit parameters for the F4+0.2eV $N = 0$ fit are $b_1 = 1.91$, $b_2 = -0.362$, and $\sigma_v = 3.22$; and these are relatively unchanged from the best-fit parameters in the varying N case. For the F4+0.2eV $N = 0$ fit we have $\chi_r^2 = 1.46$, demonstrating the quality of the fit is negligibly different from the varying N case. As before, the fact that the best-fit for the ‘correct’ model is relatively stable in response to changes to the fitting procedure while the ‘incorrect’ model is not may prove useful for constraining $(|f_{R0}|, m_\nu)$. The MCMC contours for this fixed N case displayed in Fig. 4.4 show that fixing N yields much stronger constraints on the remaining model parameters. In fact the constraints on b_1 are strong enough to make the GR+0.06eV $N = 0$ fit inconsistent at the 2σ level with the value estimated from the simulation data, although for this small a magnitude of discrepancy we should question how well we can estimate b_1 from the simulation data before we make a firm conclusion. The F4+0.2eV $N = 0$ fit still recovers a b_1 value that is consistent with the simulation data estimate despite the tight constraints.

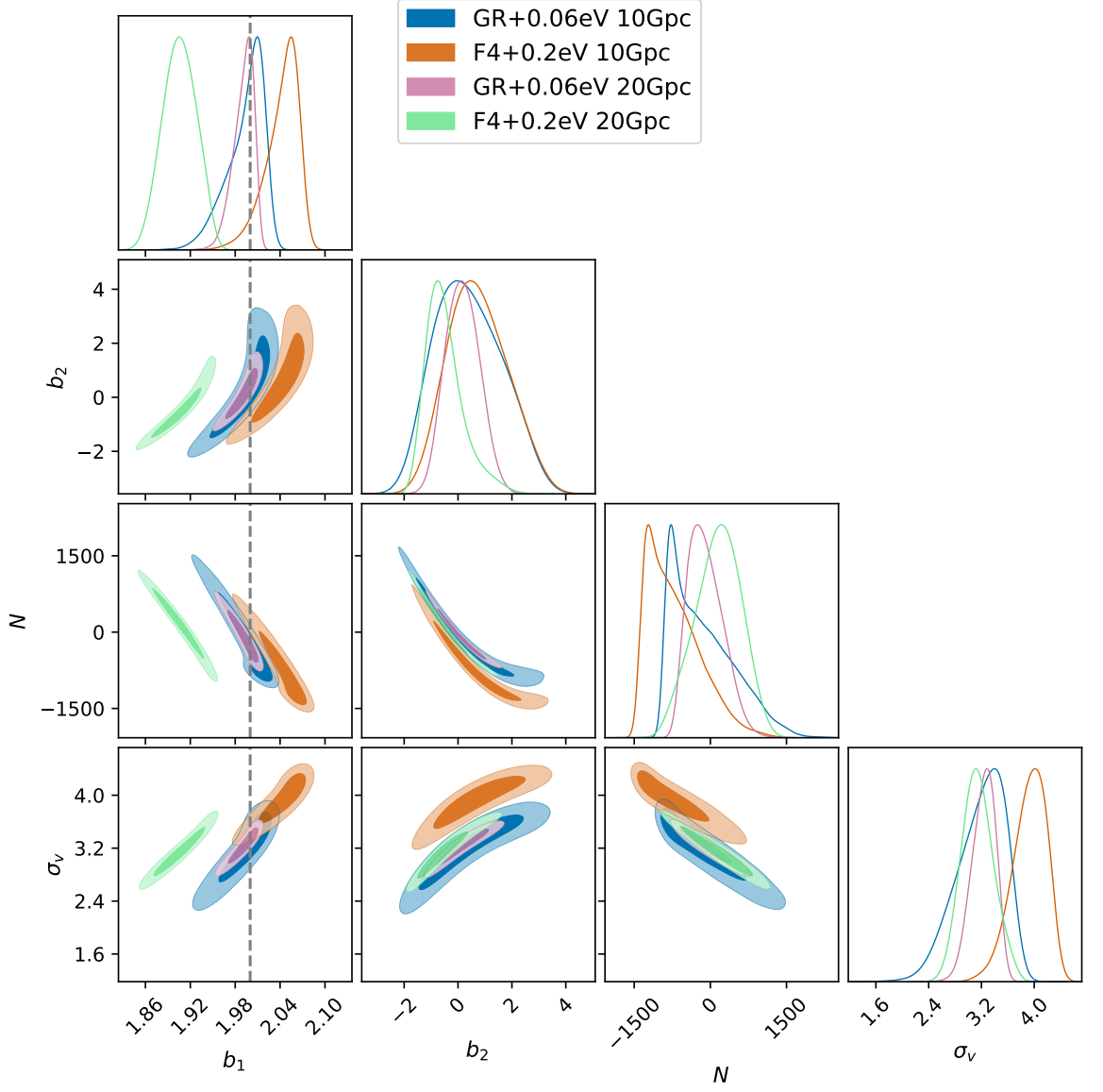


Figure 4.2: Contours for the MCMC fits to GR+0.06eV simulation data. The inner solid and outer shaded contours represent the 1σ (68%) and 2σ (95%) marginalised confidence levels respectively. The vertical dashed line for $b_1 = 2.00$ is the linear bias estimated from the simulation; $b_1 = \sqrt{P_{\text{halo}}^{\text{sim}}/P_{\text{DM}}^{\text{sim}}|_{k_{\text{lin}}}}$. The blue and orange contours correspond to the GR+0.06eV and F4+0.2eV fits using the initial setup with $N_k = 20$ and $V_s = 10\text{Gpc}^3/h^3$. The pink and green contours correspond to the GR+0.06eV and F4+0.2eV fits using the refined setup with $N_k = 24$ and $V_s = 20\text{Gpc}^3/h^3$.

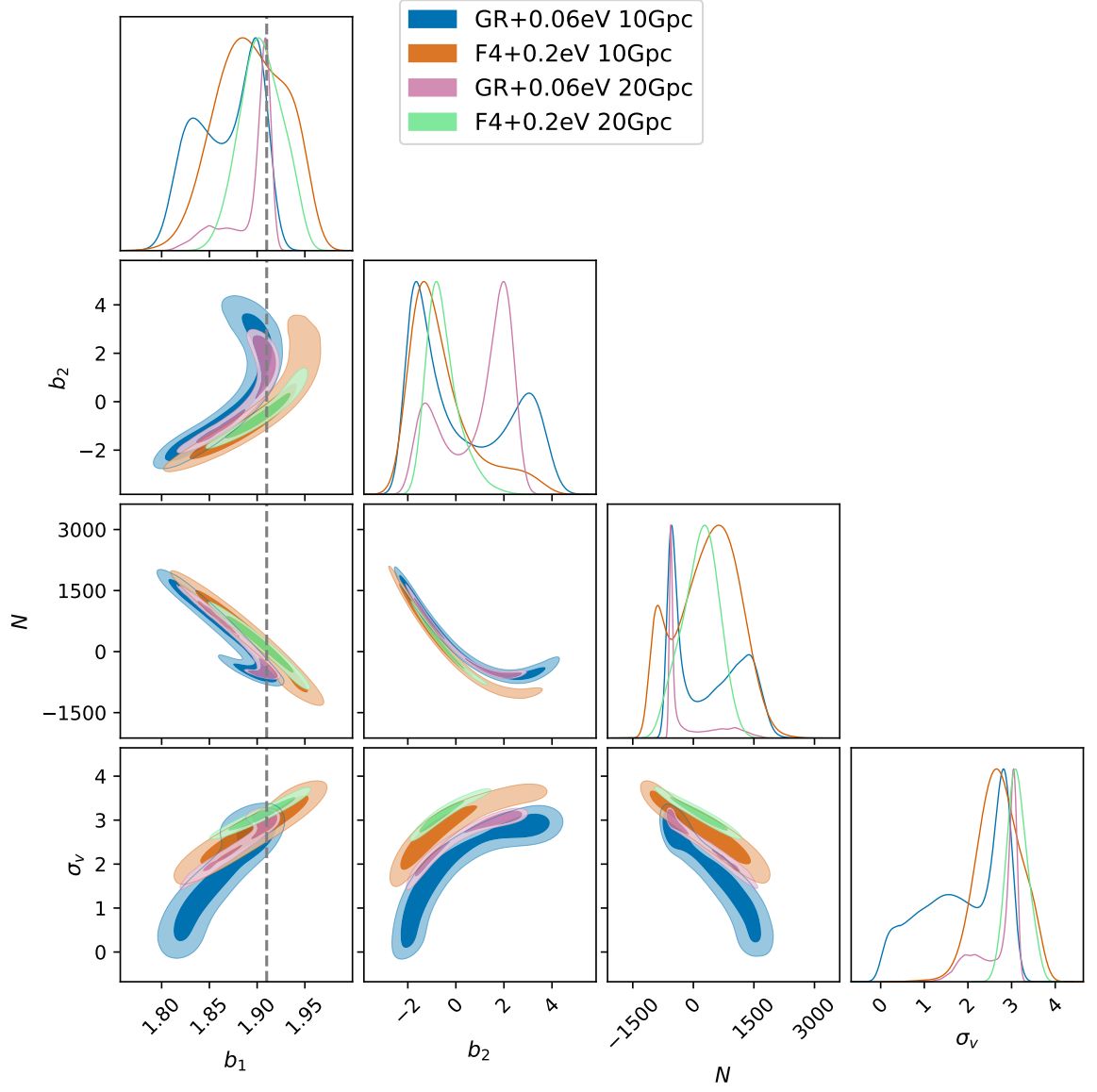


Figure 4.3: MCMC contours as described in Fig. 4.2, but for fits to the F4+0.2eV simulation data. The linear bias estimated from the F4+0.2eV simulations is shown by the vertical dashed line for $b_1 = 1.91$.

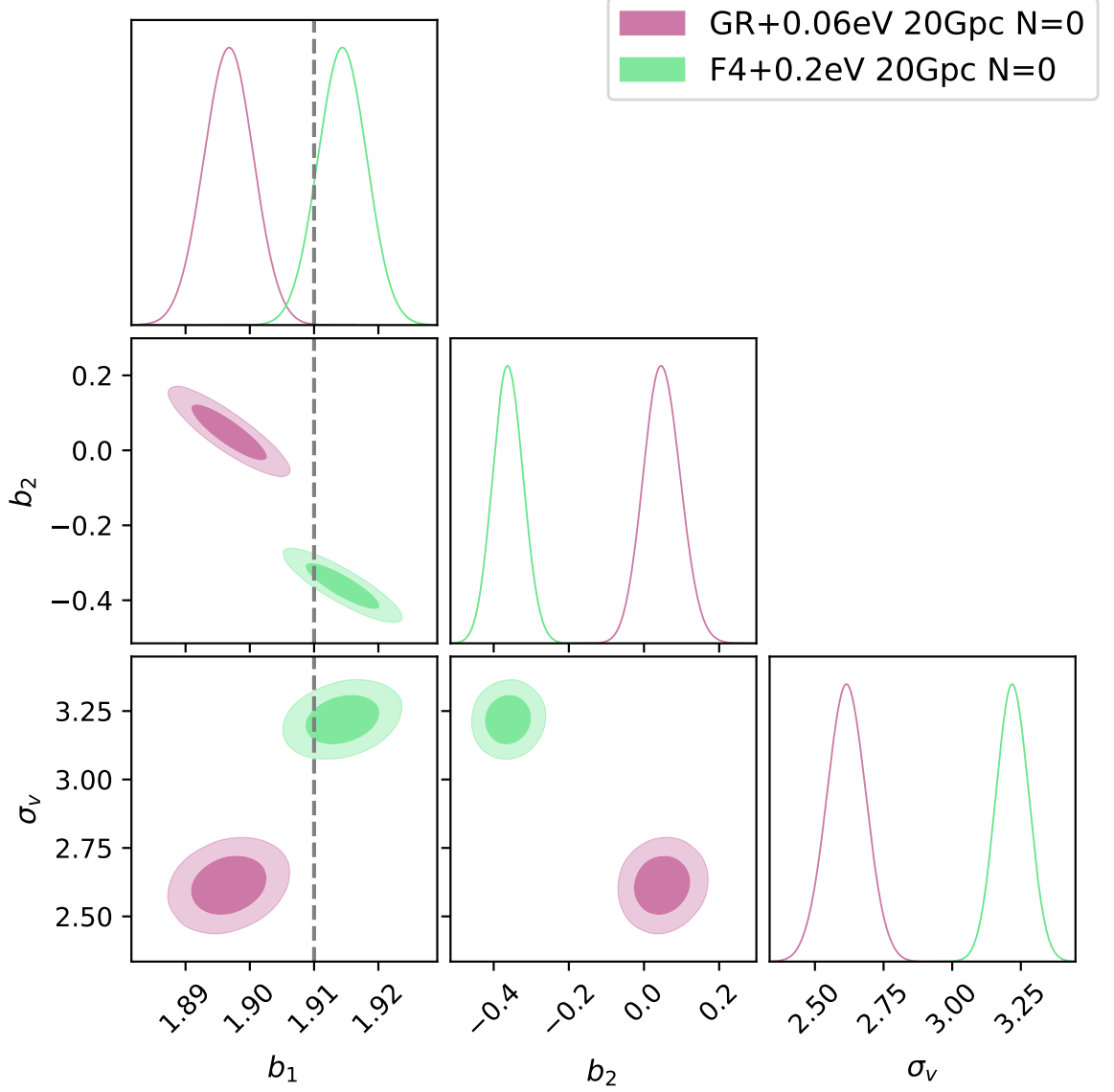


Figure 4.4: Contours for the MCMC fits to F4+0.2eV simulation data with N fixed at 0 and using the refined setup with $N_k = 24$ and $V_s = 20\text{Gpc}^3/h^3$. The inner solid and outer shaded contours represent the 1σ (68%) and 2σ (95%) marginalised confidence levels respectively. The pink and green contours correspond to the GR+0.06eV and F4+0.2eV models respectively. The vertical dashed line for $b_1 = 1.91$ is the linear bias estimated from the F4+0.2eV simulation; $b_1 = \sqrt{P_{\text{halo}}^{\text{sim}}/P_{\text{DM}}^{\text{sim}}}|k_{\text{lin}}|$.

Finally, we can study how well the model captures the changes to the redshift-space multipoles introduced by F4+0.2eV in comparison to GR+0.06eV. The upper panel of Figure 4.5 shows the ratio of the redshift-space power spectrum multipoles in F4+0.2eV to GR+0.06eV, for both the MG-PICOLA simulations and the ‘correct’ best-fit model in the initial fitting setup. The lower panel displays the same but where the fits considered used the refined fitting setup. While the model captures the effect of

F4+0.2eV relative to GR+0.06eV well for the monopole P_0 , it does less well for the quadrupole P_2 , which may limit the ability of our model to constrain $(|f_{R0}|, m_\nu)$.

We can also compute $\chi_{\text{MG}+m_\nu}^2$ to quantify the difference between the redshift-space power spectrum multipoles in cosmological models with different $(|f_{R0}|, m_\nu)$:

$$\chi_{\text{MG}+m_\nu}^2 = \frac{1}{N_{\text{DoF}}} \sum_{l=0,2} \sum_{k=k_{\min}}^{k_{\max}} \text{Cov}_{l,l}^{-1}(k) [P_l^{\text{F4}+0.2\text{eV}}(k) - P_l^{\text{GR}+0.06\text{eV}}(k)]^2, \quad (4.27)$$

where $N_{\text{DoF}} = 2N_k - 1$ since we compare N_k points for both P_0 and P_2 . For the initial fitting we have 20 k bins between $k_{\min} = 0.0368 \text{ h/Mpc}$ and $k_{\max} = 0.153 \text{ h/Mpc}$ such that $N_{\text{DoF}} = 39$, whereas for the refined fitting we have 24 k bins between $k_{\min} = 0.0368 \text{ h/Mpc}$ and $k_{\max} = 0.178 \text{ h/Mpc}$ yielding $N_{\text{DoF}} = 47$. For the **MG-PICOLA** simulations we find $\chi_{\text{MG}+m_\nu}^2 = 19.61$ with $k_{\max} = 0.153 \text{ h/Mpc}$ and $\chi_{\text{MG}+m_\nu}^2 = 24.40$ for $k_{\max} = 0.178 \text{ h/Mpc}$, while for the ‘correct’ best-fit model we get $\chi_{\text{MG}+m_\nu}^2 = 19.57$ with $k_{\max} = 0.153 \text{ h/Mpc}$ and $\chi_{\text{MG}+m_\nu}^2 = 22.37$ with $k_{\max} = 0.178 \text{ h/Mpc}$. This suggests that the model is effective at capturing the changes to the redshift-space multipoles introduced by F4+0.2eV in comparison to GR+0.06eV, but becomes less effective the higher k_{\max} is set. Note that the values of the equivalent statistic for the dark matter-only multipoles in Section 3.3.2 were only of order $\mathcal{O}(1)$ for $z = 1$. The values are much larger for halos because, as we show in Fig. 4.5, the monopole P_0 is smaller for F4+0.2eV than GR+0.06eV, which is largely due to the difference in linear bias between the two models, whereas Fig. 3.9 showed that P_0 is relatively similar for F4+0.2eV and GR+0.06eV in the dark matter only case. Conversely, Fig. 4.5 shows that P_2 is quite similar in the two models for halos, whereas in Fig. 3.9 P_2 was more different in the two models than P_0 for dark matter. The form of the analytic covariance we use is such that a difference in P_0 contributes to $\chi_{\text{MG}+m_\nu}^2$ more than a difference in P_2 does, hence the larger value for halos than dark matter only. Because the difference in P_0 for halos is due largely to a difference in linear bias between the models, it makes it more difficult to identify the ‘correct’ model when fitting to data since the difference can be compensated for by a change in the b_1 model parameter. While the difference in P_2 between models is not as large as for the dark matter only scenario, it is still useful for distinguishing between models as the difference can not be so easily replicated by a change in b_1 .

Ultimately, we have shown that identifying the ‘correct’ bias model and fitting setup is crucial to breaking the modified gravity-massive neutrino degeneracy for biased tracers such as halos.

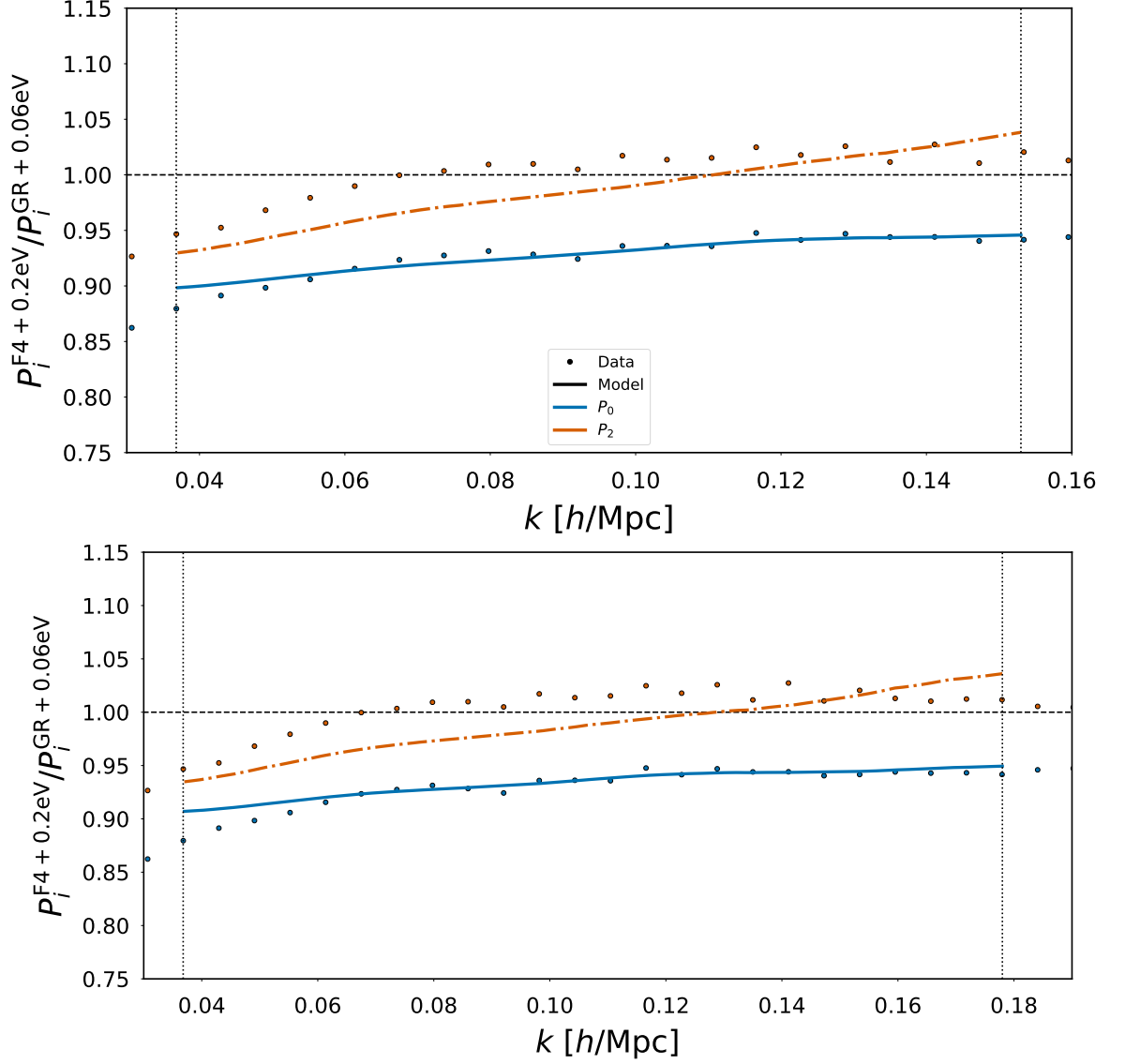


Figure 4.5: The ratio of the redshift-space halo power spectrum multipoles in F4+0.2eV and GR+0.06eV at $z = 1$. Points represent the results of paired-fixed MG-PICOLA N -body simulations, while solid lines are the result of fitting Eq. (4.1) to the simulations. For the upper panel, the fitting used the initial setup with 20 k bins between $k_{\min} = 0.0368$ h/Mpc and $k_{\max} = 0.153$ h/Mpc and $V_s = 10\text{Gpc}^3/h^3$. For the lower panel, the fitting used the refined setup with 24 k bins between $k_{\min} = 0.0368$ h/Mpc and $k_{\max} = 0.178$ h/Mpc and $V_s = 20\text{Gpc}^3/h^3$. The blue points and solid line give the monopole P_0 , while the orange points and dashed-dotted line give the quadrupole P_2 .

Chapter 5

Discussion and Conclusions

5.1 Summary of results

First, in Chapter 2 we have presented a code, **MG-PICOLA**, that simulates large-scale structure formation using the COLA approach and includes the effects of modified gravity and massive neutrinos. The code comes with a general implementation of an approximate method for including the three most common types of screening one finds in modified gravity theories. We have also implemented a general parameterisation of scalar-tensor theories of the chameleon form using the $\{m(a), \beta(a)\}$ formulation together with commonly studied models like $f(R)$, nDGP and Jordan-Brans-Dicke. For the inclusion of massive neutrinos in the particle mesh part of the COLA algorithm we use the grid-based method of [172] where massive neutrinos are kept in Fourier space and evolved linearly according to the neutrino growth factors. Tools for doing on-the-fly computation of (friend-of-friend) halo catalogues plus both real space and redshift space matter power spectra are built-in to the code.

In order to test the modified gravity implementation, we have compared **MG-PICOLA** to full modified gravity simulations and the results demonstrate that the approach works very well. The boost-factors $X/X_{\Lambda\text{CDM}}$ for clustering statistics like power spectra and halo mass function computed with **MG-PICOLA** are able to recover the true N -body result to percent level accuracy deep into the non-linear regime ($k \sim 3h/\text{Mpc}$) even when using a low number of COLA time steps. A comparison to full N -body simulations of massive neutrino cosmologies, both for ΛCDM and $f(R)$ gravity, shows that we can match N -body results to percent level accuracy for $k \lesssim 1 h/\text{Mpc}$ in both the total and CDM matter power spectra with our approach. In order to be able to judge the accuracy of our massive neutrino scheme more directly we would need to do a comparison to full N -body simulations where we use exactly the same initial conditions

in COLA, and this option was not available to us at the time this study was performed.

The addition of scale-dependent growth does have the drawback of slowing down the COLA approach relative to Λ CDM by a factor of $\sim 3-4$ in the current implementation, but as we have shown, and was previously found in [191], for $f(R)$ (and likely other models of this form) one can get away with using the Λ CDM growth-factor making this approach only about $\sim 30\%$ slower than Λ CDM. However, the scale-dependent implementation is still needed to verify this approximation and there is no guarantee it will hold for a general model. For the nDGP models we tested (which should also hold for Galileon models in general) the growth-factors remain scale-independent to second order and the only computational overlay for these simulations is in the computation of the screening factor which requires one extra Fourier transform per step making it only $\sim 30\%$ slower than the corresponding Λ CDM simulation.

We have also shown that the Eisenstein-Hu fitting formulae for the growth factors in massive neutrino cosmologies are a good approximation for a wide range of modified gravity theories as long as we replace the Λ CDM growth factor by the modified gravity counterpart.

MG-PICOLA is a vital tool due to its speed in comparison to full N -body simulation methods and has proven useful for a number of different studies by the community [243, 244, 245, 246, 240, 247, 248].

Next, in Chapter 3 we have studied the potential for redshift-space distortions to break the degeneracy between the enhancement of structure growth provided by modifications to gravity and suppression of structure growth due to massive neutrinos, at the level of the dark matter field. For combinations of modified gravity parameters and neutrino masses that have similar matter power spectra at a given redshift, the growth rates are different and will remain distinguishable. This degeneracy-breaking growth rate information is encoded via velocities into redshift-space distortions. To carry out this work, we have modelled the effects of both modified gravity and massive neutrinos on real- and redshift-space CDM+baryon power spectra with Standard Perturbation Theory through the code **MG-Copter**. We found the implementation of modified gravity and massive neutrinos in **MG-Copter** produces a good agreement for both real- and redshift-space power spectra with the simulation results from the code **MG-PICOLA** in the case of Hu-Sawicki $f(R)$ gravity at the level of the dark matter field.

We have then investigated the degeneracy and shown that the quadrupole of the redshift-space CDM+baryon power spectrum retains enough of the velocity information to distinguish between GR with light neutrinos and Hu-Sawicki $f(R)$ with heavy neutrinos, and our model is capable of capturing this degeneracy-breaking informa-

tion. We have also briefly studied how the degeneracy evolves with redshift. There is a clear evolution of the degeneracy with redshift even for the matter power spectrum; for combinations of modified gravity and neutrino mass parameters that give comparable matter power spectra at one redshift, the matter power spectra at another redshift are in general likely to be distinguishable. The tomographic nature of weak lensing is particularly well suited to investigating this approach to breaking the degeneracy, although weak lensing systematics such as baryonic effects and intrinsic alignments could cause complications. Alternatively, if modified gravity is only a low redshift effect, a constraint on neutrino mass from clustering at higher redshift, for example from HI intensity mapping [249], would help break the degeneracy.

However, our original **MG-Copter**-based RSD model only functions at the level of dark matter. Therefore, in order to bring this method closer to the point where it can be applied to observational data from galaxy surveys, in Chapter 4 we have added biased tracers to the modelling. To do so, we followed the approach of [233], which adds 3 bias parameters $\{b_1, b_2, N\}$ to σ_v from the original model. We tested this extended **MG-Copter**-based model by fitting the redshift-space multipoles to halo catalogues created with **MG-PICOLA**, which necessitated the use of an MCMC approach due to the increase in the number of free parameters. Since our approach requires $(|f_{R0}|, m_\nu)$ to be fixed, we fitted both ‘correct’ models, where $(|f_{R0}|, m_\nu)$ in the model matched that used to create the simulation it was being fitted to, and ‘incorrect’ models, where $(|f_{R0}|, m_\nu)$ was different in the model and simulation.

We have shown that it is necessary to identify an appropriate fitting setup, for example through the maximum fitting scale k_{max} and the volume of the survey assumed when computing the covariance V_s , in order to ensure the model does not overfit the data. Once we had refined the fitting setup for our approach, we were able to show that the ‘correct’ fit was excellent for GR+0.06eV and still good for F4+0.2eV, although the stronger deviation from scale-independent growth does degrade the quality of the fit partially in this cosmology. As well as modifying k_{max} and V_s , we also repeated the analysis of the fits to the F4+0.2eV simulation with the stochasticity model parameter N fixed to 0. We have shown that doing so removes degeneracies between model parameters, particularly the strong degeneracy between N and b_2 that is seen in the MCMC contours, and as a result enables significantly tighter constraints to be placed on the bias parameters and σ_v . We have also investigated how well our model is able to recover the linear bias b_1 that we estimated from the simulation and have demonstrated that the ‘correct’ model fits were fully consistent with the b_1 value estimated from the simulations in each scenario we tested. For the ‘incorrect’ F4+0.2eV model fitted to

the GR+0.06eV simulation data, we found that the quality of the fit is consistently worse than the ‘correct’ GR+0.06eV model fit for the two fitting setups investigated. Additionally, for the refined setup the b_1 value recovered by the ‘incorrect’ F4+0.2eV mode was not consistent with the value estimated from the GR+0.06eV simulation at 2σ level. For the ‘incorrect’ GR+0.06eV model fitted to the F4+0.2eV simulation data, we found that the quality of the fit is as good as that of the ‘correct’ F4+0.2eV model fit, and that the b_1 value recovered is still consistent with the simulation estimate. We identified that this was due to the ‘incorrect’ GR+0.06eV model fit preferring a double peaked parameter distribution. Only for the fit where N had been fixed to 0 did this double peak disappear, the quality of the fit degrade in comparison to the ‘correct’ F4+0.2eV model fit, and the recovered b_1 value become inconsistent with the simulation estimate at the 2σ level. Throughout we observed that the best-fit parameters for the ‘incorrect’ model fits depend significantly on the fitting setup, whereas the ‘correct’ model fits were relatively stable to changes to the fitting setup; this may be useful when constraining $(|f_{R0}|, m_\nu)$. Finally, we investigated the $f(R)$ -massive neutrino degeneracy for the halo redshift-space power spectrum multipoles. In comparison to the CDM+baryon multipoles we investigated in Chapter 3, we found that the difference between the GR+0.06eV and F4+0.2eV halo multipoles measured from the MG-PICOLA simulations is greater, largely due to the effect of the different linear biases on the monopole P_0 . We have demonstrated that the MG-Copter-based model is capable of capturing this difference in the halo multipoles well, although it may become less effective the higher k_{max} is set.

5.2 Future work

So far, our RSD model has been limited by the necessity to fix the values of $(|f_{R0}|, m_\nu)$ as well as the base cosmological parameters. This is necessary because it is necessary to recompute the loop integrals in SPT whenever these parameters are changed, which is extremely time consuming. However, this issue has been overcome in the standard Λ CDM model using the FFTLog approach [231]. The logical next step is to confirm that we can use the computationally inexpensive modelling of RSD in MG-Copter to recover a fiducial combination of $|f_{R0}|$ and m_ν from a mock data set. An important open question for this endeavour is whether the process of fitting σ_v and the bias parameters introduces new degeneracies, where for example σ_v can dampen the redshift-space multipoles of a model with incorrect $|f_{R0}|$ and m_ν values in a way that makes them difficult to distinguish from those of the fiducial simulation. In order to be able to

apply our model to data where the true values of $(|f_{R0}|, m_\nu)$ are unknown, we plan to construct an emulator by interpolating between fits of our model to **MG-PICOLA** simulations for many different values across the $(|f_{R0}|, m_\nu)$ parameter space.

One typical downside to cosmological simulations is the need to specify a particular modified gravity model. However, when using observations to apply constraints, it is generally more effective to have a parameterisation of a class of theories and constrain these parameters. One such example is the α parameterisation of Horndeski modified gravity [250], which is connected to the effective field theory of modified gravity [251]. However, this parameterisation is problematic because it applies only to linear perturbations. To model non-linear structure formation it is necessary to specify a screening model, which narrows the coverage of theory space. As discussed in Appendix C, we have implemented a general $\{m(a), \beta(a)\}$ models [208] in **MG-PICOLA**. We are interested in implementing other parameterisations in **MG-PICOLA** and investigating whether the degeneracy with massive neutrinos persists in other models.

Appendix A

MG-PICOLA implementation details

The main change we need to implement is to account for the scale-dependent growth-factors. This is easily done by storing the Fourier transform of the initial displacement-fields, multiplying by the growth-factors and performing a Fourier transform to get the real-space displacement-fields at every time-step. Having computed the displacement-fields we assign the displacement-vector $\vec{\Psi}(\vec{q}, \tau)$ to the particles. This needs to be done at every step.

An additional complication comes when we run with several processors. The particles require the displacement-field at their original Lagrangian positions so for particles that have crossed a CPU boundary we need inter-CPU communication to obtain this. This is done by storing the original CPU-id and q -coordinate with each particle which requires $8 \cdot N_{\text{particles}}$ bytes of memory. Additional (temporary) memory is needed to store both $\frac{d\vec{\Psi}}{d\tau}$ and $\frac{d^2\vec{\Psi}}{d\tau^2}$ which adds another $12 \cdot 4 = 48$ bytes per particle compared to Λ CDM.

Finally we also need extra memory to store the initial displacement-fields (in k -space), temporary memory to perform the Fourier-transforms, and temporary memory to compute the screening factor. This makes the scale-dependent implementation much more memory expensive than the standard Λ CDM implementation.

Appendix B

Summary of the general equations solved by MG-PICOLA

The fiducial choice for the background expansion is Λ CDM, however it is easy to modify this by redefining the function $H(a)$ and $\frac{dH(a)}{da}$.

For the linear perturbations the user must provide $\mu(k, a)$ (and possibly γ_2 if one has this available, otherwise put this to 0). The growth factors are then determined by

$$\frac{d^2 D_1}{d\tau^2} - \kappa \mu(k, a) D_1 = 0, \quad (\text{B.1})$$

$$\frac{d^2 D_2}{d\tau^2} - \kappa \mu(k, a) D_2 = -\kappa \mu(k, a) D_1^2(k, a) \times \left(1 + \frac{2\gamma_2 a^4 H^2}{\kappa \mu(k, a)} \right). \quad (\text{B.2})$$

For the N -body part of the code we have implemented routines to solve any field equation of the form

$$\nabla_{\mathbf{x}}^2 \phi = m^2(a) a^2 \phi + C(a) \cdot \kappa \delta \cdot \epsilon_{\text{screen}}(\Phi_N, |\vec{\nabla}_{\mathbf{x}} \Phi_N|, \nabla_{\mathbf{x}}^2 \Phi_N), \quad (\text{B.3})$$

where ϕ is normalized such that the total force on the particles is $\vec{\nabla}_{\mathbf{x}} \Phi_N + \vec{\nabla}_{\mathbf{x}} \phi$. This covers the three most widely known screening mechanisms: chameleon, k-Mouflage and Vainhstein. The user can pick any of these three screening methods (i.e. either screening by potential, gradient or density) and the screening-function ϵ_{screen} needs to be specified.

For potential screening this is done automatically by the code (see next section) as long as the user specifies the two functions $m(a)$ and $\beta(a)$ (and in this case $C(a) = 2\beta^2(a)$).

For gradient (k-Mouflage) screening arising from $P(X = \frac{1}{2}(\nabla_{\mathbf{x}} \phi)^2)$ Lagrangians with a conformal coupling to matter of the form $e^{\frac{\beta \phi}{M_{\text{Pl}}}}$ then the screening function is

determined by

$$P_X^2(X_*)X_* = (2\beta M_{\text{Pl}})^2 |\vec{\nabla}_{\mathbf{x}} \Phi_N|^2, \quad (\text{B.4})$$

$$\epsilon_{\text{screen}}(|\vec{\nabla}_{\mathbf{x}} \Phi_N|) = \text{Min} \left[1, \frac{1}{P_X(X_*)} \right]. \quad (\text{B.5})$$

For these models we have $C(a) = 2\beta^2$ and the linear growth factor is determined by $\mu = \frac{2\beta^2}{P_X(X(a))}$ where $X(a)$ is the cosmological value of X . As no N-body simulation of these types of models is found in the literature we have not yet tested this approach, but all of the methods needed have been included in the code and one only needs to provide an expression for $X_*(|\vec{\nabla}_{\mathbf{x}} \Phi_N|^2)$ and $X(a)$ to use it.

For Vainshtein screening (DGP, Galileon models) one needs to specify $\epsilon_{\text{screen}}(\nabla_{\mathbf{x}}^2 \Phi_N \propto \rho)$ and the coupling $C(a)$ which for nDGP is simply $C(a) = \frac{1}{3\beta_{\text{DGP}}(a)}$ as shown in Eq. (2.64). For these models we have $m(a) = 0$, i.e. the range of the fifth-force is infinite. Since the density is highly resolution dependent we need to use a smoothed density field to compute the screening. We have implemented three common choices for the Fourier space smoothing filter, namely the Gaussian, top-hat and sharp- k window functions. The user only needs to choose a smoothing filter and a smoothing scale R_{smooth} .

Appendix C

MG-PICOLA implementation of general $\{m(a), \beta(a)\}$ models

As shown in [208] a general scalar-tensor theory with a potential and a conformal coupling to matter that shows the screening effect is uniquely defined by specifying two time-dependent functions on the cosmological background: the coupling strength of the fifth-force $\beta(a)$ and the mass of the scale (inverse range of the fifth-force) $m(a)$. Given these functions we can reconstruct the potential $V(\phi)$ and the conformal coupling $A(\phi)$. Examples of models of this form are the chameleon, the symmetron, and the environmental dependent dilaton model. N -body simulations for several different functional forms of $m(a)$ and $\beta(a)$ were performed in [252, 253].

Here we will describe the implementation of a general $\{m(a), \beta(a)\}$ model in our code. At the level of linear perturbations we have

$$\mu(k, a) = 1 + 2\beta^2(a) \frac{k^2}{k^2 + a^2 m^2(a)} , \quad (\text{C.1})$$

and to second order we have

$$\gamma_2^{\text{E}} = \frac{m^2(a) \frac{dm^2(a)}{da} \beta^2(a) \Omega_m}{2H_0^4 \Pi(k) \Pi(k_1) \Pi(k_2)} \frac{k^2}{a^4 H^2} , \quad (\text{C.2})$$

where $\Pi(k) = \left(\frac{k}{aH_0}\right)^2 + \frac{m^2(a)}{H_0^2}$. For the N -body part the field equation reads

$$\nabla_{\mathbf{x}}^2 \phi = m^2(a) a^2 \phi + 2\beta^2(a) \cdot 4\pi G \delta\rho \cdot \epsilon_{\text{screen}}(\Phi_N) , \quad (\text{C.3})$$

where ϕ is normalized such that $\vec{\nabla}_{\mathbf{x}} \Phi_N + \vec{\nabla}_{\mathbf{x}} \phi$ is the total force on the particles. The screening function is given by

$$\epsilon_{\text{screen}}(\Phi_N) = \text{Min} \left[1, \left| \frac{\Phi_{\text{crit}}(a)}{\Phi_N} \right| \right] , \quad (\text{C.4})$$

where the critical potential for screening is

$$\Phi_{\text{crit}}(a) = \Phi_{\text{crit}}(a_{\text{ini}}) + \frac{9\Omega_m}{2\beta(a)} \int_{a_{\text{ini}}}^a \frac{\beta(a')}{\frac{m^2(a')}{H_0^2} a^4} da'. \quad (\text{C.5})$$

The code solves the integral above for $\Phi_{\text{crit}}(a)$, however if analytical expressions are available then it's recommended to use these instead.

For example the ($n = 1$) Hu-Sawicky $f(R)$ model can be recast of this form with

$$\beta(a) = \frac{1}{\sqrt{6}}, \quad (\text{C.6})$$

$$m^2(a) = H_0^2 \frac{\Omega_m + 4\Omega_\Lambda}{2|f_{R0}|} \left(\frac{\Omega_m a^{-3} + 4\Omega_\Lambda}{\Omega_m + 4\Omega_\Lambda} \right)^3, \quad (\text{C.7})$$

and the integral above gives rise to (in the limit $a_{\text{ini}} \rightarrow 0$)

$$\Phi_{\text{crit}}(a) = \frac{3f_{R0}}{2} \left(\frac{\Omega_m a^{-3} + 4\Omega_\Lambda}{\Omega_m + 4\Omega_\Lambda} \right)^2. \quad (\text{C.8})$$

Another example is the symmetron model for which

$$\beta(a) = \beta_* \sqrt{1 - \frac{a_*^3}{a^3}}, \quad (\text{C.9})$$

$$m^2(a) = m_*^2 \left(1 - \frac{a_*^3}{a^3} \right), \quad (\text{C.10})$$

where β_* , $\frac{m_*}{H_0}$, a_* are dimensionless parameters and we take $\beta(a) = m(a) = 0$ if $a < a_*$. The critical screening value becomes (we put $a_{\text{ini}} = a_*$ as the fifth-force is not active for $a < a_*$)

$$\Phi_{\text{crit}}(a) = \frac{3\Omega_m}{2a_*^3} \frac{H_0^2}{m_*^2}. \quad (\text{C.11})$$

In this simple formulation we have ignored the additional screening effect in high density regions coming from the fact that $\beta(\phi) \rightarrow 0$ as the ambient density gets larger and larger. This illustrates how easy it is to include a new model of this form.

Appendix D

Modified gravity models

In this section we give a brief overview of the modified gravity models we are using in our research, focusing on the equations that are needed for our COLA implementation. For a more thorough review of these models, and modified gravity in general, see [51, 52].

D.1 $f(R)$ gravity

For $f(R)$ gravity [254] the growth of linear perturbations is determined by

$$\mu_{\text{MG}}(k, a) = 1 + \frac{1}{3} \frac{k^2}{k^2 + a^2 m^2(a)}, \quad (\text{D.1})$$

where $m(a)$ depends on the model in question. For the Hu-Sawicki model [255], which is the $f(R)$ model we will consider in our research, $m(a)$ is given by

$$m^2(a) = \frac{1}{3f_{RR}} = \frac{H_0^2(\Omega_{\text{m}} + 4\Omega_{\Lambda})}{(n+1)|f_{R0}|} \left(\frac{\Omega_{\text{m}} a^{-3} + 4\Omega_{\Lambda}}{\Omega_{\text{m}} + 4\Omega_{\Lambda}} \right)^{n+2}, \quad (\text{D.2})$$

where

$$f_R(a) = f_{R0} \left(\frac{\Omega_{\text{m}} + 4\Omega_{\Lambda}}{\Omega_{\text{m}} a^{-3} + 4\Omega_{\Lambda}} \right)^{n+1}. \quad (\text{D.3})$$

The γ_2^E factor is likewise given by [140]

$$\gamma_2^E = -\frac{9\Omega_{\text{m}}^2}{48a^6|f_{R0}|^2} \left(\frac{k}{aH} \right)^2 \times \frac{(\Omega_{\text{m}} a^{-3} + 4\Omega_{\Lambda})^5}{(\Omega_{\text{m}} + 4\Omega_{\Lambda})^4} \frac{1}{\Pi(k, a)\Pi(k_1, a)\Pi(k_2, a)}, \quad (\text{D.4})$$

where

$$\Pi(k, a) = \left(\frac{k}{aH_0} \right)^2 + \frac{(\Omega_{\text{m}} a^{-3} + 4\Omega_{\Lambda})^3}{2|f_{R0}|(\Omega_{\text{m}} + 4\Omega_{\Lambda})^2}. \quad (\text{D.5})$$

D.2 nDGP gravity

In nDGP we have a Λ CDM background expansion, but with modified growth of perturbations. The growth of linear perturbations are determined by

$$\mu(k, a) = 1 + \frac{1}{3\beta_{\text{DGP}}(a)}, \quad (\text{D.6})$$

$$\beta_{\text{DGP}}(a) = 1 + 2r_c H(a) \left(1 + \frac{\dot{H}}{3H^2} \right), \quad (\text{D.7})$$

and γ_2^E is given by [256]

$$\gamma_2^E = - \left(\frac{H_0}{H} \right)^2 \frac{(r_c H_0)^2 \Omega_m^2}{6\beta_{\text{DGP}}^3(a) a^6} \left(1 - \frac{(\vec{k}_1 \cdot \vec{k}_2)^2}{k_1^2 k_2^2} \right). \quad (\text{D.8})$$

For this model, and likely for Galileons in general, the γ_2 terms have the same k_1, k_2 dependence as in Λ CDM so the second order growth-factor becomes a function of time only. This means that it behaves just as Λ CDM albeit with different growth-factors.

D.3 Symmetron

In the symmetron model [203]:

$$\mu_{\text{MG}}(k, a) = 1 + \frac{2\beta^2(a)k^2}{k^2 + a^2 m^2(a)}, \quad (\text{D.9})$$

$$\begin{aligned} \gamma_2^E(k, a) &= \frac{m^2(a) \frac{dm^2(a)}{da} \beta^2(a) \Omega_m}{2H_0^4 \Pi(k, a) \Pi(k_1, a) \Pi(k_2, a)} \frac{k^2}{a^4 H^2} \\ &= \frac{3\Omega_m \beta_\star^2}{2\xi_\star^4} \frac{a_\star^3 k^2}{a^8 H^2 \Pi(k, a) \Pi(k_1, a) \Pi(k_2, a)} \left(1 - \frac{a_\star^3}{a^3} \right)^2, \end{aligned} \quad (\text{D.10})$$

if $a > a_\star$ and 0 otherwise where

$$\beta(a) = \begin{cases} \beta_\star \sqrt{1 - \frac{a_\star^3}{a^3}} & \text{if } a > a_\star \\ 0 & \text{otherwise} \end{cases}, \quad (\text{D.11})$$

$$m(a) = \begin{cases} \frac{H_0}{\xi_\star} \sqrt{1 - \frac{a_\star^3}{a^3}} & \text{if } a > a_\star \\ 0 & \text{otherwise} \end{cases}. \quad (\text{D.12})$$

D.4 Dilaton

In the dilaton model [257]:

$$\mu_{\text{MG}}(k, a) = 1 + \frac{2\beta^2(a)k^2}{k^2 + a^2m^2(a)} , \quad (\text{D.13})$$

$$\begin{aligned} \gamma_2^{\text{E}}(k, a) &= \frac{m^2(a) \frac{dm^2(a)}{da} \beta^2(a) \Omega_m}{2H_0^4 \Pi(k, a) \Pi(k_1, a) \Pi(k_2, a)} \frac{k^2}{a^4 H^2} \\ &= -\frac{R\beta_0^2 \Omega_m}{\xi_0^4} \frac{k^2}{a^{5+4R} H^2 \Pi(k, a) \Pi(k_1, a) \Pi(k_2, a)} \exp^{\frac{2S}{2R-3}(a^{2R-3}-1)} , \end{aligned} \quad (\text{D.14})$$

where

$$\beta(a) = \beta_0 \exp^{\frac{S}{2R-3}(a^{2R-3}-1)} , \quad (\text{D.15})$$

$$m(a) = \frac{H_0}{\xi_0} a^{-R} . \quad (\text{D.16})$$

Appendix E

Comparison of MG-PICOLA neutrino approach to SPT and alternative schemes for modelling the non-linear neutrino density

In this appendix we show a comparison of our code with linear theory and standard perturbation theory (SPT). The SPT results were obtained by following the method of [213] using the Einstein-de Sitter approximation. We have also carried out a test using an alternative scheme to include the neutrino density in the Poisson equation, Eq. (2.70). In this scheme we use

$$\delta_\nu = \delta_{cb} \frac{\delta_\nu^{\text{lin}}}{\delta_{cb}^{\text{lin}}} , \quad (\text{E.1})$$

where δ_{cb} is the non-linear CDM+baryon density contrast. Here the ratio of the non-linear neutrino and CDM+baryon density contrasts is approximated by the linear ratio of the two, instead of simply having $\delta_\nu = \delta_\nu^{\text{lin}}$ as we had previously. This alternative scheme is what [215] calls the improved external source scheme.

Fig. (E.1) shows that our implementation gives a result for the total matter power spectrum that lies between SPT and linear theory on quasi-linear scales. The differences we see with respect to SPT for the slightly larger wavenumbers is expected (see Fig. (10) in [215]) as SPT slightly underestimates the power on these scales. The improved external source scheme is seen to slightly overestimate the power on linear scales and generally performs slightly worse on linear scales and at low redshift than the scheme we have used in this research, especially for larger values of the neutrino mass.

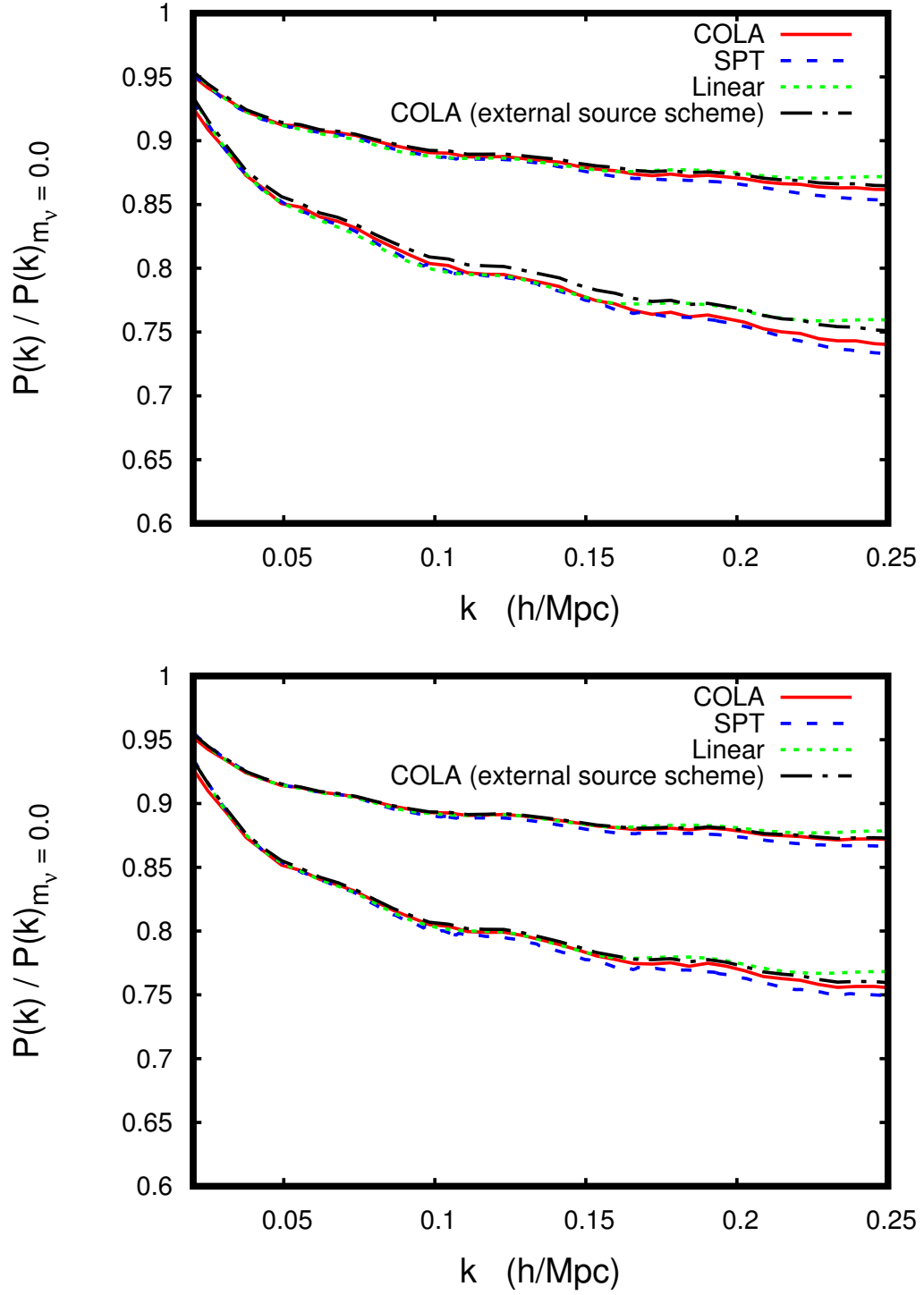


Figure E.1: The total matter power spectrum for a GR+ m_ν cosmology relative to the GR case where $m_\nu = 0.0$ at $z = 0.0$ (above) and $z = 1.0$ (below). We show the results of a COLA run compared to linear theory, SPT and what we get when we use the external source scheme in COLA. The upper lines in each figure shows the results for $m_\nu = 0.2$ eV and the lower lines shows the results for $m_\nu = 0.4$ eV.

Additionally, [215] warns of inaccuracies at large scales when treating neutrinos in a purely linear way with $\delta_\nu = \delta_\nu^{\text{lin}}$ as a consequence of violation of momentum conservation. This can be seen as large deviation from the full non-linear scheme at large scales due to D_2 not vanishing as $k \rightarrow 0$. [215] showed that the previously mentioned improved external source scheme reduces the deviation at large scales, but does not completely eliminate it. However, although such inaccuracies would appear from Eqs. (2.47) and (2.55), our method does not suffer from them because the approximations we make to maintain the speed of our COLA approach in Eqs. (2.48) and (2.59) demand that $D_{2,\text{cb}}(\vec{k}, \vec{k}_1, \vec{k}_2, \tau) = \left(1 - \frac{(\vec{k}_1 \cdot \vec{k}_2)^2}{k_1^2 k_2^2}\right) \hat{D}_{2,\text{cb}}(k, \tau) \rightarrow 0$ as $k \rightarrow 0$.

FORM UPR16

Research Ethics Review Checklist

Please include this completed form as an appendix to your thesis (see the Research Degrees Operational Handbook for more information)



Postgraduate Research Student (PGRS) Information		Student ID:	UP833865
PGRS Name:	William Simcoe Wright		
Department:	ICG, Technology	First Supervisor:	Kazuya Koyama
Start Date: (or progression date for Prof Doc students)	01/10/2016		
Study Mode and Route:	Part-time <input type="checkbox"/> Full-time <input checked="" type="checkbox"/>	MPhil <input type="checkbox"/> PhD <input checked="" type="checkbox"/>	MD <input type="checkbox"/> Professional Doctorate <input type="checkbox"/>

Title of Thesis:	Modelling non-linear structure formation with modified gravity and massive neutrinos
Thesis Word Count: (excluding ancillary data)	27,121

If you are unsure about any of the following, please contact the local representative on your Faculty Ethics Committee for advice. Please note that it is your responsibility to follow the University's Ethics Policy and any relevant University, academic or professional guidelines in the conduct of your study

Although the Ethics Committee may have given your study a favourable opinion, the final responsibility for the ethical conduct of this work lies with the researcher(s).

UKRIO Finished Research Checklist:

(If you would like to know more about the checklist, please see your Faculty or Departmental Ethics Committee rep or see the online version of the full checklist at: <http://www.ukrio.org/what-we-do/code-of-practice-for-research/>)

a) Have all of your research and findings been reported accurately, honestly and within a reasonable time frame?	YES <input checked="" type="checkbox"/> NO <input type="checkbox"/>
b) Have all contributions to knowledge been acknowledged?	YES <input checked="" type="checkbox"/> NO <input type="checkbox"/>
c) Have you complied with all agreements relating to intellectual property, publication and authorship?	YES <input checked="" type="checkbox"/> NO <input type="checkbox"/>
d) Has your research data been retained in a secure and accessible form and will it remain so for the required duration?	YES <input checked="" type="checkbox"/> NO <input type="checkbox"/>
e) Does your research comply with all legal, ethical, and contractual requirements?	YES <input checked="" type="checkbox"/> NO <input type="checkbox"/>

Candidate Statement:

I have considered the ethical dimensions of the above named research project, and have successfully obtained the necessary ethical approval(s)

Ethical review number(s) from Faculty Ethics Committee (or from NRES/SCREC):	AE46-D529-A06E-C8C2-0DB2-EA64-17FC-F739
---	---

If you have *not* submitted your work for ethical review, and/or you have answered 'No' to one or more of questions a) to e), please explain below why this is so:

Signed (PGRS):	<i>William Wright</i>	Date:	16/12/2019
-----------------------	-----------------------	--------------	------------



Certificate of Ethics Review

Project Title:	Non-linear structure formation in modified gravity models
User ID:	833865
Name:	William Simcoe Wright
Application Date:	15/09/2017 15:30:48

You must download your certificate, print a copy and keep it as a record of this review.

It is your responsibility to adhere to the University Ethics Policy and any Department/School or professional guidelines in the conduct of your study including relevant guidelines regarding health and safety of researchers and University Health and Safety Policy.

It is also your responsibility to follow University guidance on Data Protection Policy:

- General guidance for all data protection issues
- University Data Protection Policy

You are reminded that as a University of Portsmouth Researcher you are bound by the UKRIO Code of Practice for Research; any breach of this code could lead to action being taken following the University's Procedure for the Investigation of Allegations of Misconduct in Research.

Any changes in the answers to the questions reflecting the design, management or conduct of the research over the course of the project must be notified to the Faculty Ethics Committee. Any changes that affect the answers given in the questionnaire, not reported to the Faculty Ethics Committee, will invalidate this certificate.

This ethical review should not be used to infer any comment on the academic merits or methodology of the project. If you have not already done so, you are advised to develop a clear protocol/proposal and ensure that it is independently reviewed by peers or others of appropriate standing. A favourable ethical opinion should not be perceived as permission to proceed with the research; there might be other matters of governance which require further consideration including the agreement of any organisation hosting the research.

GovernanceChecklist

A1-BriefDescriptionOfProject: We will investigate the effects of modified gravity on non-linear structure formation using theory, computation, and possibly comparison to astronomical data.

A2-Faculty: Technology

A3-VoluntarilyReferToFEC: No

A5-AlreadyExternallyReviewed: No

B1-HumanParticipants: No

HumanParticipantsDefinition

Certificate Code: AE46-D529-A06E-C8C2-0DB2-EA64-17FC-F739 Page 1

B2-HumanParticipantsConfirmation: Yes
C6-SafetyRisksBeyondAssessment: No
D2-PhysicalEcologicalDamage: No
D4-HistoricalOrCulturalDamage: No
E1-ContentiousOrIllegal: No
E2-SociallySensitiveIssues: No
F1-InvolvesAnimals: No
F2-HarmfulToThirdParties: No
G1-ConfirmReadEthicsPolicy: Confirmed
G2-ConfirmReadUKRIOCodeOfPractice: Confirmed
G3-ConfirmReadConcordatToSupportResearchIntegrity: Confirmed
G4-ConfirmedCorrectInformation: Confirmed

Bibliography

- [1] A. Font-Ribera, P. McDonald, N. Mostek, B. A. Reid, H.-J. Seo and A. Slosar, *DESI and other Dark Energy experiments in the era of neutrino mass measurements*, *Journal of Cosmology and Astro-Particle Physics* **2014** (May, 2014) 023, [1308.4164].
- [2] M. Baldi, F. Villaescusa-Navarro, M. Viel, E. Puchwein, V. Springel and L. Moscardini, *Cosmic degeneracies - I. Joint N-body simulations of modified gravity and massive neutrinos*, *MNRAS* **440** (May, 2014) 75–88, [1311.2588].
- [3] A. G. Lemaître, *Contributions to a British Association Discussion on the Evolution of the Universe.*, *Nature* **128** (Oct., 1931) 704–706.
- [4] A. A. Starobinsky, *A new type of isotropic cosmological models without singularity*, *Physics Letters B* **91** (Mar., 1980) 99–102.
- [5] A. H. Guth, *Inflationary universe: A possible solution to the horizon and flatness problems*, *PRD* **23** (Jan., 1981) 347–356.
- [6] K. Sato, *First-order phase transition of a vacuum and the expansion of the Universe*, *MNRAS* **195** (May, 1981) 467–479.
- [7] A. D. Linde, *A new inflationary universe scenario: A possible solution of the horizon, flatness, homogeneity, isotropy and primordial monopole problems*, *Physics Letters B* **108** (Feb., 1982) 389–393.
- [8] A. Linde, *Inflationary Cosmology*, in *Inflationary Cosmology* (M. Lemoine, J. Martin and P. Peter, eds.), vol. 738 of *Lecture Notes in Physics*, Berlin Springer Verlag, p. 1, 2008. 0705.0164. DOI.
- [9] D. Baumann and H. V. Peiris, *Cosmological Inflation: Theory and Observations*, *ArXiv e-prints* (Oct., 2008) , [0810.3022].
- [10] A. A. Starobinskii, *Spectrum of relict gravitational radiation and the early state of the universe*, *ZhETF Pisma Redaktsiiu* **30** (Dec., 1979) 719–723.

- [11] V. F. Mukhanov and G. V. Chibisov, *Quantum fluctuations and a nonsingular universe*, *ZhETF Pisma Redaktsiiu* **33** (May, 1981) 549–553.
- [12] S. W. Hawking, *The development of irregularities in a single bubble inflationary universe*, *Physics Letters B* **115** (Sept., 1982) 295–297.
- [13] A. A. Starobinsky, *Dynamics of phase transition in the new inflationary universe scenario and generation of perturbations*, *Physics Letters B* **117** (Nov., 1982) 175–178.
- [14] A. H. Guth and S.-Y. Pi, *Fluctuations in the new inflationary universe*, *Physical Review Letters* **49** (Oct., 1982) 1110–1113.
- [15] J. M. Bardeen, P. J. Steinhardt and M. S. Turner, *Spontaneous creation of almost scale-free density perturbations in an inflationary universe*, *PRD* **28** (Aug., 1983) 679–693.
- [16] A. A. Penzias and R. W. Wilson, *A Measurement of Excess Antenna Temperature at 4080 Mc/s.*, *ApJ* **142** (July, 1965) 419–421.
- [17] D. J. Fixsen, G. Hinshaw, C. L. Bennett and J. C. Mather, *The Spectrum of the Cosmic Microwave Background Anisotropy from the Combined COBE FIRAS and DMR Observations*, *ApJ* **486** (Sept., 1997) 623–628, [[astro-ph/9704176](#)].
- [18] C. L. Bennett, D. Larson, J. L. Weiland, N. Jarosik, G. Hinshaw, N. Odegard et al., *Nine-year Wilkinson Microwave Anisotropy Probe (WMAP) Observations: Final Maps and Results*, *ApJS* **208** (Oct., 2013) 20, [[1212.5225](#)].
- [19] Planck Collaboration, R. Adam, P. A. R. Ade, N. Aghanim, Y. Akrami, M. I. R. Alves et al., *Planck 2015 results. I. Overview of products and scientific results*, *A&A* **594** (Sept., 2016) A1, [[1502.01582](#)].
- [20] L. Kofman, A. Linde and A. A. Starobinsky, *Reheating after inflation*, *Physical Review Letters* **73** (Dec., 1994) 3195–3198, [[hep-th/9405187](#)].
- [21] B. A. Bassett, S. Tsujikawa and D. Wands, *Inflation dynamics and reheating*, *Reviews of Modern Physics* **78** (Apr., 2006) 537–589, [[astro-ph/0507632](#)].
- [22] R. Allahverdi, R. Brandenberger, F.-Y. Cyr-Racine and A. Mazumdar, *Reheating in Inflationary Cosmology: Theory and Applications*, *Annual Review of Nuclear and Particle Science* **60** (Nov., 2010) 27–51, [[1001.2600](#)].

- [23] PARTICLE DATA GROUP collaboration, M. Tanabashi et al., *Review of Particle Physics*, *Phys. Rev.* **D98** (2018) 030001.
- [24] W. H. Press and P. Schechter, *Formation of Galaxies and Clusters of Galaxies by Self-Similar Gravitational Condensation*, *ApJ* **187** (Feb., 1974) 425–438.
- [25] J. R. Bond, L. Kofman and D. Pogosyan, *How filaments of galaxies are woven into the cosmic web*, *Nature* **380** (Apr., 1996) 603–606, [astro-ph/9512141].
- [26] R. van de Weygaert, S. Shandarin, E. Saar and J. Einasto, eds., *The Zeldovich Universe: Genesis and Growth of the Cosmic Web*, vol. 308 of *IAU Symposium*, Oct., 2016. 10.1017/S174392131601098X.
- [27] A. J. Benson, *Galaxy formation theory*, *Physics Reports* **495** (Oct., 2010) 33–86, [1006.5394].
- [28] V. Desjacques, D. Jeong and F. Schmidt, *Large-Scale Galaxy Bias*, *ArXiv e-prints* (Nov., 2016) , [1611.09787].
- [29] M. Bartelmann and P. Schneider, *Weak gravitational lensing*, *Physics Reports* **340** (Jan., 2001) 291–472, [astro-ph/9912508].
- [30] M. Kilbinger, *Cosmology with cosmic shear observations: a review*, *Reports on Progress in Physics* **78** (July, 2015) 086901, [1411.0115].
- [31] A. G. Riess, A. V. Filippenko, P. Challis, A. Clocchiatti, A. Diercks, P. M. Garnavich et al., *Observational evidence from supernovae for an accelerating universe and a cosmological constant*, *The Astrophysical Journal* **116** (Sept., 1998) 1009–1038, [astro-ph/9805201].
- [32] S. Perlmutter, G. Aldering, G. Goldhaber, R. A. Knop, P. Nugent, P. G. Castro et al., *Measurements of Ω and Λ from 42 high-redshift supernovae*, *The Astrophysical Journal* **517** (June, 1999) 565–586, [astro-ph/9812133].
- [33] Planck Collaboration, N. Aghanim, Y. Akrami, M. Ashdown, J. Aumont, C. Baccigalupi et al., *Planck 2018 results. VI. Cosmological parameters*, *arXiv e-prints* (Jul, 2018) arXiv:1807.06209, [1807.06209].
- [34] M. Ata, F. Baumgarten, J. Bautista, F. Beutler, D. Bizyaev, M. R. Blanton et al., *The clustering of the SDSS-IV extended Baryon Oscillation Spectroscopic Survey DR14 quasar sample: first measurement of baryon acoustic oscillations between redshift 0.8 and 2.2*, *MNRAS* **473** (Feb, 2018) 4773–4794, [1705.06373].

- [35] H. Gil-Marín, J. Guy, P. Zarrouk, E. Burtin, C.-H. Chuang, W. J. Percival et al., *The clustering of the SDSS-IV extended Baryon Oscillation Spectroscopic Survey DR14 quasar sample: structure growth rate measurement from the anisotropic quasar power spectrum in the redshift range $0.8 < z < 2.2$* , *MNRAS* **477** (Jun, 2018) 1604–1638, [1801.02689].
- [36] J. Hou, A. G. Sánchez, R. Scoccimarro, S. Salazar-Albornoz, E. Burtin, H. Gil-Marín et al., *The clustering of the SDSS-IV extended Baryon Oscillation Spectroscopic Survey DR14 quasar sample: anisotropic clustering analysis in configuration space*, *MNRAS* **480** (Oct, 2018) 2521–2534, [1801.02656].
- [37] F. Köhlinger, M. Viola, B. Joachimi, H. Hoekstra, E. van Uitert, H. Hildebrandt et al., *KiDS-450: the tomographic weak lensing power spectrum and constraints on cosmological parameters*, *MNRAS* **471** (Nov, 2017) 4412–4435, [1706.02892].
- [38] T. M. C. Abbott, F. B. Abdalla, A. Alarcon, J. Aleksić, S. Allam, S. Allen et al., *Dark Energy Survey year 1 results: Cosmological constraints from galaxy clustering and weak lensing*, *PRD* **98** (Aug, 2018) 043526, [1708.01530].
- [39] L. Knox and M. Millea, *The Hubble Hunter’s Guide*, *arXiv e-prints* (Aug, 2019) arXiv:1908.03663, [1908.03663].
- [40] E. Macaulay, I. K. Wehus and H. K. Eriksen, *Lower Growth Rate from Recent Redshift Space Distortion Measurements than Expected from Planck*, *PRL* **111** (Oct, 2013) 161301, [1303.6583].
- [41] H. Hildebrandt, F. Köhlinger, J. L. van den Busch, B. Joachimi, C. Heymans, A. Kannawadi et al., *KiDS+VIKING-450: Cosmic shear tomography with optical+infrared data*, *arXiv e-prints* (Dec, 2018) arXiv:1812.06076, [1812.06076].
- [42] W. Handley, *Curvature tension: evidence for a closed universe*, *arXiv e-prints* (Aug, 2019) arXiv:1908.09139, [1908.09139].
- [43] E. Di Valentino, A. Melchiorri and J. Silk, *Planck evidence for a closed Universe and a possible crisis for cosmology*, *arXiv e-prints* (Nov, 2019) arXiv:1911.02087, [1911.02087].
- [44] C. M. Will, *The Confrontation between General Relativity and Experiment*, *Living Reviews in Relativity* **17** (June, 2014) 4, [1403.7377].

- [45] C. Isham, *Structural Issues in Quantum Gravity*, *ArXiv General Relativity and Quantum Cosmology e-prints* (Oct., 1995) , [gr-qc/9510063].
- [46] R. P. Woodard, *How far are we from the quantum theory of gravity?*, *Reports on Progress in Physics* **72** (Dec., 2009) 126002, [0907.4238].
- [47] Y.-Y. Xu and X. Zhang, *Comparison of dark energy models after Planck 2015*, *European Physical Journal C* **76** (Nov., 2016) 588, [1607.06262].
- [48] A. Heavens, Y. Fantaye, E. Sellentin, H. Eggers, Z. Hosenie, S. Kroon et al., *No evidence for extensions to the standard cosmological model*, *ArXiv e-prints* (Apr., 2017) , [1704.03467].
- [49] S. Weinberg, *The cosmological constant problem*, *Reviews of Modern Physics* **61** (Jan., 1989) 1–23.
- [50] H. E. S. Velten, R. F. vom Marttens and W. Zimdahl, *Aspects of the cosmological “coincidence problem”*, *European Physical Journal C* **74** (Nov., 2014) 3160, [1410.2509].
- [51] T. Clifton, P. G. Ferreira, A. Padilla and C. Skordis, *Modified gravity and cosmology*, *Physics Reports* **513** (Mar., 2012) 1–189, [1106.2476].
- [52] K. Koyama, *Cosmological tests of modified gravity*, *Reports on Progress in Physics* **79** (Apr., 2016) 046902, [1504.04623].
- [53] D. Lovelock, *The Einstein Tensor and Its Generalizations*, *Journal of Mathematical Physics* **12** (Mar., 1971) 498–501.
- [54] D. Lovelock, *The Four-Dimensionality of Space and the Einstein Tensor*, *Journal of Mathematical Physics* **13** (June, 1972) 874–876.
- [55] C. Brans and R. H. Dicke, *Mach’s Principle and a Relativistic Theory of Gravitation*, *Physical Review* **124** (Nov., 1961) 925–935.
- [56] C. H. Brans, *Mach’s Principle and a Relativistic Theory of Gravitation. II*, *Physical Review* **125** (Mar., 1962) 2194–2201.
- [57] H. A. Buchdahl, *Non-linear Lagrangians and cosmological theory*, *MNRAS* **150** (1970) 1.
- [58] G. Dvali, G. Gabadadze and M. Porrati, *4D gravity on a brane in 5D Minkowski space*, *Physics Letters B* **485** (July, 2000) 208–214, [hep-th/0005016].

- [59] P. Brax, *Screening mechanisms in modified gravity*, *Class. Quant. Grav.* **30** (2013) 214005.
- [60] Y. L. Bolotin, A. Kostenko, O. A. Lemets and D. A. Yerokhin, *Cosmological evolution with interaction between dark energy and dark matter*, *International Journal of Modern Physics D* **24** (Dec., 2015) 1530007, [1310.0085].
- [61] B. Wang, E. Abdalla, F. Atrio-Barandela and D. Pavón, *Dark matter and dark energy interactions: theoretical challenges, cosmological implications and observational signatures*, *Reports on Progress in Physics* **79** (Sept., 2016) 096901, [1603.08299].
- [62] J. Khoury and A. Weltman, *Chameleon Fields: Awaiting Surprises for Tests of Gravity in Space*, *Physical Review Letters* **93** (Oct., 2004) 171104, [astro-ph/0309300].
- [63] J. Khoury and A. Weltman, *Chameleon cosmology*, *PRD* **69** (Feb., 2004) 044026, [astro-ph/0309411].
- [64] P. Brax, C. van de Bruck, A.-C. Davis and D. Shaw, *Dilaton and modified gravity*, *PRD* **82** (Sept., 2010) 063519, [1005.3735].
- [65] K. Hinterbichler and J. Khoury, *Screening Long-Range Forces through Local Symmetry Restoration*, *Physical Review Letters* **104** (June, 2010) 231301, [1001.4525].
- [66] E. Babichev, C. Deffayet and R. Ziour, *k-MOUFLAGE Gravity*, *International Journal of Modern Physics D* **18** (2009) 2147–2154, [0905.2943].
- [67] A. I. Vainshtein, *To the problem of nonvanishing gravitation mass*, *Physics Letters B* **39** (May, 1972) 393–394.
- [68] B. P. Abbott, R. Abbott, T. D. Abbott, F. Acernese, K. Ackley, C. Adams et al., *Gravitational Waves and Gamma-Rays from a Binary Neutron Star Merger: GW170817 and GRB 170817A*, *ApJL* **848** (Oct, 2017) L13, [1710.05834].
- [69] L. Lombriser and N. A. Lima, *Challenges to self-acceleration in modified gravity from gravitational waves and large-scale structure*, *Physics Letters B* **765** (Feb, 2017) 382–385, [1602.07670].

- [70] D. Bettoni, J. M. Ezquiaga, K. Hinterbichler and M. Zumalacárregui, *Speed of gravitational waves and the fate of scalar-tensor gravity*, *PRD* **95** (Apr, 2017) 084029, [1608.01982].
- [71] P. Creminelli and F. Vernizzi, *Dark Energy after GW170817 and GRB170817A*, *PRL* **119** (Dec, 2017) 251302, [1710.05877].
- [72] J. Sakstein and B. Jain, *Implications of the Neutron Star Merger GW170817 for Cosmological Scalar-Tensor Theories*, *PRL* **119** (Dec, 2017) 251303, [1710.05893].
- [73] J. M. Ezquiaga and M. Zumalacárregui, *Dark Energy After GW170817: Dead Ends and the Road Ahead*, *PRL* **119** (Dec, 2017) 251304, [1710.05901].
- [74] T. Baker, E. Bellini, P. G. Ferreira, M. Lagos, J. Noller and I. Sawicki, *Strong Constraints on Cosmological Gravity from GW170817 and GRB 170817A*, *PRL* **119** (Dec, 2017) 251301, [1710.06394].
- [75] M. Crisostomi and K. Koyama, *Self-accelerating universe in scalar-tensor theories after GW170817*, *PRD* **97** (Apr, 2018) 084004, [1712.06556].
- [76] S. Peirone, K. Koyama, L. Pogosian, M. Raveri and A. Silvestri, *Large-scale structure phenomenology of viable Horndeski theories*, *PRD* **97** (Feb, 2018) 043519, [1712.00444].
- [77] W. Hu and I. Sawicki, *Models of $f(R)$ cosmic acceleration that evade solar system tests*, *PRD* **76** (Sept., 2007) 064004, [0705.1158].
- [78] M. A. Luty, M. Porrati and R. Rattazzi, *Strong interactions and stability in the DGP model*, *Journal of High Energy Physics* **2003** (Sep, 2003) 029, [hep-th/0303116].
- [79] A. Nicolis, R. Rattazzi and E. Trincherini, *Galileon as a local modification of gravity*, *PRD* **79** (Mar, 2009) 064036, [0811.2197].
- [80] K. Koyama, *Ghosts in the self-accelerating brane universe*, *PRD* **72** (Dec, 2005) 123511, [hep-th/0503191].
- [81] D. Gorbunov, K. Koyama and S. Sibiryakov, *More on ghosts in the Dvali-Gabadaze-Porrati model*, *PRD* **73** (Feb, 2006) 044016, [hep-th/0512097].
- [82] K. Koyama, *TOPICAL REVIEW: Ghosts in the self-accelerating universe*, *Classical and Quantum Gravity* **24** (Dec, 2007) R231–R253, [0709.2399].

- [83] C. Charmousis, R. Gregory, N. Kaloper and A. Padilla, *DGP spectroscopy*, *Journal of High Energy Physics* **2006** (Oct, 2006) 066, [[hep-th/0604086](#)].
- [84] K. Koyama, *Structure formation in modified gravity models*, *JCAP* **3** (Mar., 2006) 017, [[astro-ph/0601220](#)].
- [85] P. Brax and P. Valageas, *Structure formation in modified gravity scenarios*, *PRD* **86** (Sept., 2012) 063512, [[1205.6583](#)].
- [86] B. S. Wright and B. Li, *Type Ia supernovae, standardizable candles, and gravity*, *PRD* **97** (Apr, 2018) 083505, [[1710.07018](#)].
- [87] E. Taylan Hanimeli, B. Lamine, I. Tutusaus and A. Blanchard, *Time-dependent G in Einstein's equations as an alternative to the cosmological constant*, *arXiv e-prints* (Oct, 2019) [arXiv:1910.08325](#), [[1910.08325](#)].
- [88] W. Zhao, B. S. Wright and B. Li, *Constraining the time variation of Newton's constant G with gravitational-wave standard sirens and supernovae*, *JCAP* **2018** (Oct, 2018) 052, [[1804.03066](#)].
- [89] Y. Fukuda, T. Hayakawa, E. Ichihara, K. Inoue, K. Ishihara, H. Ishino et al., *Measurements of the Solar Neutrino Flux from Super-Kamiokande's First 300 Days*, *Physical Review Letters* **81** (Aug., 1998) 1158–1162, [[hep-ex/9805021](#)].
- [90] SNO COLLABORATION collaboration, Q. R. Ahmad, R. C. Allen, T. C. Andersen, J. D. Anglin, G. Bühler, J. C. Barton et al., *Measurement of the rate of $\nu_e + d \rightarrow p + p + e^-$ interactions produced by ^8B solar neutrinos at the sudbury neutrino observatory*, *Phys. Rev. Lett.* **87** (July, 2001) 071301.
- [91] S. Eidelman, K. Hayes, K. Olive, M. Aguilar-Benitez, C. Amsler, D. Asner et al., *Review of Particle Physics*, *Physics Letters B* **592** (2004) 1+.
- [92] P. S. Cooper, *The masses of the neutrinos*, *ArXiv e-prints* (May, 2016) , [[1605.03159](#)].
- [93] A. Strumia and F. Vissani, *Neutrino masses and mixings and...*, *ArXiv High Energy Physics - Phenomenology e-prints* (June, 2006) , [[hep-ph/0606054](#)].
- [94] S. Dodelson, E. Gates and A. Stebbins, *Cold + Hot Dark Matter and the Cosmic Microwave Background*, *ApJ* **467** (Aug, 1996) 10, [[astro-ph/9509147](#)].

- [95] A. J. Nishizawa, *The integrated Sachs-Wolfe effect and the Rees-Sciama effect*, *Progress of Theoretical and Experimental Physics* **2014** (Jun, 2014) 06B110, [1404.5102].
- [96] A. Lewis and A. Challinor, *Weak gravitational lensing of the CMB*, *Physics Reports* **429** (Jun, 2006) 1–65, [astro-ph/0601594].
- [97] J. R. Bond, G. Efstathiou and J. Silk, *Massive neutrinos and the large-scale structure of the universe*, *Physical Review Letters* **45** (Dec., 1980) 1980–1984.
- [98] E. Giusarma, M. Gerbino, O. Mena, S. Vagnozzi, S. Ho and K. Freese, *Improvement of cosmological neutrino mass bounds*, *PRD* **94** (Oct., 2016) 083522, [1605.04320].
- [99] A. J. Cuesta, V. Niro and L. Verde, *Neutrino mass limits: Robust information from the power spectrum of galaxy surveys*, *Physics of the Dark Universe* **13** (Sept., 2016) 77–86, [1511.05983].
- [100] N. Palanque-Delabrouille, C. Yèche, J. Lesgourgues, G. Rossi, A. Borde, M. Viel et al., *Constraint on neutrino masses from SDSS-III/BOSS Ly α forest and other cosmological probes*, *JCAP* **2** (Feb., 2015) 045, [1410.7244].
- [101] F. Beutler, S. Saito, J. R. Brownstein, C.-H. Chuang, A. J. Cuesta, W. J. Percival et al., *The clustering of galaxies in the SDSS-III Baryon Oscillation Spectroscopic Survey: signs of neutrino mass in current cosmological data sets*, *MNRAS* **444** (Nov., 2014) 3501–3516, [1403.4599].
- [102] G.-B. Zhao, S. Saito, W. J. Percival, A. J. Ross, F. Montesano, M. Viel et al., *The clustering of galaxies in the SDSS-III Baryon Oscillation Spectroscopic Survey: weighing the neutrino mass using the galaxy power spectrum of the CMASS sample*, *MNRAS* **436** (Dec., 2013) 2038–2053, [1211.3741].
- [103] J. Lesgourgues and S. Pastor, *Massive neutrinos and cosmology*, *Physics Reports* **429** (July, 2006) 307–379, [astro-ph/0603494].
- [104] A. Kiakotou, Ø. Elgarøy and O. Lahav, *Neutrino mass, dark energy, and the linear growth factor*, *PRD* **77** (Mar, 2008) 063005, [0709.0253].
- [105] A. Lewis, A. Challinor and A. Lasenby, *Efficient Computation of Cosmic Microwave Background Anisotropies in Closed Friedmann-Robertson-Walker Models*, *ApJ* **538** (Aug., 2000) 473–476, [astro-ph/9911177].

- [106] R. E. Smith, J. A. Peacock, A. Jenkins, S. D. M. White, C. S. Frenk, F. R. Pearce et al., *Stable clustering, the halo model and non-linear cosmological power spectra*, *MNRAS* **341** (Jun, 2003) 1311–1332, [[astro-ph/0207664](#)].
- [107] S. Hannestad, *Neutrino physics and precision cosmology*, *ArXiv e-prints* (May, 2016) , [[1605.03829](#)].
- [108] R. Jimenez, T. Kitching, C. Peña-Garay and L. Verde, *Can we measure the neutrino mass hierarchy in the sky?*, *JCAP* **2010** (May, 2010) 035, [[1003.5918](#)].
- [109] C. P. Garay, L. Verde and R. Jimenez, *Neutrino footprint in large scale structure*, *Physics of the Dark Universe* **15** (Mar, 2017) 31–34, [[1602.08430](#)].
- [110] F. Simpson, R. Jimenez, C. Pena-Garay and L. Verde, *Strong Bayesian evidence for the normal neutrino hierarchy*, *JCAP* **2017** (Jun, 2017) 029, [[1703.03425](#)].
- [111] H. Motohashi, A. A. Starobinsky and J. Yokoyama, *Cosmology Based on $f(R)$ Gravity Admits 1 eV Sterile Neutrinos*, *Physical Review Letters* **110** (Mar., 2013) 121302, [[1203.6828](#)].
- [112] J.-h. He, *Weighing neutrinos in $f(R)$ gravity*, *PRD* **88** (Nov., 2013) 103523, [[1307.4876](#)].
- [113] B. Hu, M. Raveri, A. Silvestri and N. Frusciante, *Exploring massive neutrinos in dark cosmologies with *eftcamp*/*EFTCosmoMC**, *PRD* **91** (Mar., 2015) 063524, [[1410.5807](#)].
- [114] J. Harnois-Déraps, D. Munshi, P. Valageas, L. van Waerbeke, P. Brax, P. Coles et al., *Testing modified gravity with cosmic shear*, *MNRAS* **454** (Dec, 2015) 2722–2735, [[1506.06313](#)].
- [115] H. Motohashi, A. A. Starobinsky and J. Yokoyama, *Matter Power Spectrum in $f(R)$ Gravity with Massive Neutrinos*, *Progress of Theoretical Physics* **124** (Sept., 2010) 541–546, [[1005.1171](#)].
- [116] N. Bellomo, E. Bellini, B. Hu, R. Jimenez, C. Pena-Garay and L. Verde, *Hiding neutrino mass in modified gravity cosmologies*, *JCAP* **2** (Feb., 2017) 043, [[1612.02598](#)].
- [117] D. Alonso, E. Bellini, P. G. Ferreira and M. Zumalacárregui, *Observational future of cosmological scalar-tensor theories*, *PRD* **95** (Mar., 2017) 063502, [[1610.09290](#)].

- [118] S. Hagstotz, M. Costanzi, M. Baldi and J. Weller, *Joint halo-mass function for modified gravity and massive neutrinos - I. Simulations and cosmological forecasts*, *MNRAS* **486** (Jul, 2019) 3927–3941, [1806.07400].
- [119] G.-B. Zhao, L. Pogosian, A. Silvestri and J. Zylberberg, *Searching for modified growth patterns with tomographic surveys*, *PRD* **79** (Apr., 2009) 083513, [0809.3791].
- [120] A. Hojjati, L. Pogosian and G.-B. Zhao, *Testing gravity with CAMB and CosmoMC*, *JCAP* **8** (Aug., 2011) 005, [1106.4543].
- [121] A. Zucca, L. Pogosian, A. Silvestri and G.-B. Zhao, *MGCAMB with massive neutrinos and dynamical dark energy*, *JCAP* **1905** (2019) 001, [1901.05956].
- [122] DES Collaboration, T. M. C. Abbott, F. B. Abdalla, S. Avila, M. Banerji, E. Baxter et al., *Dark Energy Survey Year 1 Results: Constraints on Extended Cosmological Models from Galaxy Clustering and Weak Lensing*, *arXiv e-prints* (Oct, 2018) arXiv:1810.02499, [1810.02499].
- [123] A. Peel, V. Pettorino, C. Giocoli, J.-L. Starck and M. Baldi, *Breaking degeneracies in modified gravity with higher (than 2nd) order weak-lensing statistics*, *A&A* **619** (Nov., 2018) A38, [1805.05146].
- [124] C. Giocoli, M. Baldi and L. Moscardini, *Weak lensing light-cones in modified gravity simulations with and without massive neutrinos*, *MNRAS* **481** (Dec., 2018) 2813–2828, [1806.04681].
- [125] J. Merten, C. Giocoli, M. Baldi, M. Meneghetti, A. Peel, F. Lalande et al., *On the dissection of degenerate cosmologies with machine learning*, *MNRAS* **487** (Jul, 2019) 104–122, [1810.11027].
- [126] A. Peel, F. Lalande, J.-L. Starck, V. Pettorino, J. Merten, C. Giocoli et al., *Distinguishing standard and modified gravity cosmologies with machine learning*, *arXiv e-prints* (Oct., 2018) arXiv:1810.11030, [1810.11030].
- [127] S. Hagstotz, M. Gronke, D. Mota and M. Baldi, *Breaking cosmic degeneracies: Disentangling neutrinos and modified gravity with kinematic information*, *arXiv e-prints* (Feb., 2019) arXiv:1902.01868, [1902.01868].
- [128] K. S. Dawson and et al., *The SDSS-IV Extended Baryon Oscillation Spectroscopic Survey: Overview and Early Data*, *The Astronomical Journal* **151** (Feb., 2016) 44, [1508.04473].

- [129] The Dark Energy Survey Collaboration, *The Dark Energy Survey*, *ArXiv Astrophysics e-prints* (Oct., 2005) , [astro-ph/0510346].
- [130] H. Aihara, N. Arimoto, R. Armstrong, S. Arnouts, N. A. Bahcall, S. Bickerton et al., *The Hyper Suprime-Cam SSP Survey: Overview and Survey Design*, *ArXiv e-prints* (Apr., 2017) , [1704.05858].
- [131] DESI Collaboration, A. Aghamousa, J. Aguilar, S. Ahlen, S. Alam, L. E. Allen et al., *The DESI Experiment Part I: Science, Targeting, and Survey Design*, *ArXiv e-prints* (Oct., 2016) , [1611.00036].
- [132] Z. Ivezic, J. A. Tyson, B. Abel, E. Acosta, R. Allsman, Y. AlSayyad et al., *LSST: from Science Drivers to Reference Design and Anticipated Data Products*, *ArXiv e-prints* (May, 2008) , [0805.2366].
- [133] R. Laureijs, J. Amiaux, S. Arduini, J. . Auguères, J. Brinchmann, R. Cole et al., *Euclid Definition Study Report*, *ArXiv e-prints* (Oct., 2011) , [1110.3193].
- [134] R. S. de Jong, O. Bellido-Tirado, C. Chiappini, É. Depagne, R. Haynes, D. Johl et al., *4MOST: 4-metre multi-object spectroscopic telescope*, in *Ground-based and Airborne Instrumentation for Astronomy IV*, vol. 8446 of *Proceedings of the SPIE*, p. 84460T, Sept., 2012. 1206.6885. DOI.
- [135] D. Spergel, N. Gehrels, J. Breckinridge, M. Donahue, A. Dressler, B. S. Gaudi et al., *Wide-Field InfraRed Survey Telescope-Astrophysics Focused Telescope Assets WFIRST-AFTA Final Report*, *ArXiv e-prints* (May, 2013) , [1305.5422].
- [136] V. Martinez and E. Saar, *Clustering statistics in cosmology*, in *Astronomical Data Analysis II* (J.-L. Starck and F. D. Murtagh, eds.), vol. 4847 of *Proceedings of the SPIE*, pp. 86–100, Dec., 2002. astro-ph/0209208. DOI.
- [137] N. Christensen, R. Meyer, L. Knox and B. Luey, *Bayesian methods for cosmological parameter estimation from cosmic microwave background measurements*, *Classical and Quantum Gravity* **18** (July, 2001) 2677–2688, [astro-ph/0103134].
- [138] E. Di Dio, F. Montanari, R. Durrer and J. Lesgourgues, *Cosmological parameter estimation with large scale structure observations*, *JCAP* **1** (Jan., 2014) 042, [1308.6186].
- [139] A. Taruya, *Constructing perturbation theory kernels for large-scale structure in generalized cosmologies*, *PRD* **94** (July, 2016) 023504, [1606.02168].

- [140] B. Bose and K. Koyama, *A perturbative approach to the redshift space power spectrum: beyond the Standard Model*, *JCAP* **8** (Aug., 2016) 032, [1606.02520].
- [141] J. Carlson, M. White and N. Padmanabhan, *Critical look at cosmological perturbation theory techniques*, *PRD* **80** (Aug., 2009) 043531, [0905.0479].
- [142] A. J. S. Hamilton, *Linear Redshift Distortions: a Review*, in *The Evolving Universe* (D. Hamilton, ed.), vol. 231 of *Astrophysics and Space Science Library*, p. 185, Jan, 1998. astro-ph/9708102. DOI.
- [143] C. Alcock and B. Paczynski, *An evolution free test for non-zero cosmological constant*, *Nature* **281** (Oct, 1979) 358.
- [144] N. Kaiser, *Clustering in real space and in redshift space*, *MNRAS* **227** (July, 1987) 1–21.
- [145] J. C. Jackson, *A critique of Rees’s theory of primordial gravitational radiation*, *MNRAS* **156** (Jan, 1972) 1P, [0810.3908].
- [146] A. Taruya, T. Nishimichi and S. Saito, *Baryon acoustic oscillations in 2D: Modeling redshift-space power spectrum from perturbation theory*, *PRD* **82** (Sept., 2010) 063522, [1006.0699].
- [147] M. Trenti and P. Hut, *Gravitational N-body Simulations*, *ArXiv e-prints* (June, 2008) , [0806.3950].
- [148] W. Dehnen and J. I. Read, *N-body simulations of gravitational dynamics*, *European Physical Journal Plus* **126** (May, 2011) 55, [1105.1082].
- [149] M. Kuhlen, M. Vogelsberger and R. Angulo, *Numerical simulations of the dark universe: State of the art and the next decade*, *Physics of the Dark Universe* **1** (Nov., 2012) 50–93, [1209.5745].
- [150] M. Baldi, *Dark Energy simulations*, *Physics of the Dark Universe* **1** (Nov., 2012) 162–193, [1210.6650].
- [151] H. Oyaizu, *Nonlinear evolution of $f(R)$ cosmologies. I. Methodology*, *PRD* **78** (Dec., 2008) 123523, [0807.2449].
- [152] K. C. Chan and R. Scoccimarro, *Large-scale structure in brane-induced gravity. II. Numerical simulations*, *PRD* **80** (Nov., 2009) 104005, [0906.4548].

- [153] F. Schmidt, *Self-consistent cosmological simulations of DGP braneworld gravity*, *PRD* **80** (Aug., 2009) 043001, [0905.0858].
- [154] J. Khoury and M. Wyman, *N-body simulations of DGP and degeneration theories*, *PRD* **80** (Sept., 2009) 064023, [0903.1292].
- [155] B. Li and J. D. Barrow, *N-body simulations for coupled scalar-field cosmology*, *PRD* **83** (Jan., 2011) 024007, [1005.4231].
- [156] G.-B. Zhao, B. Li and K. Koyama, *N-body simulations for $f(R)$ gravity using a self-adaptive particle-mesh code*, *PRD* **83** (Feb., 2011) 044007, [1011.1257].
- [157] B. Li, G.-B. Zhao, R. Teyssier and K. Koyama, *ECOSMOG: an Efficient COde for Simulating MOdified Gravity*, *JCAP* **1** (Jan., 2012) 051, [1110.1379].
- [158] E. Puchwein, M. Baldi and V. Springel, *Modified-Gravity-GADGET: a new code for cosmological hydrodynamical simulations of modified gravity models*, *MNRAS* **436** (Nov., 2013) 348–360, [1305.2418].
- [159] C. Llinares, D. F. Mota and H. A. Winther, *ISIS: a new N-body cosmological code with scalar fields based on RAMSES. Code presentation and application to the shapes of clusters*, *A&A* **562** (Feb., 2014) A78, [1307.6748].
- [160] H. A. Winther, F. Schmidt, A. Barreira, C. Arnold, S. Bose, C. Llinares et al., *Modified gravity N-body code comparison project*, *MNRAS* **454** (Dec., 2015) 4208–4234, [1506.06384].
- [161] J. Adamek, D. Daverio, R. Durrer and M. Kunz, *gevolution: a cosmological N-body code based on General Relativity*, *JCAP* **2016** (Jul, 2016) 053, [1604.06065].
- [162] S. Bose, B. Li, A. Barreira, J.-h. He, W. A. Hellwing, K. Koyama et al., *Speeding up N-body simulations of modified gravity: Chameleon screening models*, *ArXiv e-prints* (Nov., 2016) , [1611.09375].
- [163] A. Barreira, S. Bose and B. Li, *Speeding up N-body simulations of modified gravity: Vainshtein screening models*, *JCAP* **12** (Dec., 2015) 059, [1511.08200].
- [164] H. A. Winther and P. G. Ferreira, *Fast route to nonlinear clustering statistics in modified gravity theories*, *PRD* **91** (June, 2015) 123507, [1403.6492].

- [165] J. Brandbyge, S. Hannestad, T. Haugbølle and B. Thomsen, *The effect of thermal neutrino motion on the non-linear cosmological matter power spectrum*, *JCAP* **2008** (Aug, 2008) 020, [0802.3700].
- [166] M. Viel, M. G. Haehnelt and V. Springel, *The effect of neutrinos on the matter distribution as probed by the intergalactic medium*, *JCAP* **2010** (Jun, 2010) 015, [1003.2422].
- [167] S. Agarwal and H. A. Feldman, *The effect of massive neutrinos on the matter power spectrum*, *MNRAS* **410** (Jan, 2011) 1647–1654, [1006.0689].
- [168] S. Bird, M. Viel and M. G. Haehnelt, *Massive neutrinos and the non-linear matter power spectrum*, *MNRAS* **420** (Mar., 2012) 2551–2561, [1109.4416].
- [169] F. Villaescusa-Navarro, F. Marulli, M. Viel, E. Branchini, E. Castorina, E. Sefusatti et al., *Cosmology with massive neutrinos I: towards a realistic modeling of the relation between matter, haloes and galaxies*, *JCAP* **3** (Mar., 2014) 011, [1311.0866].
- [170] E. Castorina, C. Carbone, J. Bel, E. Sefusatti and K. Dolag, *DEMNUi: the clustering of large-scale structures in the presence of massive neutrinos*, *JCAP* **7** (July, 2015) 043, [1505.07148].
- [171] J. D. Emberson, H.-R. Yu, D. Inman, T.-J. Zhang, U.-L. Pen, J. Harnois-Déraps et al., *Cosmological neutrino simulations at extreme scale*, *Research in Astronomy and Astrophysics* **17** (Aug, 2017) 085, [1611.01545].
- [172] J. Brandbyge and S. Hannestad, *Grid based linear neutrino perturbations in cosmological N-body simulations*, *JCAP* **5** (May, 2009) 002, [0812.3149].
- [173] Y. Ali-Haïmoud and S. Bird, *An efficient implementation of massive neutrinos in non-linear structure formation simulations*, *MNRAS* **428** (Feb., 2013) 3375–3389, [1209.0461].
- [174] J. Liu, S. Bird, J. M. Zorrilla Matilla, J. C. Hill, Z. Haiman, M. S. Madhavacheril et al., *MassiveNuS: cosmological massive neutrino simulations*, *JCAP* **2018** (Mar, 2018) 049, [1711.10524].
- [175] J. Brandbyge and S. Hannestad, *Resolving cosmic neutrino structure: a hybrid neutrino N-body scheme*, *JCAP* **2010** (Jan, 2010) 021, [0908.1969].

- [176] A. Banerjee and N. Dalal, *Simulating nonlinear cosmological structure formation with massive neutrinos*, *JCAP* **11** (Nov., 2016) 015, [1606.06167].
- [177] J. Dakin, J. Brandbyge, S. Hannestad, T. HaugbØlle and T. Tram, *ν CONCEPT: cosmological neutrino simulations from the non-linear Boltzmann hierarchy*, *JCAP* **2019** (Feb, 2019) 052, [1712.03944].
- [178] J. Brandbyge, S. Hannestad, T. HaugbØlle and Y. Y. Y. Wong, *Neutrinos in non-linear structure formation - the effect on halo properties*, *JCAP* **9** (Sept., 2010) 014, [1004.4105].
- [179] E. Castorina, E. Sefusatti, R. K. Sheth, F. Villaescusa-Navarro and M. Viel, *Cosmology with massive neutrinos II: on the universality of the halo mass function and bias*, *JCAP* **2** (Feb., 2014) 049, [1311.1212].
- [180] M. Costanzi, F. Villaescusa-Navarro, M. Viel, J.-Q. Xia, S. Borgani, E. Castorina et al., *Cosmology with massive neutrinos III: the halo mass function and an application to galaxy clusters*, *JCAP* **12** (Dec., 2013) 012, [1311.1514].
- [181] P. Monaco, T. Theuns and G. Taffoni, *The pinocchio algorithm: pinpointing orbit-crossing collapsed hierarchical objects in a linear density field*, *MNRAS* **331** (Apr., 2002) 587–608, [astro-ph/0109323].
- [182] L. A. Rizzo, F. Villaescusa-Navarro, P. Monaco, E. Munari, S. Borgani, E. Castorina et al., *Simulating cosmologies beyond Λ CDM with PINOCCHIO*, *JCAP* **1** (Jan., 2017) 008, [1610.07624].
- [183] J. R. Bond and S. T. Myers, *The Peak-Patch Picture of Cosmic Catalogs. I. Algorithms*, *ApJS* **103** (Mar., 1996) 1.
- [184] R. Scoccimarro and R. K. Sheth, *PTHALOS: a fast method for generating mock galaxy distributions*, *MNRAS* **329** (Jan., 2002) 629–640, [astro-ph/0106120].
- [185] M. Manera, R. Scoccimarro, W. J. Percival, L. Samushia, C. K. McBride, A. J. Ross et al., *The clustering of galaxies in the SDSS-III Baryon Oscillation Spectroscopic Survey: a large sample of mock galaxy catalogues*, *MNRAS* **428** (Jan., 2013) 1036–1054, [1203.6609].
- [186] M. Manera, L. Samushia, R. Tojeiro, C. Howlett, A. J. Ross, W. J. Percival et al., *The clustering of galaxies in the SDSS-III Baryon Oscillation*

- Spectroscopic Survey: mock galaxy catalogues for the low-redshift sample*, *MNRAS* **447** (Feb., 2015) 437–445, [1401.4171].
- [187] M. White, J. L. Tinker and C. K. McBride, *Mock galaxy catalogues using the quick particle mesh method*, *MNRAS* **437** (Jan., 2014) 2594–2606, [1309.5532].
- [188] F.-S. Kitaura, G. Yepes and F. Prada, *Modelling baryon acoustic oscillations with perturbation theory and stochastic halo biasing*, *MNRAS* **439** (Mar., 2014) L21–L25, [1307.3285].
- [189] S. Avila, S. G. Murray, A. Knebe, C. Power, A. S. G. Robotham and J. Garcia-Bellido, *HALOGEN: a tool for fast generation of mock halo catalogues*, *MNRAS* **450** (June, 2015) 1856–1867, [1412.5228].
- [190] S. Tassev, M. Zaldarriaga and D. J. Eisenstein, *Solving large scale structure in ten easy steps with COLA*, *JCAP* **6** (June, 2013) 036, [1301.0322].
- [191] G. Valogiannis and R. Bean, *Efficient simulations of large scale structure in modified gravity cosmologies with COLA*, *ArXiv e-prints* (Dec., 2016) , [1612.06469].
- [192] S. Tassev, D. J. Eisenstein, B. D. Wandelt and M. Zaldarriaga, *sCOLA: The N-body COLA Method Extended to the Spatial Domain*, *ArXiv e-prints* (Feb., 2015) , [1502.07751].
- [193] J. Koda, C. Blake, F. Beutler, E. Kazin and F. Marin, *Fast and accurate mock catalogue generation for low-mass galaxies*, *MNRAS* **459** (June, 2016) 2118–2129, [1507.05329].
- [194] F. Leclercq, J. Jasche and B. Wandelt, *Bayesian analysis of the dynamic cosmic web in the SDSS galaxy survey*, *JCAP* **6** (June, 2015) 015, [1502.02690].
- [195] A. Izard, M. Crocce and P. Fosalba, *ICE-COLA: towards fast and accurate synthetic galaxy catalogues optimizing a quasi-N-body method*, *MNRAS* **459** (July, 2016) 2327–2341, [1509.04685].
- [196] E. Munari, P. Monaco, J. Koda, F.-S. Kitaura, E. Sefusatti and S. Borgani, *Testing approximate predictions of displacements of cosmological dark matter halos*, *ArXiv e-prints* (Apr., 2017) , [1704.00920].
- [197] C.-H. Chuang, C. Zhao, F. Prada, E. Munari, S. Avila, A. Izard et al., *nIFTy cosmology: Galaxy/halo mock catalogue comparison project on clustering statistics*, *MNRAS* **452** (Sep, 2015) 686–700, [1412.7729].

- [198] R. E. Angulo and A. Pontzen, *Cosmological N-body simulations with suppressed variance*, *MNRAS* **462** (Oct., 2016) L1–L5, [1603.05253].
- [199] F. Villaescusa-Navarro, S. Naess, S. Genel, A. Pontzen, B. Wandelt, L. Anderson et al., *Statistical Properties of Paired Fixed Fields*, *ApJ* **867** (Nov., 2018) 137, [1806.01871].
- [200] C. Howlett, M. Manera and W. J. Percival, *L-PICOLA: A parallel code for fast dark matter simulation*, *Astronomy and Computing* **12** (Sept., 2015) 109–126, [1506.03737].
- [201] J. Khoury and A. Weltman, *Chameleon cosmology*, *PRD* **69** (Feb., 2004) 044026, [astro-ph/0309411].
- [202] D. F. Mota and D. J. Shaw, *Evading equivalence principle violations, cosmological, and other experimental constraints in scalar field theories with a strong coupling to matter*, *PRD* **75** (Mar., 2007) 063501, [hep-ph/0608078].
- [203] K. Hinterbichler and J. Khoury, *Screening Long-Range Forces through Local Symmetry Restoration*, *Physical Review Letters* **104** (June, 2010) 231301, [1001.4525].
- [204] K. A. Olive and M. Pospelov, *Environmental dependence of masses and coupling constants*, *PRD* **77** (Feb., 2008) 043524, [0709.3825].
- [205] M. Pietroni, *Dark energy condensation*, *PRD* **72** (Aug., 2005) 043535, [astro-ph/0505615].
- [206] E. Babichev, C. Deffayet and R. Ziour, *k-MOUFLAGE Gravity*, *International Journal of Modern Physics D* **18** (2009) 2147–2154, [0905.2943].
- [207] A. I. Vainshtein, *To the problem of nonvanishing gravitation mass*, *Physics Letters B* **39** (May, 1972) 393–394.
- [208] P. Brax, A.-C. Davis, B. Li and H. A. Winther, *Unified description of screened modified gravity*, *PRD* **86** (Aug., 2012) 044015, [1203.4812].
- [209] P. Brax, A.-C. Davis and B. Li, *Modified gravity tomography*, *Physics Letters B* **715** (Aug., 2012) 38–43, [1111.6613].
- [210] A. Aviles and J. L. Cervantes-Cota, *A Lagrangian perturbation theory for modify gravity*, *ArXiv e-prints* (May, 2017) , [1705.10719].

- [211] H. A. Winther, K. Koyama, M. Manera, B. S. Wright and G.-B. Zhao, *COLA with scale-dependent growth: applications to screened modified gravity models*, *JCAP* **8** (Aug., 2017) 006, [1703.00879].
- [212] S. Saito, M. Takada and A. Taruya, *Impact of massive neutrinos on nonlinear matter power spectrum*, *Phys. Rev. Lett.* **100** (2008) 191301, [0801.0607].
- [213] S. Saito, M. Takada and A. Taruya, *Nonlinear power spectrum in the presence of massive neutrinos: perturbation theory approach, galaxy bias and parameter forecasts*, *Phys. Rev.* **D80** (2009) 083528, [0907.2922].
- [214] Y. Y. Y. Wong, *Higher order corrections to the large scale matter power spectrum in the presence of massive neutrinos*, *JCAP* **10** (Oct., 2008) 035, [0809.0693].
- [215] D. Blas, M. Garny, T. Konstandin and J. Lesgourgues, *Structure formation with massive neutrinos: going beyond linear theory*, *JCAP* **11** (Nov., 2014) 039, [1408.2995].
- [216] D. J. Eisenstein and W. Hu, *Power Spectra for Cold Dark Matter and Its Variants*, *ApJ* **511** (Jan., 1999) 5–15, [astro-ph/9710252].
- [217] H. Oyaizu, M. Lima and W. Hu, *Nonlinear evolution of $f(R)$ cosmologies. II. Power spectrum*, *PRD* **78** (Dec., 2008) 123524, [0807.2462].
- [218] F. Schmidt, M. Lima, H. Oyaizu and W. Hu, *Nonlinear evolution of $f(R)$ cosmologies. III. Halo statistics*, *PRD* **79** (Apr., 2009) 083518, [0812.0545].
- [219] A. De Felice and S. Tsujikawa, *$f(R)$ Theories*, *Living Reviews in Relativity* **13** (Dec., 2010) 3, [1002.4928].
- [220] G. Dvali, G. Gabadadze and M. Porrati, *4D gravity on a brane in 5D Minkowski space*, *Physics Letters B* **485** (July, 2000) 208–214, [hep-th/0005016].
- [221] R. Maartens and K. Koyama, *Brane-World Gravity*, *Living Reviews in Relativity* **13** (Dec., 2010) 5, [1004.3962].
- [222] R. Teyssier, *Cosmological hydrodynamics with adaptive mesh refinement. A new high resolution code called RAMSES*, *A&A* **385** (Apr., 2002) 337–364, [astro-ph/0111367].
- [223] B. Bose, K. Koyama, W. A. Hellwing and G.-B. Zhao, *Theoretical Accuracy in Cosmological Growth Estimation*, *ArXiv e-prints* (Feb., 2017) , [1702.02348].

- [224] V. Springel, *The cosmological simulation code GADGET-2*, *MNRAS* **364** (Dec., 2005) 1105–1134, [[astro-ph/0505010](#)].
- [225] P. S. Behroozi, R. H. Wechsler and H.-Y. Wu, *The ROCKSTAR Phase-space Temporal Halo Finder and the Velocity Offsets of Cluster Cores*, *ApJ* **762** (Jan., 2013) 109, [[1110.4372](#)].
- [226] S. Tassev, M. Zaldarriaga and D. J. Eisenstein, *Solving large scale structure in ten easy steps with COLA*, *JCAP* **6** (June, 2013) 036, [[1301.0322](#)].
- [227] X. Qian and P. Vogel, *Neutrino mass hierarchy*, *Progress in Particle and Nuclear Physics* **83** (Jul, 2015) 1–30, [[1505.01891](#)].
- [228] A. Upadhye, R. Biswas, A. Pope, K. Heitmann, S. Habib, H. Finkel et al., *Large-Scale Structure Formation with Massive Neutrinos and Dynamical Dark Energy*, *Phys. Rev.* **D89** (2014) 103515, [[1309.5872](#)].
- [229] M. C. Cautun and R. van de Weygaert, *The DTFE public software - The Delaunay Tessellation Field Estimator code*, *arXiv e-prints* (May, 2011) [arXiv:1105.0370](#), [[1105.0370](#)].
- [230] P. Virtanen, R. Gommers, T. E. Oliphant, M. Haberland, T. Reddy, D. Cournapeau et al., *SciPy 1.0–Fundamental Algorithms for Scientific Computing in Python*, *arXiv e-prints* (Jul, 2019) [arXiv:1907.10121](#), [[1907.10121](#)].
- [231] M. Simonović, T. Baldauf, M. Zaldarriaga, J. J. Carrasco and J. A. Kollmeier, *Cosmological perturbation theory using the FFTLog: formalism and connection to QFT loop integrals*, *JCAP* **2018** (Apr, 2018) 030, [[1708.08130](#)].
- [232] B. Bose, A. Pourtsidou, K. Marković and F. Beutler, *Assessing non-linear models for galaxy clustering II: model selection and forecasts for Stage IV surveys*, *arXiv e-prints* (May, 2019) [arXiv:1905.05122](#), [[1905.05122](#)].
- [233] P. McDonald and A. Roy, *Clustering of dark matter tracers: generalizing bias for the coming era of precision LSS*, *JCAP* **2009** (Aug, 2009) 020, [[0902.0991](#)].
- [234] F. Beutler, S. Saito, H.-J. Seo, J. Brinkmann, K. S. Dawson, D. J. Eisenstein et al., *The clustering of galaxies in the SDSS-III Baryon Oscillation Spectroscopic Survey: testing gravity with redshift space distortions using the power spectrum multipoles*, *MNRAS* **443** (Sep, 2014) 1065–1089, [[1312.4611](#)].

- [235] F. Beutler, H.-J. Seo, S. Saito, C.-H. Chuang, A. J. Cuesta, D. J. Eisenstein et al., *The clustering of galaxies in the completed SDSS-III Baryon Oscillation Spectroscopic Survey: anisotropic galaxy clustering in Fourier space*, *MNRAS* **466** (Apr, 2017) 2242–2260, [1607.03150].
- [236] K. C. Chan, R. Scoccimarro and R. K. Sheth, *Gravity and large-scale nonlocal bias*, *PRD* **85** (Apr, 2012) 083509, [1201.3614].
- [237] T. Baldauf, U. Seljak, V. Desjacques and P. McDonald, *Evidence for quadratic tidal tensor bias from the halo bispectrum*, *PRD* **86** (Oct, 2012) 083540, [1201.4827].
- [238] S. Saito, T. Baldauf, Z. Vlah, U. Seljak, T. Okumura and P. McDonald, *Understanding higher-order nonlocal halo bias at large scales by combining the power spectrum with the bispectrum*, *PRD* **90** (Dec, 2014) 123522, [1405.1447].
- [239] K. Markovic, B. Bose and A. Poursidou, *Assessing non-linear models for galaxy clustering I: unbiased growth forecasts from multipole expansion*, *arXiv e-prints* (Apr, 2019) arXiv:1904.11448, [1904.11448].
- [240] B. Bose, K. Koyama and H. A. Winther, *Assessing non-linear models for galaxy clustering III: theoretical accuracy for stage IV surveys*, *JCAP* **2019** (Oct, 2019) 021, [1905.05135].
- [241] R. K. Sheth, *The distribution of pairwise peculiar velocities in the non-linear regime*, *MNRAS* **279** (Apr, 1996) 1310, [astro-ph/9511068].
- [242] A. Lewis, *GetDist: a Python package for analysing Monte Carlo samples*, *arXiv e-prints* (Oct, 2019) arXiv:1910.13970, [1910.13970].
- [243] B. Bose, K. Koyama, M. Lewandowski, F. Vernizzi and H. A. Winther, *Towards precision constraints on gravity with the Effective Field Theory of Large-Scale Structure*, *JCAP* **2018** (Apr, 2018) 063, [1802.01566].
- [244] W. A. Hellwing, M. Bilicki and N. I. Libeskind, *Uneven flows: On cosmic bulk flows, local observers, and gravity*, *PRD* **97** (May, 2018) 103519, [1802.03391].
- [245] B. Bose and A. Taruya, *The one-loop matter bispectrum as a probe of gravity and dark energy*, *JCAP* **2018** (Oct, 2018) 019, [1808.01120].
- [246] H. Winther, S. Casas, M. Baldi, K. Koyama, B. Li, L. Lombriser et al., *Emulators for the non-linear matter power spectrum beyond Λ CDM*, *arXiv e-prints* (Mar, 2019) arXiv:1903.08798, [1903.08798].

- [247] K. Naidoo, L. Whiteway, E. Massara, D. Gualdi, O. Lahav, M. Viel et al., *Beyond two-point statistics: using the minimum spanning tree as a tool for cosmology*, *MNRAS* **491** (Jan, 2020) 1709–1726, [1907.00989].
- [248] B. Bose, A. Pourtsidou, S. Casas, L. Lombriser, Q. Xia, M. Cataneo et al., *Hybrid $P_\ell(k)$: general, unified, non-linear matter power spectrum in redshift space*, *arXiv e-prints* (Nov, 2019) arXiv:1911.04391, [1911.04391].
- [249] F. Villaescusa-Navarro, P. Bull and M. Viel, *Weighing Neutrinos with Cosmic Neutral Hydrogen*, *ApJ* **814** (Dec, 2015) 146, [1507.05102].
- [250] E. Bellini and I. Sawicki, *Maximal freedom at minimum cost: linear large-scale structure in general modifications of gravity*, *JCAP* **2014** (Jul, 2014) 050, [1404.3713].
- [251] S. Tsujikawa, *The effective field theory of inflation/dark energy and the Horndeski theory*, *Lect. Notes Phys.* **892** (2015) 97–136, [1404.2684].
- [252] P. Brax, A.-C. Davis, B. Li, H. A. Winther and G.-B. Zhao, *Systematic simulations of modified gravity: chameleon models*, *JCAP* **4** (Apr., 2013) 029, [1303.0007].
- [253] P. Brax, A.-C. Davis, B. Li, H. A. Winther and G.-B. Zhao, *Systematic simulations of modified gravity: symmetron and dilaton models*, *JCAP* **10** (Oct., 2012) 002, [1206.3568].
- [254] A. De Felice and S. Tsujikawa, *$f(R)$ Theories*, *Living Reviews in Relativity* **13** (June, 2010) 3, [1002.4928].
- [255] W. Hu and I. Sawicki, *Models of $f(R)$ cosmic acceleration that evade solar system tests*, *PRD* **76** (Sept., 2007) 064004, [0705.1158].
- [256] B. Bose and K. Koyama, *A perturbative approach to the redshift space power spectrum: beyond the Standard Model*, *JCAP* **8** (Aug., 2016) 032, [1606.02520].
- [257] P. Brax, C. van de Bruck, A.-C. Davis and D. Shaw, *Dilaton and modified gravity*, *PRD* **82** (Sept., 2010) 063519, [1005.3735].